The Effect of Primary Blast Shock Wave on Skeletal Muscle



Robert Michal Taylor Staruch
Magdalen College
University of Oxford

A thesis submitted for the degree of
Doctor of Philosophy
Michaelmas 2022

© Crown copyright (2023), Dstl and Royal Centre for Defence Medicine. This material is licensed under the terms of the Open Government Licence except where otherwise stated. To view this licence, visit https://www.nationalarchives.gov.uk/doc/open-government-licence/version/3/ or write to the Information Policy Team, The National Archives, Kew, London TW9 4DU, or email: psi@nationalarchives.gsi.gov.uk.

This thesis is dedicated to members of the Armed Forces who have injured whilst serving in Her Majesty's Armed Forces, and those who will be injured in wars to come.

This work is driven by the personal ambition that part of this work, or subsequent future work may contribute to improving the care given to combat casualties, or those injured in conflict.

"Oh, I get by with a little help from my friends
Mm, gonna try with a little help from my friends"

Lennon & McCartney
The Beatles

Acknowledgements

I would like to acknowledge the following organisations that funded and enabled this work: The Defence Science & Technology Laboratories (Dstl), The Defence Medical Services (DMS), The Academic Department of Military Surgery and Trauma (ADMST), The Engineering Physical Sciences Research Council (EPSRC) and The Drummond Foundation.

Firstly, I am grateful to Surgeon Captain Professor Rory Rickard for providing me with much needed military academic mentorship, and giving me 'plenty of rope' to explore science during my surgical career.
Dr Abigail Spear has been inspirational in training and guiding me to be a better scientist. I am so lucky for her friendship and guidance.
Dr Andrew Sedman been a fountain of knowledge, support and an enthusiastic tutor on the subject of blast, shock waves and shock tubes.
Sara Macildowie and Lucy Cork have been invaluable in helping perform experimental work at Dstl (and in sharing parenting tips), without them this work would never have come to fruition.

In Oxford, I am grateful to Professor Mark Thompson for allowing me the opportunity to study at Oxford University and pursue this novel research idea within the Engineering Department.

Professor Sarah Snelling and her research group have provided no end of support, training and donuts in understanding RNA sequencing and computational analysis. She has been a fantastic scientific inspiration and confidante!

I am incredibly grateful to Professor Robin Cleveland. He has not only patiently developed my mind as a postgraduate engineer, but has been a valuable sounding board for numerous research discussions. The BUBBL group have provided a friendly supportive environment in the latter parts of my thesis.

Finally I would like to personally thank Dr Jolet Mimpen – who was a much needed support, scientific teacher and friend in the latter development of this thesis.

Major's Matt Wordsworth & Rachel Howes, fellow Military Plastic Surgeons, deserve medals for the numerous coffee and phone chats that took place when the going got tough!

I am truly grateful to the band of Magdalen College postgraduates and rowers who I befriended in year 1. Thomas Kirk, Adam Barker, Steven Ettema, Toby McCarroll and Ercole Durini Du Monza to name but a few.

My parents and brother: Barbara, Stash and Maz, have continued to be a beacon of encouragement throughout the past 4 years. They taught me the value of hard work as a child. My father also said knowledge is the only thing that cannot be taken away from you. I have remembered this quote daily during this work. This thesis is for them.

Celia and Michael Beverly, my in laws, have shown incredible generosity, patience, interest and help during the last 4 years, pastorally and academically. Thank you.

I owe my wife Anair Beverly everything. She is patient, kind and has given me so much to allow me to finish this work. Thank you Anair for everything, my love for you knows no bounds. I am so grateful of our life together.

Finally to Orielle & Amelie – the two greatest outputs from this thesis and achievements of my life. I hope whatever dreams and aspirations you have as children come to fruition. You have blessed my world since your arrival.

Other Work

The Pandemic of 2020-2021 had wide ranging effects on the work conducted in this thesis. On one hand it provided a time for reflection and appraisal of the initial experimental approaches adopted in this work. However it also provided new constraints to experimental work that reduced the depth and extent of work that could be conducted. The period also presented new opportunities for research and innovation. I instigated and lead two University COVID projects. The first, a ventilator development project, became part of the UK's Ventilator Challenge. Oxvent secured £8 million of government funding for manufacture with Smith & Nephew PLC. A detailed overview of this project can be found at the Magdalen College webinar, or in the publication in *Lancet ebiomedicine*. The Oxvent was the winner of the Institute for Engineering & Technology (IET) Global Challenge award in 2020.

The second COVID project was the design, development and implementation of a website to facilitate route optimisation of housebound patients for the COVID vaccination programme. 'Vaximap' (www.vaximap.org), provides a free online tool to enable community healthcare workers to upload and download optimised routes to conduct home visits in the community. This tool has been utilised to visit (and vaccinate) over 530,459 patients in the UK. The project received funding and support from Magdalen College, Oxford University Innovation and JHUB MED. Full details of Vaximap's deployment can be found in the publication in *NPJ Digital Medicine*.

During this period I also was involved in the Steering group of the James Lind Alliance research priority setting partnership for Burn injury lead by Professor Amber Young. This work is ongoing, but has received over 1600 responses from 70 countries around the world. The protocol for this work can be read in BMJ Open. This work has taken on new importance due to the passing of its leader, Professor Amber Young, who died from Breast Cancer in 2022. She had become a mentor and friend.

Oxvent Links
Ebiomedicine - http://bitly.ws/xhAX
Webinar - http://bitly.ws/xhB5

Vaximap Links
Vaximap - https://www.vaximap.org
Publication - http://bitly.ws/xVSq

Burns PSP
Protocol - http://bitly.ws/xhBi

Abstract

Explosives continue to be one of the main mechanisms of injury of military personnel and civilians in conflict zones. The range of explosive devices (e.g., mines, artillery shells, improvised explosive devices (IEDs) and grenades) and the variety of environments in which they detonate (e.g., buried in the ground, on the surface, in the air or in confined spaces) means that the mechanical insult to the body and the subsequent injuries are highly variable. One unexplained phenomenon that can follow a blast injury is progressive tissue loss (PTL) in which apparently healthy soft tissue decays in the days and weeks afterwards. The overarching goal of this thesis is to study the effects of primary blast shock wave on the cellular microenvironment of skeletal muscle, in order to understand the role that a blast wave has on the onset of PTL. RNA analysis was carried out on legacy tissue samples from two in vivo experiments involving the exposure of skeletal muscle to a shock wave. The analysis showed that there were several common pathways between the models, and no single mechanism of cell death predominated. Instead, apoptosis, necrosis and necroptosis were upregulated to similar degrees. Therefore indicating that there is a cellular response in skeletal muscle when exposed to a blast wave.

Following a review of the literature a 3D model of skeletal muscle was developed by seeding a hydrogel with muscle cells, which demonstrated alignment and myotube fusion after 13 days. Sequencing of the hydrogel RNA revealed expression of key myotube differentiation markers, including Myosin heavy chain isoforms, Paired box proteins 7 and Myogenin. The 3D model was attached to deformable posts and the deflection of the post used to determine the tension generated by the muscle model. Hydrogen peroxide was used as a positive control for injury and the response was characterised using metabolic and RNA sequencing data.

The response of the 3D hydrogels to a blast wave was investigated by placing them in an explosively-driven frustum shock tube. The tube was calibrated for a range of explosive charges and measurements showed that 30 g of PE7 explosive produced a blast wave at the target location with a peak overpressure of 697 kPa and a positive phase duration of $2.39 ms^{-1}$. The blast wave was equivalent to 3.23 kg-TNT at 2 m (assuming a hemispherical blast) and using a blast lethality model was predicted to be more than 50% lethal. A charge of 5 g produced a blast wave that was predicted to be non-lethal. Skeletal muscle hydrogels showed different responses to explosive loading: the 30 g charge resulted in a significant drop in cellular metabolic activity at 2 hours which failed to return to baseline by day 7. The 5 g charge resulted in an increase in metabolic activity over baseline by day 7 indicating that the cells has recovered. There was no detectable change in the tension generated by the hydrogels for either blast condition.

In conclusion, this thesis has demonstrated that there is cellular injury from primary blast shock waves, reflected in alterations in metabolic activity and creatinine kinase release, and that this cellular response can be seen in analysis of *in vivo* tissue samples and captured with a 3D *in vitro* tissue scaffold model using an experimental blast tube. This suggest that primary blast wave could be responsible for initiating the signalling pathway that results in PTL.

Contents

Table of contents	Title		Page
1	**Chapter One**	An Overview of Blast Injury	
1.1	Introduction		18
1.2	Primary Blast Injury		23
1.2.1	'Idealised' Air blast Waves – The Modified Friedlander Equation		23
1.2.2	Factors affecting real life blast waves		26
1.2.2.1	Energy Source		26
1.2.2.2	Explosive quantity and distance		26
1.2.2.3	Charge geometry		30
1.2.2.4	Charge encasement		30
1.3	Blast wave interaction with an object		30
1.3.1	Idealised blast waves interacting with an object		31
1.3.2	Complex blast waves and real scenarios		32
1.4	Evaluating existing physical platforms to investigate the mechanobiology of blast		32
1.5	Designing tissue models to measure the molecular and cellular response to the blast		36
1.6	Choosing models of tissue for blast-relevant mechanobiological study		40
1.7	Aims of this thesis		42
2	**Chapter Two**	Application of Bulk RNA Sequencing to Blast Exposed Skeletal Muscle From Two Different In Vivo Models.	
2.1	Introduction		45
2.1.1	How could mechanotransduction contribute to PTL after blast?		45
2.1.2	What kind of cell death is progressive tissue loss?		46
2.1.3	Unbiased techniques for transcriptome analysis		47
2.2	Methods		49
2.2.1	Porcine Model		49
2.2.1.1	Injury		51
2.2.1.2	Endpoints		51
2.2.2	Rabbit Model		52
2.2.3	Bulk RNA Sequencing		53
2.2.3.1	RNA Homogenisation		53
2.2.3.2	RNA Quality Control		54
2.2.3.3	Library Preparation		54
2.2.4	Experimental Methodology for DESeq2 data analysis		54
2.2.4.1	Analysis in R		55
2.2.4.2	DESEQ2 data adjustments		55
2.2.4.3	Data Normalisation		56
2.2.5	Adaptations of pathway analysis		56
2.2.5.1	Cell death enrichment analysis		57
2.3	Results		58
2.3.1	Alignment, dispersion & variance		58
2.3.1.1	Porcine sample distribution		59
2.3.1.2	Rabbit sample distribution		61
2.3.2	Changes in gene expression in skeletal muscle exposed to shock wave		63
2.3.2.1	Porcine model		63
2.3.2.2	Rabbit model		63
2.3.2.3	Top 25 genes of significance		65
2.3.2.4	Hallmark Gene set enrichment analysis		68
2.3.3	Investigating inter-model differences in cell death		70

2.3.3.1	Apoptosis		70
2.3.3.2	Necroptosis		71
2.3.3.3	Necrosis		71
2.4	Discussion		74
2.4.1	Investigating inter model differences		74
2.4.2	Cell death mechanisms		75
2.4.3	The feasibility of RNA-seq for probing blast shock wave		78
2.4.4	Limitations		79
2.5	Conclusions		81
3	**Chapter Three**	A Systematic Review of Three-Dimensional Models of Skeletal Muscle Under Tension and Methods to Induce Traumatic Injury.	
3.1	Introduction		83
3.2	Methods		85
3.2.1	Search Strategy		85
3.2.2	Inclusion & Exclusion criteria		85
3.2.2.1	Inclusion criteria		85
3.2.2.2	Exclusion criteria		86
3.2.3	Study Selection		86
3.2.4	Outcomes		87
3.2.5	Data Extraction		87
3.2.6	Quality assessment		87
3.2.7	Office of Health assessment and translation (OHAT) risk of bias tool		87
3.3	Results		89
3.3.1	Study Characteristics		100
3.3.2	Study demographics – Models without injury		100
3.3.2.1	Models without injury – Hydrogel Manufacture		100
3.3.2.2.	Models without injury - Imaging		101
3.3.2.3	Models without injury – Quantitative Reverse Transcription Polymerase Chain Reaction (qRT-PCR) Differentiation Primers		101
3.3.3	Study demographics – Models with injury		103
3.3.3.1	Model with injury – Hydrogel Manufacturer		103
3.3.3.2	Model with injury – Imaging		103
3.3.3.3	Model with injury - Quantitative Reverse Transcription Polymerase Chain Reaction (qRT-PCR) Differentiation Primers		104
3.3.3.4	Model with injury – Injury Mechanism		104
3.3.3.5	Model with injury – Injury Duration		104
3.3.3.6	Force quantification		106
3.3.4	Outcome reporting in models		107
3.3.5	Quality of reporting in included studies		109
3.6	Discussion		112
3.6.1	Reporting of details of force generation – standard reporting		114
3.6.2	Outcome measurements		115
3.6.3	Contextualising and characterising injury models.		116
3.6.4	Implications for model development for trauma		118
3.6.5	Limitations		118
3.7	Conclusions & Future directions		119

4	**Chapter Four**	Development and Validation Of A Three Dimensional *in vitro* Model Of Skeletal Muscle For Blast Loading.	
4.1		Introduction	121
4.2.		Methods	123
4.2.1		Cell culture media	123
4.2.2		Routine maintenance of cell lines	123
4.2.3		Skeletal muscle hydrogel fabrication and differentiation	124
4.2.4		Post & Jig manufacture	125
4.2.5		Metabolic assessment	126
4.2.6		RNA Homogenisation from hydrogels	127
4.2.7		RNA Extraction from hydrogels	127
4.2.8		Library Preparation & Sequencing	128
4.2.9		Bulk RNA sequencing analysis	129
4.2.10		Housekeeping gene identification	129
4.2.11		Imaging	130
4.2.12		Immunofluorescence staining	130
4.2.13		Volume Measurements	130
4.2.14		Deflection Measurements	131
4.2.15		Analytic Model	131
4.2.16		Finite Element Model	134
4.2.17		Hydrogen Peroxide injury	136
4.2.17.1		Monolayer injury	136
4.2.17.1.1		Apoptosis/Necrosis Stain	136
4.2.17.1.2		Bulk Sequencing	136
4.2.17.2		3D Model injury	137
4.2.17.2.1		Cell metabolism	137
4.2.17.2.2		Post deflection	137
4.2.17.2.3		Bulk sequencing	137
4.3		Results	138
4.3.1		Skeletal muscle model characterisation	138
4.3.2		Functional Characterisation	140
4.3.3		Analysis Of Skeletal Muscle Differentiation in 3D cultures	142
4.3.4		Development of an injury protocol for 3D muscle constructs	144
4.3.4.1		Analysis of injury after H_2O_2 treatment in monolayers	144
4.3.4.2		Analysis of H2O2 injury in 3D constructs	147
4.3.5		Gene Transcription after Hydrogen Peroxide injury	149
4.3.5.1		Expression of genes associated with apoptosis, necroptosis and necrosis.	152
4.3.6		Evaluating gene expression over time	153
4.3.6.1		Likelihood ratio test	154
4.3.7		Regenerative capacity	157
4.4		Discussion	158
4.4.1		Model Optimisation	158
4.4.2		Model Characterisation	159
4.4.3		Functional Characterisation	160
4.4.4		Development of injury model	161
4.4.5		Bulk sequencing shows changes in gene expression at different timepoints after injury	162
4.4.6		Programmed cell death	163
4.4.7		Skeletal muscle regeneration	164
4.4.8		Limitations	164
4.5		Conclusions	166

5	**Chapter Five**	Development Of A Frustum Pyramidal Shock Tube For Cell Culture.	
5.1	Introduction		168
5.1.1	Review of blast parameters and other shock tubes		169
5.1.2	Improvised explosive device		169
5.1.3	Existing shock tubes		170
5.2	Considerations for design of a conical shock tube		171
5.2.1	Target size		171
5.2.2	Frustum Geometry		172
5.2.3	Calculation of Blockage Ratio		173
5.2.4	Cross sectional shape		173
5.2.5	Tube design downstream of the target		174
5.2.6	Truncation of the tube		175
5.3	Shock tube construction		175
5.3.1	Gauges		178
5.3.1.1	Shock tube mounted gauges		178
5.3.1.2	Target arm mounted gauges		179
5.4	Development of Flexible tissue culture plate		180
5.5	Validation of Frustum Shock Tube		182
5.5.1	Commissioning trial		182
5.5.2	Peak pressure and driver charge mass		182
5.5.3	Characterisation tests		185
5.5.4.	Tube Characterisation		188
5.6	Design considerations of Culture Plate		191
5.7	Discussion		193
5.8	Conclusions		197
6	**Chapter Six**	The effect Of Primary Shock Wave On Skeletal Muscle *in vitro*.	
6.1	Introduction		199
6.2	Methods		200
6.2.1	Explosive trial Logistics		200
6.2.1.1	Trial Methodology		200
6.2.1.2	Target		200
6.2.1.3	Silicone Culture Mould		201
6.2.1.5	Cell Culture Logistics		201
6.2.1.4	Experimental Power		202
6.2.2	Trial Methodology		203
6.2.2.1	Loading silicone moulds		203
6.2.2.2	Treatment plates		204
6.2.2.3	Control Plates		204
6.2.3	Post blast exposure analysis		204
6.2.3.1	Timepoints		204
6.2.3.2	Metabolic assessment		205
6.2.3.3	Cell culture media		205
6.2.3.4	RNA Preservation		206
6.2.3.5	RNA Extraction		206
6.2.3.6	Library Preparation and Sequencing		206
6.2.3.7	Storage for Imaging		207
6.2.3.8	Creatinine Kinase		207
6.3	Results		208
6.3.1	Experimental power		208
6.3.2	Cell metabolism		210
6.3.3	Creatinine Kinase		212
6.4	Discussion		213

	6.5	Conclusions	217
7		**Chapter 7** Conclusions & Future Directions	
	7.1	An overview of Blast	220
	7.2	Association of Bulk RNA Sequencing to Blast Exposed Skeletal Muscle from Two different In Vivo Models.	221
	7.3	A Systematic Review of Three Dimensional Models of Skeletal Muscle under Tension and Methods to Induce Traumatic Injury.	222
	7.4	Development and validation of a three dimensional *in vitro* model of skeletal muscle for blast loading	223
	7.5	Development of a Frustum Pyramidal Shock Tube for Cell Culture.	225
	7.6	A model to assess effects of primary shock wave on *in vitro* skeletal muscle.	225
	7.7	Future Directions	226
	7.8	Conclusion	228
		Appendices	
		All appendix material can be found at the following Repository	
		https://robstaruchox.github.io/appendix/	

List of Figures

Chapter One	Page
Figure 1.1: Classes of Blast injury (Primary to Quinary) as defined by Zuckerman. The fifth category has been added to the figure.	Page 21
Figure 1.2: Representative images of soft tissue damage from blast injury.	Page 22
Figure 1.3: Plot of curve generated from the Modified Friedlander equation.	Page 25
Figure 1.4: Figure outlining Spherical Free Air Burst (SFAB) and a Hemispherical Surface Burst (HSB).	Page 27
Figure 1.5: Illustrative plot of the influence of distance and charge size on peak pressure, and the form of the Modified Friedlander curve.	Page 28
Figure 1.6: Diagram of a soldier's proximity to a real life scenario explosion, a buried device, and the potential boundaries of the near field (orange), midfield (green) and far-field (blue).	Page 29
Chapter Two	
Figure 2.1: Outline of cell death pathways.	Page 48
Figure 2.2: Timeline of interventions in porcine blast trials.	Page 50
Figure 2.3: Timeline of experimental procedures for rabbit model.	Page 53
Figure 2.4: Pictorial demonstration of matching Human ensembl ID's to Gene ID's.	Page 57
Figure 2.5: Porcine sample analysis.	Page 60
Figure 2.6: Rabbit sample analysis.	Page 62
Figure 2.7: Volcano plot showing differential gene expression blast vs control in the Porcine model	Page 64
Figure 2.8: Volcano plot showing differential gene expression blast vs control in the Rabbit model	Page 64
Figure 2.9: Dot plot of gene set enrichment analysis on both species.	Page 69
Figure 2.10: Venn diagrams of gene overlap & heatmaps of gene expression for different cell death mechanisms.	Page 72
Figure 2.11: Bar charts of gene expression in each cell death mechanism. The percentage of significant genes, non-significant genes and those not found in the analysis are represented.	Page 73
Chapter Three	
Figure 3.1: PRISMA flowchart of included studies	Page 89
Figure 3.2: Model Characteristics of studies without injury	Page 102
Figure 3.3: Model Characteristics of studies with injury	Page 105
Figure 3.4: Outcome reporting in standard models	Page 108
Figure 3.5: Outcome reporting in standard models	Page 108
Chapter Four	
Figure 4.1: Representative images of silicone casting moulds for hydrogel model.	Page 124
Figure 4.2: Dimensions of 3D printed post.	Page 125
Figure 4.3: Outline of muscle model and attachment to posts.	Page 131
Figure 4.4: Representative diagram of the deflection of a cantilever beam, length l, when subject to a distributed load over a length l-a.	Page 132
Figure 4.5: Outline of distributed load from muscle hydrogel constructs on posts.	Page 133
Figure 4.6: Finite Element Model..	Page 134
Figure 4.7: Output of analytic model	Page 135
Figure 4.8: Characterisation of 3D *in vitro* model of Skeletal Muscle.	Page 139
Figure 4.9: Plot of post to post distance in *in vitro* hydrogels over time.	Page 140
Figure 4.10: An analytic model was used to estimate the deflection of a partially distributed load of various dimensions along a cantilever beam fixed at one end.	Page 141
Figure 4.11: Heatmap of log2fold change of genes associated with skeletal muscle differentiation expressed in 3D hydrogels over 13 days of culture.	Page 143
Figure 4.12: Percentage in C2C12 monolayer metabolism after hydrogen peroxide injury for a range of concentrations.	Page 145
Figure 4.13: Representative images of Apoptosis/Necrosis stain in monolayer cultures after exposure to Hydrogen Peroxide.	Page 146

Figure 4.14: Bar chart of genes with significant changes in log 2 fold expression associated with gene sets for apoptosis, necroptosis and necrosis. Page 146
Figure 4.15: Bar plot of metabolic changes of C2C12 hydrogels after exposure to H_2P_2 injury. Error bars are standard deviation. Page 148
Figure 4.16: Line graph of changes to hydrogel length after exposure of hydrogel to hydrogen peroxide. Page 148
Figure 4.17: Volcano plot of gene expression at timepoints after injury with Hydrogen Peroxide. Page 150
Figure 4.18: Dot plots of up and down regulated biological processes at 4 hours and 7 days after hydrogen peroxide injury. Page 151
Figure 4.19: Heatmaps of significant changes in log2fold in genes found in cell death. Page 152
Figure 4.20: Line graph of gene expression for the top 10 significantly expressed genes Page 153
Figure 4.21: Cluster diagrams from liklihood ratio test analysis of injury experimental data. Page 156
Figure 4.22: Gene changes associated with skeletal muscle regeneration. Page 157

Chapter Five

Figure 5.1: Literature shock tube data (duration and peak overpressure) overlaid on Bowen Curves of lethality. Page 171
Figure 5.2: Schematic of proposed shock tube. Page 176
Figure 5.3: Representative image of shock tube with sample arm inserted. Page 176
Figure 5.4 Pictures of Shock tube during Trials. Page 177
Figure 5.5: Location of mounted gauges on shock tube. Page 178
Figure 5.6: Pictures of target mounted pressure plate with gauges 6,7,8,9 Page 180
Figure 5.7: Trial 1: Peak incident pressure and driver charge mass Page 183
Figure 5.8: Bowen curves with calibration data. Page 184
Figure 5.9: Section of (unfiltered) pressure records for incident pressure gauges mounted at target location (target removed). Page 186
Figure 5.10: Section of (unfiltered) pressure records for incident pressure gauges mounted at target location (target removed). Page 187
Figure 5.11: Bowen curves with peak overpressure & duration data from high (green dots) and low (red cross) blast exposure groups. Page 187
Figure 5.12: Roof gauge pressure plotted against measured incident pressure. Page 189
Figure 5.13: Reflection coefficient of Measured Incident Pressures. Page 189
Figure 5.14: Low pressure data recorded from 4 gauges on target plate Page 190
Figure 5.15: High pressure data recorded from 4 gauges on target plate. Page 190
Figure 5.16: Schematic of mould for cell culture plate Page 191
Figure 5.17: Picture of Silicone plate Page 192

Chapter Six

Figure 6.1: Layout of samples in cell culture plate for trial. Page 202
Figure 6.2: Power curve of hydrogels. Page 208
Figure 6.3: Shock tube set up. Page 209
Figure 6.4: Cell Metabolism of treated and control samples. Page 211
Figure 6.5: Creatinine Kinase on treatment and control samples Page 212

List of Tables

Chapter One	Page
Table 1.1 : Advantages and disadvantages of current experimental platforms employed for *in vitro* blast research.	Page 35
Table 1.2: Considerations for future experimental design for exploring the mechanobiology of blast	Page 38
Table 1.3: Review of *in vitro* model types, their advantages and disadvantages for studying the mechanobiology of primary blast.	Page 39
Chapter Two	
Table 2.1: Nomenclatures for groups in experimental data sets.	Page 54
Table 2.2: Top 25 significantly expressed genes in Porcine model.	Page 66
Table 2.3: Top 25 significantly expressed genes in Rabbit model.	Page 67
Chapter Three	
Table 3.1: The OHAT Risk of bias questions.	Page 88
Table 3.2: 3D *in vitro* models under tension. Table of included studies and model information (Author, Year, Post materials, cell type).	Page 90-92
Table 3.3: 3D *in vitro* models under tension. Table of included studies and outcome data recorded in studies.	Page 93-96
Table 3.4: 3D *in vitro* models with an injury. Table of included studies and model information (Author, Year, Post materials, cell type).	Page 97
Table 3.5: 3D *in vitro* models with an injury. Table of included studies and Outcome data.	Page 98-99
Table 3.6: Table of force generation *characteristics from standard models*	Page 106
Table 3.7: Table of force generation characteristics from Injury Models.	Page 107
Table 3.8: Assessment of risk of bias in included standard model studies using the OHAT tool.	Page 110
Table 3.9: Assessment of risk of bias in included injury model studies using the OHAT tool	Page 111
Chapter Four	
Table 4.1: Top 10 Significant Genes at 4 hours	Page 154
Table 4.2: Top 10 Significant Genes at Day 7	Page 154
Chapter Five	
Table 5.1: The explosive capacity is expressed at TNT equivalence	Page 169
Table 5.2: Literature shock tube data	Page 170
Table 5.3: Parameters of tube.	Page 173
Table 5.4: Design considerations of shock tube	Page 174
Table 5.5: Design considerations of culture plate	Page 181
Table 5.6: Table of charge mass and peak incident overpressure (in kPa) measured by the pencil gauges on the target arm in the tube.	Page 183
Chapter Six	
Table 6.1: Proposed sample requirements for analysis.	Page 206

List of Abbreviations

2D	Two Dimensions
3D	Three Dimensions
ADP	Adenosine diphosphate
ANOVA	Analysis of Variance
Atm	Atmosphere
ATP	Adenosine Triphosphate
BH	Benjamini-Hockberg correction
BP	Biological Processes
C2C12	Mus Musculus cell line that is a sub clone from a myoblast line established from normal adult C3H mouse leg muscle1
CC	Cellular Component
cDNA	Complementary Deoxyribonucleic Acid
CK	Creatinine Kinase
DAPI	4′,6-diamidino-2-phenylindole
DM	Differentiation Media
DMEM	Dulbecco's Modified Eagle Medium
DMSO	Dimethyl Sulfoxide
DNA	Deoxyribonucleic Acid
DstI	Defence Science & Technology Laboratories
E	Elastic modulus
ECG	electrocardiogram
ECM	Extracellular Matrix
EDC	Ethylene Dichloride
ESWT	Extracorpeal shock wave therapy
FBS	Foetal Bovine Serum
FDM	Fused deposition modelling
FDR	False discovery rate
FEA	Finite Element Analysis
FEM	Finite Element Model
g	Grams
GM	Growth Media
GMP	Good Manufacturing Practice
GSEA	Gene set enrichment analysis
H&E	Haemotoxylin & Eosin
H_2O_2	Hydrogen Peroxide
HSB	Hemispherical Surface Burst
I	Second moment of the area
ID	Identification
IDRM	Institute of Development & Regenerative Medicine
IPA	Isopropryl alcohol
IPSC	Induced Pluripotent Stem Cell
ISO	International Standards Organisation
kD	Kilodaltons
kg	Kilograms
kPa	Kilopascal
LRT	Likelihood ratio test
MF	Molecular Function
MH_z	Megahertz
ml	millilitre
µl	Microliter
mM	Millimolar
mm	Millimetre
µN	Micronewtons
mN	Millinewtons

mN/mm^2	Millinewtons per millimetre squared
MPa	Megapascal
mRNA	Messenger Ribonucleic Acid
ms	Millisecond
MW	Molecular Weight
Myf	Myogenic Factor 5
Myh	Myosin Heavy Chain
MyoD	myoblast determination protein 1
N	Newtons
NC3R	National centre for the Replacement, Refinement and Reduction of Animals in Research
NDORMS	Nuffield Department of Rheumatology and Musculoskeletal Sciences
Ns	Not significant
OHAT	Office of Health assessment and translation
Padj	Adjusted P value
Pax	Paired Box Protein
PBS	Phosphate Buffered Saline
PC	Principal Component
PCA	Principal Component Analysis
PCR	Polymerase chain reaction
PCr	Phosphocreatine
PDMS	Polydimethylsiloxane
PE7	Plastic Explosive 7
PEG	Polyethylene Glycol
PFA	Paraformaldehyde
Pinc	Incident pressure
Po	Ambient pressure
Pref	Reflected pressure
PTL	Progressive Tissue Loss
PTN	Progressive Tissue Necrosis
qRT-PCR	Quantitative reverse transcription polymerase chain reaction
R	Reflection coefficient
RDX	Research Department eXplosive/ Hexagon
RIN	RNA Integrity Number
RNA	Ribonucleic Acid
ROS	Reactive Oxygen Species
rRNA	Ribosomal RNA
s	seconds
SFAB	Spherical Free Air Burst
CK	Creatinine Kinase
PCr	Phosphocreatine
ADP	Adenosine diphosphate
ATP	Adenosine Triphosphate
NC3R	National centre for the Replacement, Refinement and Reduction of Animals in Research
STRATIS	Soft Tissue Regeneration and Tissue Injury

1

An Overview of Blast injury

1.1 Introduction

Blast injury is defined as *a " complex type of physical trauma resulting from direct or indirect exposure to an explosion"*(1). In recent conflicts, Improvised Explosive Devices (IEDs) containing more explosive than military antipersonnel land mines have become an increasing threat. These devices produce a complex injury involving the soft tissues, skeletal trauma and physiological disturbance that is not seen with other traumatic injuries such as road traffic collisions. Key differences that might lead to the difference in the aetiology of injury include the energy associated with each injury mechanism which is coupled into the body and the generally more dysregulated, widespread, and on-going perturbations in physiological and immune responses. Certain tissues have received particular attention when it comes to research into blast injury, for example bone injury and healing, traumatic brain injury and burns(2, 3). By comparison, although the effects of antipersonnel mines on limb injury have been studied, the effect of explosive shock waves on extremity soft tissue injury has received less attention, even though it is a frequent feature of this injury mechanism(4).

The nomenclature used to ascribe energy to trauma varies across the literature. Scientists in the field of biomechanics discuss the strain rate (s^{-1}) of a force acting on an object (in this case tissue). Strain rate can be used to differentiate between low (heart beat in systole - $1\text{-}10^1$ s^{-1}), moderate (car-crash – 10^2 - 10^4 s^{-1}), high and very high strain (10^3 - 10^7 s^{-1}) rate loading(5, 6). Conversely, clinicians have often referred to traumatic injury as 'low energy' or 'high energy', based solely on perceived energy transfer rather than measured data. As such, the term high energy has been applied to a spectrum of traumatic injuries, from road traffic collisions to blast or ballistic injury. These mechanisms cover a variety of different strain rates. The term strain rate cannot solely categorise all traumatic injury, as not all high or very high strain rate loads yield a shock wave. Therefore this excludes conditions such as primary blast

shock waves. In this thesis, the work concerns primary blast shock wave loading, equivalent to strain rates of 10^5 - 10^6 s^{-1}(7).

In a situation such as blast and ballistic injury which involve very high energy transfer and high strain rate loads to extremity soft tissue, there appears to be a unique pathophysiology, termed progessive tissue necrosis (PTN). This has been reported anecdotally by surgeons, such as described by Evriviades *et al*., from recent combat experience in Afghanistan. PTN is characterised as a loss of soft tissue, such as skin, fat, fascia and muscle over the subsequent 7-10 days from injury to cell death. This can occur despite multiple trips to the operating theatre to debride apparently necrotic tissue. However, the precise pathology is yet to be fully defined(8). The underlying cellular and molecular mechanisms remain to be determined. PTN has immediate effects on the patient and on medical resources and significant implications for long-term outcomes. PTN contributes to progressive limb shortening at discharge(9). Shorter proximal leg lengths cause greater metabolic burden and require longer to achieve mobilisation with prosthetics. Reducing limb shortening may influence the speed of rehabilitation and a return to independent daily living and enhanced quality of life.

In Iraq and Afghanistan, 54% of casualties sustained extremity injuries that included musculoskeletal soft tissue trauma. The overall number of people injured from explosions has increased in recent decades. In Afghanistan, there was also an increase survival rate of UK service personnel from large explosive injury(8, 10). In a study of the UK's military amputees, the overall cost of their care requirements as a population for the next 40 years was estimated at £288 million (highlighting the financial burden of these injuries) (11) (12). In addition, there is an impact on civilians. In one review of 58,578 civilian injuries across multiple conflicts, explosions accounted for 50.2% of injuries (13). In post-conflict states with poor health infrastructure, this represents a considerable additional socio-economic burden. Research to understand the cellular and tissue damage from blast injury is therefore relevant both to military and civilian populations. Previously most research has been militarily led, but

in future combined civilian-military partnership will be required (14). This is because of the increasing costs of conducting such research, the predominately civilian patient population and the need for civilian scientific expertise.

Progressive tissue necrosis to the extremities, also termed 'progressive tissue loss', could be caused by several factors. These might include, but are not limited to, an overwhelming and/or dysregulated inflammatory response or a microvascular endotheliopathy. The latter in itself may occur as a result of an inflammatory response as well as by direct mechanical injury. Invasive infection, perhaps aided or exacerbated by a mechanobiological response at the cellular or molecular level detrimental to appropriate anti-microbial responses, may also contribute. While some or all of these, may contribute to a tissue environment that is incompatible with cellular viability, the sequence of events that leads to that situation has not been confirmed. My thesis aims to investigate the contribution that the mechanical stimulus from an explosive shock wave has on cell viability and signalling.

To understand injuries from explosions, it is important to consider the various mechanisms by which they might occur. Zuckerman used evidence from WWII air raids to classify injury with respect to injurious hazards (15). He divided them into four categories, with the later addition of a fifth class of injury. The five categories are shown in Figure 1.1 (15, 16).

The severity of each class of injury depends on many different factors including the weapon, the environment, and the individual involved. Such aspects include; the quantity and type of explosive, the construction of the explosive device, the proximity of the casualty to the explosion, the environment in which the charge is located and the mechanism by which energy is transmitted to, and absorbed by, the person. An individual's size, posture, orientation, clothing and protective wear will also be relevant.

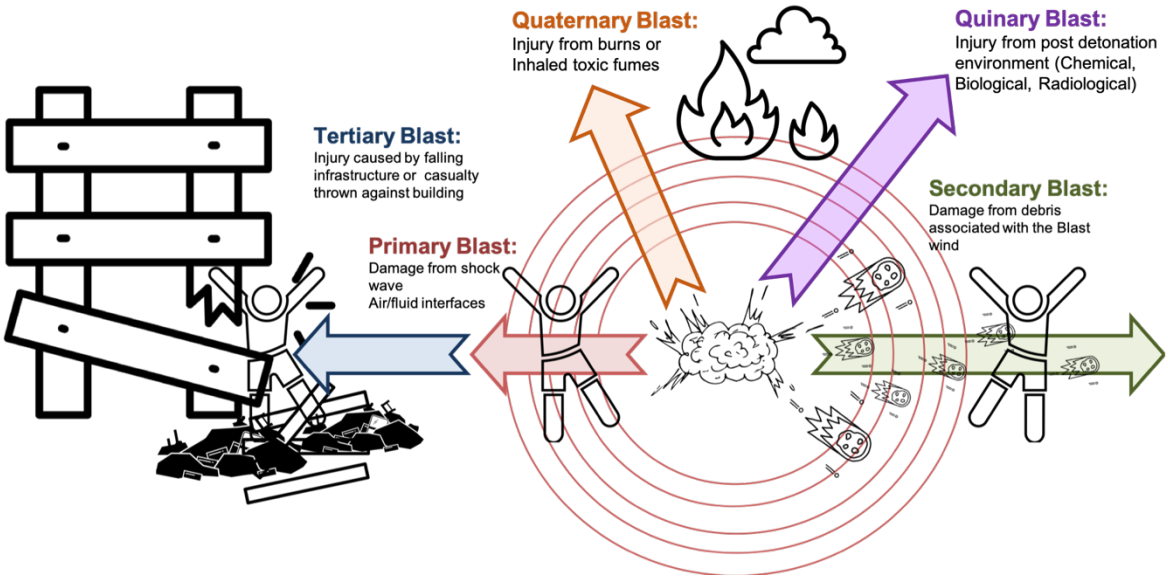

Figure 1.1: *Classes of blast injury (Primary to Quinary) as defined by Zuckerman(15). The fifth category has been added to the figure.*

While accepting several different mechanisms of injury and their contribution to the overall condition of a casualty, this thesis focuses on the effect, at a cellular and molecular level, of an airborne shock wave coupling into tissues, commonly termed a 'primary blast injury'(17). The mechanical response will be very different depending on the physical properties of the tissue such as the presence of an air-tissue interface and its location in the body, for example, if protected by other organs. The biological reaction is dependent on other variables. The response also depends on the length and time scales at which they are examined. To understand fully the entire tissue injury from blast might require a large multi-disciplinary research effort. This thesis contributes to that effort by focusing on primary blast injury to skeletal muscle which is the principle component of extremity soft tissue (Figure 1.2).

To research the biological reaction to primary blast loading, work was also required on how the effects of primary blast shock waves on skeletal muscle can be evaluated in the laboratory in a method that ensures relevance to the real world. Initially the mechanics of the primary blast shock wave have been reviewed along with previous biological models that investigate shock wave interaction with tissue and their suitability for further mechanobiological study. From the reviews, it was possible to outline the experimental considerations for translational

research. This offered advances in three areas. Firstly, it informed the design and manufacture of a new apparatus to deliver blast loading to cell cultures *in vitro* of real-world relevance. Secondly, it optimized a three-dimensional cellular model of skeletal muscle and then exposed this to blast loading. Thirdly, it applied ribonucleic acid (RNA) sequencing techniques to evaluate gene transcription at time points after blast injury.

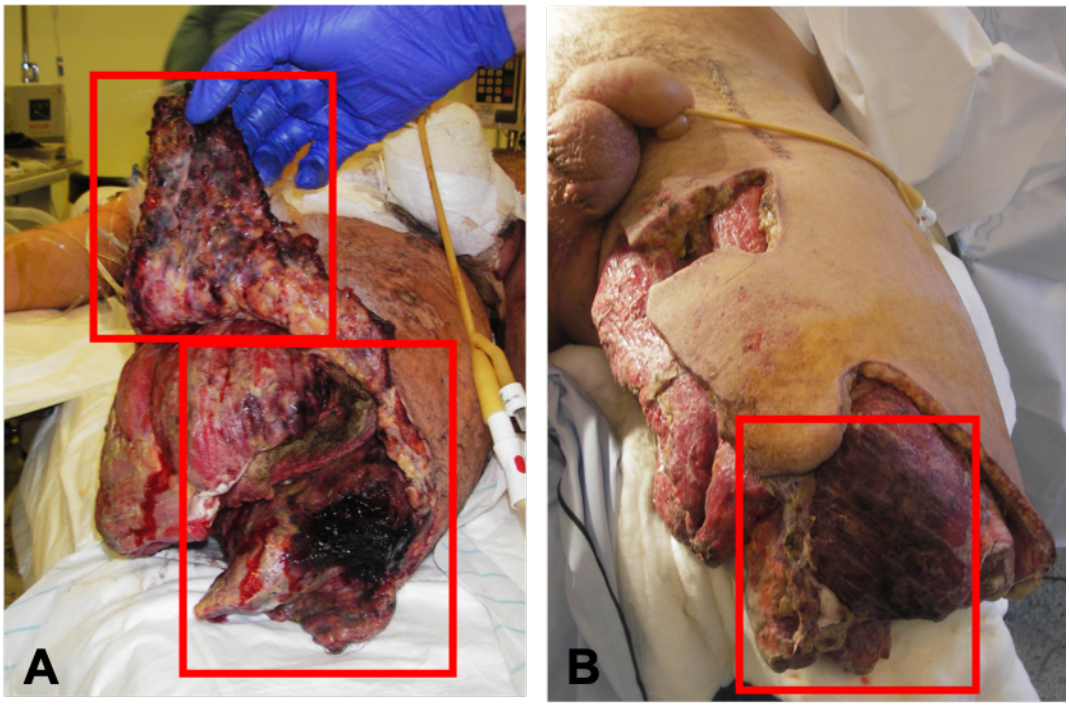

Figure 1.2: *Representative images of soft tissue damage from blast injury. Images show areas of 'progressive tissue necrosis' or proposed skeletal muscle death (black/grey) outlined in the red box. Images were taken preoperatively of different patients who had had primary debridement, before a further surgical debridement. Images show:*
***A** – Distal wound of the residual right limb. Extensive PTN to skin flap (in blue glove) and the underlying soft tissues.*
***B** – Wound over the medial and distal aspect of the residual left limb. A large area of black discoloration was seen in the muscle at the distal end.*
Images with permission, courtesy of Lt Col SLA Jeffery RAMC.

1.2 **Primary Blast Injury**

During an explosion, there is a rapid release of energy resulting in an abrupt and violent increase in pressure and temperature. The pressure disturbance propagates outwards, and due to the compression of the air, the front of this disturbance travels supersonically which steepens the waveform, until it forms a shock front which can be approximated as an instantaneous jump in pressure, density and temperature. The shock front forms the initial feature of the blast wave. By contrast, a linear acoustic wave involves infinitesimal pressure changes, which move at sonic speed, and do not steepen to form a shock (18). These differences have consequences for both the transmission and reflection of energy at the tissue interfaces and the shape of the pressure loading on the cells.

1.2.1 'Idealised' Air blast Waves – The Modified Friedlander Equation

Blast shock waves are normally described in terms of the pressure changes with respect to time for a point, or measurement location, within the air at a distance from the explosion. In the 'idealised' description a Spherical Free Air Blast (SFAB) is an explosion in an open environment without any interactions (a free-field blast expanding radially from a point source). The start of the blast wave is signified by a pressure jump, followed by a decay, a subsequent under pressure or negative phase followed by recovering to ambient pressure. A hemispherical surface burst (HSB) describes the detonation of a surface explosive on a plane surface with no ground reflection. The HSB is a potentially more relevant replication of the real-world scenario.

Several equations have been used to represent simple blast waves, especially the initial positive phase(18). The original Friedlander equation (19), provided a good description of blast waves below 100 kPa (1 atm). Dewey (20) modified this to describe accurately the shape of the blast waves at much shorter radial distances, up to the boundary of the detonation products. The form presented here, Equation 1, is based on that presented by Baker and by

Dewey (18, 20). Figure 1.3 plots the graph of Equation 1.1 of overpressure against time from detonation.

$$P(t) = P_{so}\,(1 - (t - t_a)/T^{+})\,e^{-(t-t_a)/\alpha} \qquad \textbf{(1.1)}$$

Where;

P(t) is the overpressure (pressure above the ambient pressure),

P_{so} is the peak overpressure (of the shock front,)

t_a is the arrival time of the shock front,

T^{+} is the positive phase duration, and

α is the decay time

e is Euler's constant (~2.71)

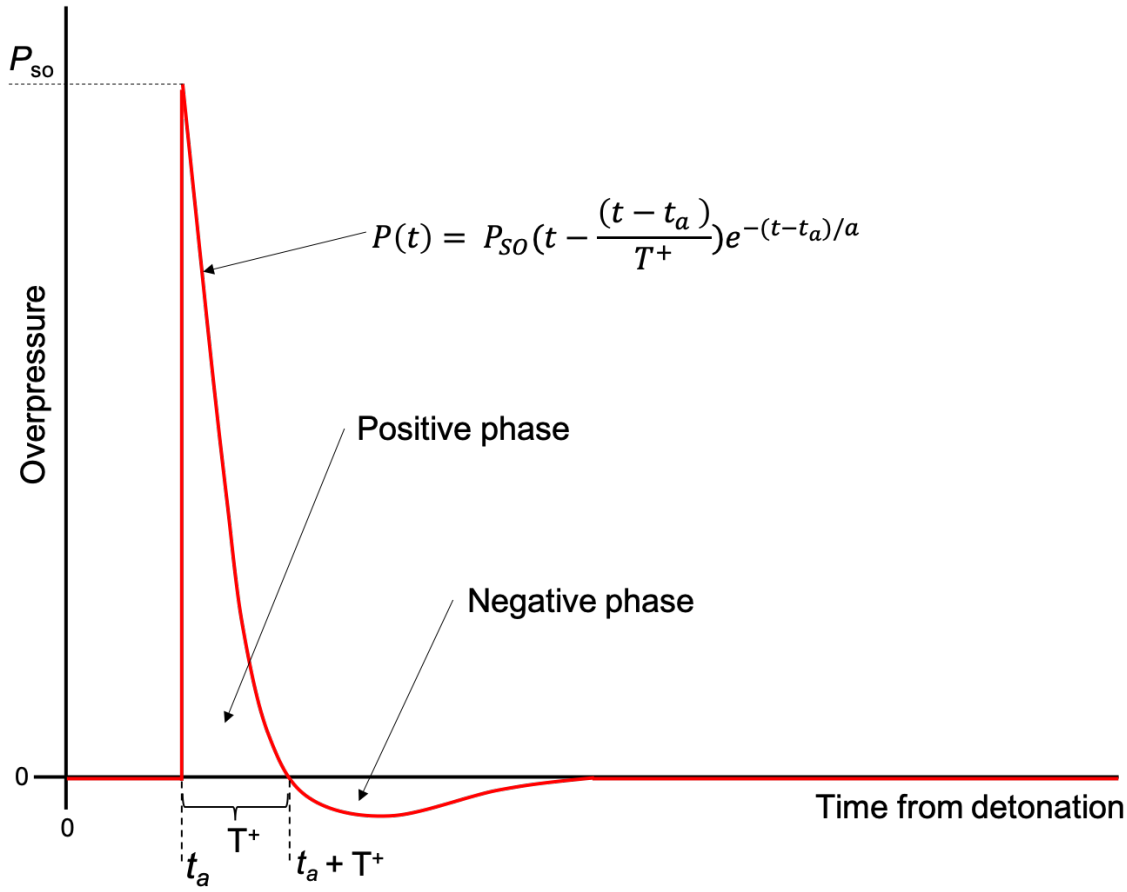

Figure 1.3: Plot of curve generated from the Modified Friedlander equation. The equation (outlined in Equation 1) describes the positive phase duration and the decay of the curve. It does not describe the gradient of the rise time to the peak overpressure. This is assumed to be instantaneous.

1.2.2 Factors Affecting Real Life Blast Waves

A range of factors influences the form of real blast waves, some of which are outlined below.

1.2.2.1 Energy Source

Many different energy sources can generate blast waves. Furthermore, there are considerable nuances in the types of explosive material and methods chosen to encase and detonate such material that affect the magnitude and type of waves produced. Traditionally, condensed explosives are broadly divided into two forms, High Explosive (HE) or Low Explosive (LE), based on the combustion front velocity within the material. In HE, the front travels supersonically causing a detonation, whereas, in LE, the combustion is sub-sonic and produces a deflagration, and thus a more gradual pressure rise in the surrounding air.

1.2.2.2 Explosive Quantity and Distance

Two factors dominate the characteristics of the resultant blast wave: the amount of explosive (energy released) and the distance of the measurement location from the explosion (the volume that energy has been released into). Figure 1.4 outlines the detonation of both an SFAB and HSB. The influence of both of these factors is shown in Figure 1.5 which outlines a representation of an SFAB alongside the reduction of peak pressure with distance from the charge. Figures 1.5 (1), (2) and (3) show the effect of the change in measurement location (red, orange, yellow and green lines) for one of the charge masses on the characteristics of the shock wave. It is noticeable that the time of arrival (at the same measurement location) is greater for the lower pressures. This is a consequence of the positive correlation between the magnitude of a shock front and its velocity. It is also noticeable that while a similar peak pressure may occur at a distance from a large charge as occurs closer to a smaller charge, the positive phase duration is smaller in the latter case (compare C for $10x$ kg with A for x kg).

The relationships between the quantity, distance, and blast wave parameters can be more formally expressed via scaling laws(18, 21, 22).

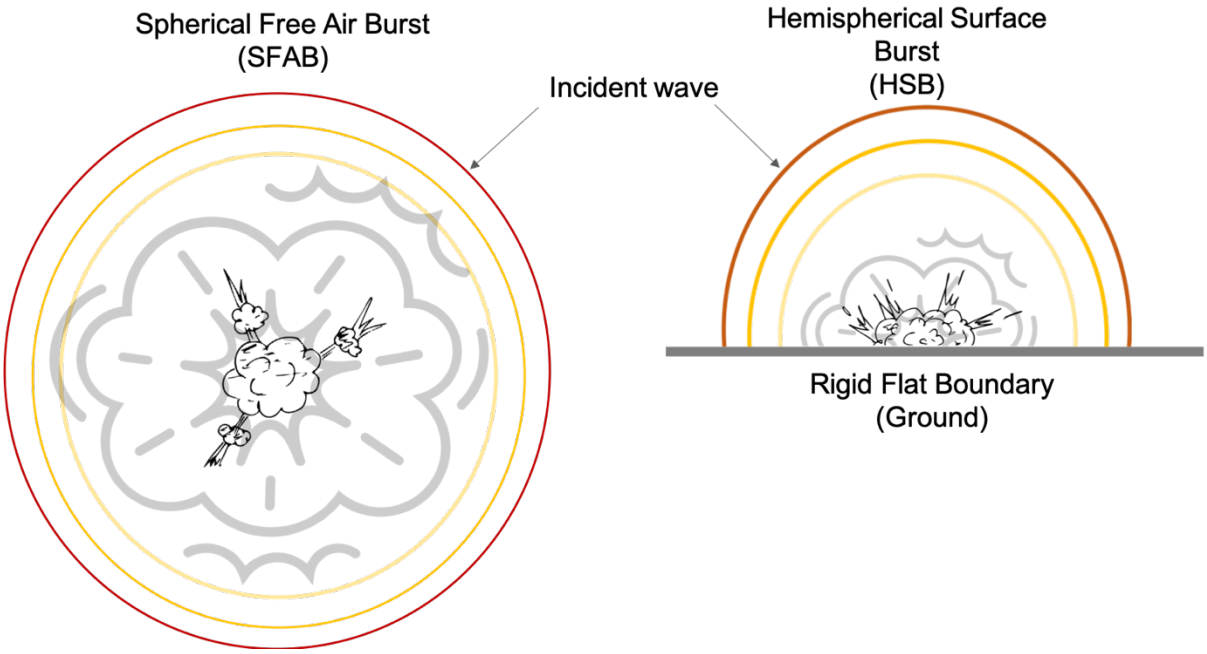

Figure 1.4: *Figure outlining Spherical Free Air Burst (SFAB) and a Hemispherical Surface Burst (HSB). A spherical free-air burst is an explosion of bare explosives with no interactions with the blast wave at all. A hemispherical surface burst is a detonation of an explosive on the surface of the ground. The surface is plane and there is no ground reflection - essentially a hemisphere on a plane.*

Image reproduced from reference 19.

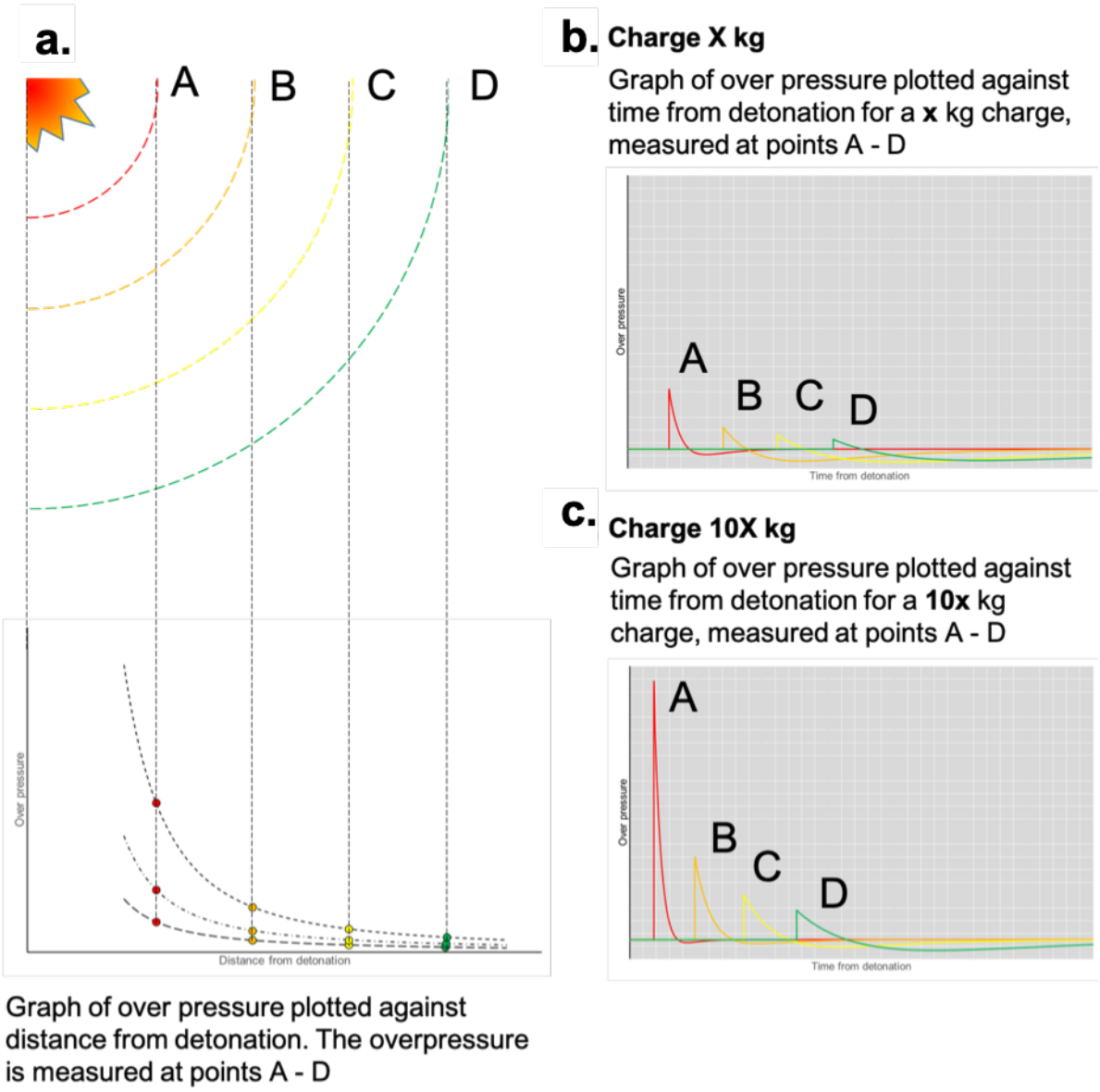

Figure 1.5: a. *Illustrative plot of the influence of distance and charge size on peak pressure, and the form of the Modified Friedlander curve. The peak overpressure is measured at increasing distances from the epicentre denoted by coloured circles red, orange, yellow and green. These measurement points are replicated on plots (b) and (c).*
The figure shows a segment (quarter) of an SFAB with four measurement locations from the blast epicentre. The peak overpressures at each location (A to D) is plotted in a. Then the time from detonation, for each position A to D, is plotted against overpressure for a charge of x kg and $10x$ kg. *© Crown copyright (2023), Dr Andrew Sedman & Colleagues, Dstl.*

As Figure 1.5 shows, as the shock wave propagates from the blast epicentre, the pressure (and thus energy) dissipates. The decay in energy overpressure over time can be characterized into three 'fields' at increasing distance from the blast epicentre, the near field, the midfield, and the far field (Figure 1.6). The sizes of these fields depend on the size of the

explosive device. However, by way of example, for a small device such as 1kg TNT the near field may be up to one meter from the explosion, the midfield up to two meters and the far field beyond five meters. These distances differ from, and should not be confused with, those cited by security services to cordon off explosive devices. These distances are much greater and denote the area likely to be free from shrapnel.

In the near field, the blast is typically characterised by extremely high magnitude, highly spatial and temporally non-uniform loads. (23) Considered simplistically this is in part due to the curvature of the shock front at this distance. However, the issue is complicated by differences in the physical properties of the expanding detonation products and the surrounding air, leading to additional shocks. In the near field the modified Friedlander equation is not an accurate representation of the pressure profile(23).

In the mid-field, the shock has separated from the detonation products so its pressure pulse travels through the air. This pulse is well described by the Modified Friedlander Equation. As the pulse travels outward its peak declines, its duration increases and its velocity reduces. That trend continues into a region commonly referred to as the far field. Eventually the shock front is lost and the energy continues to propagate as a sound wave. The divisions between these regions are not absolute but rules of thumb based on scaled distances.

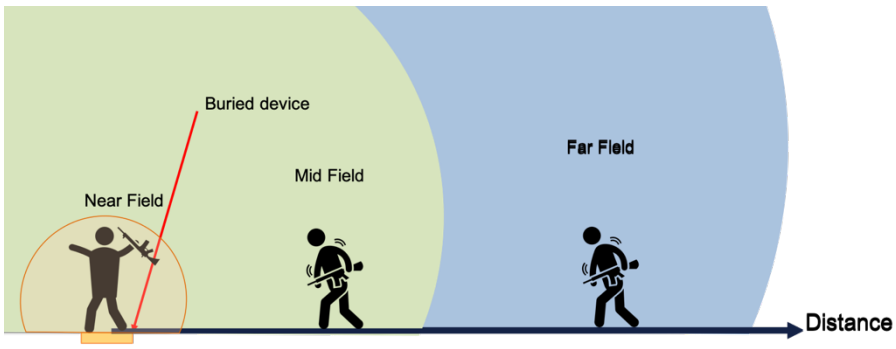

Figure 1.6: Diagram of a soldier's proximity to a real life scenario explosion, a buried device, and the potential boundaries of the near field (orange), midfield (green) and far-field (blue).

1.2.2.3 Charge Geometry

The shape of a bare explosive charge influences the blast wave. Real blast sources have different geometries, for example, muzzle blast, line charges and sheet explosive. These geometries influence the overall shape of the expanding blast wave, and thus the applicability of the standard scaling laws. As the distance from the blast source increases this influence declines and the overall shape tends to a spherical expansion (18).

Charge geometry is not only related to the shape of the explosive mass but also to the point(s) at which it is detonated. In most theoretical air blast work, the source of the blast energy is assumed to be a point or a centrally detonated spherical charge.

1.2.2.4 Charge Encasement

The type of container that constrains the gas generated from the explosion until it rapidly bursts can be used to generate a larger shock wave.

In many military munitions, the high explosive is surrounded by a casing to produce primary fragments. The casing may break up in response to flaws or inconsistencies in its structure when subjected to the internal pressure loading from the detonation of the explosive, producing so-called ‘natural fragments’. Alternatively, the casing may be machined to cause a preferential fracture pattern or be made from preformed fragments. While fragment injury, which in itself can produce a high transfer into the tissue, is not the focus of this paper, the constraint provided by, and the energy required to break up, such casings influence the blast wave output.

1.3 Blast Wave Interaction With An Object

Up to now we have only considered blast waves in relation to a point measurement location within a volume of air. In order to consider an experimental design for the exposure of cell

culture models to a relevant blast wave it is important to understand what happens when that blast wave encounters an object.

1.3.1 Idealised Blast Waves Interacting With An Object

The most basic interaction considered is the normal reflection of a plane shock from a rigid flat boundary with an angle of incidence of zero. At the reflecting surface, the approaching incident particles are arrested, the particle velocity becomes zero, and the pressure, density, and temperature all increase above the value of the incident wave. The overpressure at the boundary surface is commonly called the reflected overpressure (or reflected pressure). For very weak shocks (P_{so} « the ambient pressure) the acoustic approximation of the reflected overpressure (that measured at the boundary) being twice the incident pressure may be reasonable. However, for stronger incident shocks this ratio is greater, with values in excess of 20:1 (18). Ghoshal demonstrated that perfect gas assumptions hold up to incident pressures of about 0.7 MPa, and presented a model indicating a ratio of 16:1 at 100 MPa (24). This range is relevant to the pressure amplitudes expected in blast injury.

In the case where a plane shock is obliquely incident on a rigid boundary, it will be reflected at an angle that is not the same as the incident angle. Generally, increasing the angle of incidence increases the angle of reflection and also affects the strength of the reflected shock wave. On increasing further, the incident reaches a critical value beyond which this type of reflection does not occur, but transitions into a Mach reflection (25).

These concepts have important influences on experimental design, for example the placement of pressure transducers within a shock tube to characterise accurately the shock wave. A pressure transducer flush mounted in a wall of the test section of a shock tube, would only record the ambient and then (the so-called) incident pressure as the wave pattern moves along the wall, and there are likely to be boundary effects influencing this part of the shock

wave. Whereas a target with a flush mounted pressure transducer in the centre of the tube is likely to see a loading on its front face, more akin to a plane reflected pressure.

1.3.2 Complex Blast Waves And Real Scenarios

Idealised air blast waves occur in modelling, specifically designed trials, or in limited regions of real blast events. IED blasts will likely contain objects with complex geometries exposed to complex blast waves. Furthermore, real objects are unlikely to be immutable in the face of such loading. Such factors will influence the blast waveform, producing shocks of different magnitudes travelling in different directions. Within such environments, two pressure gauges placed a small distance apart may experience very different pressure histories. Enclosed blast wave environments may even record a gradual increase in pressure. Such events are beyond the scope of this experimental work. However, they are important considerations in blast research, and its application to the real world.

1.4 Evaluating Previous Physical Platforms To Investigate The Mechanobiology of Blast

Since the work of Zukerman, research on blast injuries has considered the issue at progressively shorter length scales and in finer detail; from whole subjects to individual organs and tissue types, with the focus now shifting to the cellular and molecular level. This shift requires more realistic and often complex biological models that must integrate with physical methods capable of replicating an appropriate range of loading conditions. Differences between existing models make it more difficult to understand the mechanical loading that the cells are subject to and to make inferences on the role of underlying biophysical mechanisms.

Multiple platforms have been used to expose *in vitro* and *in vivo* models to loading pulses in the name of replicating primary blast injury. These platforms are outlined in Table 1.1 (26-31) and include shock tubes, lithotripters, laser shock plates, split Hopkinson pressure bars and

drop weights. Pressure vs time profiles for each of these platforms can be found in the chapter appendices (Figure 1.1) Cylindrical shock tubes can reproduce aspects of the real-life waveform including the amplitude and duration (but specific designs are needed to obtain representative pressure profiles) and have been applied to both *in vitro* and *in vivo* systems. Lithotripters, used medically to break kidney stones, can generate very high amplitude shock waves with very short durations, when compared to modified Friedlander explosions, and therefore cannot accurately replicate blast loading. Laser shock plates use lasers to generate a shock wave between metal plates. These also yield high amplitude short duration shock waves that do not accurately replicate explosive loading. Their specialised apparatus also makes them challenging to adapt to cell culture. Other equipment researchers have adapted to cell research include Split Hopkinson pressure bars (SHPB). which were designed to test the effects of high strain rate loading on hard materials, such as ceramics, which is different to blast loading. Platforms such as the SHPB or drop weight rigs, were designed to test the bulk properties of structural materials (32), although they have been adapted for softer materials associated with *in vitro* models(33, 34). Drop weights have also been adopted to investigate blast loading; however, whilst they generate high strain rate loads, they do not generate shock waves. Whilst shock waves themselves involve high strain rate loading, not all high strain rate loading generates a shock wave. Hence for specifically recapitulating shock waves from blast explosions, SPHBs and drop weights are inadequate platforms.

Not all of these modalities deliver shock waves in air, some delivery shock waves underwater, and these scenarios therefore do not truly replicate the desired loading environment. The rise time and duration of the pressure profile from these sources vary greatly, indicating variability in the stimulus generating the mechanobiological effects. In addition to differences in the veracity of the pressure profile, each source has its own experimental advantages and constraints such as the capacity for live imaging, immediate sample analysis or use of live tissue.

Ideally, loading values must be comparable between studies, relatable to expected loading at different tissue depths and correlated to a clinical degree of injury. Generally, these aspects are not adequately addressed in the existing literature. One approach is to use equipment that can deliver an explosively-driven blast loading onto a representative tissue target (*in vitro* or *ex vivo*). This may yield much of the data sought above, and lead to the tissue characterization necessary to expand this field. Realistically, different approaches may be relevant for modelling different facets of the mechanical stimulus from a blast event. A framework for selecting an appropriate loading modality and conditions would enable greater comparison to be made between studies and cross-validation of the observed effect.

Method	Example of use in combination with a biological model for the investigation of explosive injury.	Amplitude of waveform produced	Duration	Advantages (+)/ Disadvantages (-) for modelling explosive shock wave
Shock tubes (gas or charge driven)	Hippocampal slice Endothelial monolayer Ex vivo rat spinal cord Aggregate cultures	Wave amplitude is dependent on the diameter and length of the tube design and source of the shock Can be >25MPa. In biologically related experimentation requiring much lower amplitude values up to 1MPa have been obtained using smaller tubes.	≥ 1ms Wave duration dependent on the temperature, ambient pressure of the tube and medium of the tube (air or water for example).	+ Capable of very high strain rate loading +Capable of accurately reproducing air blast loading equivalent to 'real life' munitions. -Detonation results in shock wave with thermal components (could be a confounding stimulus to biological samples). -Design of tube, flange & target will have implications on waveform & flow that will affect loading seen.
ESWT/ lithotripter	Monolayer culture: Muscle derived primary cells. Cell suspensions: osteoblasts, adipose-derived stem cells, mesenchymal stem cells.	Up to 110MPa. Amplitude is related to the size of the source crystal/coil or spark source and the accuracy of the focal point. Focal zones and design features can vary greatly between lithotripter type (electrohydraulic, electromagnetic, piezoelectric).	1μs duration	+Can achieve a longer pulse duration +More control over shape and consistency of wave. +Capable of exploring shock wave transition through liquid and cell medium over air. -Duration of waveform much shorter than found in live explosive/Friedlander explosions. - Rise time also much steeper than explosive shock waves.
Laser shock plate	Endothelial monolayer.	Gas breakdown results in a shock wave. The wavelength of the laser, gas pressure and laser pulse duration all control the parameters of the laser waveform produced. Reported up to 31.9MPa	<50ns up to microseconds	+Capable of large overpressures and very high strain rate loading. + Generates air shock wave. + Highly reproducible shock waves. -Highly specialized experimental set up. -Difficult apparatus to integrate with *in vitro* models.
Hopkinson bar	Mesenchymal stem cells on coverslips. Mesenchymal stem cells culture in agarose hydrogel. Cell suspension – PLB985 (diploid cell line from acute nonlymphocytic leukemia) MSC's, neutrophils.	The striker bar velocity, constituent bar material properties and dimensions all contribute to the types of pulses capable of being fired onto the specimen. Sample to bar impedance matching is critical to ensuring pulse delivery to the sample. Stress wave pulses of > 70Mpa have been generated with metal bars. Alternative systems using polymeric bars are available.	100s – milliseconds Wave duration is dependent on the length of the striker bar and elastic wave speed. Altering striker bar length will change wave duration.	+Highly controllable uniaxial stress wave. +Well defined using strain gauges. +Projectile velocity of striker determines amplitude of stress wave. Manipulating the striker length can alter stress wave amplitude. -SPHB set ups were designed to test impact & material properties (such as polymers/biologics). -Material mismatch and impedance mismatch can alter applied load to cell culture. -Without appropriate considerations of assumptions (friction, dispersion effects, stress equilibrium) and limitations of the SPHB set up, there can be found significant discrepancies in the amount of the delivered stress pulse delivered to samples.
Drop Weight	Cell laden hydrogels – periosteal stem cells	Low velocity impact apparatus consisting of a frame, weight assembly (or impactor) and a base plate. Altering the weight and geometry of the impactor can influence the mass effect on the specimen. Up to 10MPa	10's of milliseconds	+Able to generate impulses less than 1MPa in amplitude. +Alterations in the size of weight and apparatus. Height can allow for experiments at lower impact overpressures. -Strain rate determined by weight velocity. -Energy losses can result in overestimation of the experimental results. -Drop weight systems are not performed at constant strain rates, to achieve this large mass and low drop height apparatus must be used. -Structural vibrations on the text equipment can limit accuracy of test equipment.

Table 1.1 : Advantages and disadvantages of current experimental platforms employed for *in vitro* blast research. The waveform parameters from each modality (amplitude and duration) are presented for comparison.

1.5 Designing Tissue Models to measure the cellular and molecular response to the blast.

The previous two sections of this chapter focus on the complexity and importance of modelling the loading 'input' in mechanobiology studies of blast injury. To achieve meaningful results, however, careful attention also needs to be given to the ‘output;’ this includes the method of modelling the tissue of interest, as well as the readouts collected and their interpretation.

The cellular and molecular response of tissue to a blast-relevant load could be complex and depend on several factors. Although soft tissues generally can be modelled as viscoelastic media, the mechanical properties at bulk, macro and micro scales are distinct and vary within and across different tissues. This lies beyond the scope of this thesis.

Similarly, the mechanobiological response could be highly dynamic with molecular changes occurring immediately and over minutes, hours and potentially days. The current literature on the cellular and molecular responses to blast loading is relatively small and has largely focused on blast-induced neurotrauma (35-43). There are limits to interpreting this work and making cross-comparisons. These limits include a lack of information on what explosive scenarios modelled, such as the distance from the event and the size of the device. Furthermore, there is a lack of information on scaling, peak overpressure and the duration of the real explosive event itself. This makes it challenging to compare the experimental setup against the desired real-world event. This emphasises the complexity of conducting and interpreting these highly interdisciplinary research studies and the gaps in terms of relevance to ‘real-world’ injury type and mechanism. Such gaps can be explained by considering the different ways of approaching the task of elucidating the cellular and molecular response to blast loading (Table 1.2). In each of these scenarios, a relevant biological target is required. Its relevance includes its similarity to humans in a biological sense, its size and therefore any consequent requirement for scaling,

and its recapitulation of the mechanical properties of tissue (44). The target could be modelled *in vitro, ex vivo* or *in vivo* and each has particular advantages and disadvantages. A mixed approach with cross-referencing and validation is often a prudent strategy when trying to unpick complex biological mechanisms. Considerations for setting blast injury studies *in vivo* have been covered elsewhere (45, 46) (Appendices, Chapter 1, table 1.1). Subsequent sections of this chapter will, therefore, explore *in vitro* and *ex vivo* systems including work to date and future prospects.

Approach to modelling blast-relevant mechanobiology	Approach to modelling blast-relevant mechanobiology	Advantages	Knowledge gaps/disadvantages
Modelling the 'real-world' scenario	*The 'real world' scenario, or a range of scenarios, can be reconstructed as closely as possible.* For example a relevant amount of live explosive can be detonated at a relevant distance from an appropriately sized and relevant biological target.	*Does not require knowledge of forces experiences within the tissue as these will be generated by capitulation of the complex 'real-world' environment of injury (e.g. use of real explosives).* *Use of validation/verification.*	*Requires capability for explosive trials involving biological materials.* Experiments are costly and logistically challenging.
Modelling loading within tissue	*Aspects of loading experienced by a tissue in scenarios of interest can be recapitulated using laboratory equipment (i.e. not necessarily live explosive) against a relevant biological target.*	*Can be undertaken by a wider variety of research groups which enables more capacity for the work and the cross-pollination of ideas* *Experiments are not prohibitively costly or logistically difficult.*	*Requires a precise understanding of mechanical stimuli that occur within a specific tissue, at different points within the tissue for a variety of 'real-world' loading scenarios.* This information is currently lacking at a cellular scale for most tissues making it difficult to prove the relevance of these studies. *These methods are more likely to reduce the loading down to one specific aspect of a blast event.* To represent the overall effect will need collation not only of the understanding of each mechanism, but of any synergistic effects between mechanisms. *These may alter their significance when views in isolation.*
Modelling relevant cellular and molecular responses based on clinical data	*Once the biological response of a tissue to blast has been fully elucidated from clinical samples, the biological responses of a can be modelled in the laboratory using any method which generates an appropriate response.*	*Such biological and clinical data may remove the need for representative mechanical loading, or loading at all – if the biology could be accurately generated using alternative means (such as chemical injury).* This wold open up the research field even further to different disciplines and likely reduce costs.	*This will require a comprehensive knowledge and understanding of the cellular and molecular response to blast injury in a range of real-world scenarios from clinical samples.* This data is currently lacking.

Table 1.2: *Considerations for future experimental design for exploring the mechanobiology of blast*

Model Type	Advantages of Model	Disadvantages of Model	Examples
2D – Monolayer systems **Describes cells cultured on tissue culture plastic or coverslips**	○ Appropriate for most cell types, including primary cultures. ○ Capable of high-fidelity imaging – both *in situ* and post injury. ○ The majority of commercially-available and published assays are optimized for 2D culture thus providing a broad choice for downstream assays. ○ Reduced experimental variability between wells/plates. ○ Reduced wet lab costs compared to 3D culture systems. ○ Straightforward to integrate into current mechanical loading systems to study blast/shock waves.	○ Cells require passaging and growth is limited by surface area. ○ 2D systems lack key environmental cues found in 3D environment. ○ Stiffness of tissue culture plastic not representative of host, and thus particularly unsuitable for study of mechanobiological representation of in vivo tissue.	Endothelial monolayer. Monolayer cultures – Muscle derived primary cells. Mesenchymal stem cells on coverslip.
2D/3D – Cell Suspension systems **Describes cells in culture medium in suspension, cells cultured in medium that form aggregates, or bioreactor systems that through medium agitation keep cells suspended.**	○ Easier to passage, but requires daily cell counts + viability to follow growth patterns. ○ Easy scale up as growth is limited by concentration of cells. ○ Doesn't require tissue culture treated plastic. ○ Cells in suspension more representative of host environment mechanics (circulating in blood etc., physical properties of fluids over air). ○ Have already been integrated into models for evaluating shock wave. ○ Widely adopted for expansion of stem cells, cancer cells, spheroids and tissue like constructs.	○ Appropriate only for cell lines adapted to suspension in culture or that are non-adhesive – e.g. hematopoietic. ○ Cells in suspension may form aggregates, making it more difficult to study individual responses over micro tissue response. ○ Cells are rounded rather than under tension(unlike in vivo). ○ Fluid presents added challenges with studying shock wave interactions (cavitation, changes in speed of sound in air vs fluid). ○ Only smaller populations of cells a be studied in 2D – one vial per experiment vs 1 plate in monolayer. ○ Free floating aggregates (suspension) or monolayers lack the considerable mechanical loads that alter matrix and cell function.	Cell suspensions. Cell suspension – Acute Myeloid Leukaemia cell line. Aggregate cultures.
Cells encapsulated in 3D Material/Organoid Tissue models **Describes cells encapsulated in hydrogels or 3D polymers, or encapsulated cells helped under tension on or between scaffolds.** **Describes pluripotent or adult derived cell populations that are differentiated into 3D functional microtissues, displaying either architectural similarities or functional properties (or both).**	○ Material can be designed to be more mechanically representative of host environment. ○ Presence of cell-ECM adhesion helps drive final tissue organization. ○ Cells in 3D culture have different response to the 2D environment. ○ All focused & tuned study of specific cell populations in isolation from whole organ. ○ Present like for like environment with multiple cell types, molecular cues and tissue architecture. ○ Excellent for recapitulating the developmental process of tissue. ○ Reflects tissue hierarchy. ○ Allow for a snapshot of tissue effects without cost + logistics of *in vivo* work. ○ Integration with mechanical loading systems could generate high quality data sets and reduced requirement for *in vivo* testing.	○ *In vitro* models' culture can result in spatial organization of the cells different to what is found *in vivo.* ○ 3D materials alone aren't truly biomimetic. ○ Materials lack the molecular cues found in tissue/body environment. ○ Increased cost associated with material manufacture and wet labs. ○ Many *in vitro* assays not scaled for 3D culture, limiting experimental outputs available to measure effect. ○ High wet lab costs associated with production. ○ Due to required cell types, often can be low yield – i.e. cannot be mass produced to large scale. ○ High fidelity imaging techniques can be more challenging that for 2D culture. ○ Cell sorting/ separation requires significant optimization with often moderate to low cell population yields. ○ Lack innervation, microvasculature or immune cells, meaning disease process are only partially recapitulated.	Mesenchymal stem cells cultured in agarose hydrogel. Organ on a chip 3D skeletal muscle models

Table 1.3: Review of *in vitro* model types, their advantages and disadvantages for studying the mechanobiology of primary blast.

1.5 Choosing models of tissue for blast-relevant mechanobiological study

Adopting a representative *in vitro* model should enable the translation of findings from *in vitro* to *ex vivo* and preclinical work. The selection of appropriate models to probe the mechanobiology of blast can be guided by the model's ability to address some broad research questions, including;

1. What happens to cells after blast?

2. How does the cell response correlate with the wider tissue injury, and more broadly the systemic injury?

3. Can we correlate a systemic outcome measure (such as blood pressure) to cellular injury to obtain a common comparator between models (such as achieved *in vivo* with haemorrhage research)?

These questions overlap and can be evaluated in a bottom-up approach. This evaluation is fundamental to enabling downstream research. Robust *in vitro* models provide the most flexibility to optimise, measure and probe the cellular effects after an explosive blast. *In vitro* experiments offer the advantage of higher throughput, greater sample number and therefore a higher level of granularity (Table 1.3). However, as Table 1.3 details, various types of *in vitro* models have been utilized from monolayers through to 3D systems. Whilst 2D systems are potentially easier to culture and analyse, the 2D environment is arguably not sufficiently representative of real tissue when assessing the response to mechanical insult. Conversely, 3D systems can more closely mimic the native environment but are more challenging to analyse experimentally. Furthermore, *in vitro* systems are much more sensitive to the cell culture environment. The aspiration is for a broad assessment of the cellular and molecular responses (e.g. via '-omic' analysis) that enables unbiased evaluation of response that can then be linked to a functional or clinical outcome. The higher throughput of *in vitro* work, with the ability to sample at multiple time points, enables the collection of huge amounts of data. This, however, brings its own challenges. It difficult to judge the significance of vast quantities of cellular and molecular data if is divorced from clinically relevant outcomes. Multiple cell

types have been used within such *in vitro* models (Table 1.3) (47) (26) (48). However, the fundamental constituents of the blast injury wounds such as adipocytes, skeletal muscle, fibroblasts, keratinocytes and osteoblasts have yet to be characterized *in vitro* with respect to blast loading (8, 49). Adopting techniques such as spatial single-cell sequencing could enable the characterization of these cell types within a biomimetic 3D model, rather than in isolation in 2D culture. Such a model may provide a new tool to address the three questions posed above.

As our understanding of the cellular picture grows, the use of *ex vivo* systems may be more useful than *in vitro* models. *Ex vivo* systems, particularly *ex vivo* perfusion (EVP) systems, which have been developed for a variety of organs, including whole limb perfusion, may hold promise (Appendices, Chapter 1, Table 1.2). These systems offer the advantage of higher throughput analysis, as with *in vitro* models, and with great relevance to whole-organ physiology. *Ex vivo* models of whole limbs may present a significant opportunity for blast research and the trauma field as a whole**.** In the experimental study of other facets of combat trauma (such as haemorrhage) physiological markers (such as blood pressure) provide indicators of injury severity (50, 51). No such equivalents exist for quantifying tissue-level injury *in vitro*. This makes it difficult to validate the loading conditions employed to translate into a clinically-relevant tissue model response. As far as possible attempts must be made to link broad molecular and cellular readouts to clinically relevant and/or functional readouts.

Finally, correlating tissue and cellular injury to systemic outcomes would enable a greater degree of comparison between injury conditions and models. However, that requires a comprehensive understanding of the cellular and molecular injury.

In summary it would appear that a simple, repeatable and relevant *in vitro* model offers a means of procuring sufficient quantities of data in a rapid and cost effective manner. Such a model may allow analysis at the cellular and molecular level and possible later correlation with whole organ, limb or bedside data.

1.7 Aims of this thesis

The body of knowledge of the whole-body physiological effects of blast, and its concurrent and consequent injury mechanisms, such as haemorrhage, has grown during recent decades. However, our understanding of the detailed cellular and molecular effects of blast in individual tissues is still lacking. At present, there are no therapeutic approaches that focus on ameliorating the detrimental effects of blast shock waves on tissue, from a mechanobiological sense. It is therefore important to take steps to characterise the injury at the cellular and molecular level

The aim of this research is the development of a mechanically relevant model of primary blast shock wave exposure of skeletal muscle in order to probe the transcriptome expression after explosive injury.

The experimental work undertaken is described in the following chapters:

Chapter 2 uses historical *in vivo* samples that were exposed to explosive blast shock waves to validate a method to extract and examine bulk gene transcription through RNA sequencing techniques.

Chapter 3 systematically reviews the literature concerning three-dimensional models of skeletal muscle held under tension. It describes the methods employed to manufacture these models, and which, if any, have developed reproducible methods for damaging these models. The chapter aims to appraise the most valuable method to adopt to probe the effects of blast injury on skeletal muscle.

Chapter 4 outlines the development of a three-dimensional model of skeletal muscle for blast loading. It is proposed that the functional capacity of skeletal muscle can be evaluated using the deflection of anchor posts used to culture skeletal muscle. It also hypothesises that there are key logistical considerations that will influence the type and source of cells used for 3D models for large-scale explosive trials.

Chapter 5 outlines the design considerations and validation of a custom frustum shock tube for applying blast loading to cell culture. It demonstrates that an equivalent explosive loading source to that of a hemi-spherical surface burst can be titrated onto cell culture samples using relatively small amounts of explosive.

Chapter 6 deploys the 3D model described in Chapter 4 within the shock tube described in Chapter 5 to run a field trial to assess the cellular effects of explosive blast on skeletal muscle cells. It is suggested that blast shock waves will have a detrimental effect on skeletal muscle metabolism, and will also alter gene transcription to initiate programmed cell death.

Chapter 7 discusses these experiments and the implications of their findings on the wider field, along with proposals for future work in this area.

2

Application of Bulk RNA Sequencing to Blast Exposed Skeletal Muscle From Two Different *In Vivo* Models

2.1 Introduction

Tissue loss following blast injury in recent conflict has been termed 'progressive tissue necrosis' (PTN)(8). This is defined as a loss of soft tissues such as skin, fat, fascia and muscle over the subsequent 7-10 days from injury despite multiple debridement's and appropriate wound management. PTN often leads to progressive limb shortening. The use of the term necrosis within this description suggests that the mechanism of this phenomenon has been characterised. However, this is not the case and, while it is highly likely that necrosis plays a role, the contribution of other mechanisms of cell death has not been evaluated. Therefore, in this thesis, PTN may also be referred to as Progressive Tissue Loss (PTL), to prevent confusion on the potential mechanisms underlying this condition. Underlying causes of PTL may include dysregulation of the systemic inflammatory response (52), microvascular endotheliopathy of trauma(53, 54), invasive infection from tissue contamination(55-59) or a mechanobiological cellular injury(60). Some, or all, of these, may contribute to a tissue environment that is not compatible with cell survival. However, the precise cause(s), and relative contribution of each, have not yet been elucidated. A brief overview of their potential contribution to tissue loss will be outlined below.

2.1.1 How could mechanotransduction contribute to PTL after blast?

As described in Chapter 1 a blast event can confer a variety of mechanical insults on to tissue. Most of these can/may also occur in other traumatic injury (e.g. displacement of the body against an object). However, exposure of tissues to a very high energy shock wave is a particular facet of blast injury, either through coupling of the primary shock wave from air into tissues, or via penetration of very high energy fragments. Primary blast shock waves could directly and/or indirectly cause cell death in any/all of the cell types within the wound, as well as potentially increasing susceptibility of the wound to infection.

Literature studies suggest that the short term response to high strain rate loads, such as blast, appears to be characterised by increased plasma membrane tension with a reciprocal loss of the caveolae and redistribution of tension to the sub membrane actin cytoskeleton(61, 62). Tensile forces have also been implicated in raising plasma membrane tension(63). When the membrane tension threshold is overcome by shock waves the membrane integrity is lost, resulting in permeabilization(26, 64), ion translocation(65, 66) and oxidative stress(67-70). More widely, shock waves have been implicated in membrane sonoporation and indeed this has been investigated as a mechanism of drug delivery (71, 72).

2.1.2 What Kind Of Cell Death Is Progressive Tissue Loss?

Programmed cell death was historically defined as apoptosis. More recently a subtly different programmed cell death has also been described, driven by immunological factors, termed necroptosis. This can be described as a programmed form of necrosis. Figure 2.1 outlines the different pathways of cell death.

Unlike the relatively 'aseptic' cell death induced by apoptosis, necrosis and necroptosis are 'dirty'. Necroptosis is initiated by the binding of tumour necrosis factor – alpha and the Fas ligand to their cell surface receptors that results in the release of intracellular contents into the surrounding space(73). By comparison, necrosis is an unregulated digestion of cell components due to cellular trauma caused by physical or environmental factors (infection, toxin, ischaemia etc.). Necroptosis and apoptosis share a variety of common signalling factors. Necroptosis has been associated with a variety of conditions including, atherosclerosis(74), pancreatitis(75, 76), inflammatory bowel disease(76, 77), cancer(78)(89) as well as amyotrophic lateral sclerosis(79, 80)and Alzheimer's(81)(92).

2.1.3 Unbiased Techniques For Transcriptome Analysis

To characterise tissue injury after blast, experiments must chronicle the downstream interactions and signalling immediately after injury form mRNA transcription through to protein translation and interaction. Bulk RNA sequencing, which shows the global mRNA expression at a tissue level that drives functional phenotype, is one approach. It is novel compared to previous work on blast that has focused specifically on genes of interest though real-time quantitative polymerase chain reaction (RT-qPCR), rather than evaluating the entire transcriptome. Bulk sequencing allows an appreciation of both known genes and novel transcripts. It is relatively cost and time efficient, and measures average gene expression across a cell population. It is potentially the broadest, least biased approach to examine RNA transcription. Conversely, bulk sequencing is unable to give detailed information on cell heterogeneity, cell subpopulations or protein level expression.

Unfortunately no skeletal muscle was bio banked from UK casualties during recent military deployments. Samples taken from validated models of blast injury are therefore a reasonable alternative. Using stored tissue from previous *in vivo* experiments conducted at Dstl is also advantageous as it fulfils the 3R (reduce, refine and replace) requirements of animal research.

To demonstrate the utility of bulk RNA sequencing to deliver unbiased data to appreciate tissue signalling after blast, bulk sequencing analysis was applied to RNA extracted from skeletal muscle samples taken from two different species and models of blast injury conducted at Dstl.

The primary aim of this chapter was to evaluate effects of blast shock waves on skeletal muscle gene expression. The secondary aim was to evaluate the expression between models. The tertiary aim was to investigate which mechanisms of cell death.

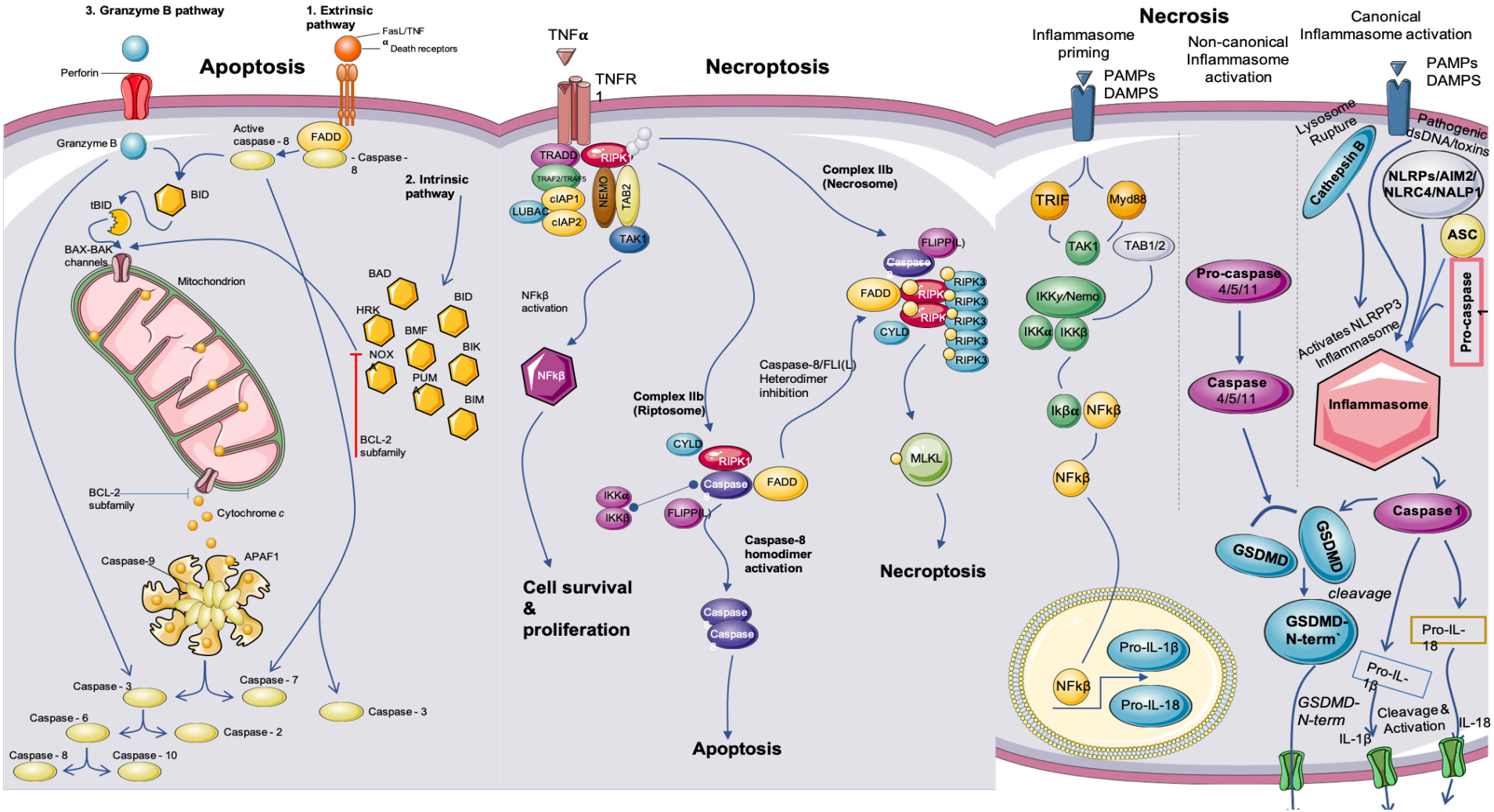

Figure 2.1: Outline of cell death pathways. **Apoptosis** is mediated either by an extrinsic, intrinsic or Granzyme B pathway through FADD and caspase 3 mediated cell death. **Necroptosis** is a TNF induced inflammatory programme cell death through RIPK and MLKL. **Necrosis** is uncontrolled cell death through inflammasome priming via PAMPS & DAMPS that results in membrane pore formation and release of cytoplasmic contents and active cytokines. It is unclear which, if any predominates after blast injury in skeletal muscle. Imagee produced by Robert Staruch

2.2 Methods

This study analysed the RNA from two different animal species, pig and rabbit, exposed to two different sources of blast shock waves, live explosive and compressed air device, and then applied bulk RNA sequencing techniques. This examined the RNA expression and gene enrichment data for common pathways, gene sets or individual genes.

Muscle samples for this chapter's bulk RNA transcriptome analysis were obtained from pigs (porcine model) or rabbits (rabbit model) used in the studies outlined in detail by Kirkman(50, 51) and Spear(82). All animal work described here was conducted following local ethical approval and performed under the authority of the Animals (Scientific Procedures) Act 1986. These samples were stored at the time of these experiments (Rabbit – 2011, Porcine – 2015), and then used with permission for this analysis.

2.2.1 Porcine Model

To facilitate discussion of the sequencing results, the porcine experimental methods are briefly paraphrased below, for full methods please see the published studies(50, 51). Figure 7 outlines the experimental timeline for the porcine trials. In this experiment, 'treatment' refers to animals exposed to blast, haemorrhage and a local tissue injury. 'Control' refers to animals that did not receive a blast, but did receive the haemorrhage and local tissue injury.

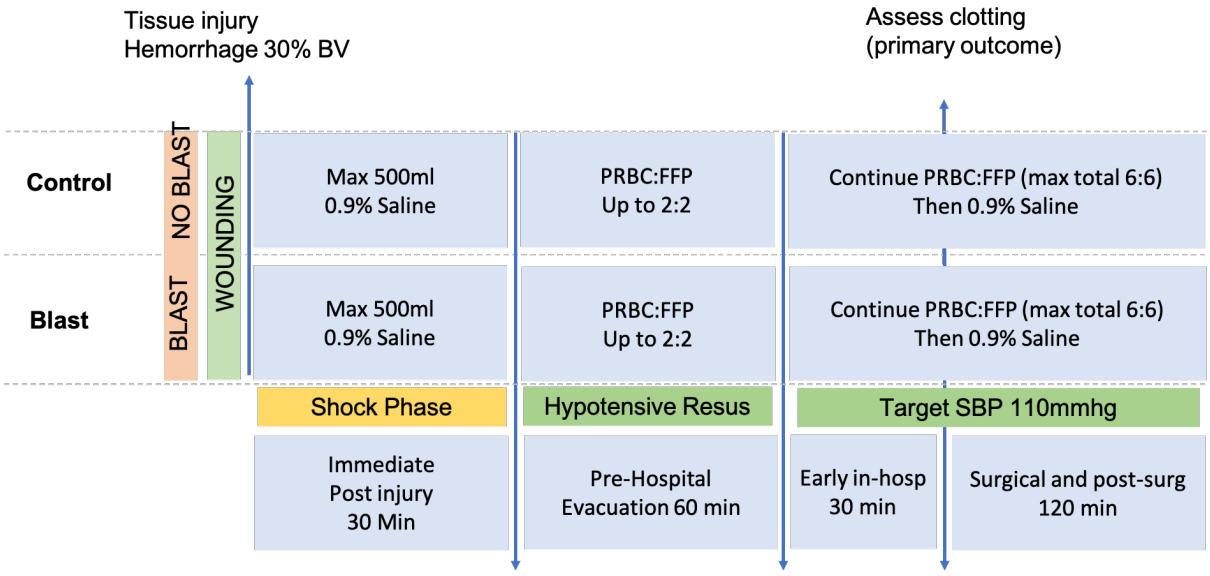

Figure 2.2: *The protocol for the control and treatment samples analysed in this chapter. The diagram is reproduced from Figure 3 of the full publication found at (51). © Crown copyright (2023). Reproduced with Permission of Authors.*

Anaesthetised animals (mean weight 55.9kg, 45-65kg) were wrapped in a 12 ply Kevlar blanket for protection against secondary and tertiary blast effects (debris etc). Animals were secured supine onto a wheeled trolley on a fixed steel platform on an open air blast range. The animal's right side faced a bare charge of 2.2kg of ethylene dichloride, EDC 1, commercial explosive (QinetiQ, Fort Halstead, UK), mounted on a 1M cardboard tube with a stand-off distance of 2.0-2.5m from the animal. During blast, animal monitoring was limited to ECG and respiratory waveform tracings. Anaesthesia was maintained via syringe driver. After remote detonation of the charge and safety period, the animal was moved via trolley to the laboratory.

In this experiment control refers to animals prepared for blast, taken to the open air blast range and then not exposed to a blast, but otherwise treated the same as blast-exposed animals (e.g. control animals were still subjected to a controlled soft tissue injury (outlined below)).

Treatment animals were exposed to blast and then subjected to a controlled soft tissue injury (outlined below).

2.2.1.1 Injury

After exposure (blast or control) a controlled haemorrhage insult was initiated over 9 min through a femoral arterial cannula with a computer controlled pump (Masterflex L/S model 7550-17; Cole Palmer Instrument Company, Chicago I11). Haemorrhage of 30% of total blood volume was performed. All animals received a controlled soft tissue injury using a captive bolt gun (CASH Special Knocker; Accles & Shelvoke, Sutton Coldfield, UK) four times to the right hindquarter.

2.2.1.2 Endpoints:

The primary endpoint of the model was clotting status assessed by thromboelastogram after 30 minutes of in hospital resuscitation. All animals were euthanised at eight hours. Animals underwent post-mortems to inspect lung parenchyma and intra-abdominal blood volume. Biopsies of skeletal muscle were taken at the end of the experiment post-mortem and stored in RNA stabilisation solution for bulk RNA sequencing.

2.2.2 Rabbit Model:

Rabbit hindlimb were treated with blast waves generated by a compressed air cylinder. Briefly, a 20,216 kPa compressed air cylinder charged an air storage chamber (150mL). A solenoid valve discharged the stored air to the blast nozzle where an aluminium disc ruptures, forming a shock wave that is emitted from the nozzle. Altering the distance between the nozzle and target allowed the delivery of different blast loads. The nozzle was checked daily using a pressure sensor data capture system and a minimum of three exposures to ensure consistency of loading at different blast distances. The full blast apparatus is described in detail elsewhere(82).

Shortly after baseline measurements (heart rate, blood pressure, arterial blood gas) both rabbit hindlimbs, centred on gastrocnemius, were exposed either to blast or no blast (control).

In this experiment, 'treatment' group refers to animals were exposed to a blast wave from a compressed air device. The device is described below. Each treatment rabbit's limb received five successive blasts to expose the whole caudal aspect of the limb between the knee and ankle (stifle to hock) to a blast injury.

In this experiment, 'control' group refers to animals who received no blast wave exposure.

The left gastrocnemius was excised post-mortem and divided longitudinally. One half was divided into three 0.25cm^3 sections and placed into RNA stabilisation solution and stored at -20°C as per manufacturer's instructions until required.

Rabbit tissue was taken at the end of the experiment (12 hr) post-mortem as per the following methods that are paraphrased from the full publication by Spear et al(82). Figure 2.3 outlines the methodological timeline.

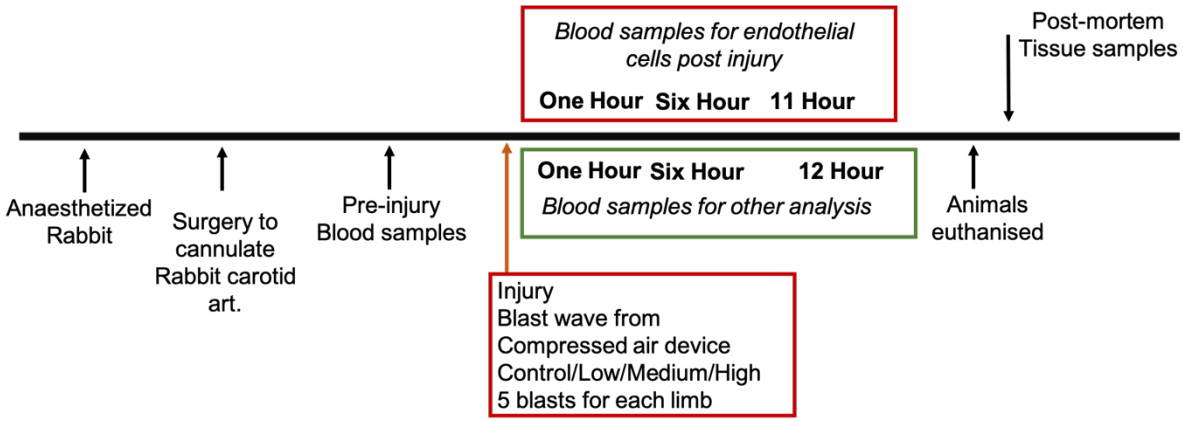

Figure 2.3: Timeline of experimental procedures for rabbit model. A detailed set of methods can be found in the paper from Spear et al. Only animals exposed to High compressed air shock waves, and controls, were analysed in this work. Image a reproduction from publication. Permission to reproduce from Authors.

2.2.3 Bulk RNA Sequencing

2.2.3.1 RNA Homogenisation

Harvested skeletal muscle samples were cut into smaller pieces (<5mm) using a scalpel and then homogenised with a Qiagen Tissueruptor II handheld device (Qiagen Ltd) with the appropriate volume of Trizol (1ml per 0.1g of tissue). Homogenised samples were incubated at room temperature for 5 minutes. Then, chloroform was added to the homogenate (0.2ml chloroform per ml Trizol) and the sample shaken vigorously for 20 seconds then allowed to sit at room temperature for 2-3 minutes. The aqueous top phase was then slowly aspirated into a new sterile RNase-free tube. Following this an equal volume of 99-100% RNA-free ethanol was slowly added to the sample. Samples were then loaded into an RNeasy column in 700µl aliquots and spun for 30 seconds at 8000 xg. RNA extraction was then undertaken as per the Qiagen RNeasy miniprep kit protocol.

2.2.3.2 RNA Quality Control

RNA was tested using 1 μl aliquots on a nanodrop spectrophotometer (Implen Ltd) to assess for RNA concentration, 260/280 and 260/230 ratios. Quality was assessed using an Agilent Tape station as per published protocols using high sensitivity D1000 tape and 1μl of RNA. Data was inputted into an Excel spreadsheet (Microsoft Corporation) to calculate total RNA quantity in 60μl. RNA Integrity Number (RIN) was determined and all samples used in this study had a RIN number greater than >8.8.

2.2.3.3 Library Preparation

Library preparation and sequencing was conducted by Source Biosciences Ltd.. Libraries were prepared using the NEBNext Ultra II Directional RNA Library Prep Kit for Illumina with the NEBNext Poly(A) mRNA Magnetic Isolation Module following the manufacturer's protocol.

2.2.4 Experimental Methodology for DESeq2 Data Analysis

Table 2.1: Nomenclatures for groups in experimental data sets. Full samples lists can be found in the Chapter 2 Appendix, Table 2.4 & 2.5

Species	Control	Treatment
Porcine	Group A (Control)	Group B (Blast)
Rabbit	Group S (Control)	Group H (High Blast)

2.2.4.1 Analysis in R

Counts matrices were imported into R (R Foundation for Statistical computing, Vienna, Austria) and RStudio (version 1.2.5042) for differential expression Gene Set Enrichment analysis (GSEA). To undertake data visualisation, comma separated value ,csv, counts data files were imported into R Studio, converted into a data frame and then results analysed using DESeq2 package, Enhanced Volcano, ggplot2, complex heatmap, fgsea and enrichr library packages. Validated analysis pipelines were gifted from Professor Adam Cribbs (Botnar Research Centre, University of Oxford). New pipelines were constructed from Bioconductor Vignettes (www.bioconductor.org) and online tutorials. Full R markdowns are found in a Github repository online (link in appendices). Gene Ontology and Gene Set Enrichment analysis was undertaken using hallmark gene sets from the msigdb (molecular signature database). Table 2.1 outlines the nomenclatures for groups in experimental data sets used for analysis in R studio.

2.2.4.2 DESEQ2 Data Adjustments

Differential expression was analysed in the data using the DESeq2 R Studio package. To do this, counts matrices were first normalised, then dispersion estimated in the data. Finally generalised linear models were fitted to the data and a Wald test applied. The Wald test is applied for large datasets (>30 samples). The Wald test, or Wald Chi-Squared Test, is a method to investigate if explanatory variables in a model are significant (i.e. whether their effect on the outcome is significant). The null hypothesis in the Wald test is that two experimental observations are equal in their value. Finally the DESeq2 estimates dispersion within the samples.

Then the dataset was filtered to remove genes with count values less than 10 across all experimental samples. This reduces the computational load of the analysis by reducing the overall data size and removing outliers.

2.2.4.3 *Data Normalisation*

DESeq2 normalises data through distribution. In DESeq2 a pseudo reference value is calculated (termed a geometric mean) by multiplying the counts across samples and then taking the square root of this value. Sample ratios for each gene are then calculated by dividing the gene counts by the pseudo reference values. The median sample ratio across all genes is taken as the normalisation or 'size' factor. Gene counts are then divided by the median sample ratio (normalisation factor) to normalise counts across all genes and samples. Log base 10 transformation is applied to the data to reduce it into comprehensive plots.

To reduce the likelihood of false positives, through multiple statistical testing, the adjusted p-value (padj) is adopted. The padj is calculated in DESeq2 using the Benjamini-Hockberg (BH) correction (5% False discovery rate). The BH method ranks all p values in ascending order. Then a p values rank is divided by the total number of tests performed and multiplied by the FDR.

Due to the large dataset, a variance-stabilising transformation (vst) was applied to the data.

To evaluate the degree of variance on the data, as well as what factor is contributing the most variance, Principal component analysis (PCA) was undertaken. PCA evaluates the principal influence of variation from the experimental conditions on the results using geometrical analysis of the data.

2.2.5 Adaptations Of Pathway Analysis

In order to undertake gene set enrichment analysis, the molecular signature database (msigdbr) was used to evaluate pathway enrichment through hallmark pathway sets. The hallmark sets have been developed for a defined set of species, of which the rabbit (*Oryctolagus cuniculus*) is not one. To reduce inconsistencies between the pathway

terminology between hallmark species sets, it was decided to apply human species enrichment to both models.

To do this human ensembl IDs were mapped to the gene names that were mapped to the original species ensembl IDs (using species specific Biomart libraries). Figure 2.4 shows this process. Where no gene ID is reported on enssembl.org for that species, an ensemble ID is reported.

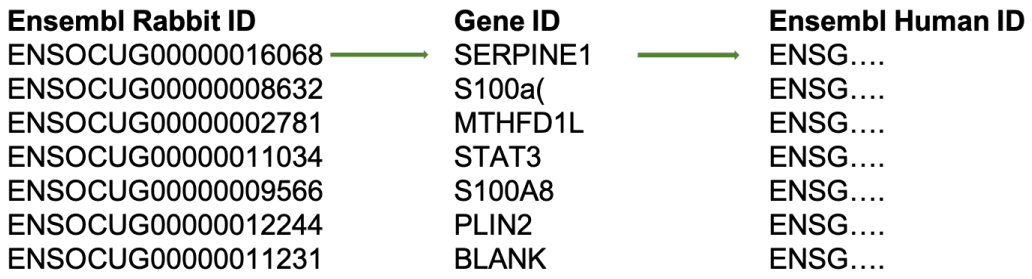

Figure 2.4: Pictorial demonstration of matching Human ensembl ID's to Gene ID's. Gene ID's were matched to the rabbit ensembl ID's. This reduced errors and enabled pathway

2.2.5.1 Cell Death Enrichment Analysis

To explore cell death signalling, gene sets for apoptosis, necrosis and necroptosis were constructed using term lists on ensembl.org. Then these gene lists were searched in our sample gene lists. Genes that were found were then grouped into their cell death mechanism.

2.3 Results

A full list of samples (table 2.4 & 2.5), raw paired end reads and percentage alignment for each species can be found in chapter 2 appendices (table 2.2 & 2.3).

2.3.1 Alignment, Dispersion & Variance

In the porcine model, the total number of significant genes from DEseq analysis was 5444, the number of upregulated significant genes with a log2fold change >1 was 777. The number of downregulated significant genes with a log2fold change > than -1 is 572.

In the rabbit model, the total number of significant genes was 5950. The number of upregulated significant genes with a log2fold > 1 was 1628. The number of downregulated significant genes with a log2fold < -1 was 576.

Mean sample alignment in the porcine samples was 87.06%, whilst the mean alignment was 82.92% in the rabbit samples.

Full figures for evaluation of dispersion, differentially expressed genes and sample variance in the principal component can be found for both species in Chapter 2 Appendices.

2.3.1.1 Porcine Sample Distribution

Figure 2.5 outlines the principal component analysis (A), heatmap of counts (B) and heatmap of sample to sample distances (C) for the porcine samples. In these samples, the PC1, the most variation in the data, is 43% and PC2, the second most variation in the data, 20%. The majority of blast samples are well grouped together with a moderate variance in the PC1 and PC2 components. There is however one notable outlier to the group. In the control group the samples have a wider PC1 variance, but are closely clustered in the second principal component. There are two notable outliers in this group. The scree plot of principal component variance shows that the third principal component (PC3) contributes over 10% of variance (Chapter 2 appendices).

Figure 2.5, (B) shows the top 25 genes by counts. The samples are clustered by condition into two comparable groups, and demonstrates that COX1, ACTA1, COX3, ATTP6 and GAPDH are the genes with the highest counts in this model.

Figure 2.5, (C) shows the sample clustering on a heatmap of sample to sample distances. It adopts hierarchical clustering to show how samples data is grouped. This heat map illustrates that the treatment and control groups are well clustered into distinct groups, indicating there was a clear difference in the treatment and control environments to induce distinct effects. It also shows that three treatment samples are not clustered together, which may indicate that influences, such as sample handling technique or animal house, may have increased sample variation (sample technique, animal housing etc).

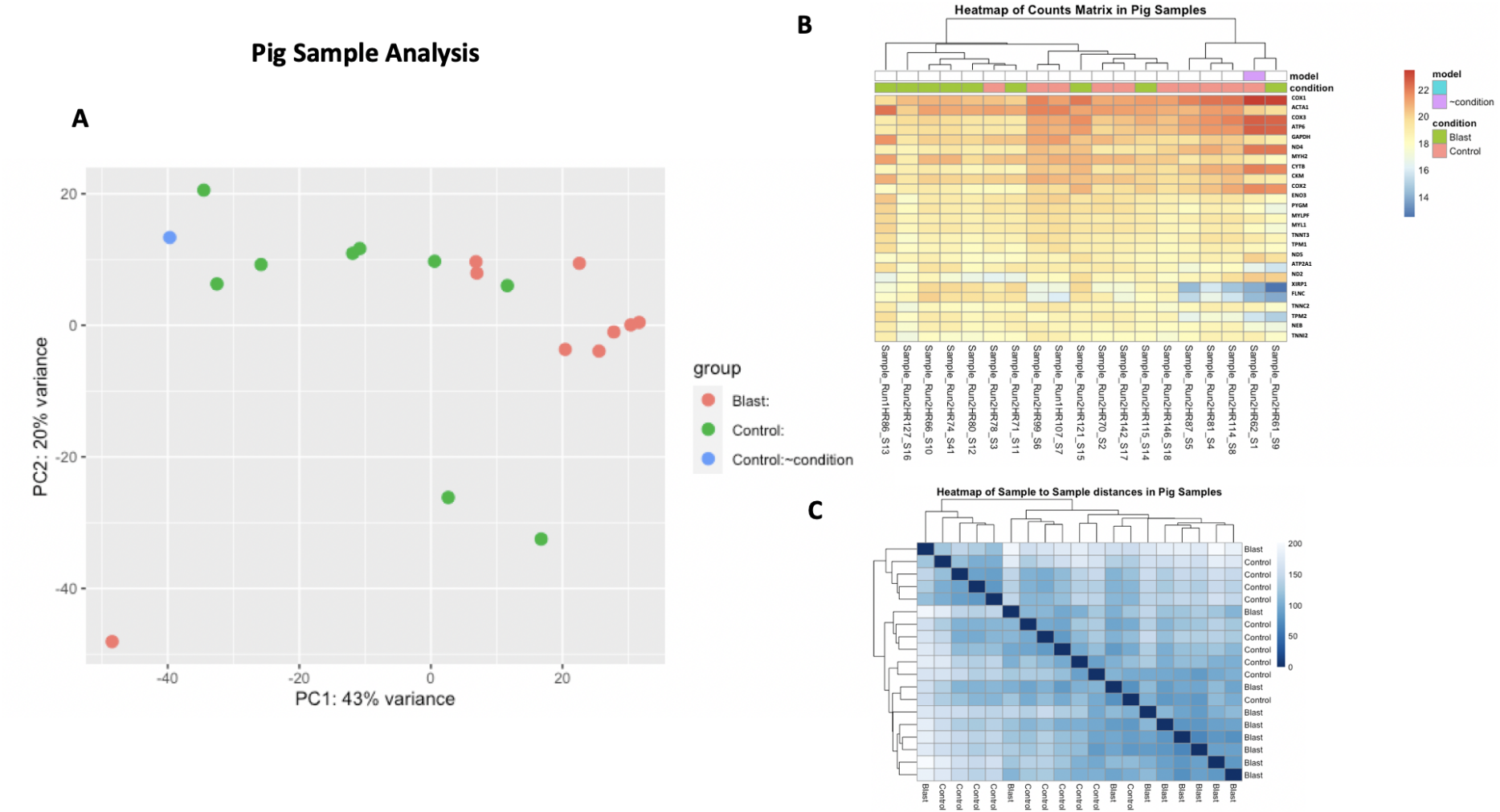

Figure 2.5: Porcine sample analysis: **A.** Principal component analysis of Porcine samples. **B.** Heatmap of counts of Porcine samples. The Top 25 genes with the largest counts are listed. **C.** Heatmap of sample to sample distances in the Porcine sample.

2.3.1.2 Rabbit Sample Distribution

Figure 2.6 outlines the principal component analysis (A), heatmap of counts (B) and heatmap of sample to sample distances (C) for the rabbit samples. In the rabbit model, the PC1 is 47%, the PC2 is 19%. The blast samples show the most variation along PC1, with a narrow PC2 variance except for two outlier samples. In the control group, the samples show the greatest variation on the PC2 axis, but are tightly clustered along PC2. The control group also has 2 outlier samples along PC2. The heatmap of sample to sample distances shows the clustering of the groups, which are well aligned into two distinct clusters of blast and control. The heatmap of counts confirms this sample clustering, and shows that actin alpha 1(ACTA1), Nyosin-1 (MMYH1), Aldolase A (ALDOA) and cyclooxygenase 2 (COX2) are the genes with the highest counts in the rabbit model.

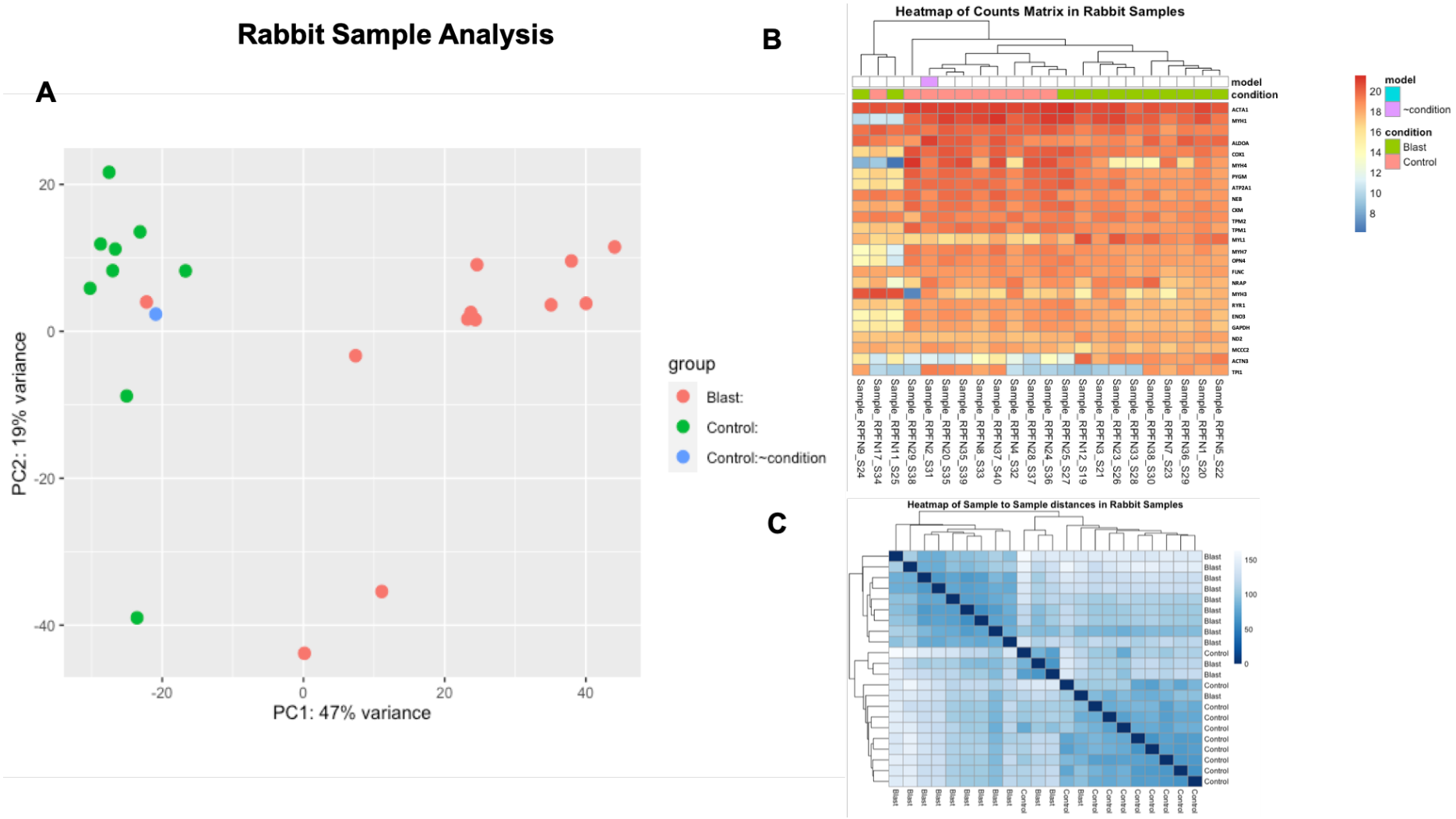

Figure 2.6: Rabbit sample analysis: **A.** Principal component analysis of Rabbit samples. **B.** Heatmap of counts of Rabbit samples. The Top 25 genes with the largest counts are listed. **C.** Heatmap of sample to sample distances in the Rabbit sample.

2.3.2 Changes in gene expression in skeletal muscle exposed to shock wave

2.3.2.1 Porcine Model

Figure 2.7 shows a volcano plot of the difference in gene expression for porcine samples vs control. It shows that the skew of gene expression was towards those that were upregulated (positive log fold change). The gene AGT had the largest P value. The plot also highlights that the range of log2fold change was from -5 to +5.

2.3.2.2 Rabbit Model

Figure 2.8 is a volcano plot of gene expression for rabbit blast samples vs control. It confirms the findings of the MA plot which shows a large number of genes that reach the significance and log2fold threshold (red dots). The gene with the largest P value is Ras Related Glycolysis Inhibitor and Calcium Channel Regulator (RRAD), whilst the gene with the largest log fold change (that reached significance) is IL1RL1. In the rabbit model, there is a strong skew towards gene upregulation (over downregulation). In those genes that were downregulated (negative log2fold expression), gene Zinc Finger AN1-Type Containing 5 (ZFAND5) had the greatest p value and the largest negative log fold change. Finally, the volcano plot shows that the range of log2fold change in samples was form -5 to +10.

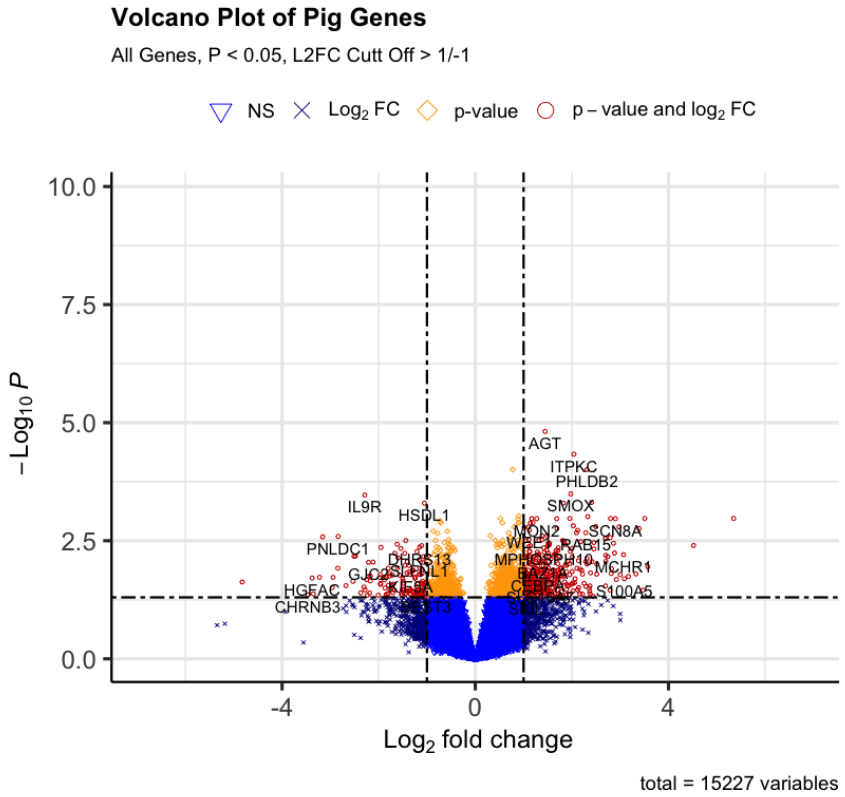

Figure 2.7: *Volcano plot showing differential gene expression blast vs control in the Porcine model*

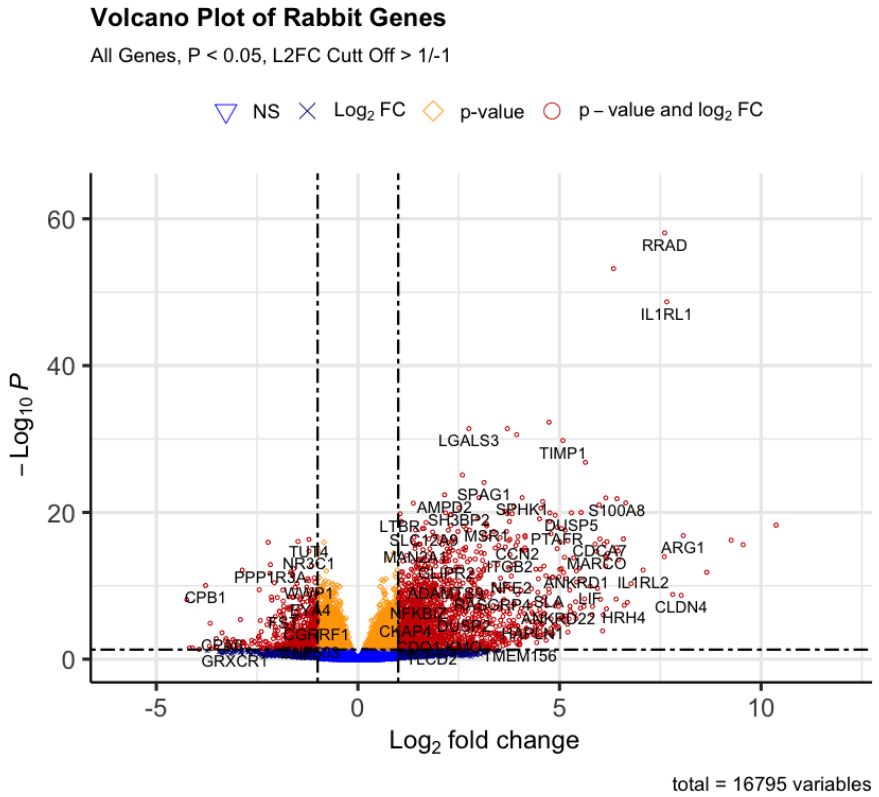

Figure 2.8: *Volcano plot showing differential gene expression blast vs control in the Rabbit model*

2.3.2.3 Top 25 Genes Of Significance:

Table 2.2 and 2.3 outline the top 25 significant genes expressed in each model based on adjusted P value. In the porcine model, the top 25 significantly expressed genes were involved in both intracellular and extracellular signal transduction(Transmembrane 4 superfamly,TM4SF1, G Protein Subunit Gamma 8,GNG8, Sodium voltage-gated channel alpha subunit 8m, SCN8A), inflammation (Interleukin 9, IL9R, Hydroxysteroid Dehydrogenase Like 1,HSDL1, Baculoviral IAP Repeat Containing 3, BIRC3, Spermine Oxidase, SMOX) RNA transcription(Cyclin Dependent Kinase 12,CDK12), cytoskeletal organisation (Pleckstrin Homology Like Domain Family B Member 2, PHLDB2, G Protein subunit Gamma 8, GNG8) and cellular function (Spermine Oxidase, SMOX, DNA Cross-Link Repair 1B, DCLRE1B). Interestingly, BIRC3 (which inhibits apoptosis through Tumour necrosis factor receptor (TNFR) associated factor 1, TRAF1/Tumour necrosis factor receptor (TNFR) associated factor 2 ,TRAF2, binding) featured in the top 25 expressed genes.

In the rabbit model the top 25 genes were involved in inflammation (Serpin Family E Member 1, SERPINE1, Interleukin 1 Receptor Like 1, IL1RL1, Galactin 3, LGALS3, Colony Stimulating Factor 3 Receptor, CSF3R), extracellular matrix remodelling (TIMP metallopeptidase inhibitor 1, TIMP1, Microtubule Associated monooxygenase, Calponin and LIM Domain Containing 1,MICAL1) and cell homeostasis(S100 Calcium Binding Protein A8, S100A8, Perilipin 2, PLIN2, Deltex E3 Ubiquitin Ligase 4, DTX4).

Gene ID	Log2FoldChange	Padj	Function
AGT	1.444	1.53E-05	*Production of Angiotensinogen protein*
ITPKC	2.042	4.64E-05	*Catalyses phosphorylation of inositol 1,4,5-trisphosphate*
PHLDB2	2.313	9.83E-05	*Enables cadherin binding, cytoskeletal organisation*
SMOX	1.976	3.22E-04	*Cell cycle modulation, scavenging ROS, control of gene expression*
IL9R	-2.287	3.41E-04	*Cytokine receptor that modulates interleukin 9*
ENSSSCG00000030300	2.407	4.89E-04	NA
HSDL1	-1.053	5.06E-04	*Enables oxidoreductase activity*
SCD	1.821	5.06E-04	*Fatty acid biosynthesis, particularly oleic acid*
MMP19	2.329	9.76E-04	*Breakdown of extracellular matrix*
ENSSSCG00000011297	2.798	0.00106	NA
ENSSSCG00000030278	1.956	0.00106	NA
LEP	3.508	0.00106	*Regulation of energy homeostasis,*
ENSSSCG00000049394	5.348	0.00106	NA
SCN8A	2.900	0.00107	*Sodium channel alpha subunit family, rapid membrane depolarisation*
MON2	1.272	0.00107	*Involved in Golgi to endosome transport*
ARMC12	1.686	0.00107	*Located in nucleus, key for sperm mitochondrial sheath + fertility*
TM4SF1	1.169	0.00107	*Cell surface proteins involved in signal transduction*
CDK12	1.194	0.00130	*Phosphorylation of RNA polymerase II & RNA transcription activity*
ENSSSCG00000037910	1.140	0.00134	NA
BIRC3	2.029	0.00152	*Inhibits apoptosis by binding to TRAF1 & TRAF2*
DCLRE1B	2.495	0.00158	*Telomere maintenance & protection in S Phase*
CLDND1	1.102	0.00160	*Cell surface protein*
GNG8	2.976	0.00160	*Modulator and transducer of transmembrane signalling*
ENSSSCG00000012481	1.012	0.00166	NA
SDR16C5	3.390	0.00174	*Involved in reduction of retinol to retinaldehyde & NAD+/NADH*

Table 2.2: Top 25 significantly expressed genes in Porcine model in descending order of adjusted p value with their corresponding log2fold change. Individual gene function has been listed where information was available.

Gene ID	Log2FoldChange	Padj	Function
e	7.610	8.25E-59	*GTP binding and calcium channel regulator activity*
ENSOCUG00000021126	6.341	6.06E-54	*NA*
IL1RL1	7.661	2.07E-49	*Proinflammatory receptor involved in T helper cell function*
ENSOCUG00000029235	4.739	5.05E-33	*NA*
LGALS3	2.753	3.86E-32	*Involved in neutrophil activation*
ENSOCUG00000024096	3.707	3.86E-32	*NA*
RUNX1	3.936	2.58E-31	*Stabilises RUNX1 in hematopoietic cell differentiation*
TIMP1	5.085	1.63E-30	*Inhibitors of matrix metalloproteinases*
ENSOCUG00000034927	5.641	1.53E-27	*NA*
AVPI1	2.592	8.07E-26	*Upstream/positive regulation of MAPK cascade*
SPAG1	3.130	8.67E-25	*May regulate GTP signalling in spermatogenesis*
AMPD2	2.150	4.01E-23	*Involved in purine metabolism*
MTHFD1L	3.005	9.77E-23	*Synthesis of tetrahydrofolate in mitochondria*
SPHK1	4.074	9.77E-23	*Sphingosine-1-phosphate synthesis for cell function*
ENSOCUG00000008632	6.149	1.05E-22	*NA*
S100A8	6.424	1.36E-22	*Regulation of cell cycle progression & differentiation*
ENSOCUG00000012892	4.583	3.30E-22	*NA*
CSF3R	6.643	5.08E-22	*Cytokine that controls granulocyte production/function*
DTX4	1.373	5.64E-22	*Involved in Notch signalling and protein ubiquitination*
SERPINE1	5.984	9.32E-22	*Inhibitor of fibrinolysis through Urokinase & tPA*
PLIN2	3.871	1.48E-21	*Development and maintenance of adipose tissue*
SH3BP2	2.505	2.46E-21	*Binds SH3 domains for signal transduction pathways*
ENSOCUG00000005408	4.537	2.55E-21	*NA*
MICAL1	3.649	6.73E-21	*Enzyme that facilitates actin filament depolarisation*
ENSOCUG00000000877	5.536	1.02E-20	*NA*

Table 2.3: Top 25 significantly expressed genes in Rabbit model in descending order of adjusted p value with their corresponding log2fold change. Individual gene function has been listed where information was available.

2.3.2.4 Hallmark Gene Set Enrichment Analysis

Several pathways were common to both injury models, outlined in Figure 2.9. In particular, TNF-α signalling via NFκB, inflammatory response, Mtorc1 signalling, IL2 Stat5 signalling, kras signalling up and hypoxia were common to both with large dot sizes indicating high counts. These terms were also highly significant according to their adjusted p value. Interestingly apoptosis was found in the rabbit model as an enriched term, but was not seen in the porcine model. Furthermore oxidative phosphorylation was strongly enriched in the rabbit model compared to the porcine. In the porcine model, oestrogen response early, apical surface and xenobiotic metabolism were enriched but had weak adjusted p-values.

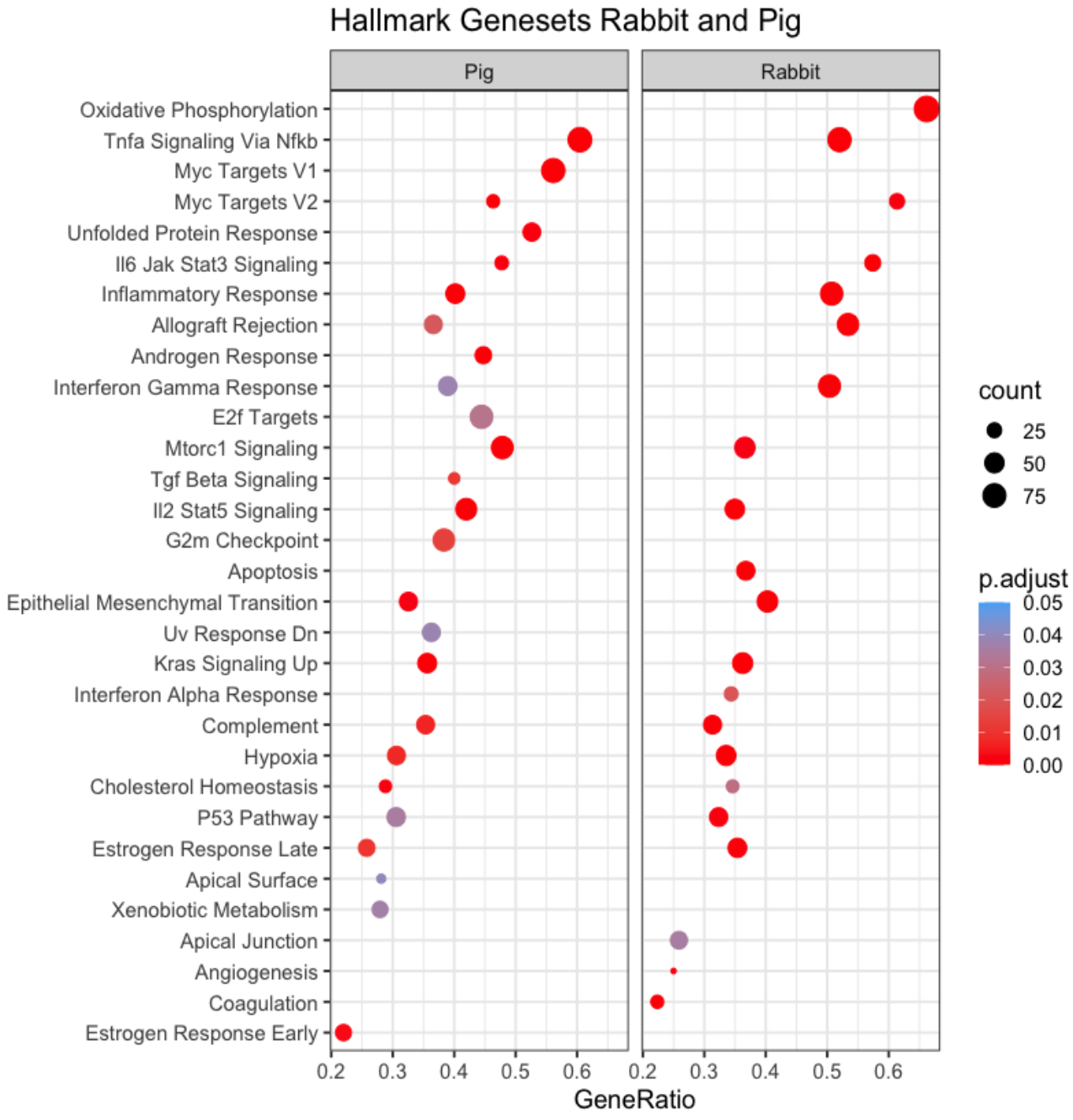

Figure 2.9: *Dot plot of gene set enrichment analysis on both species.* Figure 15 shows the output from the gene set enrichment analysis for both the pig and rabbit models in a dot plot. The dot plot plots the gene ratio, the number of genes found in the samples as a ratio of the total number of genes in the gene set term, against the gene set terms. The size of the dots corresponds to the counts – the number of genes found in the samples for that particular term. The colour of the dots correspond to the adjusted p value. The figure shows that there were common hallmark pathways enriched in both samples, despites the different mechanisms of recreating blast.

2.3.3 Investigating Inter-Model Differences In Cell Death

Gene expression data was analysed for similarities between the two models (Figure 2.10 and 2.11). The models themselves are very different (different species, different mechanism of shock wave generation) but both involve skeletal muscle exposed to a high energy shock wave. Any similarities identified would suggest that the regulation of those genes was independent of species and method of shock wave generation and may indicate a universal mechanobiological response.

2.3.3.1 Apoptosis

For apoptosis (Figure 2.10a), only two genes were found to be differentially regulated in both models (Cytochrome P450 family 1 subfamily B, CYP1B1, Splicing Factor Proline and Glutamine Rich, SQPQ).There were fewer genes differentially expressed in the rabbit model with log2 fold change less than 2. In the porcine model, three genes had a log2 fold change greater than three (Hexokinase 3, HK3, Solute Carrier Family 7 Member 11, SLC7A11 & Integrin Subunit Alpha M, ITGAM). Pejvakin, PJVK was the most downregulated apoptotic gene in this model. Figure 2.10 shows the number of genes identified in each model for each cell death term. This figure shows that in both models, greater than a third of the gene terms were not found. This could be accounted for poor gene identification in these two species compared to the human genome.

2.3.3.2 Necroptosis

In necroptosis, seen in Figure 2.10b, the rabbit model had more genes identified than the porcine model. However, of these identified genes, the porcine model had a greater number of significantly expressed genes (29 Porcine vs 13 Rabbit). There were a similar number of genes not found in both models (29). There were two common genes (Baculoviral IAP Repeat Containing 3, BIRC3 & CASP8 and FADD Like Apoptosis Regulator, CFLAR) in both models. In the Pig model, BIRC3 was highly expressed after blast exposure(log2fold change 3.11, $P<0.05$), whilst CFLAR had a smaller log fold change but reached significance (log2fold 0.91, $P<0.05$). BIRC3 inhibits apoptosis through inactivation of caspases. Conversely CFLAR is caspase and FADD-like apoptosis regulator which is a potent regulator of apoptosis and inhibition of Fadd Fas associated via death domain, TNFRSF6, mediated apoptosis mediated cell death.

2.3.3.3 Necrosis

In necrosis, (Figure 2.10c), the number of genes identified in each model were the same. Although the number of significantly expressed genes was greater in the rabbit than the porcine model (30 vs 11). Again, BIRC3 and CFLAR were significantly upregulated in both models in necrosis. This is expected due to the overlap between necroptosis and necrosis. Solute Carrier Family 6 Member 6, SLC6A6 was also significantly expressed in this group. SLC6A6 is a gene that encodes for sodium and chloride ion dependent channels.

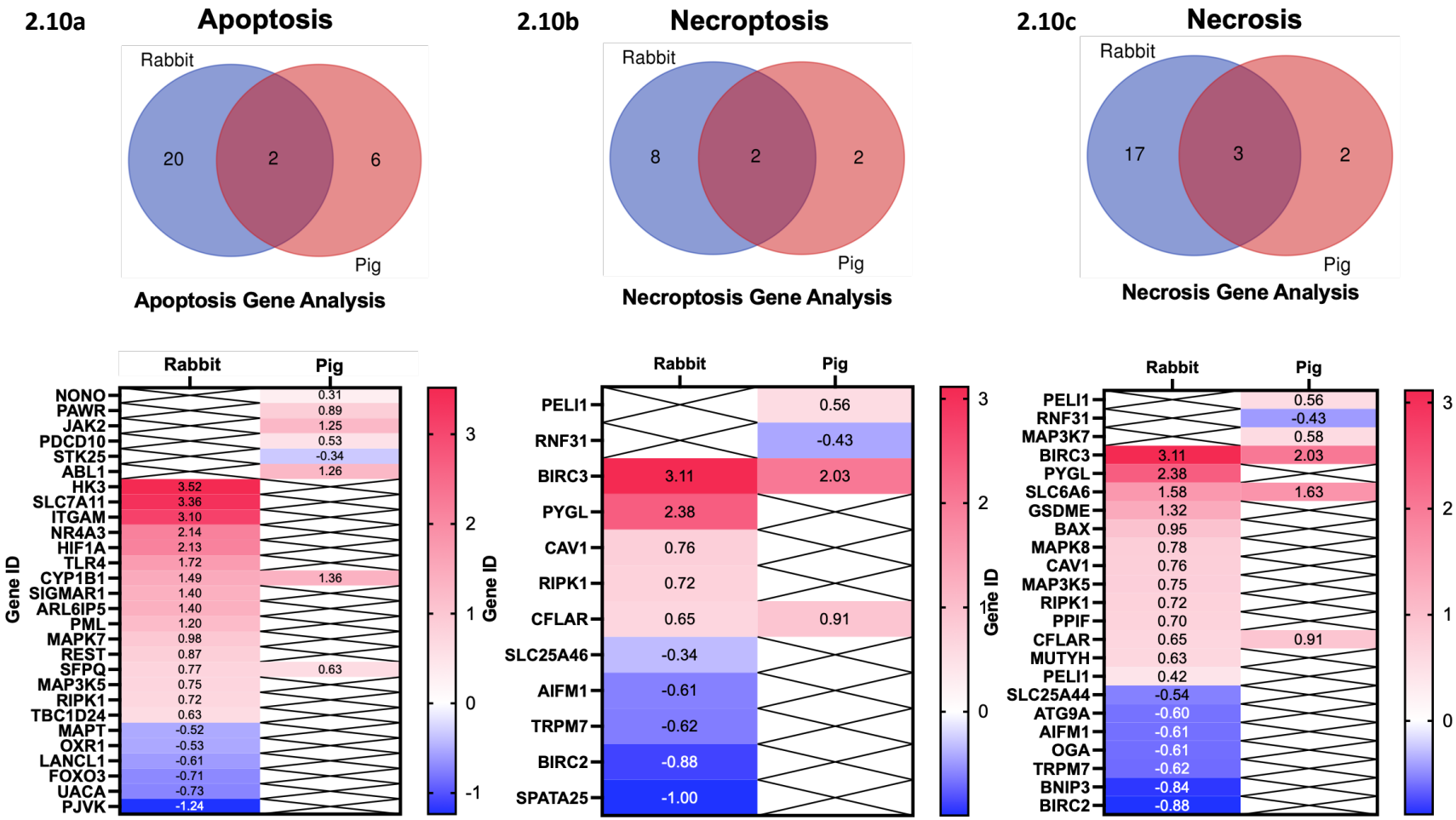

Figure 2.10: *Venn diagrams of gene overlap & heatmaps of gene expression for different cell death mechanisms.*

2.11a **Pig Cell Death Analysis**

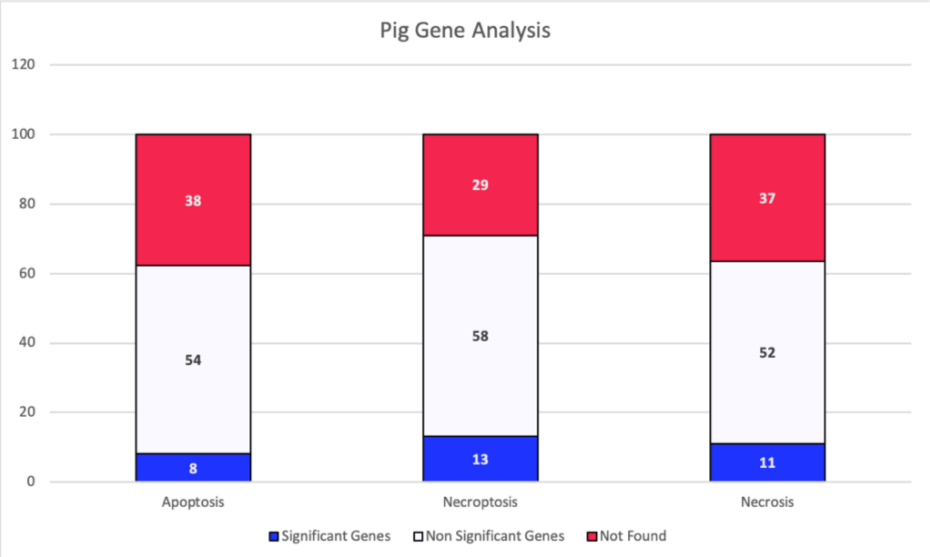

2.11b **Rabbit Cell Death Analysis**

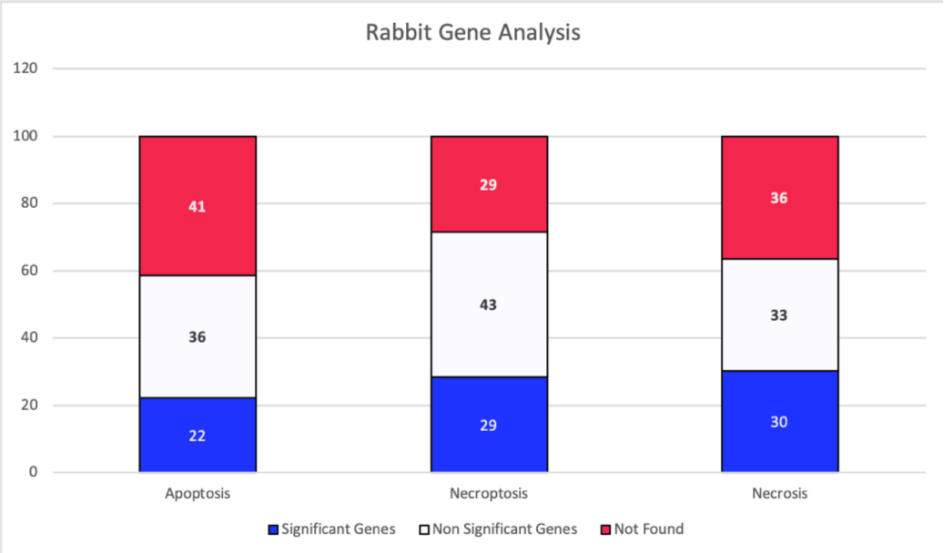

Figure 2.11: *Bar charts of gene expression in each cell death mechanism. The percentage of significant genes, non-significant genes and those not found in the analysis are represented*

2.4 Discussion

To probe what could be driving PTL after blast injury, bulk RNA sequencing techniques were applied to *in vivo* samples to obtain a snapshot of gene transcription after shock wave exposure.

The primary aim of this chapter was to evaluate the effects of blast shock waves on skeletal muscle gene expression. The secondary aim was to compare the expression between models. The tertiary aim was to investigate what mechanisms of cell death predominated.

2.4.1 Investigating Inter Model Differences

The results presented show that the rabbit blast injury model resulted in a greater number of differentially expressed genes at the timepoint the samples were taken. Furthermore there was a skew towards upregulation when compared to the porcine gene data (~5900 rabbit vs ~5400 genes Porcine). This could be explained by the differences in explosive experimental conditions. Firstly, the porcine group were covered with a Kevlar blanket before exposure to blast. The Kevlar blanket could have reduced the shock wave energy propagating into tissues, reducing any tissue effects. Secondly, the rabbit model exposed tissue to a blast shock wave at a closer proximity than the porcine model. The porcine model utilised a 2 metre stand-off distance to the blast source, whilst the rabbit model used the pressure gun at close proximity and with multiple exposures to ensure full limb coverage. Potentially some areas of rabbit tissue could have been exposed to multiple shock waves, which could be a confounding factor when appraising the gene expression data. The more proximal the target to the blast source, the larger the shock wave peak overpressure which could result in more severe tissue injury. These factors may explain any differences seen between the two groups gene expression patterns.

The mechanical and timing differences between both models precludes direct comparisons of gene expression between. Some genes are common to both species and have similar changes might suggest these genes being a strong feature of blast injury.

2.4.2 Cell Death Mechanisms

The hallmark gene analysis shows which pathways are enriched. The top 5 pathways enriched all relate to cell stress, inflammation and immune axis activation namely oxidative phosphorylation, Tnfα signalling, Myc targets V1, Myc targets V2, unfolded protein response and IL6 Jak stat. One hypothesis driving this analysis was what mechanism of programmed cell death was driving progressive tissue loss seen after blast injury. The GSEA dot plot shows that apoptosis features as an enriched pathway in the rabbit model, but not in the porcine model. The exact circumstances surrounding shock wave exposure will influence the tissue response. As outlined in chapter 1, the size of the explosion and the distance from the source will control the size of peak overpressure which hits the tissue interface. These experimental disparities may explain the differences in pathway enrichment. A limitation of this approach is the lack of human hallmark pathway for necroptosis.

To overcome this limitation, a necroptosis gene set was adopted using gene lists from the ensembl website. The predominant type of cell death in each model was determined by preforming a manual gene set enrichment analysis. Gene expression data was searched using hallmark and ensembl gene sets for necrosis, apoptosis and necroptosis. Heatmaps were built and analysed to determine which mechanism predominated. The results showed that all three cell death mechanism; were stimulated in similar degrees across both models. Although the total genes expressed for each group were the same, the proportion of significantly and not significant genes differed between groups. In the rabbit model, the proportion of significantly expressed genes was globally larger than in the porcine models across all cell death mechanisms. This implies that multiple cell signalling mechanisms are

probably driving the cell death associated with blast injury. It might also be that that different cell populations are dying from necrosis, apoptosis and/or necroptosis rather than all cells dying from a similar mechanism. Given the complexity of both the injury mechanism, and of animal physiology, this finding is perhaps less surprising than if a single cell death mechanism had been found. Cellular and molecular mechanisms are rarely executed by one single or factor, but through the influence of a heterogenous group of factors.

Although two common genes were found between necrosis and necroptosis, BIRC3 and CFLAR, these genes appear to drive two, almost opposite, biological pathways – BIRC3 inhibiting and CFLAR propagating apoptosis. In the rabbit model, RIPK1 was significantly expressed. RIPK1 is critical in the necroptosis signalling cascade. Experimental work over several time points after injury might elucidate any causative role that RIPK1 expression has in injury progression in blast. CYP1B1, which has been implicated in mitochondria-dependent apoptosis in cancer cells, and SFPQ, a transcriptional co-activate, were common to both species in apoptosis geneset expression. Although RIPK1 initiates the necroptosis cascade, and subsequent upregulation of MLKL, it is capable of initiating apoptosis. Upregulation of caspase 8, and the formation of complex IIB with FADD can lead to apoptosis. This could explain the dual upregulation of genes inhibiting and propagating apoptosis. The interplay of these factors would require further investigation.

The role of inflammation in traumatic injury led to the hypothesis tissue loss would result from necroptosis rather than apoptosis. The role of inflammation in blast shock wave tissue injury is suggested across both models in this data. Previous studies use different packages for pathway enrichment, preventing direct comparisons. Wang and colleagues, using KEGG analysis, showed pathway enrichment including integrin signalling, leukocyte extravasation and Fc receptor phagocytosis(83). Furthermore IL-10 and IL 6 signalling were also upregulated. Conversely calcium T cell apoptosis, iCOS-iCOSL signalling in T cells, and T cell receptor signalling were all downregulated. The data confirms that inflammation is playing a role in tissue loss.

Transcriptomic sequencing has been used to gain deeper insight into mechanisms of injury, specifically blunt trauma(3, 84), burns(85), traumatic brain injury(86) and blast lung injury(83). Xiao's study describing 'the genomic storm' of inflammation following blunt injury in humans is a key paper in understanding the immune response to trauma(3). A difference between our study and Xiao's was the standoff distance. In their work, animals were 35 metres from the blast epicentre. The energy dose to tissue in Xiao's experiment was probably less than in the rabbit and porcine models here. Their study identified maximum upregulation of NB1 (CD177), MMP8 (neutrophil collagenase), LTF(lactotransferrin) and HP (haptoglobin) at 12 hours. Our data demonstrates LTF expression in both models, although significant expression was found only in the rabbit model. MMP8 expression was found only in the porcine model but did not reach statistical significance. Our data showed the enrichment of JAK stat signalling, allograft rejection and inflammation. Samples were collected at 12 hours (Rabbit) and 8 hours (Porcine). More recently, bulk RNA sequencing was undertaken of goat lungs exposed to free air spherical blast(64). In that analysis, the study also examined the role of the JAK Stat signalling pathway and allograft rejection in their samples. Christie and colleagues, investigating acute lung injury from major trauma, found PPFIA1 (a gene encoding liprin alpha involved in cell adhesion and cell matrix interactions) as a candidate risk gene for acute lung injury(83). In our work, we found this gene expressed to much lower, non-significant, levels in the porcine experimental set up.

Xiao's work compared genes to datasets from burns and endotoxemia, in human subjects, and found a 98% and 88% match respectively. This work suggests that, in humans at least, there is a 'common pathway' of gene expression that is not unique to each different injury mechanism. Our data suggests that the intensity of the stimulus controls the size of the gene response (more energy ~ greater inflammatory response). There was a 62% overlap in genes expressed between models. This overlap is larger than was expected, given the differences in the animal species and the type of apparatus used to generate a blast shock wave. The gene set analysis revealed similarities in gene expression between models. Supporting the notion that the intensity of the injury drives a common injury response. This may have to be explored

over further experimental work, but is demonstrated here where two similar injuries with different deliveries.

2.4.3 The Feasibility Of RNA-seq For Probing Blast Shock Wave

The results demonstrate the use of bulk RNA sequencing as a tool to characterise tissue level gene expression after blast injury. Before undertaking this work, it was thought that the RNA might not be of sufficient quality to undertake sequencing. Cellular damage from blast followed by prolonged sample storage, was thought to preclude sequencing analysis. It is not clear whether rates of RNA decay are similar across conditions, or whether they are accelerated in dying tissues prior to storage. As the sample data shows (Appendix Table 2.1), the quantity and quality of samples was sufficient for these techniques. This analysis used samples with a RIN values greater than 8. Achieving these RIN values is straightforward in monolayer cultures. However in tissue or three dimensional systems, impurities from the extracellular components can reduce the quality of RNA yields. RNA quality is important for sequencing, as poor quality RNA results in a lower proportion of mappable reads. Over time RNA decay influences expression levels. This may have implications on pathway analysis. In this work, samples were stored in RNA preservation solution at -80°C prior to RNA extraction. This should reduce RNA degradation from storage. One experimental approach was to evaluate the change in the RIN quality scale over time alongside gene specific degradation. This enables a comprehensive understanding on how the RNA quality influences the gene level data, particularly the level of gene expression seen(87).

This work has confirmed the hypothesis that blast exposed tissue samples may be stored for bulk RNA sequence analysis. Future work should quantify the variability in RNA quantity in blast exposed samples, and explore the use of single cell sequencing.

2.4.4 Limitations

There a notable differences between the two models compared in this chapter that should be noted when comparing transcription data.

Firstly, the loading conditions in each group were very different which precludes direct comparison (Porcine model overpressure - 0.2 to 0.7 MPa, Rabbit model overpressure – 0.4 – 2.5 MPa). However similarly regulated genes were discovered in both models. This suggests that these molecules might be important in blast mechanotransduction regardless of precise shock wave generation.

Secondly, the proximity of the animal to the shock wave source was different between models. The rabbit model exposed tissue to an compressed air shock device at very close proximity, whilst the pigs were 2.2 metres away from the explosive source. This could also impact the cell transcription. To formally explore whether distance from target influences gene transcription, a more refined experimental set up would be required. The proximity and size of the blast, and the resultant characteristics of the shock wave entering and exiting the tissue, must be considered in future experimental design. This is due to the magnitude of the load reaching the target and the distance between the target and source. In a strict mechanobiological sense a direct comparison is prevented between these models. Future work must define and match environments for comparison.

Thirdly, the animals adopted in these models are vastly different in their size. The lethality threshold for a rabbit's tissue could be significantly different from that of a pig. Hence, the shock waves may have produced very different traumatic injuries in each animal. The injury in the rabbit model could have resulted in a much more severe systemic injury than that seen in the pig model.

These studies were not specifically designed to look at gene enrichment after blast. In particular the genome variability between animals within each species needs to be considered when looking for significant differences between treatment and controls. In this work, the rabbits were inbred, which reduces genetic variability, whilst the pigs were outbred which

increases genetic variation. Human studies for bulk RNA sequencing require upwards of 24 individuals to achieve statistical power, and to account for sample variability. Lastly, earlier timepoints would be required to understand how cell signalling evolves.

The data demonstrates similar pathway enrichment between the two models, but does not reflect this in similar expression of individual genes. At this individual level the lists of most expressed genes are markedly different between the two models. On one hand this could reflect the differences in magnitude of trauma injury. On the other hand it could reflect methodological inconsistences. The rabbit genome is not as well annotated as the pig genome. As such there are numerous unlabelled genes seen in the rabbit data. This may influence the pathway enrichment data. Furthermore, as the gene list are converted into the human gene lists through conversion (as shown in the methods), this could result in alterations to gene labelling and enrichment. This may explain how the gene lists and pathway enrichment are different.

RNA was extracted from skeletal muscle several years after the original experimental work. RNA extraction from fibrous tissue, such as skeletal muscle, is particularly difficult, with lower expected yields. Traumatic injury also increases the number of enzymes that can reduce RNA quality. Despite this, the quality of the RNA extracted was above the threshold required for bulk sequencing.

.

A further limitation for this work is the lack of protein quantification of genes. Such confirmation is important to demonstrate that RNA expression has led to protein synthesis, as RNA expression alone is not proof of any downstream effect. This data analysis represents potential pathways and gene enrichment, rather than a characterisation of protein enrichment from primary blast shock injury.

2.5 Conclusions

This chapter has demonstrated that RNA can be successfully extracted from samples of skeletal muscle after prolonged storage. The data presented shows analysis of RNA expression of skeletal muscle after exposure to two different models and mechanisms of blast injury. Bulk RNA sequencing data highlights the top 25 significantly expressed genes, as well the general trend of gene expression in both models. More interestingly, gene set enrichment analysis revealed several common pathways between the models, despite the difference in species and loading. These included Tnfα signalling via HFk, Mtorc1 signalling, Ill2 Stat5 and Hypoxia. Finally, cell death gene set evaluation demonstrated that, globally, blast exposure results in cell death through a variety of mechanisms rather than one predominate pathway. Specifically, this analysis revealed that similar genes were altered for necroptosis and necrosis, such as BIRC3 and CFLAR.

This work has provided novel insights into RNA signalling after blast injury that can be used to guide future experimental work.

3

A Systematic Review Of Three-Dimensional Models Of Skeletal Muscle Under Tension And Methods To Induce Traumatic Injury.

3.1 Introduction:

Whether through wound evolution over time, or immediately from the initial trauma, explosions can result in large volumetric muscle loss (VML). This is defined as the significant loss of skeletal muscle as a result of surgical intervention or traumatic injury that leads to an impairment of regenerative capacity. Specifically, in blast injury, there are multiple tissue types involved (vasculature, nerve) and wound evolution results in further tissue loss and associated disability. Blast also evokes systemic responses, such as widespread inflammation, that can impede wound healing. This can result in tissue scarring and altered function, particularly in skeletal muscle.

Initial surgical strategies for blast injured patients include marginal debridement, tissue preservation and wound temporisation. Subsequent reconstructive strategies included skin grafting, muscle transfers and/or locoregional tissue transfer.

Currently available research models for chronic wounds, such as those caused by diabetes, potentially study more straightforward wounding environments and do not account for the more complex and challenging wounds seen in traumatic VML. As current wound models focus on inapplicable modalities or species, developing appropriate experimental models to probe traumatic injury is a key future requirement for this research field.

To probe the effects of blast on skeletal muscle, more representative *in vitro* models of tissue are required to generate a deeper cellular picture prior to pre-clinical validation. Whilst *in vivo* models are an invaluable pre-clinical environment, they are an expensive and lower throughput platform for discovery research. *In vitro* models are advantageous in this regard, in terms of relative throughput, start up and logistical costs compared to animal models. *In vitro* models that adopt human cells lines can be more relevant and appropriate for deducing information on the native human environment. Although recovery animal models can go on for prolonged timepoints, the type of severe injury models required for this field preclude length *in vivo*

recovery models. Ethically it would not be justifiable to the animal. *In vitro* work, by contrast, is capable of longer culture time periods but with the limitations of current 3D model architecture. Hence, an experimental balance must be sought.

The adoption of *in vitro* 3D systems for the purpose of drug discovery, screening and exploring cell signalling is receiving increasing attention across multiple disciplines(88). However, there has been limited adoption of these systems for understanding traumatic injury(14, 89). The current focus has been on demonstrating that 3D models are able to recapitulate skeletal muscle structure and physiology in health and disease. Techniques have included explanted tissue models, microfluidic systems and cell encapsulation in hydrogels cultured between anchor points. Anchor systems are advantageous as they induce an axis of strain on the fibres thereby attempting to replicate the physiological environment. Some of these systems have utilised chemicals & toxins to induce injury to demonstrate, and study, a regenerative capacity within their model. To understand how these models could be adopted to probe the cellular effects of traumatic injury, an understanding of previous work in this area is useful.

To date, no systematic review exists of current 3D *in vitro* models of skeletal muscle, nor those that propose methods to induce repeatable injury in such 3D environments. Such a review would contextualise the current knowledge and future research gaps to identify whether a more advanced/different experimental platform is required to study traumatic VML.

Therefore, the primary aim of this chapter is to evaluate the current literature on 3D skeletal muscle models under tension. Its secondary aim is to evaluate the mechanisms that been used to induce injury in these models.

3.2 Methods

The Cochrane Handbook for Systematic Review of Interventions was used and is reported in compliance with the PRISMA 2020 checklist(90, 91). The protocol was developed prospectively in collaboration with a research librarian at the Nuffield Department of Rheumatology and Musculoskeletal Sciences (NDORMS). The protocol was internally reviewed but not registered on the PROSPERO database as it was not a clinically focused systematic review.

3.2.1 Search Strategy

The OVID database was used to search MEDLINE (1946 – present) and EMBASE (1974-present) on 03/12/2021. Furthermore, using the search terms developed for OVID, a search was conducted on the Web of Science database. The search strategy was developed by collaboration between the primary author (RS) and a medical information specialist (NT) (Chapter 3 appendices). No date or language limits were applied. Free text, medical index and bibliographic searches were performed and then merged.

3.2.2 Inclusion & Exclusion Criteria

3.2.2.1 Inclusion Criteria

In vitro studies that utilised any skeletal muscle cell lines (primary or immortalised, single or multicellular) of any species cultured with an anchor system were eligible for inclusion. Specifically, models that utilised anchors, or the equivalent, to impose axial strain or loading onto the constructs were included. Models that used organic hydrogel compounds native to the human body (fibrin or collagen) were included. Where studies reported minor experimental

modifications of previously reported models (with detailed methods), the most comprehensive study or studies were included.

3.2.2.2 Exclusion Criteria

Models that did not impose axial strain or loading, self-assembly models (spheroids etc) or tissue explant models (including slice culture) were excluded. *In vitro* models that cultured cells on patterned surfaces (to include orientation) were also excluded, even if they used 3D systems. *In vitro* monolayer systems were excluded. *Ex vivo* perfusion systems were also excluded. Models that synthesised hydrogels using materials that were incapable of biodegradation (breakdown of organic matter into constituent elements) within humans (or human tissue) were excluded. Studies without detailed methods, opinion pieces, reviews, letters, conference abstracts, *in vivo* work and book chapters were excluded.

3.2.3 Study Selection

Search results were exported to Endnote (Endnote X9, Clarivate Analytics, USA), de-duplicated, merged and exported into Rayyan (www.rayyan.ai) for screening(92). All screening was undertaken by a single author (RS). First, abstracts were screened then, full text articles were pulled for included abstracts. These full texts were screened and their bibliographies reviewed for further articles.

3.2.4 Outcomes

The primary outcome was the model adopted to induce strain in the hydrogel. The Secondary outcome was the technique utilised to induce injury in 3D models. The tertiary outcome was the techniques used to quantify the effects of these injuries in 3D models.

3.2.5 Data Extraction

Data was extracted by a single author (RS) and included study demographics (cell type, post type, hydrogel material), injury type and duration and finally outcome measures. Data was exported into Microsoft excel (Excel, V 16.16.27, Microsoft Corporation). Studies that reported using primary animal cells were assumed to be using multiple cell populations (skeletal muscle, fibroblasts etc), unless they stated how they selected specific populations. Outcome measures included live/dead measurements, techniques for imaging and force characterisation (using electrical stimulation or otherwise). Data was analysed descriptively. A meta-analysis could not be performed due to the lack of comparative studies and heterogeneity in outcome data.

3.2.6 Quality Assessment

The risk of bias was assessed by a single author (RS) and reviewed with senior authors (SS & AS) using the office of health assessment and translation (OHAT) risk of bias rating tool for human and animal studies(93). This tool has been amended to allow assessment of *in vitro* studies.

3.2.7 Office Of Health Assessment And Translation (OHAT) Risk Of Bias Tool

The Office Of Health Assessment and Translation uses a 7 step process for evaluating evidence to assess environmental chemicals, physical substances or mixtures for the national

toxicology program in the United States. Their evaluation process for systematic review includes a risk of bias analysis for human and clinical studies that has been adapted for assessing animal and *in vitro* evidence. The OHAT tool for *in vitro* studies was the only tool found to evaluate bias and therefore was adopted on this basis. The tool evaluates the evidence along seven bias questions. These are outlined in Table 3.1. Each question is given a low/moderate or high bias rating. Overall bias is calculated based on the proportion of bias found in the majority of questions.

Number	Question
Q1	Same experimental conditions
Q2	Blinding during study
Q3	Incomplete data
Q4	Exposure characterisation
Q5	Outcome assessment
Q6	Outcome Reporting
Q7	Other

Table 3.1: The OHAT Risk of bias questions. Each question evaluates whether the study applied these experimental approaches.

3.3 Results

The total number of articles found from the three search strategies was 666. Figure 3.1 outlines included studies. Through abstract review and bibliographic screening a total of fifty-seven articles were included for extraction. Forty-five articles that described models of skeletal muscle using anchors were found. Furthermore, twelve articles that specifically induced an injury in their skeletal muscle model were included for extraction. Data from these studies can be found in tables 3.2 (3D models) & 3.3 (3D models with injury).

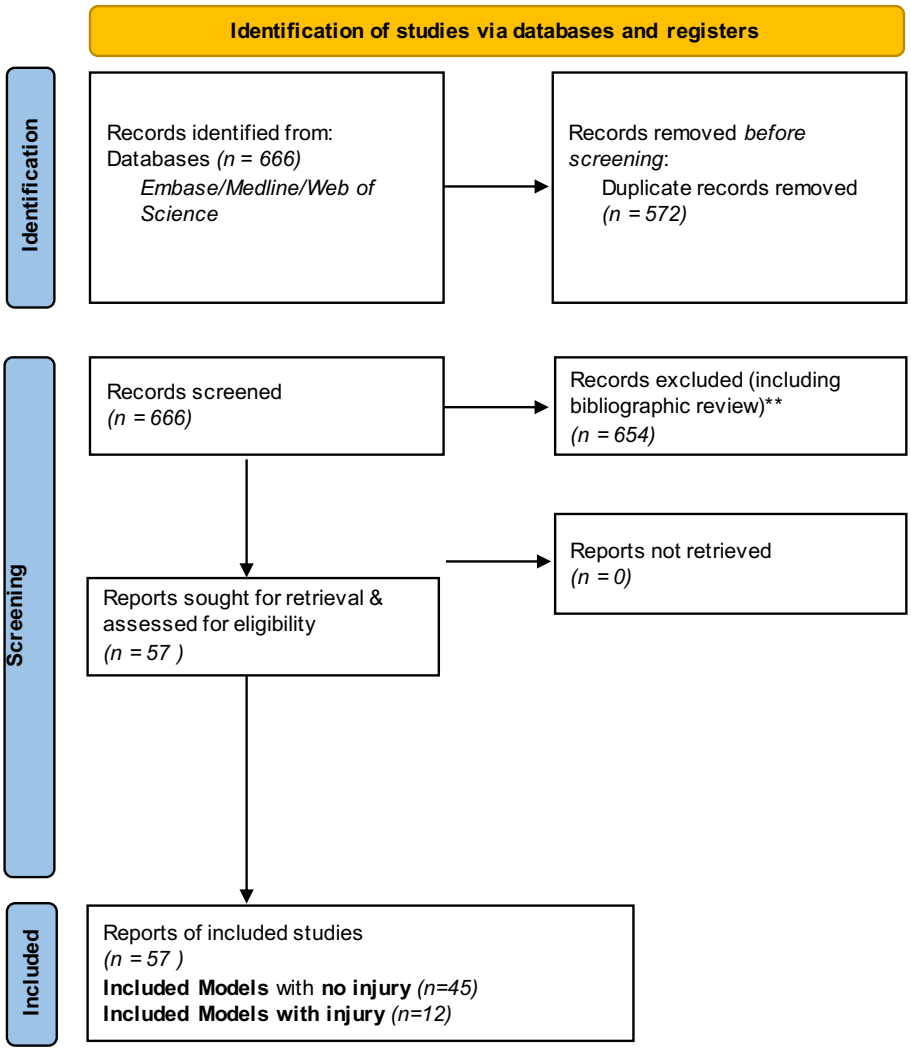

Figure 3.1: *PRISMA flowchart of included studies(91)*

Paper Demographics			Model					Model Components		
No.	*Author*	*Year*	*3D Material*	*Posts*	*Cell Type*	*Single/ Multi Cell*	*Material Conc.*	*Gellator Conc.*	*Cell Seeding Conc.*	*Ref*
1	Heher P, Fuchs C	2015	Fibrin	Magnetic storage rack	C2C12	Single	Fibrinogen 40mg/ml/10mg/ml Fibrinogen	Thrombin 4U/ml (0.625U/ml)	$3.2x10^6$	(94)
2	Cheema U, Brown RA	2003	Collagen	Polyethylene mesh	Smooth Muscle + Fibroblasts + C2C12	Multi	4ml of rat tail type I collagen (2.035mg/ml)	5M NaOH	$5x10^6$	(95)
3	Kim JH, Lee SJ	2018	Fibrinogen	PCL end bars	Primary human skeletal muscle cells	Multi	20mg/ml Fibrinogen	35mg/ml Gelatin, 10% Glycerol	$30x10^6$ (1-20,30,50)	(96)
4	Vandenburgh H, Farr L	1988	Collagen	Stain Steel mesh/nylon washer	Primary avian skeletal muscle cells	Single	500µl collagen gel (250ug/ml)	0.1M NaOH		(97)
5	Afshar Bakoshli M, Gilbert PM	2019	Fibrin	Nylon hooks	CD56+ myoblasts + CD56- fibroblasts cells.	Multi	Fibrinogen 10mg/ml	Thrombin 0.2U/mg of fibrinogen	$3x10^6$	(98)
6	Afshar M, Gilbert P	2020	Fibrin	PDMS	Primary human skeletal muscle cells	Multi	4mg Fibrinogen	Thrombin 0.2 – 0.5U/ml	15×10^6 cells/ml	(99)
7	Donnelly K, Baar K	2010	Collagen	Stainless steel	Primary avian skeletal muscle or neonatal rat myoblasts	Single	Collagen Rat tail	NaOH 1M	$5\text{-}7.5 \times 10^4$/well in 1ml or $4x\ 10^6$ cells/0.750ml	(100)
8	Acosta F, Rathbone C	2020	Fibrin	Metal Pins	Primary rat skeletal muscle cells + primary rat adipose cell	Multi	Fibrin (5.7mg/ml)	Thrombin	$1.25x10^6$cells/ml	(101)
9	Ramada A, Boudou	2014	Collagen	PDMS	C2C12	Single	Collagen 1 & 2mg	NaOH 1M	100-1000 cells/well	(102)
10	Powell C, Vandenburgh H	1999	Collagen	Velcro Straps	Primary human skeletal myoblast	Multi	Rat Tail collagen 1.6mg/ml + Matrigel	NaOH 1M	2×10^6 cells/400µl mould	(103)
11	Player DJ, Lewis M	2014	Collagen	Mesh flotation bars on metal	C2C12	Single	Rat tail collagen 1.6mg/ml + Matrigel	NaOH 1M	12×10^6 cells in 0.1ml GM/ 4×10^6 cells/ml	(104)
12	Kalson N, Kadler K	2010	Fibrin	Pins + Suture	ECMTT cells	Single	20mg/ml Fibrinogen	10ul of 200U/ml Thrombin	6.15×10^5 cells in 400µl media	(105)
13	Madden L, Bursac N	2015	Fibrin	Laser cut cerex frames	Primary human skeletal muscle cells	Multi	10ul Matrigel + 10µl of 20mg/ml Fibrinogen + 11ul media	2ul of 50U/ml Thrombin	15×10^6 (7.5×10^5 cells per myobundle).	(106)
14	Smith AST, Lewis M	2012	Collagen	Flotation bars on metal	Primary rat skeletal muscle cells	Multi	Collagen 300µl, 2.6ml Type I rat tail collagen	NaOH 0.1M acetic acid	Unspecified	(107)
15	Fan T, Gu QI	2011	Fibrinogen	PDMS	C2C12	Single	Fibrinogen 40mg/ml (500µl) + Gelatin 14% w/v (250µl)	20U/ml Thrombin	4×10^7cells/ml	(108)
16	Shah R, Lewis M	2016	Collagen	Stainless steel frame	Primary human skeletal muscle cells	Multi	6ml Collagen rat tail 2.1-2.12mg/ml in 0.6% acetic acid	Not specified	7.2×10^6 cells/ml	(109)

Table 3.2: 3D in vitro models under tension. Table of included studies and model information (Author, Year, Post materials, cell type).

17	Khodabukus A, Baar K	2012	Fibrin	Sutures	C2C12	Single	100µl of 200mg/ml fibrinogen	10U/ml Thrombin, 0.2µg/ml Genipin, 0.5µg/ml Aprotinin	100 000 cells (90k C2C12 + 10k 3T3 fibroblasts)	(110)
18	Hansen A, Eschenhagen T	2010	Fibrin	PDMS	Primary rat skeletal muscle cells	Single	5mg/ml Bovine Fibrinogen + 100ul Matrigel	Thrombin 100U/ml	4.1 x 10^6 cells/ml	(111)
19	Vandenburgh H, Crawford G	2008	Collagen	PDMS	Primary mouse skeletal muscles	Multi	1mg/ml rat tail collagen + 1 part Matrigel or 0.5mg/ml Fibrinogen	1U/ml Thrombin	Not detailed	(112)
20	Rao L, Bursac N	2018	Fibrin	PDMS	Human pluripotent stem cells	Multi	4mg/ml Fibrinogen + 20% v/v Matrigel	0.2U/mg Thrombin	12.5million cells/ml	(113)
21	Bian W, Bursac N	2008	Fibrinogen	PDMS/Velcro	C2C12 + Primary rat myoblasts	Multi	100-600ul into mould. 2mg Fibrinogen/Collagen 1mg/ml + Matrigel 10% v/v	0.4U Thrombin/NaOH	5x10^6 for myoblast, 10 x 10^6 cells/ml for SKMS	(114)
22	Sato M, Kamihira M	2011	Collagen	Metal Anchors	C2C12	Single	100µl, (170ul of Collagen) + 30µl Matrigel, 0.5mg/ml		1x10^6 Cells	(115)
23	Dennis R, Kosnik P	2000	Laminin	Myoid anchors in Sylgaard (multiple materials)	Primary rat skeletal muscle + primary rat fibroblasts	Multi	Laminin coated dishes	Not specified	Not Specified	(116)
24	Martin N, Lewis M	2013	Fibrin	Sutures	Primary human skeletal muscle cells	Multi	200mg/ml stock fibrinogen	10µl/ml Thrombin	100k, 200k, 400k densities	(117)
25	Sakar M, Asada H	2012	Collagen	PDMS mould from master silicone wafers	C2C12	Single	Not specified	Not specified	Not Specified	(118)
26	Huang YC, Baar K	2005	Fibrin		Primary rat skeletal muscle cells	Multi	20mg/ml Fibrinogen	10U/ml Thrombin	10^5cells/ml1ml added to gels.	(119)
27	Vandenburgh H, Powell CA	2002	Collagen	Steel pins	Primary Human skeletal muscle cells	Multi	Type I Rat collagen 1:6 ratio with Matrigel to Collagen	NaOH 0.15N	1 x 10^6 cells/770µl solution, 900µl per gel.	(120)
28	Bian W, Bursac N	2009	Fibrin	PDMS	Primary rat skeletal muscle cells	Single	10mg/ml Fibrinogen in DPBS	50ul stock solution in BPS/DPBS	Not detailed	(121)
29	Legant W, Chen C	2009	Collagen	PDMS	Primary mouse skeletal muscles	Single	Collagen 1.0 and 2.5mg/ml	NaOH 1M	Na	(122)
30	Lam M, Takayama S	2009	Fibrin	Micropatterned PDMS + Suture anchors	Primary	Single	Fibrinogen 20mg/ml	10U/ml Thrombin	5 x 10^5	(123)
31	Rhim C, Truskey G	2007	Collagen	Silicone tubing + steel pins & velcro	C2C12	Single	1.4mg of Type I rat tail collagen 1-2:1 collagen/Matrigel	3mM NaOH	1x10^6 – 5x 10^5 cells/BAM	(124)
32	Maffioletti S, Tedesco F	2018	Fibrin	PDMS	Primary human skeletal muscle cells	Multi	3.5mg/ml Fibrinogen + 10% Matrigel	3U/ml of Thrombin	1 x 10^6 cells for each construct.	(125)
33	Khodabakus A, Baar K	2009	Fibrin	Silk sutures	C2C12	Single	200mg/ml stock fibrinogen	Thrombin 10U/ml	100 000	(126)

Table 3.2 continued: 3D in vitro models under tension. Table of included studies and model information (Author, Year, Post materials, cell type).

34	Aklyama Y, Morishima K	2010	Collagen	PDMS	Primary rat skeletal muscle	Single	3.5mg/ml of Type I collagen – 1mg of cells	1M NaOH – 172 ul of Matrigel	1 x 10^6 cells/ml	(127)
35	Juhas M, Bursac N	2014	Fibrin	PDMS	Primary rat skeletal muscle cells	Single	4mg/ml Fibrinogen + 20% Matrigel	0.2U/mg Thrombin	10 Million cells/ml	(128)
36	Capel A, Lewis M	2019	Collagen	PLA	C2C12 + Primary human skeletal muscle	Multi	85% type I collagen (2.035mg/ml)/Matrigel	0.1M acetic acid	4 x 10^6 cells/ml	(129)
37	Shanksy J	1997	Collagen	Silicone	Primary Avian skeletal muscle + Primary rat skeletal muscle	Single	Collagen Type I 1.6mg/ml Matrigel 1:6 ratio		4 x 10^6 cells/ml	(130)
38	Xu Bin, Shen Wei	2019	Fibrin	PDMS	Precursor Skeletal muscle cells	Single	6mg/ml Fibrinogen 10% v/v Matrigel	1 Unit bovine Thrombin	7.5 x 10^6 cells/ml	(131)
39	Vandenburgh H, Shanksy J	1989	Collagen	Stainless steel wire	Primary Avian skeletal muscles	Single	Rat Tail Collagen Type I 200-400pg/0.5ml.	NaOH 0.1M	5700/mm^3 of plate	(132)
40	Brady MA, Mudera V	2008	Collagen	Stainless steel A frame	Primary Human skeletal muscle cells	Multi	4.5 Collagen Type I	NaOH 0.1M	5 x 10^6 cells/ml	(133)
41	Matsumoto T, Sohmura T	2007	Fibrin	PLGA sutures	C2C12	Single	3mg/ml Fibrinogen + Aprotinin 5mg/ml	2U/ml	2.5 x 10^6 cells/ml	(134)
42	Morimoto Y, Takeuchi S	2013	Fibrin	PDMS	C2C12	Single	Not Specified	Not Specified	Not Specified	(135)
43	Okana T, Matsuda T	1998	Collagen	Agarose ring	C2C12	Single	Na	Na	1 x 10^7 cells/ml	(136)
44	Vandenburgh H, Raven L	1996	Collagen	Silicone Rubber tubing	C2C12	Single	1.6mg/ml Collagen + Matrigel	0.1NaOH	1-4x10^6 Cells/ml	(137)

Table 3.2 continued: 3D in vitro models under tension. Table of included studies and model information (Author, Year, Post materials, cell type).

Paper Demographics			Model				Refs
No.	*Author*	*Year*	*Cell Death*	*Polymerase Chain Reaction (PCR)*	*Image Analysis*	*Force*	*Ref*
1	Heher P, Fuchs C	2015	Nil	GAPDH, MyoD, TNNT1, Myf5, Myogenin, Desmin, Pax7	MHC, Multinucleated myotube count, myotube length, diameter	Stained at 20mm/min, preload of 10mN, 6h of static strain at 10% and 18h at 3% static strain	(94)
2	Cheema U, Brown RA	2002	Nil	IGF-1,MGF	Phalloidin (F-Actin) staining	Nil	(95)
3	Kim JH, Lee SJ	2018	Live/dead assay, TUNEL assay – 1,6,9 Days	Nil	Nil	Nil	(96)
4	Vandenburgh H, Farr L	1988	Nil	Nil	Haematoxylin & Eosin staining	Nil	(97)
5	Afsher Bakooshli M, Gilbert PM	2019	Nil	Nil	Hoechst, DRAq5, Myofiber size, Alpha Actinin	Vide of contraction, 12 frames/ second, stacked in Image J	(98)
6	Afshar M, Gilbert P	2020	Nil	Nil	Nil	Video images of electrical stimulation and sagittal slice of myotactic system. Contractile force at 14d – 200uN/specific force 5mN/mm^2	(99)
7	Donnelly K, Baar K	2010	Nil	Nil	Nil	Specific Force: 0.14 – 0.1kN/mm^2	(100)
8	Acosta F, Rathbone C	2021	Nil	MHC, Fas, VEGF, Myogenin, Adiponectin, ANGPT1, MyoD,	Phalloidin (F-Actin), Lectin	Nil	(101)
9	Ramade A, Boudou T	2014	Nil	Nil	Nil	Nil	(102)
10	Powell C, Vandenburgh H	1999	Nil	Nil	Sarcomeric Tropomyosin staining	Nil	(103)
11	Player DJ, Lewis M	2014	Lactate in media	IGF-I, MMP-9, Myostatin, MuRF-1, MAFBx	Nil	Nil	(104)
12	Kalson N, Kadler K	2010	Calcein Am to detect live cells	MyH9, MyH10, Col1a1, Ribosome 18	Electron Microscopy	Instron tested, 100N load cell. Determined length at failure with a strain rate of 5mm/minute 1% strain per second.	(105)
13	Madden L, Bursac N	2014	Nil	Nil	Desmin, Anti GFP, Laminin, Muscle CK, MyoD, Myogenin, Myosin Heavy Chain, Pax7, Sarcomeric Alpha Actinin, Vimentin, Phalloidin, Oil Red O, Haematoxylin & Eosin.	Custom force measurement system. PDMS float mounted to a force transducer. 40V/cm, 10ms electrical pulse. 12% stretch, 1s long 5,10,20hZ. Force frequency relationship. Peak twitch and tetanus. 4.0-6mN Tetanus, 0.8-5mN specific force – twitch 3mN/mm^2 , Tetanus – 11mN/mm^2 (Day 9)	(106)
14	Smith AST, Lewis M	2011	Nil	Nil	Desmin, DAPI, Myoblast Number, Fusion Efficiency	Nil	(107)

Table 3.3: 3D in vitro models under tension. Table of included studies and outcome data recorded in studies.

15	Fan T, Gu QI	2011	Nil	MyoD, Myf5, MyoG, Myh1, Myh2, Myh4, Myh7	MHC/ Hoechst Nuclei Staining, Myotube length, Myotube diameter, Myotube area	Stress vs strain using instron universal tester to calculate Young Modulus & Stiffness.	(108)
16	Shah R, Lewis M	2013	Alamar Blue	MyoD1, Myogenin, Myh1,2,3,6,7,8	DAPI, Demin, Alpha sarcomeric actin	Nil	(109)
17	Khodabukus A, Baar K	2012	Nil	Nil	Nil	Did not calculate force, calculated specific force relative to conditions or % change.	(110)
18	Hansen A, Eschenhagen T	2010	Nil	Ncx, Titin,	H&E Stain, Alpha actinin, DRAQ5, Lectin, Connexin, Phalloidin	Nil	(111)
19	Vandenburgh H, Crawford G	2008	Nil	Nil	Nil	Nil	(112)
20	Rao L, Bursac N	2018	Nil	G3PD, Tbx6, Msgn1, Myf5, Pax3, Pax7, MyoD, MyoG, Myh1, Myh2, Myh3, Myh7, Myh8, Casq1, Cas1, Ryr1, Serca1, Serca2, Ncx1, PMCA1, PLN	Oct4, Tra-1-1, Pax3, Myf5, MF20, GFP, Laminin, Dystrophin, CD31, MyoD, MyoG, Alpha-bungarotoxin, Phalloidin.	Nil	(113)
21	Bian W, Bursac N	2008	Nil	Syto13 Green, 5μM Ethidium	Alpha Actinin, MyoD, Myogenin, Haematoxylin & Eosin	Nil	(114)
22	Sato M, Kamihira M	2011	Creatinine Kinase	Nil	Nil	Twitch: 1-20μN, Tetanus 17-40μN, Max twitch 10-17μN, Tetanus: 27 – 35μN, 20V, width 10ms pulse, tetanic contractions – 20V, width 10ms, frequency 50hz, duration 2s – Maximum twitch 10-20μN, tetanus ~ 28-38μN (from Graphs)	(115)
23	Dennis R, Kosnik P	2000	Nil	Nil	Toluidine Blue	Peak twitch 600μN, Tetanus: 210-212μN. Peak force 600μN: tetanus 450μN. Spontaneous contractions 190-215μN. 70V 4ms wide pulse, peak twitch single 70V, 4ms wide pulse. 4ms pulse elicited twitch force of 50%. Pulse width reduced so twitch force was dropped to 50%, single twitch's of 3,6,10,15,20,25,35,40V + pulse widths 0.2,0.4,0.6,0.8,1.0,1.5,2.0ms. Max tetanic force 40V, 40hz, 1.2ms pulse	(116)
24	Martin N, Lewis M	2013	Nil	Myh1, Myh2, Myh3, Myh7, Myh8, Polr2B	Desmin, Myosin heavy chain, Fusion efficiency – Desmin positive cells incorporated into myotubes.	Nil	(117)
25	Sakar M, Asada H	2012	Nil	Nil	Phalloidin, Hoechst, Alpha actinin. Images: cross sectional images from Z Stack	Contraction from 15 independent experiments recorded at 1kh with a high speed camera at 20X mag. Deflection tracked from tracking bright spots on the myotube. 2 Different points on each myotube. Static tension, tissue cultured for 48h before phase contract images of the cantilevers using a CCD camera. Dynamic force: phase contrast/fluoro images were taken at 250Hz. Only uniform anchorage	(118)

Table 3.3 continued: 3D in vitro models under tension. Table of included studies and outcome data recorded in studies.

						was used. Caps were tracked on Image j. Spring constraints calculated using linear bending theory. Experimental measurements with a MEM captive force sensor. 13μN max force.	
26	Huang YC, Baar K	2005	Nil	Nil	Myosin Heavy Chain	Diameter, passive baseline force, peak twitch force, peak tetanic force, time dependent variables (time to peak twitch force, one half relaxation time for a twitch, half contraction time, half relaxation time for a tetanic contraction, 300-700μN).	(119)
27	Vandenburg h H, Powell CA	2002	Nil	Nil Sarcomeric tropomyosin staining, HBAM cross sectional area, myofiber diameter	Stretched at 5,10,15% strain and held at this strain for 10 minutes. Force measurements after this stretch. 500-100uN passive tension per 10^6 cells. When exposed to cytocalcein D(2-5uM) passive tension decreased 57% over 3 hour incubation. Then tension increased rising to 66% of original tension. 2-4% greater with 5-15% strains than static passive tensions.	Nil	(120)
28	Bian W, Bursac N	2009	Nil	Nil	Phalloidin (F-Actin)	Nil	(121)
29	Legant W, Chen C	2009	Nil	Nil	F-Actin	1.19μm inward baseline deflection or 3.17μm(50μM blebbistatin) + FEA model of microtissue contractility. Maximum isometric stress was 250kpa. Agreement to experimental data with 5.15, 25kPa, 1-12μN, 0.397μN/nm, 0.098μN/μm cantilevers.	(122)
30	Lam M, Takayama S	2009	Nil	Nil	Myosin Heavy Chain	Passive baseline force. Aligned Twitch - 200μN, Aligned tetanus – 400μN	(123)
31	Rhim C, Truskey G	2007	Live/dead assay kit. 1 hour incubation	Nil	Haematoxylin & Eosin, Phalloidin, Anti alpha actinin, Myosin heavy chain	Nil	(124)
32	Maffioletti S, Tedesco F	2018	Nil	GAPDH, MyoD, MYH-C, SGCA Dystrophin	Myosin heavy chain, Laminin, Laminin A'C	Nil	(125)
33	Khodabakus A, Baar K	2009	Nil	Nil	Haematoxylin & Eosin	Specific Force 0.08 – 0.014 or 0.08-0.1kn/mm^2	(126)
34	Aklyama Y, Morishima K	2010	Nil	Nil	Haematoxylin & Eosin	Nil	(127)
35	Juhas M, Bursac N	2014	Nil	Nil	Pax7, MyoD, Vimentin, Sarcomeric alpha actin Ki67 + myofiber area density	Samples were stimulated (10ms, 3V/mm pulses) and Isometric twitch contraction (response to a single pulse) and tetanic contraction (response to a 40Hz, 1 sec duration pulse train) were recorded in bundles that were stretched to 11% of their culture length. Specific contractile force of a mutual bundle was determined by	(128)

Table 3.3 continued: 3D in vitro models under tension. Table of included studies and outcome data recorded in studies.

						dividing its force of contraction with the cross-sectional muscle area measured at the centre of the bundle. Absolute force: 19-30mN, specific force: 30-45mN/mm^2, 3-8uN/myofiber.	
36	Capel A, Lewis M	2019	Nil	Nil	Phalloidin, DAPI, Desmin	Average maximal twitch force of 30.45± 7.86 μN for donor 1 and 41.52 ± 8.32μN for donor 2, as well as an average maximal tetanic force of 57.07μN for donor 1 and 36.96± 7.04μN FOR DONOR2.	(129)
37	Shanksy J	1997	Nil	Nil	Nil	Nil	(130)
38	Xu Bin, Shen Wei	2019	Nil	B2m, Myh8, Myh7, Myh3, Myh2, Myh1	Anti-sarcomeric alpha actinin, Pax7	Custom built jig, stretched at 20% of its initial length. Stimulated with 10ms of 0.5, 1,2,5,10 and 20Hx. 24V 0.27mN-0.8mN contractile force	(131)
39	Vandenburgh H, Shanksy J	1989	Nil	Nil	Haematoxylin & Eosin, Myosin heavy chain	Nil	(132)
40	Brady MA, Mudera V	2008	Nil	Myogenin, MMP-2, Type IV collagenase, GAPDH	Desmin, DAPI	Nil	(133)
41	Matsumoto T, Sohmura T	2007	Nil	Nil	Hoechst	Nil	(134)
42	Morimoto Y, Takeuchi S	2013	Nil	GAPDH, Hlxb9	Myogenin, Hoechst	Nil	(135)
43	Okana T, Matsuda T	1998	Nil	Nil	Haematoxylin & Eosin	Nil	(136)
44	Vandenburgh H, Raven L	1996	Nil	Nil	Sarcomeric Tropomyosin	Nil	(137)

Table 3.3 continued: 3D in vitro models under tension. Table of included studies and outcome data recorded in studies.

Paper Demographics			Model		Model Components			Refs
No	*Author*	*Year*	*3D Material*	*Posts*	*Cell Type*	*Material*	*Gellator*	*Cell Seeding*	
1	DJ Player, MP Lewis	2014	Collagen	Flotation bars and A frame	C2C12	2.035mg/ml protein conc.	NaOH	$12x10^6$ cells/ml	(104)
2	JW Fleming, MP Lewis	2020	Type 1 rat tail collagen + 20% Matrigel	3D printed scaffolds	Primary human skeletal muscle	65% Rat type I tail collagen, 10% media, 20% Matrigel	NaOH	$4x10^6$ cells/ml	(138)
3	Rajaban N, Andreadis S	2021	Rat tail collagen Type 1 + 20% Matrigel	PDMS micro post arrays	Primary human skeletal muscle	1mg/ml rat tail collagen	1M NaOH	5×10^5 cells per device	(139)
4	Juhas M, Bursac N	2014	Fibrin	PDMS Moulds with Velcro attachments	Primary neonatal rat skeletal muscle	4mg/ml Fibrinogen + 20% Matrigel	0.2U/mg Fibrinogen	$10x10^6$/ml	(128)
5	David B, Truskey GA	2016	Fibrin/Matrigel matrix	Cerex frame	Primary human skeletal muscle cells	11µl Media, 10µl Matrigel, 10µl of 20mg/ml Fibrinogen	50U/ml	$7.5x\ 10^5$ cells	(140)
6	Martin N, Lewis M	2017	Fibrin Matrix	Suture/PDMS	C2C12	200µl of 20mg/ml Fibrinogen	10U/ml 500µl Thrombin, 80µg/ml Aprotinin	1×10^5 cells	(141)
7	Juhas M, Bursac N	2018	Fibrin/Matrigel matrix	PDMS/Pluronic nylon frames	Primary rat skeletal muscle	7mg/ml bovine fibrinogen + Matrigel 20%	0.2U/mg Thrombin	10million cells/ml	(142)
8	Tiburcy M, Zimmermann WH	2019	Collagen/Matrigel	Circular moulds	Primary skeletal muscle	0.4mg Rat tail collagen, 10% Matrigel		1.2×10^6 cells	(143)
9	Agrawal G, Varhese S	2017	Gelatin & Methacrylate	Polyacrylamide solution (5%)	C2C12	7% GelMa solution	2mM LAP + 0.01% ascorbic acid	12.5 million cells/ml	(144)
10	Lee P, Vandenburgh H	2013	Matrigel (1 Part): Type I Collagen (6 Part)	Stainless steel pin	Primary mouse skeletal muscle	1.6/0.8mg/ml collagen		$1,2,3 \times 10^6$	(145)
11	Shimizu K, Honda H	2017	Na	Na	C2C12	Fibrinogen (10mg/ml)	Thrombin 50U/ml	$2x\ 10^6$	(146)
12	Khodabukus A, Bursac N	2020	Fibrin	PDMS & Cerex frames	Primary human skeletal muscle cells	10µl of 20mg/,l Fibrinogen + 10µl Matrigel	2µl of 50U/ml	7.5×10^5 cells	(89)

Table 3.4: 3D in vitro models with an injury. Table of included studies and model information (Author, Year, Post materials, cell type).

Paper Demographics			Model			Model Components			Refs
No	Author	Year	Injury Mechanism	Injury Duration	Cell Death	qPCR	Imaging	Electrical Stimulation/Deflection/Force	
1	DJ Player, MP Lewis	2014	Mechanical overload	Rapid static load (10% strain for 60 mins), Ramp load (continuous increasing load to achieve 10% strain over 60 mins)	Lactate	RPIIIB, Igfbp-2, MMP-9, IGF-1, Murf-1, MAFBx, Myostatin	Nil	Not measured	(104)
2	JW Fleming, MP Lewis	2020	Barium Chloride	6 Hours	NA	RPIIB, RunX2, PPARG	MYH-C, Pax7, MyoD, Laminin	Maximal twitch force – 3.6V/mm 1ms impulse and maximal tetanic force measured using a 1s pulse train at 100Hz at 3.6V	(138)
3	Rajaban N, Andreadis S	2021	Cardiotoxin (Naja Mossambica Mossambica)	6 Hours	Calcium transits following electrical pulses		MYH-C, SAA, Ki67, Pax7, Parp	The deflection of micropillar measured using ImageJ software and multiplied by the pillars spring constant 1.3 ± 0.1μN/um to calculate the force. Electrical stim force – 40μN/mm^2 Compaction force – 800μN/mm^2	(139)
4	Juhas M, Bursac N	2014	Cardiotoxin (Naja Mossambica Mossambica)	6 hours	Not measured	Pax7, Ki67, MyoD, MyoG	CD31, F-Actin, DPA, VWF, Pax7	22-26mN of active force (twitch-22/tetanus-26). Passive force – 2.5mN	(128)
5	David B, Truskey GA	2016	Mitochondrial inhibitor & uncoupler – oligomycin 11uM & Carbonyl cyanoid 4 FCCP 8uM 10uM Rotenone	30 minute incubations	Lactate dehydrogenase, Ethidium, Calcein + Hoechst dye – 6 images per bundle	Na	Na	Peak twitch and tetanus force. Fatigue assessed with rotenone or vehicle 30 minutes before testing.	(140)
6	Martin N, Lewis M	2017	Reduced Oxygen level for 24 hours – 15% 0_2, 10% 0_2, 5% 0_2, 1% 0_2	24 Hours1NA	Na	Murf-1, MAF Bx, POLR2B	Phalloidin, F-Actin, DAPI (5 images, 40 myotubes per muscle).	Na	(141)
7	Juhas M, Bursac N	2018	Cardiotoxin (Naja Mossambica Mossambica)	3 or 6 hours	Live regeneration, cells were transduced with MHCK7 – GcaMP6 – 5, 10, 15 days post CTX injury	NA	DAPI, TUNEL assay, Pax7, MyoD, MyoG, Ki67, CD206+	Na	(142)

Table 3.5: 3D in vitro models with an injury. Table of included studies and Outcome data.

8	Tiburey M, Zimmermann WH	2019	Cardiotoxin (25µg/l Latoxan)/Mechanical crush (tip width 1mm) – 3 short full squeezes 1 second duration/ single dose of 30 Gy 13 minutes gamma irradiation.	24hr/ 3 short full squeezes 1 second in duration	Adenylate kinase in cell supernatant 24 hours post injury, Toxilight assay (Lonza).	Pax7, MyoD, MyH3, Myh1,2,4,Myh7, Myh8	Pax7, Desmin, ED1/ED2, Ki67, Embryonic mouse heavy chain, tropomyosin, Laminin, M-cadherin, Caveolin-1, Caveolin 3, GFP, Prolyl-4-hydroxylase	Tetanic force corresponded to a specific force of 21± 1 kN/mm^2 (n=13)	(143)	
9	Agrawal G, Varhese S	2017	Cardiotoxin (Naja Mossambica mossambic) 0um, 0.1µm, 0.5µm	24 hours	Change in passive tension		F Actin	Passive tension		(144)
10	Lee P, Vandenburgh H	2012	Cytosine arabinoside	4 days	Lactate concentration, hydrogel length reduction	Na	Anti-tropomyosin antibody. Myofiber cross section	2587-502mN		(145)
11	Shimizu K, Honda H	2017	Dexamethasone (20mmol/mL) – 50/100/200µM	48 hours	Contractile force recovery	Atrogin, MuRF1		Stable force of 57.5 micronewtons. 57.5±12.8µN of force on Day 6 (77.5±11.1µN by day 8).		(146)
12	Khodabukus A, Bursac N	2020	Notexin	6 Hours	Na	Na	B-Spectrin, Alpha actinin	Control – Twitch 1mN, Tetanus 1.2mN		(89)

Table 3.5 continued: 3D in vitro models with an injury. Table of included studies and Outcome data.

3.3.1 Study Characteristics

All articles were experimental reports of *in vitro* models. Studies were published between 1988 and 2017. Forty-five articles described models of three dimensional skeletal muscle systems. Twelve articles described skeletal muscle and also induced a traumatic injury in them as part of their work.

3.3.2 Study Demographics – Models Without Injury

3.3.2.1 Models Without Injury – Hydrogel Manufacture

The forty-five articles utilised five different cell types, or combination of cell types. The C2C12 cell line (n=13) was the commonest cell type adopted across all articles, followed by primary human skeletal muscle cells (n=9). Figure 3.2 (a) outlines cell types used in non-injury models. Cell number, Figure 3.2 (b), varied between models, with a large number of models between 1 to 4 million cells per gel.

Hydrogels were manufactured from fibrin or collagen, in solution with growth factors (such as Matrigel) or other biocompatible materials (Gelatin). Figure 3.2 (c) and 3.2 (e) shows the combinations of compounds utilised for hydrogels. Figure 3.2 (c) outline the concentrations of Fibrin and Collagen used across models. Collagen concentrations were consistent across experimental models whilst fibrin concentrations were more variable (Mean = 1.781, range = 0.25 – 4.5).

Figure 3.2 (d) demonstrates the different anchor systems used to orientate cell laden hydrogels. The articles used 11 different techniques to anchor hydrogels in cell culture, predominantly using polydimethylsiloxane (PDMS) casted posts.

Figure 3.2 (g) shows the thrombin concentrations used to cross link fibrin hydrogels (Mean thrombin concentration – 44.48, SD = 46.36, range 0.1-200mg/ml). Sodium hydroxide concentrations ranged from 0.1-5.0 mg/ml (Mean = 0.77, SD = 1.34).

3.3.2.2 *Models Without Injury – Imaging*

Figure 3.2 (f) shows the stains used for imaging analysis of 3D models. H&E, Myosin Heavy Chain and Phalloidin (F-Actin) are the most frequent stains used for assessment of 3D constructs.

3.3.2.3 *Models Without injury – Quantitative Reverse Transcription Polymerase Chain Reaction (qRT-PCR) Differentiation Primers*

Figure 3.2 (h) outlines all the genes utilised to evaluate the differentiation of constructs. Myogenin, Myosin Heavy Chain 7 and 2 and MyoD were the most frequently-used genes to confirm cell differentiation in models. GAPDH was the most frequent reference gene.

Figure 3.2 (a)

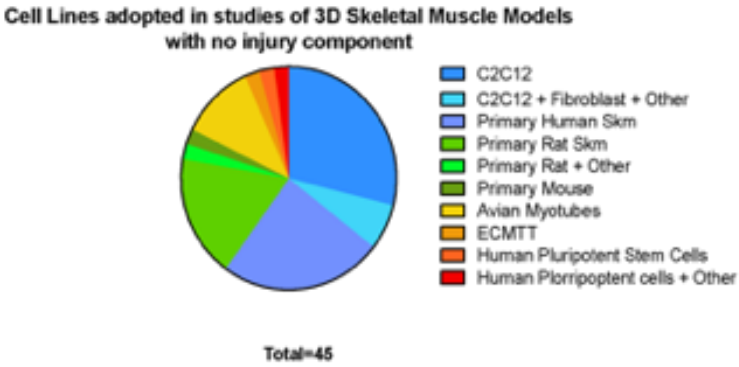

Figure 3.2 (b)

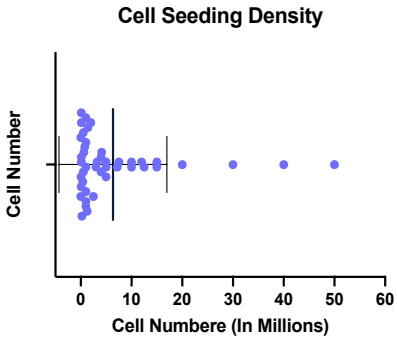

Figure 3.2 (c)

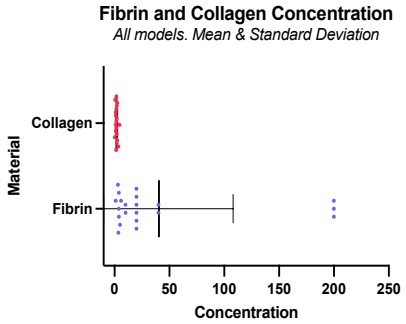

Figure 3.2 (d)

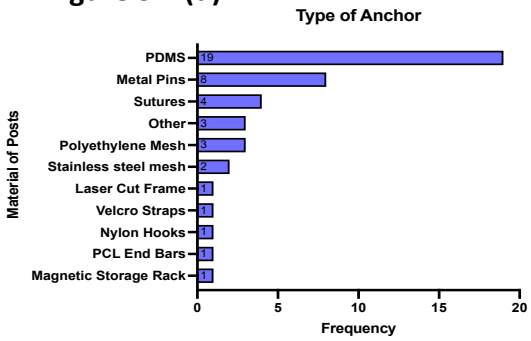

Figure 3.2 (e)

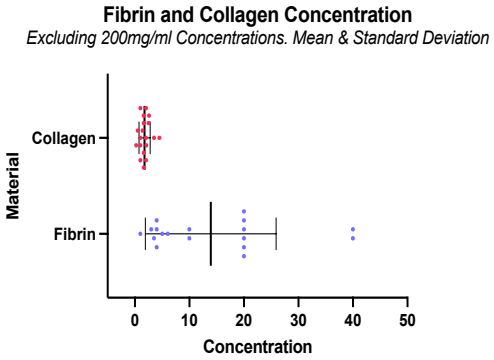

Figure 3.2 (f)

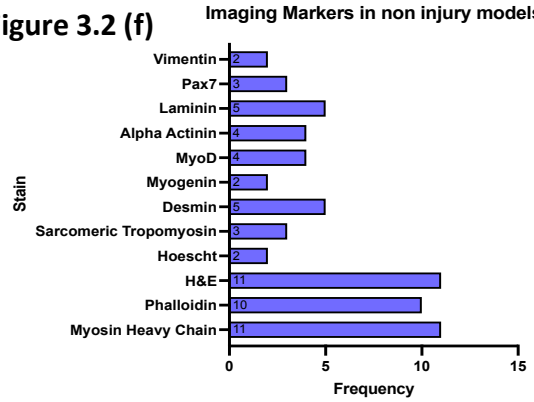

Figure 3.2 (g)

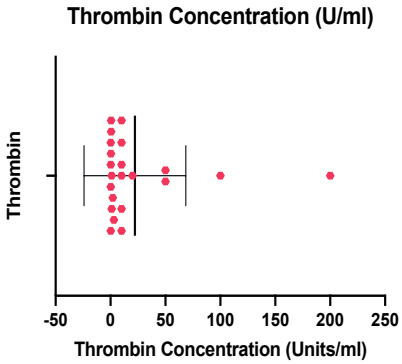

Figure 3.2 (h)

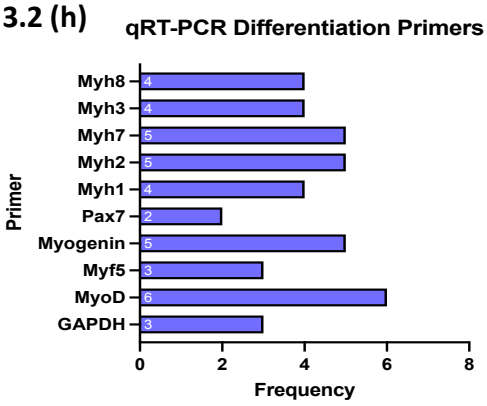

Figure 3.2 Model Characteristics of studies without injury

3.3.3 Study demographics – Models with injury

3.3.3.1 Model With injury – Hydrogel Manufacturer

The models with injury mechanisms (n = 12 articles) predominately used C2C12 cells (n=4) or primary human skeletal muscle cells (n=4). Models using primary cell culture from other species (rat & mouse) were also used. Figure 3.3 (a) outlines the types of cells used in 3D skeletal models with injury.

Figure 3.3 (b) outlines the mean cell number in injury models (Mean = 4.593 million cells/ml). Figures 3.3 (c) and 3.3(i) shows the fibrin and collagen concentrations utilised and in what combination. There was a broad range of fibrin of concentrations utilised, with a mean concentration of 13.5mg/ml(SD = 7.4). The mean collagen concentration was 1.639 (SD = 1.3) Figure 3.3 (d) shows the types of anchor points. There were seven different techniques employed to anchor hydrogels. The majority of models used PDMS with a frame or PDMS alone.

Thrombin concentration ranged from 0.8-100U/mg (Mean = 50.36, SD = 44.2). Three studies reported using sodium hydroxide at 1 M concentration to gellate collagen scaffolds.

3.3.3.2 *Model With injury – Imaging*

Figure 3.3 (e) reports the stains utilised for imaging in injury models in more than one study. Pax 7 was the most frequent antibody used for imaging in injury models (n=7). Laminin, Myosin Heavy Chain, F Actin (Phalloidin) and tropomyosin were used with equal frequency (n=2).

3.3.3.3 Model With injury - Quantitative Reverse Transcription Polymerase Chain Reaction (qRT-PCR) Differentiation Primers

Figure 3.3 (f) outlines the genes evaluated in more than one study using injury models. RP11B was the only reported reference gene amongst injury models. PAX7 and Muscle ring finger protein 1 (MuRF-1) were both utilised in equal frequency (n= 2). No studies validated their reference genes or used RNAseq or microarray to validate their models.

3.3.3.4 *Model With injury – Injury Mechanism*

Figure 3.3 (g) presents the data on techniques adopted to inflict damage on 3D models. Predominately, cardiotoxin (45.45%) was adopted in published models. Steroids, barium, mechanical injury and oxygen were adopted equally (9.09%). Mitochondrial inhibitors and cytosine arabinoside was also used in two studies (Other – 18.18%).

3.3.3.5 *Model With injury – Injury Duration*

Figure 3.3 (h) shows the duration of injury in published literature. The longest duration found was 48 hours (6.67%). The most frequent duration used was 6 hours (33.33%).

Figure 3.3 (a)

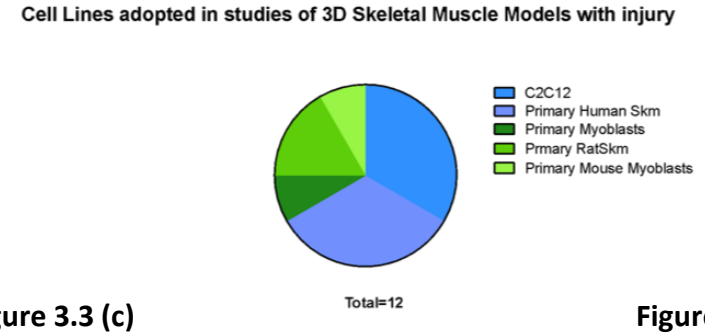

Figure 3.3 (b)

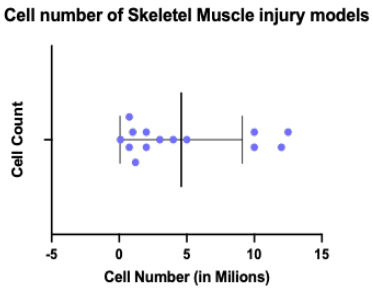

Figure 3.3 (c)

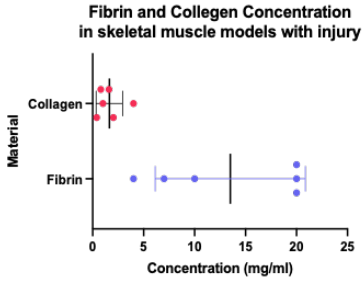

Figure 3.3 (d)

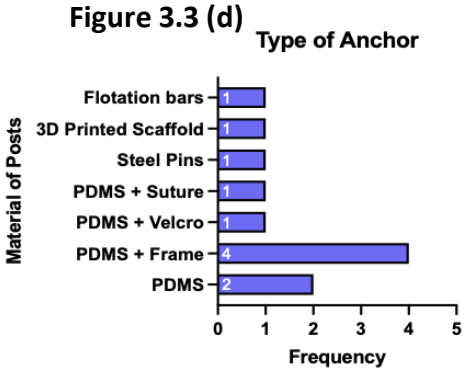

Figure 3.3 (e)

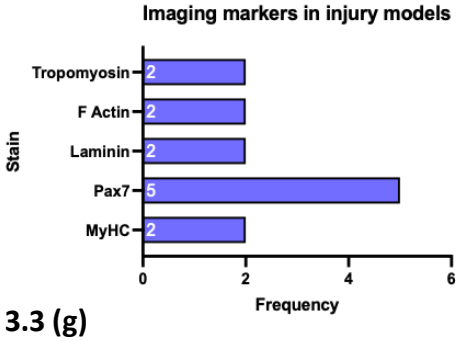

Figure 3.3 (f)

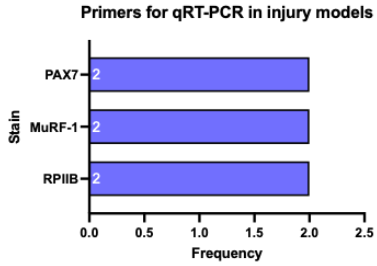

Figure 3.3 (g)

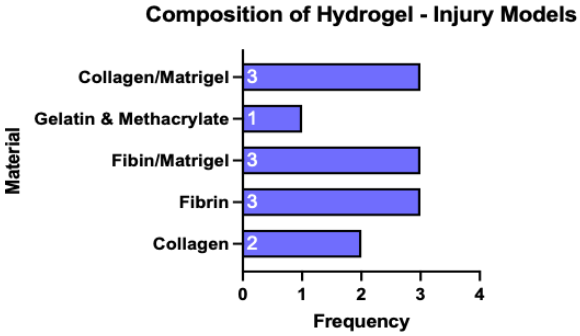

Figure 3.3 (h)

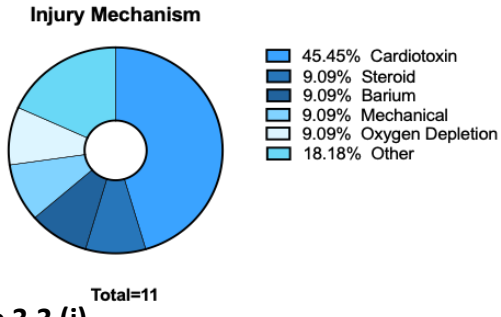

Figure 3.3 (i)

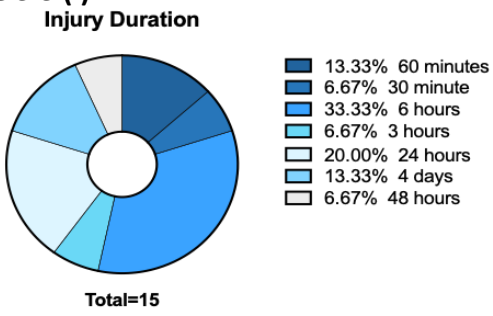

Figure 3.3 Model Characteristics of studies with injury

3.3.3.6 Force Quantification

Table 3.6 reports the data for tetanus, twitch, specific force and absolute/contractile force across studies with standard 3D skeletal muscle models (without injury). The largest tetanus reported was 450μN, twitch 200μN, specific force 0.08-0.14 and absolute force 700μN (300-700 range)

Tetanus is defined as a sustained muscle contraction evoked when the motor nerve receives action potentials at a high rate.

Muscle twitch is defined as a period of contraction and relaxation after a single stimulus.

Absolute force is defined as the maximum force achieved by the model.

Specific force is defined as a nongravitational force per unit of mass.

Table 3.7 reports this data for injury models. The largest tetanus reported for injury models was 1200μN. The greatest twitch value was 450μN, specific force 65.7μN, absolute force 3000μN. No studies evaluated the change in deflection after injury.

Table 3.6: Table Of Force Generation: Characteristics From Standard Models*. Units and terminology is directly lifted from the published literature. Note: The terminology of 'specific force' is used in literature and reported with units for pressure. Force has therefore placed in quotation marks to highlight that the term force here has been used in this field to report pressure data.*

Tetanus	Units	Twitch	Units	Specific 'Force'	Units	Absolute/Contractile 'Force'	Units
0.4-0.6	*mN*	0.8-0.5	*mN*	0.005	MPa	200	*μN*
28-38	*μN*	10-20	*μN*	0.14-0.1	MPa	600	*μN*
450	*μN*	200	*μN*	0.003	MPa	300-700	*μN*
400	*μN*	30.45±7.86	*μN*	0.011	MPa		
57.07	*μN*	42.52±8.38	*μN*	0.08-0.014	MPa		
36.96 ±7.04	*μN*			0.08-0.1	MPa		

Table 3.7: Table Of Force Generation: Characteristics From Injury Models. *Units and terminology is directly lifted from the published literature. Note: The terminology of 'specific force' is used in literature and reported with units for pressure. Force has therefore placed in quotation marks to highlight that the term force here has been used in this field to report pressure data.*

Tetanus	Units	Twitch	Units	Specific Force	Units	Absolute/Contractile Force	Units
45.9	μN	22.7	μN	0.657	MPa	42	μN
1000-1200	μN	450	μN			30	mN
						50-150	μN
						3000	μN

3.3.4 Outcome Reporting In Models

Figure 3.4 is a heat map of outcome reporting in non-injury models. Articles predominately reported results of hydrogel imaging (immunohistochemistry, immunofluorescence, haematoxylin & eosin, H&E). Data for cell health (metabolic activity, live/dead), electrical stimulation (to assess contraction) and anchor deflection were poorly reported across studies. Figure 3.4 & 3.5 highlights the lack of standardisation in outcome reporting for these models.

Figure 3.5 is a heat map of outcome reporting in injury models. Staining and electrical stimulation were the most common outcome measure reported across articles (9/12 and 8/12 respectively).

Figure 3.4: Outcome reporting in standard models.
White – Outcome measure not reported in experiment.
Red – Outcome measure reported in experiment.

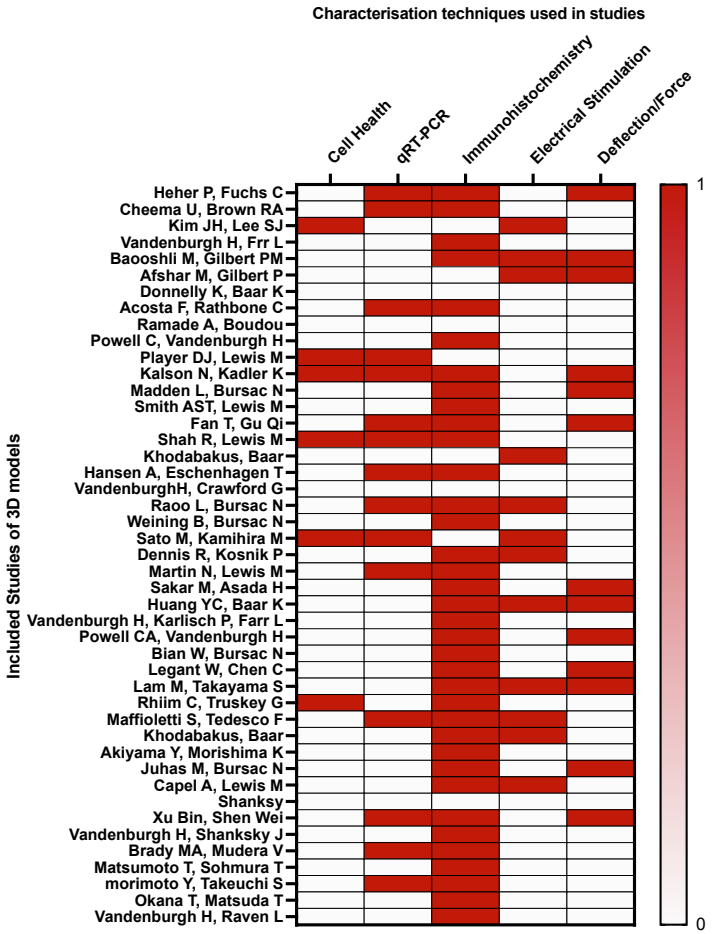

Figure 3.5: Outcome reporting in standard models.
White – Outcome measure not reported in experiment.
Red – Outcome measure reported in experiment.

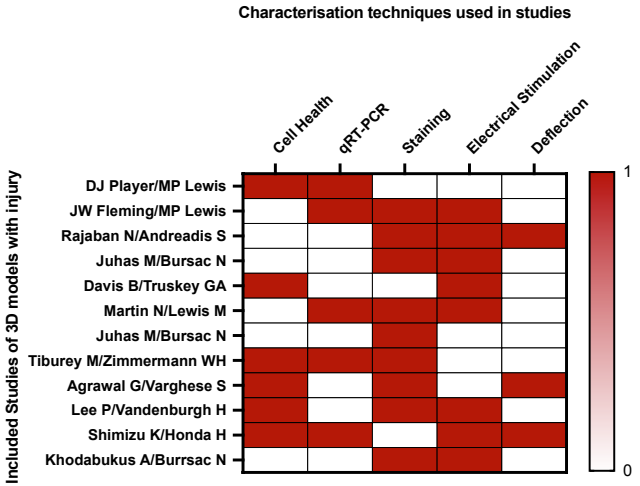

3.3.5 Quality Of Reporting In Included Studies

The risk of bias in the studies was assessed using seven questions, shown in Table 3.1, for the OHAT system. Table 3.8 shows the results for standard models and Table 3.9 the results for injury models. In the non-injury standard models, all studies reported low risk of bias. The lack of randomisation in all studies was reported as moderate bias. In the injury models, out of twelve studies, five had moderate degrees of bias, whilst 7 had a low level of bias. Common issues concerning *in vitro* studies were the lack of blinded randomisation and a lack of standardised reporting data leading to poor reporting. Figures 3.5 and 3.6 report outcome measures of included articles. The heatmaps identify a lack of consistency in characterisation techniques of 3D models. Immunostaining predominated in both 3D models alone and those with an injury. Finally, a common theme was the lack of clarity in reporting nascent information within figures or diagrams (such as not annotating force plots with the maximum and minimum force).

Number	Question
Q1	Same experimental conditions
Q2	Blinding during study
Q3	Incomplete data
Q4	Exposure characterisation
Q5	Outcome assessment
Q6	Outcome Reporting
Q7	Other

Table 3.1 (reproduced from methods): Questions for *in vitro* studies from OHAT tool.

Table: Assessment of Risk of Bias in studies using the modified OHAT system.

Name	Year	Q1	Q2	Q3	Q4	Q5	Q6	Q7	Outcome - Low	Outcome - Mod	
Heher P, Fuchs C	2015	Low	Mod	Low	Low	Low	Low		Low	XXX	Low
Cheema U, Brown RA	2002	Low	Mod	Low	Low	Low	Low		Low	XXX	Low
Kim JH, Lee SJ	2018	Low	Mod	Low	Low	Low	Low		Low	XXX	Low
Vandenburgh H, Farr L	1988	low	Mod	Low	Mod	Mod	Mod		Mod	Mod	Mod
Baoshli M, Gilbert PM	2019	Low	Mod	Low	Low	Low	Low		Low	XXX	Low
Afshar M, Gilbert P	2020	Low	Mod	Low	Low	Low	Low		Low	XXX	Low
Donnelly K, Baar K	2010	Low	Mod	Low	Low	Low	Low		Low	XXX	Low
Acosta F, Rathbone C	2021	Low	Mod	Low	Low	Low	Low		Low	XXX	Low
Powell C, Vandenburgh H	1999	Low	Mod	Low	Low	Low	Low		Low	XXX	Low
Player DJ, Lewis M	2014	Low	Mod	Low	Low	Low	Low		Low	XXX	Low
Kalson N, Kadler K	2010	Low	Mod	Low	Low	Low	Low		Low	XXX	Low
Madden L, Bursac N	2014	Low	Mod	Low	Low	Low	Low		Low	XXX	Low
Smith AST, Lewis M	2011	Low	Mod	Low	Low	Low	Low		Low	XXX	Low
Fan T, Gu Qi	2021	Low	Mod	Low	Low	Low	Low		Low	XXX	Low
Shah R, Lewis M	2013	Low	Mod	Low	Low	Low	Low		Low	XXX	Low
Khodabukus A, Baar K	2012	Low	Mod	Low	Low	Low	Low		Low	XXX	Low
Hansen A, Eschenhagen T	2010	Low	Mod	Low	Low	Low	Low		Low	XXX	Low
Vandenburgh H, Crawford G	2008	Low	Mod	Low	Low	Low	Low		Low	XXX	Low
Rao L, Bursac N	2018	Low	Mod	Low	Low	Low	Low		Low	XXX	Low
Weining B, Bursac N	2008	Low	Mod	Low	Low	Low	Low		Low	XXX	Low
Sato M, Kamihira M	2011	Low	Mod	Low	Low	Low	Low		Low	XXX	Low
Dennis R, Kosnik P	2000	Low	Mod	Low	Low	Low	Low		Low	XXX	Low
Martin N, Lewis M	2013	Low	Mod	Low	Low	Low	Low		Low	XXX	Low
Sakar M, Asada H	2012	Low	Mod	Low	Low	Low	Low		Low	XXX	Low
Huang YC, Baar K	2005	Low	Mod	Low	Low	Low	Low		Low	XXX	Low
Vandenburgh H, Karlisch P, Farr L	1988	Low	Mod	Low	Low	Low	Low		Low	XXX	Low
Powell CA, Vandenburgh H	2002	Low	Mod	Low	Low	Low	Low		Low	XXX	Low
Bian W, Bursac N	2009	Low	Mod	Low	Low	Low	Low		Low	XXX	Low
Legant W, Chen C	2009	Low	Mod	Low	Low	Low	Low		Low	XXX	Low
Lam M, Takayama S	2009	Low	Mod	Low	Low	Low	Low		Low	XXX	Low
Rhiim C, Truskey G	2007	Low	Mod	Low	Low	Low	Low		Low	XXX	Low
Maffioletti S, Tedesco F	2018	Low	Mod	Low	Low	Low	Low		Low	XXX	Low
Khodabakus A, Baar K	2009	Low	Mod	Low	Low	Low	Low		Low	XXX	Low
Akiyama Y, Morishima K	2010	Low	Mod	Low	Low	Low	Low		Low	XXX	Low
Juhas M, Bursac N	2014	Low	Mod	Low	Low	Low	Low		Low	XXX	Low
Capel A, Lewis M	2019	Low	Mod	Low	Low	Low	Low		Low	XXX	Low
Shanksy J	1997	Low	Mod	Low	Low	Low	Low		Low	XXX	Low
Xu Bin, Shen Wei	2019	Low	Mod	Low	Low	Low	Low		Low	XXX	Low
Vandenburgh H, Shanksky J	1989	Low	Mod	Low	Low	Low	Low		Low	XXX	Low
Brady MA, Mudera V	2008	Low	Mod	Low	Low	Low	Low		Low	XXX	Low
Matsumoto T, Sohmura T	2007	Low	Mod	Low	Low	Low	Low		Low	XXX	Low
Morimoto Y, Takeuchi S	2013	Low	Mod	Low	Low	Low	Low		Low	XXX	Low
Okana T, Matsuda T	1998	Low	Mod	Low	Low	Low	Low		Low	XXX	Low
Vandenburgh H, Raven L	1996	Low	Mod	Low	Low	Low	Low		Low	XXX	Low

Table 3.8: Assessment of risk of bias in included standard model studies using the OHAT tool.

Name	Year	Q1	Q2	Q3	Q4	Q5	Q6	Q7	Outcome - Low	Outcome - Mod	Final Outcome
DJ Player/MP Lewis	2014	Low	Moderate	Low	Low	Low	Low	Low	6	1	Low
JW Fleming/MP Lewis	2020	Low	Moderate	Low	Low	Low	Low	Low	6	1	Low
Rajaban N/Andreadis S	2021	Low	Moderate	Low	Low	Low	Low	Low	6	1	Low
Juhas M/Bursac N	2014	Low	Moderate	Low	Low	Low	Low	Low	6	1	Low
Davis B/Truskey GA	2016	Low	Moderate	Low	Low	Low	Low	Low	6	1	Low
Martin N,/Lewis M	2017	Low	Moderate	Low	Low	Low	Low	Low	6	1	Low
Juhas M/Bursac N	2018	Low	Moderate	Low	Low	Low	Low	Low	6	1	Low
Tiburey M/Zimmermann WH	2019	Low	Moderate	Moderate	Low	Moderate	Low	Low	5	2	Moderate
Agrawal G, Varghese S	2017	Low	Moderate	Moderate	Low	Moderate	Low	Low	5	2	Moderate
Lee P, Vandenburgh H	2012	Low	Moderate	Moderate	Low	Moderate	Low	Low	5	2	Moderate
Shimizu K, Honda H	2017	Low	Moderate	Moderate	Low	Moderate	Low	Low	5	2	Moderate
Khodabukus A, Burrsac N	2020	Low	Moderate	Moderate	Low	Moderate	Low	Low	5	2	Moderate

Table 3.9: Assessment of risk of bias in included injury model studies using the OHAT tool

3.6 Discussion

The aim of this chapter was to review systematically the literature on 3D models of skeletal muscle utilising anchor systems. The secondary aim was to evaluate specifically the methods to induce injury in 3D. The results from this review outline the characteristics of these models and specifically the types of injuries adopted to probe how skeletal muscle regenerates. The outcome data evaluated in this review was selected due to their frequency in reporting results from such models. The results identify limitations to these models both in their design (such as anchors being fixed to the tissue culture plastic) and in the outcome reporting of the experimental data.

In both groups, the immortalised mouse C2C12 cell line was most frequently used for culture followed by primary human cells and then primary rat skeletal muscle. Immortalised cells are more robust for large scale culture compared to primary cells. This is because they are not constrained by the need for human (or animal) tissue donations, or limited by expansion capacity or dedifferentiation. Due to their genetic modification, immortalised cells are capable of higher passage numbers compared to primary cell cultures. They also proliferate faster producing greater cell numbers. These factors make immortalised cells preferable for large volume *in vitro* models. This explains their preference in large 3D models that have a high cell requirement and may be more prone to infection or cell death than 2D models. Immortalised cell lines have their own limitations. The lines are engineered, through knocking out cell cycle controls, for prolonged proliferation that may influence other cellular processes and responses. Some researchers argue that immortalised lines are not an accurate representation of the normal cell population at all, but a different cellular population, expressing unique gene patterns, that have adapted over time(147). This argument has not been expressed towards induced pluripotent stem cell populations. The differences in proliferation, differentiation, morphology and surface protein expression between immortalised C2C12 cells and primary muscle progenitors cells (MPCs) has been demonstrated(148). In

particular the latter shows greater maturation, with more cross striations and greater levels of myosin heavy chain. MPCs were also more responsive to electrical stimulation than C2C12s, which accelerated sarcomere assembly(149). Primary cells are potentially more representative of their host's cellular environment and perhaps more suited for generating engineered 3D models for disease investigation. Ultimately the appropriate choice of cell line for these models is often influenced by the size and volume of culture required, the availability of donor tissues for primary cells, the available funds for culture and expertise of the researchers. These influences may also be important in the selection of 3D models for widespread adoption, injury and testing – as any selected cell line would need to be suitable for good manufacturing practice (GMP) culture and large scale expansion.

The results demonstrate that PDMS is the most frequently adopted material for the manufacture of anchors. Although the use of 3D printing in cell culture is increasingly commonplace, the accessibility and relative ease of casting PDMS explains its continued use. To synthesise PDMS anchors, authors produce negative moulds of anchors from metal. Liquid PDMS can then be poured and cured in an oven to generate anchors. Finally, they can be sterilised easily with alcohol (or UV treated) for cell culture.

Likewise, fibrin and collagen have predominated in the manufacture of 3D hydrogels for skeletal muscle. Early papers often used fibrin sealant glue by Baxter Ltd, a manufacturer of clinical grade fibrin sealant for surgery. Laboratories would be given out of date fibrin glue for use in *in vitro* models. This was a plausible naturally occurring polymer to test skeletal muscle formation. Collagen, by comparison, should be the first choice to mimic the *in situ* extracellular matrix (ECM) environment. However, for many laboratories the significant cost of collagen precludes its early adoption. Alternative models have been postulated using polymers such as Alginate, Gelatin or Polyeythylene Glycol (PEG). However, as these aren't found naturally in humans, they were excluded.

3.6.1 Reporting of details of force generation - standard reporting.

The demonstration of force production by skeletal muscle is important for *in vitro* models. As one of the key functions of skeletal muscle is movement and support to the axial skeletal, highlighting force production of *in vitro* models is key to convincing scientists these platforms are capable of replicating the native environment.

One approach is to calculate the degree of deflection achieved by the 3D model of a fixed cantilever post; however, this was infrequently undertaken by research groups. When this approach was undertaken, the methods of applying Euler beam theory were different In particular, the most common error with this method was in estimating deflection as a uniformly distributed load (i.e along the whole length of the anchor) whilst pictorially demonstrating that the hydrogel was acting as a partially distributed load at the tip of the post system. This would lead to over estimations in beam deflection, and misrepresent the degree of force generation from the model. This review found no studies that reported the change in deflection after injury on constructs. This could be a useful surrogate marker of loss of function alongside electrical elucidation of twitch and tetanus, but would need experimental validation.

By contrast, the measurement of twitch, tetanus or absolute force by constructs in response to electrical stimulation was consistently undertaken by published models. The relative voltages applied across the hydrogels differed between models. Articles typically presented the values for tetanus or they presented data on muscle twitch. Articles also reported absolute force or specific force. Comparatively, physiological studies of skeletal muscle cite specific tension, tension/cross sectional area in kN/m^2, with reference to fibre relative properties. Several experimental studies have reported values for specific tension of animal skeletal muscle within the range of ~225 $kN/m^{2.}$ (150-152), thus providing a ballpark figure against which to compare *in vitro* models. Tables 3.6 and 3.7 demonstrate the force data presented and how the reporting of these outputs was inconsistent both in the type of force reported across included studies in this review and the units reported. Due to variation in hydrogel size

in the models presented, values such as tetanus, twitch and absolute force are difficult to compare across groups. Specific force is the generated force per unit of area (such as newtons per mm^2). Although specific force was only reported in a few papers, it is much easier to compare this value across models of various scales. In the non-injury studies the range of specific force was large, between 0.11MPa to 80MPa. Conversely in the injury model groups, the specific force reported from one study was 0.0657 MPa. In this particular model, the absolute force was 200μN with a cross sectional area of 0.04mm to generate such a high specific force. Moving forwards, it is suggested that specific force be reported as standard for three dimensional models of skeletal muscle.

3.6.2 Outcome Measurements

This systematic review provides quantifiable evidence of the lack of standardisation in the outcome reporting of these *in vitro* models. The techniques used to quantify these models differed between articles, as demonstrated in Figures 3.5 & 3.6. Although themes of outcomes to be reported could be grouped (cell health, qRT-PCR, Immunostaining etc), these were not consistently demonstrated across studies. This may be due to studies having different research aims for their work. Furthermore, there is no consensus on what data to present to demonstrate a validated three-dimensional skeletal muscle model. This begs the much broader question of whether there should be core outcome sets for reporting results in *in vitro* experimental work, as for clinical data sets. Although groups predominantly demonstrate differentiation through both qualitative and quantitative techniques (immunohistochemistry, quantitative PCR), there is no accepted list of myogenic markers of differentiation that must be demonstrated. In the studies included in this review all demonstrated expression of at least one, if not more, marker of differentiation (Pax7, myosin heavy chain isoforms). This can be reflected in the data for imaging and qPCR markers in non-injury and injury models. Predominately, groups used H&E, Phalloidin (F-Actin) and Myosin heavy chain to show the

structural phenotype of differentiated cells. Whilst in injury groups, Pax7 was commonly utilised to demonstrate skeletal muscle phenotype.

Similarly, with qPCR, in non-injury models, findings were presented with primers for myosin heavy chain isoforms, Myogenin and MyoD, whilst mostly for Pax7, Murf1 and RPIIB (housekeeping gene) in injury groups.

These differences in results presentation make it challenging to evaluate the quality of cell differentiation or the functional capacity of myotubes formed, for example, against other models in the literature or native tissue.

Ideally, models would have to demonstrate the expression of a panel of terminal differentiation markers, such as MYOD1, MYF5, MYOG, MYF5, MYOD1, MYF6 and PAX7, to an agreed threshold. Secondly, such models would demonstrate image analysis employing structural analysis, such as myotube fusion count or fusion index and phenotypic staining, for example PAX7 and Myosin Heavy Chain. Finally, the functional capacity of the model would be quantified with a standard method.

3.6.3 Contextualising And Characterising Injury Models.

This review sought to evaluate 3D anchored models of skeletal muscle and to evaluate models that had inflicted an injury onto the cell population in order to study the response and regenerative capacity of skeletal muscle. In this respect, few models reported a methodology for injury. In those that did, the papers predominately utilised cardiotoxin (snake venom) to injure cell populations. The snake venom used originated from the Naja Mossambica mossambica family commonly known as the Mozambique spitting cobra. The venom consists of large protein toxins (MW ~7kD) that are involved in the depolarisation of excitable membranes in sodium and calcium transport. It is believed that phospholipid cell surfaces may also serve as receptors for these proteins that also induce cell lysis, through membrane binding(153). Hence, this toxin potentially initiates a necrotic cell death phenotype. Other methods such as steroid use, chemical injury with barium, mechanical injury and hypoxic injury

were also utilised. In this specific group of models, no methods utilised a crush injury, laceration or more primitive chemical injury such deionised water or hydrogen peroxide in order to inflict cell death. These have been used in 2D culture as first line techniques. There is no evidence from included studies to suggest whether the difference in injury mechanism produces a specific, injury associated genotype or whether the genotypic response is the same regardless of injury mechanism. Characterising how different injuries influence mRNA transcription and translation to protein is a key step in understanding how trauma influences cell function. If the mechanism of injury is unimportant, then large scale expensive models such as blast could be avoided.

No study reported a dose response curve of toxin concentration against cell viability, in order to characterise the degree of injury. The duration of the injury showed variation between models (30 minutes to 4 days). Six hours was most commonly reported incubation time.

In 2D culture, the scratch assay is a well reported method of inflicting and studying wound repair often with imaging of surface area changes over time(154). In this review no studies evaluated the degree of injury immediately after stimulus, or assessed the change in regeneration over time. No studies used a formal marker of cell health to validate the degree of injury inflicted upon the cell population. One current limitations of three-dimensional culture is the lack of bespoke validated assays. Researchers are forced to adopt and optimise, assays developed for 2D. To facilitate the translation of laboratory findings to the bedside, validated, commercially available models and injury methods will be required. However, to achieve this, injury models must be characterised in depth. No studies quantified the cellular response to the injury that was inflicted on cell populations. The studies utilised cell damage as a means to assess the effect on markers of skeletal muscle differentiation or regeneration. No studies adopted techniques such as RNA sequencing or proteomic analysis to probe the wider effects from injury. This would be an interesting avenue for future investigation as these techniques are hypothesis free, novel and allow comparison across model types.

3.6.4 Implications For Model Development For Trauma

This review aimed to understand previous research on models of skeletal muscle injury. The field of trauma research is diverse, with limited focus on understanding how muscle responds. To study the effects of blast injury on tissue, for example, a validated positive control is required. Characterised models of injury in 3D culture are lacking. They will be required to help advance the field of trauma research both from the perspective of understanding the effects of injury, but also how to mitigate them. The data in this review is important as it demonstrates the knowledge gap in this field and offers future research focus.

3.6.5 Limitations

Firstly, this is the first systematic review of three dimensional models of anchored skeletal muscle hydrogels. It is also the first systematic review of methods to inflict an injury into these models. This review is different from many literature reviews in the *in vitro* field, which often lack search criteria and reproducible methodology. Although the adoption of systematic review methodology amongst *in vitro* literature has increased, it lacks parity with clinical systematic reviews.

There are limitations to this methodology. Data reporting in *in vitro* literature is not standardised, therefore it becomes challenging to report and extract data across multiple studies. Much of the *in vitro* literature is reported in the Web of Science database, rather than on MEDLINE or EMBASE. The former database does not use the keyword structure as MEDLINE or EMBASE databases. Therefore it is necessary to translate a search strategy between databases. This could introduce errors and inconsistencies into the methodology. The approach in this chapter has attempted to reduce errors and achieve a reproducible strategy across all databases.

Although this work adopted the OHAT risk of bias tool, more work is required to develop a robust technique to assess and report bias amongst *in vitro* literature. The use of randomisation is rare in *in vitro* studies, and adopting this question within the OHAT perhaps scores unnecessary bias. Focus on cell types, seeding numbers, replicates and power calculations may be more useful ways of assessing bias within the *in vitro* literature.

3.7 Conclusions & Future Directions

This systematic review outlines the current research in the field of anchored three-dimensional skeletal muscle models with or without an injury. It demonstrates the variety of cell types used, the techniques used to construct models and the functional and morphological outcomes reported. The data suggests that immortalised cell lines may be used to develop novel PDMS based anchor models, prior to transiting to primary cell lines for deeper characterisation. The review lists techniques adopted to induce injury within skeletal muscle. The studies reveal a lack of later characterisation of cell signalling and modes of cell death in injury models. There is little if any comparison of models to *in vivo* physiology. There is a clear need for a greater understanding of how cells sense and response to injurious stimuli and for positive controls to characterise the effect of trauma on tissue. The review demonstrates the need for the development of core outcome reporting for *in vitro* tissue culture and more specifically for models of skeletal muscle. It also demonstrates the need for work to compare the effects of different injurious stimuli on signalling, transcriptomic and protein-level response. Finally, this systematic review provides evidence of how to apply systematic review methodology to *in vitro* research, including how to undertake risk of bias analysis.

4

Development And Validation Of A Three Dimensional *In Vitro* Model Of Skeletal Muscle For Blast Loading.

4.1 Introduction

Skeletal muscle makes up 40% of body composition and is vital for skeletal support, locomotion and homeostasis. Skeletal muscle architecture has been defined as the arrangement of muscle fibres relative to the axis of force generation (155). Native muscle consists of highly aligned contractile myofibers, a population of unipotent satellite cells that are required for muscle growth and repair, fibroblasts for extracellular matrix (ECM) synthesis as well as lymphocytes, vascular smooth muscle and endothelial cells for angiogenesis (156). Chapter 3 outlined the published methods to model this architecture *in vitro* in 3D using anchor posts. Developing more biomimetic *in vitro* models of muscle will be invaluable for studying skeletal muscle mechanobiology in both the healthy and injured/diseased state.

To investigate the effects of explosives on skeletal muscle function, this chapter presents a novel model of *in vitro* skeletal muscle. In this chapter, C2C12 immortalised myoblasts were used to engineer skeletal muscle tissues between 3D printed anchor posts. The design of this system takes into account the unique requirements of blast experimental platforms outlined in Chapter 1. These engineered muscle hydrogels showed organised architecture and demonstrated force generating capacity. The temporal changes in function and gene transcription of these hydrogels was then characterised. In order to evaluate their response to injurious stimuli, a method of chemical injury using hydrogen peroxide was developed and then characterised. Bulk RNA sequencing at 4 hours and 7 days after injury showed temporal changes in gene transcription and pathway enrichment. Overall, this chapter demonstrates a novel model of skeletal muscle specifically designed to investigate the effects of explosive shock waves on skeletal muscle signalling and function.

The primary aim of this chapter is to develop a representative model of skeletal muscle to probe the effects of blast shock wave on this tissue. The secondary aim was to develop a

positive control injury that could be used to contextualise future experimental data from blast injury

4.2 Methods

4.2.1 Cell Culture Media

Growth Media (GM) was composed of Dulbecco's Modified Eagle Medium, DMEM with 10% (v/v) Fetal Bovine Serum (FBS, ThermoFisher, UK) and 1% (v/v) Penicillin Streptomyocin (Pen-Strep, ThermoFisher, UK) .

Differentiation Media (DM) was composed of DMEM with 2% (v/v) Donor Equine Serum (DES, Appleton Woods), 1% (v/v) Pen-Strep, 0.3% (v/v) Insulin-Transferrin-Selenium (ITS, ThermoFisher, UK) and 0.5% (v/v) amphotericin B (Sigma-Aldrich Ltd).

4.2.2 Routine Maintenance Of Cell Lines

C2C12 Mus Musculus cells (gifted from Kennedy Institute of Rheumatology, KIR, & Dr Thomas Roberts, Institute of Developmental & Regenerative Medicine, IDRM, Oxford University) were maintained in GM. Cells were incubated at 37°C in 5% CO_2/95% air (v/v) and cultured in monolayers up to 80% confluency. Cells were passaged by removing GM, washing with warm phosphate buffered saline (PBS, Invitrogen, UK) and trypsinised (Trypsin-EDTA, ThermoFisher Ltd), centrifuged, counted (Countess cell counter, ThermoFisher Ltd) and split in a 1:10 ratio into GM in fresh T175 flasks. For storage cells were resuspended in FBS and 10% (v/v) DMSO (Sigma-Aldrich, UK) at a concentration of 10^6/ml in cryotubes and stored at -80°C.

4.2.3 Skeletal Muscle Hydrogel Fabrication And Differentiation

Matrices were synthesised by polymerisation of Bovine Fibrinogen (Sigma Aldrich, UK), Matrigel (Appleton wood Biosciences Ltd) and Bovine Thrombin (Sigma Aldrich, UK). Fibrinogen was dissolved in sterile warmed (37°c) Phosphate buffered saline (PBS, ThermoFisher scientific ltd) to a final concentration of 10 mg/ml. Thrombin (1000U/vial, Sigma Aldrich) was dissolved in GM to a final concentration of 50 U/ml (20 ml). Matrigel (Appleton wood biosciences Ltd) was thawed on ice, then dissolved in cold sterile DMEM, before aliquoting into 10 ml tubes and freezing. Aliquots of 5 ml of Matrigel were added to thrombin solution. C2C12s were expanded in T175 flasks and then dissolved in thrombin solution to give a concentration of 1 million cells/ml.

Fibrin hydrogels were synthesised in bespoke silicone moulds (Figure 4.1) by first pipetting 1ml of fibrinogen solution into wells, then adding 1ml of thrombin-cell solution. Hydrogels were polymerised at room temperature for 15-30 minutes. After 30 minutes the hydrogels were removed from the mould and placed in a 12 well tissue culture plate with growth medium for 48 hours. GM was replaced with low serum DM for 11 days (media changes every other day).

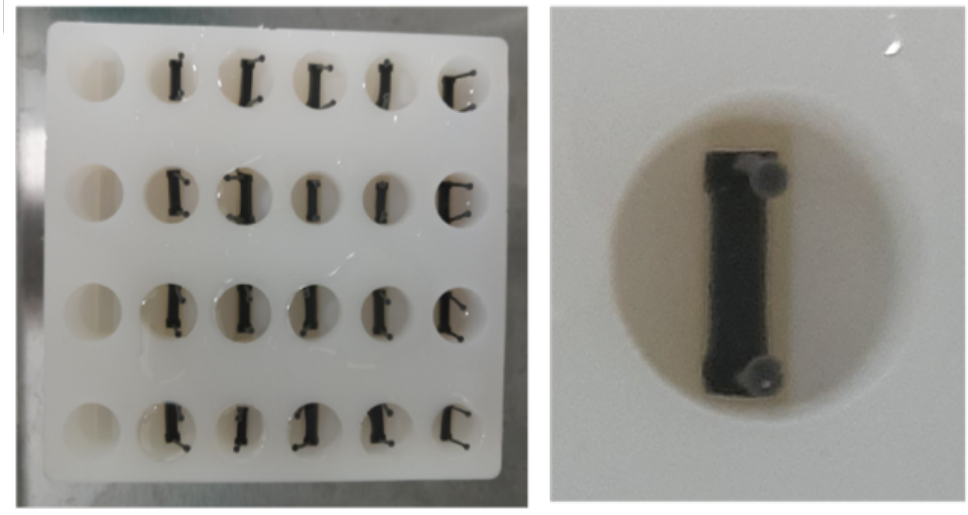

Figure 4.1 – Representative images of silicone casting moulds for hydrogel model. Flexible resin PDMS coated 3D printed posts can be seen placed in the centre of the well. Hydrogels were then polymerised around the posts prior to removal and culture in 12 well plates.

4.2.4 Post & Jig Manufacture

Posts were printed using a Formlabs Form 2 3D Stereolithographic printer (Formlabs Ltd, MA). Figure 4.2 details the final design of the posts that were printed for the model. In this thesis 'posts' refer to the 3D printed anchors designed and produced to synthesise the 3D *in vitro* model. The term 'jig' is used to refer to apparatus designed to facilitate the casting of the 3D hydrogel model. Posts were designed using Onshape (Onshape, MA),exported as stereolithography (STL) files then imported into Formlabs' PreForm software (Version 2.19.3) for printing. Posts were printed in flexible resin (Flexible Resin, Formlabs Ltd), washed in isopropyl alcohol, IPA, and cured with ultraviolet light. Posts were then coated in polydimethylsiloxane (PDMS) Sylgard silicone elastomer (Sylgard 184, Sigma Aldrich Ltd, 10:1 ratio of elastomer: monomer), baked at 80 °C in an oven for 1 hour before curing at room temperature overnight. The posts were sterilised for tissue culture by submersion in 70% EtOH for 1 hr followed by washing in PBS. Posts were then either used immediately, or stored in sterile PBS at 4 degrees.

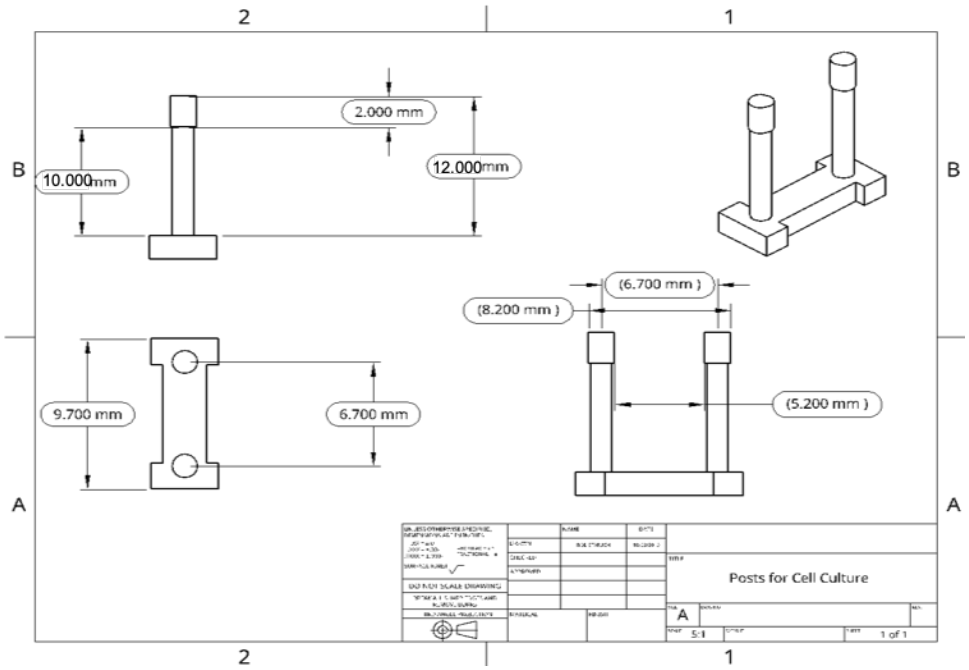

Figure 4.2: Dimensions of 3D printed post.

4.2.5 Metabolic Assessment

Presto Blue™ cell viability reagent (Thermofisher Ltd) was used to assess cell metabolism after injury. Presto blue™ is a cell permeable resazurin-based reagent. Resazurin is a blue reagent that, after diffusing into cells, is reduced by diaphorase enzymes to Resorufin, a fluorescent pink compound. To assess viability, Presto blue™ (PB) was diluted in DMEM (1:10 PB:DMEM), then 2ml of PB was added to wells containing hydrogels (12 well plate). Hydrogels were incubated at 37°C for 1.5 hours, after which 100μl aliquots of reagent were aspirated into black clear bottomed 96 well plates. Three replicate 100μl samples were taken, and read (540 Excitation/ 590 Emission spectra) on a plate reader (BMG Labtech Ltd), for each individual well with PB reagent. Three wells of presto blue diluted solution were incubated for the same duration as hydrogels, and read as background. Background readings were subtracted from those for hydrogels and mean values taken for three replicate 100 μl samples for each gel. These measurements were taken prior to and immediately after hydrogen peroxide injury. Samples were also measured at days 1, 4 and 7 after injury.

4.2.6 RNA Homogenisation From Hydrogels

Hydrogels were stored in RNA*later*™ stabilisation solution overnight and then frozen at -20*C. RNA was then extracted using the Qiagen RNeasy fibrous tissue kit (Qiagen, LOT 74704). (Thermofisher, LOT AM7021). Hydrogels were removed from RNA*later*, washed in PBS and cut into <5mm pieces with micro scissors. These pieces were then collectively placed in a FACS tube with 900µl of buffer RLT and 2- Mercaptoethanol solution (Sigma Aldrich Ltd, stock solution made up 1:10 ratio). A Qiagen tissue rupter II device (Qiagen, LOT 9002755) with disposable probe (Qiagen, LOT 990890) was then used to homogenise samples. After homogenisation, samples were left to stand for 5-10 minutes to allow any bubbles to settle. As per the Qiagen fibrous tissue kit protocol, homogenate was then aspirated in 300µl amounts into RNA/DNA free eppendorfs with 590 µl of RNAse free water and 10 µl of Proteinase K. Samples were incubated at 55°C for 10 min on a heat pad and then centrifuged for 3 minutes at 8000 xg. The supernatant from centrifuged samples was then aspirated into a lo-bind Eppendorf and stored at -80°C for RNA extraction.

4.2.7 RNA Extraction From Hydrogels

RNA Extraction was conducted as per the protocol for the Qiagen Fibrous Tissue Kit (Qiagen Ltd). To extract RNA from homogenised samples, samples were first thawed from -80°C. Then 0.5 volume of 99% Ethanol was added to the samples and mixed with a pipette until homogenous. Samples were then aspirated into RNAeasy mini spin columns in 700µl volumes, and spun for 1 minute at 10 000 xg. Once the entire volume had been passed through the spin column, 350µl of Buffer RW1 was added to the spin column and spun for 1 minute at 10 000 xg.

DNase I stock solution was mixed as per protocol (Qiagen Ltd,10µl Dnase I solution + 70µl Buffer RDD). 80µl of DNase mixture was pipetted into the spin column and left for 15 minutes

at RT. After 15 minutes, 350μl of Buffer RW1 was pipetted into the spin column and spun for 1minute at 10 000 xg.

500μl Buffer RPE was pipetted into the spin column and spun for 1 minute at 10 000 xg. This step was repeated with a 2 minute spin cycle at 10 000 xg. After this step a further spin step was added for 1 minute into a fresh Eppendorf.

To elute RNA, 30μl of RNA free water was pipetted into the spin column over a fresh RNA free Lo bind Eppendorf and spun for 1 minute at 10 000 xg. This step was repeated with another 30μl of RNA free water .

Eluted RNA was stored at -80°C prior to quality control and library preparation. Contaminated DNA was removed using Turbo Dnase as per manufacturer's instructions (Applied biosystems, Thermo Fisher Scientific, Loughborough, UK) and RNA re assessed after DNase treatment. RNA was reverse transcribed into cDNA using SuperScript III (Invitrogen) as per manufacturer's instructions with random hexamer primers.

4.2.8 Library Preparation & Sequencing

Prior to library preparation, 1μl aliquots of RNA were diluted in 9ul of RNA free water and tested on High Sensitivity RNA Screentapes (Agilent 2200 Tapestation) for quality and quantity. Library preparation was undertaken using the NEBNext Ultra II RNA library Prep Kit for illumine with poly-A selection (illumine, San Diego, CA, USA) as per the manufacturer's protocol.

In brief, RNA was extracted, fragmented, primed and then used to synthesise cDNA. Purified double-stranded cDNA was ligated with an adaptor sequence prior to enrichment using PCR. Libraries were then prepared, purified and quality assured. Following library preparation, each library was quantified for total DNA content with High Sensitivity DNA ScreenTapes (Agilent). Libraries from 24 samples with unique identifiers were pooled, and on the day of sequencing one pool was thawed, denatured with 0.2M NaOH and diluted to 1.8 pM concentration in 1.3ml

for sequencing. This pool was added to the NextSeq High Output kit (75 cycles) and the kit was sequenced on a Illumina NextSeq 500.

4.2.9 Bulk RNA Sequencing Analysis

After sequencing, raw FASTq files containing reads were generated by the Illumina software CASACA v1.8. Pseudo-alignment was undertaken with Kallisto, a pseudo-alignment tool that quantifies based on the transcription level rather than the gene level. Reads were mapped to the GRCm39 (GCA_000001635.9) *Mus Musculus* reference genome from the Ensembl Project. Data analysis, including differential expression and pathway analysis, was undertaken in R and R Studio (R Foundation for Statistical Computing, Vienna, Austria) using the dESeq2 package and msigdbr, enrichr, fgsea and cluster profiler packages. The full reproducible code for analysis can be found on Github (link in appendices).

4.2.10 Housekeeping Gene Identification

To evaluate gene changes, an endogenous control was selected. To evaluate the most appropriate housekeeping gene for this cell population, the gene expression of all housekeeping genes was examined across all timepoints. A validated list of mouse endogenous controls was used from a Taqman™ Array Mouse Endogenous Controls Plate (Applied Biosystems, Cat No: 44226699). The endogenous controls list was cross referenced to the bulk RNA sequencing outputs, to identify which genes were expressed and to what degree over time. The gene, or panel of genes, with the least change in expression over time were adopted as the endogenous controls for comparison.

4.2.11 Imaging

Hydrogels were fixed in 4% paraformaldehyde and then stored in phosphate buffered saline. To embed in wax, hydrogels were washed in PBS twice, then replaced with 70% ethanol and left overnight at 4 degrees. Hydrogels were then sequentially dehydrated through 80%, 90% and 100% ethanol before being placed inn Xylene for 1 hour. Xylene was aspirated with a pipette before filling with molten wax. Samples embedded in wax were cooled on a cold plate for 3-6 hours then stored at room temperature. To generate slides, samples were on a microtome and cut in 12 micron slices, floated in warm water and captured onto glass slides. Appropriate sections were then dried at 60°C and 37°C, sealed with a glass coverslip and stored at room temperature. The imaging protocol was gifted by Professor Stephanie Dakin, Botnar Research Centre.

4.2.12 Immunofluorescence Staining

Immunofluorescence staining was conducted with phalloidin 488 (Cell Signalling Technology, Cat No 8878) staining of F-actin and DAPI (Thermofisher ltd) to stain the nucleus. Slides were permeabilised with 0.1% triton X for 5 minutes, then washed three times with PBS. To block, 1% bovine serum albumin solution,(BSA, Sigma Aldrich Ltd dissolved in PBS, was used on slides for 45 mins, then washed with PBS three times for 5 minutes. Phalloidin was added for 30 mins (5ul per slide). Finally DAPI anti fade mountant was added to the slide dropwise and sealed with a coverslip. Slides were left overnight at room temperature.

4.2.13 Volume Measurements

Hydrogels were photographed upright in the custom silicone plate at Day 1, 3, 4, 7, 10 & 13. The surface area of the hydrogel within the well was measured using the ImageJ (Version 1.53v 21, National Institutes of Health and the Laboratory for Optical and Computational

Instrumentation) area measurement tool. The percentage coverage of the hydrogel in 2D was calculated by dividing the hydrogel surface area by the total area of the circle of the well. The change in surface area was then calculated by subtracting this value from 100.

4.2.14 Deflection Measurements

To estimate deflection, hydrogels were removed from 12 well plates and placed in sterile silicone moulds used for hydrogel manufacture. Posts were photographed prior to hydrogel seeding and labelled for tracking throughout the duration of the experiment. Photographs were taken using a smartphone (Samsung S10). Hydrogels and posts were then imaged immediately after seeding and again at Day 1, 3, 4, 7, 10 & 13. Hydrogels were photographed in 2 planes (top & side). Images were loaded in ImageJ and analysed . Inter post distance was measured and the change in distance used to estimate deflection and hydrogel force generation.

4.2.15 Analytic Model

Hydrogels with muscle cells were placed between two posts as shown in Figure 4.3. The measured deflection was related to the force applied by the muscle through Euler-Bernoulli beam theory. Figure 4.4 shows the deflection of a beam when subjected to a distributed load.

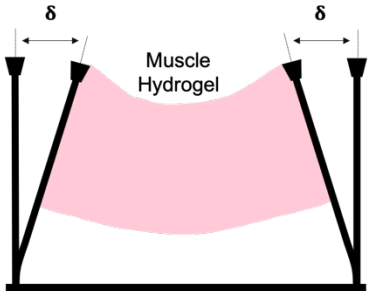

Figure 4.3: Outline of muscle model and attachment to posts. The schematic demonstrates how the hydrogel distributes its load on the post (pink shaded area), and how the post is deflected (denoted by length δ).

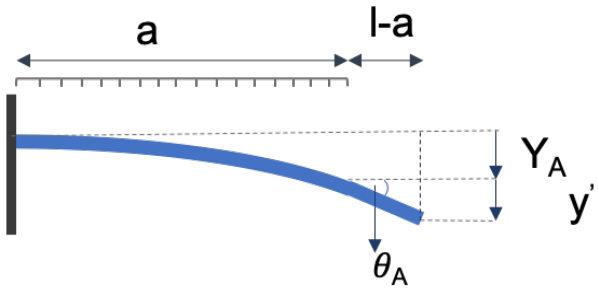

Figure 4.4: Representative diagram of the deflection of a cantilever beam, length l, when subject to a distributed load over a length l-a. Y_A is the deflection at location 'a', the unloaded portion of the beam. y' is the deflection at the end of the load at 'l-a'. θ_A is the angle at the location l-a and y'.

The expression for the deflection, Y_A, at the end of the distributed load is :

$$Y_A = \frac{a^4}{8EI}\,\omega \tag{4.1}$$

Where E is the elastic modulus of the beam material, I is the second moment of the area,

Where: $\mathrm{I} = \pi R^4/2$ for a solid circle of Radius R_1, and ω is load unit length in the this formula:

The angle of deflection at the end of the distributed load is

$$\theta_A = \frac{a^3}{6EI}\,\omega \tag{4.2}$$

The additional deflection of the free portion of the beam is:

$$y' = (l\text{-}a)\sin\theta \cong (l-a)\theta \tag{4.3}$$

The total deflection at the tip of the beam is:

$$Y_L = \frac{a^4}{8EI}\,\omega + \frac{a^3(l-a)}{6EI}\,\omega \tag{4.3}$$

The muscle/hydrogel constructs will only provide distributed load between two heights, h_1 and h_2 in Figure 4.5, and therefore the deflection at the tip, δ, can be expressed as the difference between the two loadings:

$$\delta = \frac{(h_1)^4}{8EI}\omega + \frac{{h_1}^3(h_o - h_1)}{6EI}\omega - [\frac{{h_2}^4}{8EI}\omega + \frac{{h_2}^3(h_o - h_2)}{6EI}\omega] \quad (4.5)$$

Which can be simplified to

$$\delta = [{h_1}^3(4h_o - h_1) - {h_2}^3(4h_o - h_2)]\frac{\omega}{24EI} \quad (4.6)$$

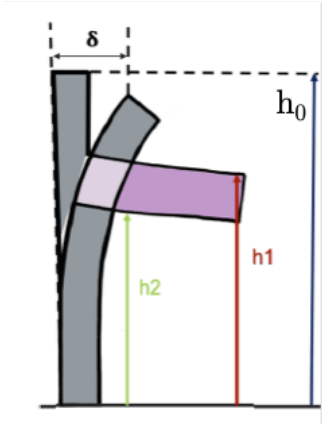

Figure 4.5: Outline of distributed load from muscle hydrogel constructs on posts. The hydrogels will only provide load between two heights, h_1 and h_2, on a beam of total height h_0.

The following assumptions of Euler-Bernoulli theory were met for the analytic model to be valid:

1. The beam is longer in length than its cross sectional area.
2. The beam's cross section remains planar after deformation.
3. Cross-sections that are perpendicular to the neutral axis remain perpendicular after deformation.
4. The material is homogenous, isotropic and linearly elastic.
5. Stresses are within the elastic limit of the material.

4.2.16 Finite Element Model

Euler-beam theory is appropriate for thin beams undergoing small deflections. The analytical expression was compared to an FEM model of a beam using the non-linear simulation function in Solidworks (Solidworks Corps). The beam was a 12 mm high, 1 mm diameter, circular post and a partially distributed load was applied over an area 1mm wide and 1 mm tall. The force applied to the loading area was varied from 0 to 1 mN. This was felt to be the best replication of the loading effect of the *in vitro* hydrogel model on the beam tip. Figure 4.6 outlines the parameters of the finite element model. Figure 4.7 outlines the output of the analytic model.

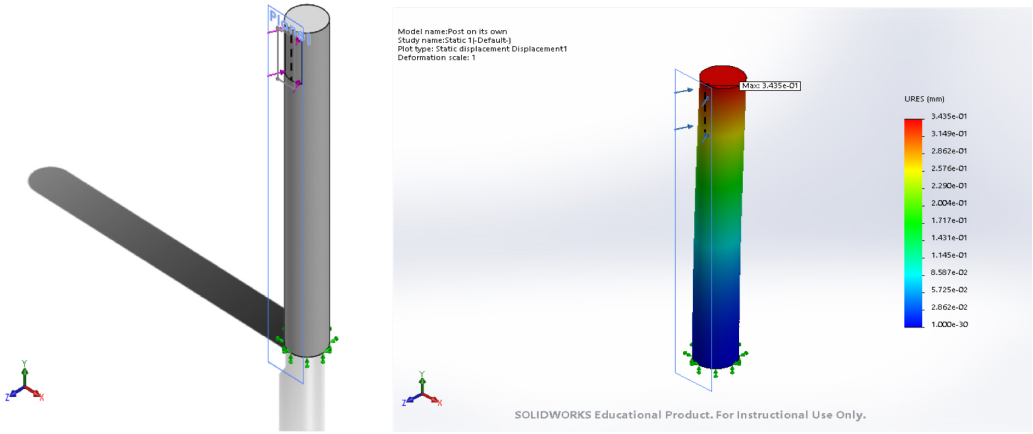

Figure 4.6: **Finite Element Model.** Representative images of Solidworks simulation parameters. The image on the left outlines the 3D model constructed in Solidworks. The image on the right shows the output after a simulation has been run. The color gradient indicates the deflection in mm along the beam due to the force applied uniformly along the black dotted line at the tip, in the direction perpendicular to the direction of the beam (blue arrows).

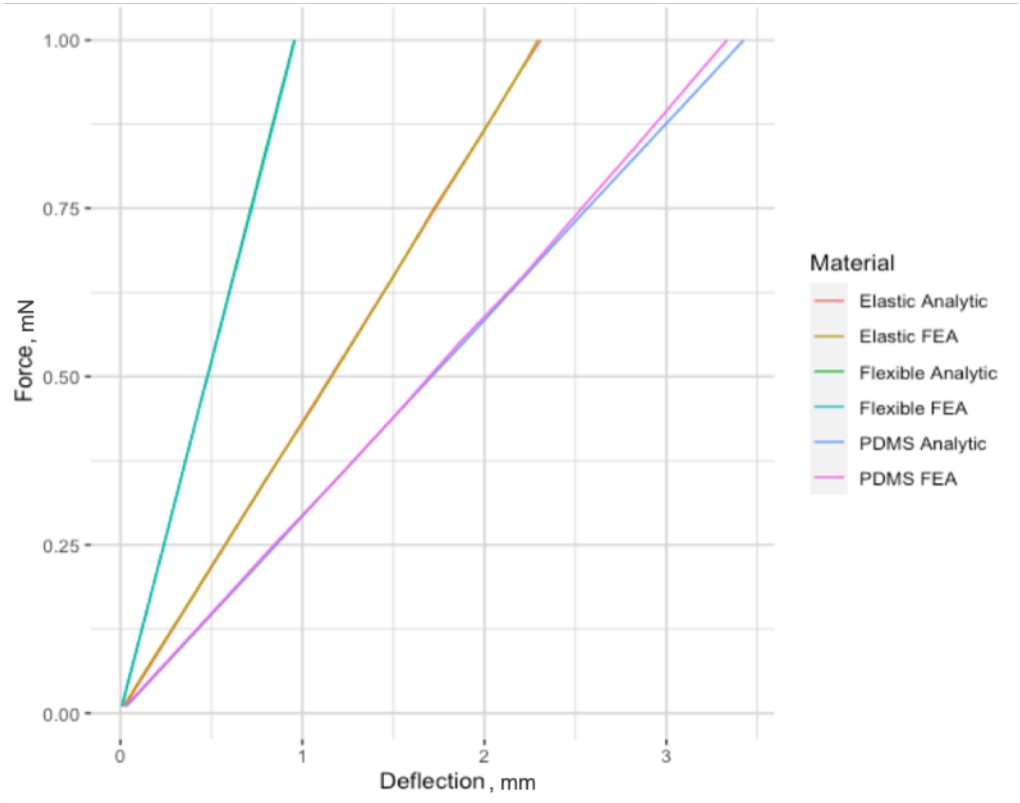

Figure 4.7: Output of analytic model. Comparison of force-deflection prediction from Euler Bernoulli theory and FEA model for 3 different post materials Elastic resin, Flexible resin and PDMS. The curves show good agreement with a small divergence in PDMS posts for deflection ~3 mm.

4.2.187 Hydrogen Peroxide Injury

Hydrogen Peroxide, H_20_2(Sigma Aldrich Ltd,) was purchased and diluted in DMEM to concentrations of 0.1mM, 0.5mM, 1mM, 2.5mM, 5mM and 10mM. Monolayer cultures of C2C12 cells were treated with these increasing concentrations of H_20_2 to evaluate the effect of concentration on cell metabolism and microscopic evidence of cell death.

4.2.17.1 Monolayer Injury

C2C12s were seeded in 96 well plates at 10 000 cells/ well. All conditions were undertaken on a minimum of three replicate wells on three different plates of cells at different passages. Monolayers cells were treated with 0.1mM, 0.5mM, 1mM, 2.5mM, 5mM and 10mM H_2O_2 and cell metabolism assessed every 30 minutes.

4.2.17.1.1 Apoptosis/Necrosis Stain

Effects on cell metabolism were confirmed using an Abcam apoptosis/necrosis staining kit (LOT ab176750). Cells were washed in assay buffer (200μl). Then a stock solution of assay buffer (200μl / well), Apopxin green (early apoptotic cells, 2μl per well), 7-AAH (necrosis or late apoptosis, 1μl per well), CytoCalcein (healthy cells, 1μl per well) was made up and added to wells. After 60 minute incubation at room temperature, wells were visualised using a Celligo plate reader (Nexcelom ltd).

4.2.17.1.2 Bulk Sequencing

Monolayer cultures treated with H_20_2, or untreated controls, were trypsinised and centrifuged into a cell pellet and underwent RNA extraction as previously described.

4.2.17.2 3D Model injury

Differentiated 13 day old hydrogels were exposed to 5 mM of hydrogen peroxide(made up as described) for 4 hours. After injury H_20_2 was aspirated from cultures and replaced with DM.

4.2.17.2.1 Cell Metabolism

Cell metabolism was measured before and after injury and at day 1, 4 and 7 using the Presto Blue™ cell viability reagent as previously described .

4.2.17.2.2 Post Deflection

Post deflection was assessed as previously outlined.

4.2.17.2.3 Bulk Sequencing

Pre and post injury hydrogels were stored in RNA*Later* stabilisation solution for RNA Extraction for sequencing and analysis.

4.3 Results

4.3.1 Skeletal Muscle Model Characterisation

After optimising the constructs, the hydrogels were characterised to demonstrate their capacity to generate functional skeletal muscle. Background information on model optimisation can be found in Chapter 4 Appendix. This was done through quantifying: 1) hydrogel remodelling, 2) demonstrating force generation, 3) image verification and 4) transcriptome analysis with bulk sequencing.

Figure 4.8 shows images of the skeletal muscle model. Figure 4.8(A) shows images of the hydrogel volume taken over time. It shows how the volume decreases as the cells remodel the fibrin matrices and align between the two printed anchor posts. The hydrogel is imaged in the casting mould. To quantify this matrix remodelling, the surface area of the hydrogel was evaluated. Figure 4.8(B) presents a bar graph of hydrogel surface over time. This quantifies the reduction in 2D hydrogel surface area. To see if this effect was due to the fibrin matrix alone, or the cells acting on the matrix, acellular hydrogels were cast and observed in a similar manner. The observation demonstrated that hydrogels remained at the same volume as they were cast (Figure 4.8(A), Day 0) when acellular and demonstrated no remodelling. Hence the cells cast in the matrix were assumed responsible for the matrix remodelling effect. Figure 4.8(C) shows a representative image of a single skeletal muscle hydrogel system. It shows the width of the base as 12.7mm and the capacity for the model to generate passive tension on the flexible resin posts. This characteristic was quantified as a surrogate marker of function.

Figure 4.8(D) shows an image of immunofluorescence staining on a paraffin embedded section of hydrogels after differentiation. It shows fused myotubes (green) with multiple nuclei (blue) that are characteristic of differentiated skeletal muscle.

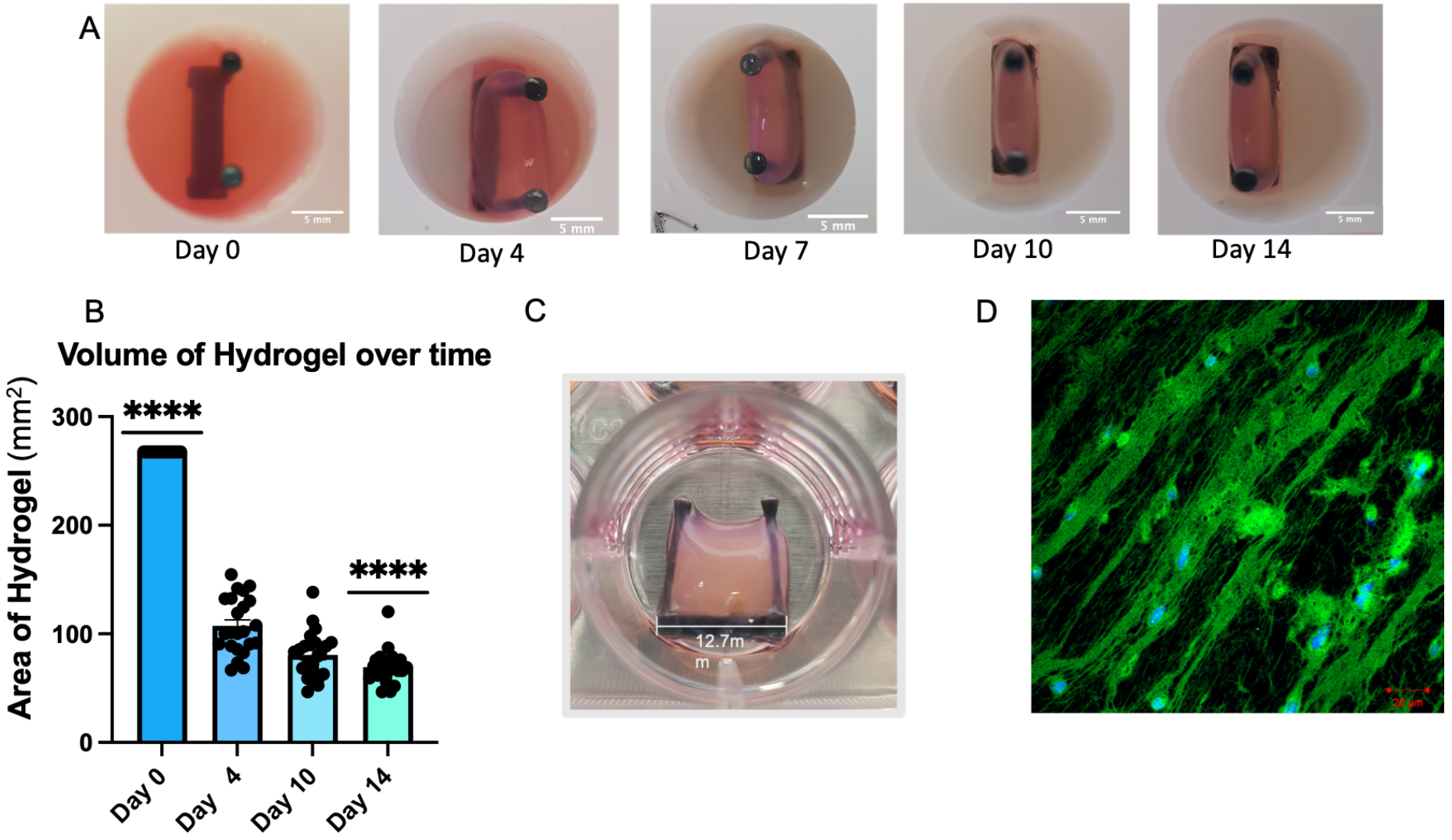

Figure 4.8– Characterisation of 3D in vitro model of Skeletal Muscle. **A.** Images over time of hydrogel remodelling around 3D printed posts. **B.** Graph of hydrogel surface area over time.**** = p<0.0001(two tailed t-test). **C.** Image of individual hydrogel with post deflection. **D.** Representative confocal image of skeletal muscle hydrogel. Stained with F-Actin (Phalloidin) & DAPI.

4.3.2 Functional Characterisation

Figure 4.8(c) shows a side view of the constructs after 14 days of culture. The image demonstrates that the flexible resin anchor posts have deflected. The deflection is a direct marker of force generation by the cell seeded hydrogels.

Fig 4.9 shows the tip-to tip distance of the posts as a function of time. It can be seen at 4 days the distance has decreased from 8mm to 6.6mm and this deflection holds out to 14 days. This indicated that each post has deflected approximately 0.7mm.

Figure 4.10 shows the predicted deflection of the post tip, based on Euler-Bernoulli bending for variations in the heights, h_1 and h_2 of the hydrogel on the flexible post. A minimum hydrogel height was set at 2mm, and a fixed 1mN load was applied. The largest deformation, ~0.9mm, occurred when the hydrogel position as close to the ends of the post. Taking the gels to extend from h_1 = 5mm too h_2 = 10mm, then from Fig 4.10 this corresponds to a tension in the hydrogel of 0.5mN.

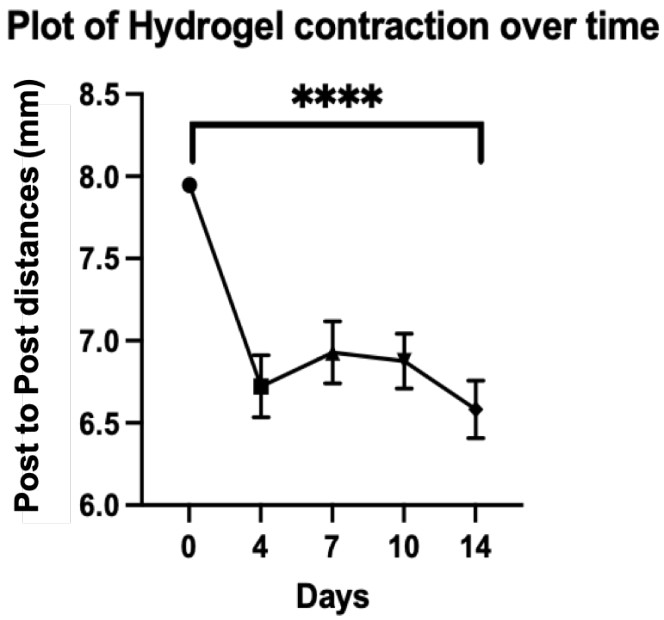

Figure 4.9 –Plot of post to post distance in *in vitro* hydrogels over time. Post to post distance is presented as a surrogate marker of deflection. Two tailed t test. **** = p<0.0001.

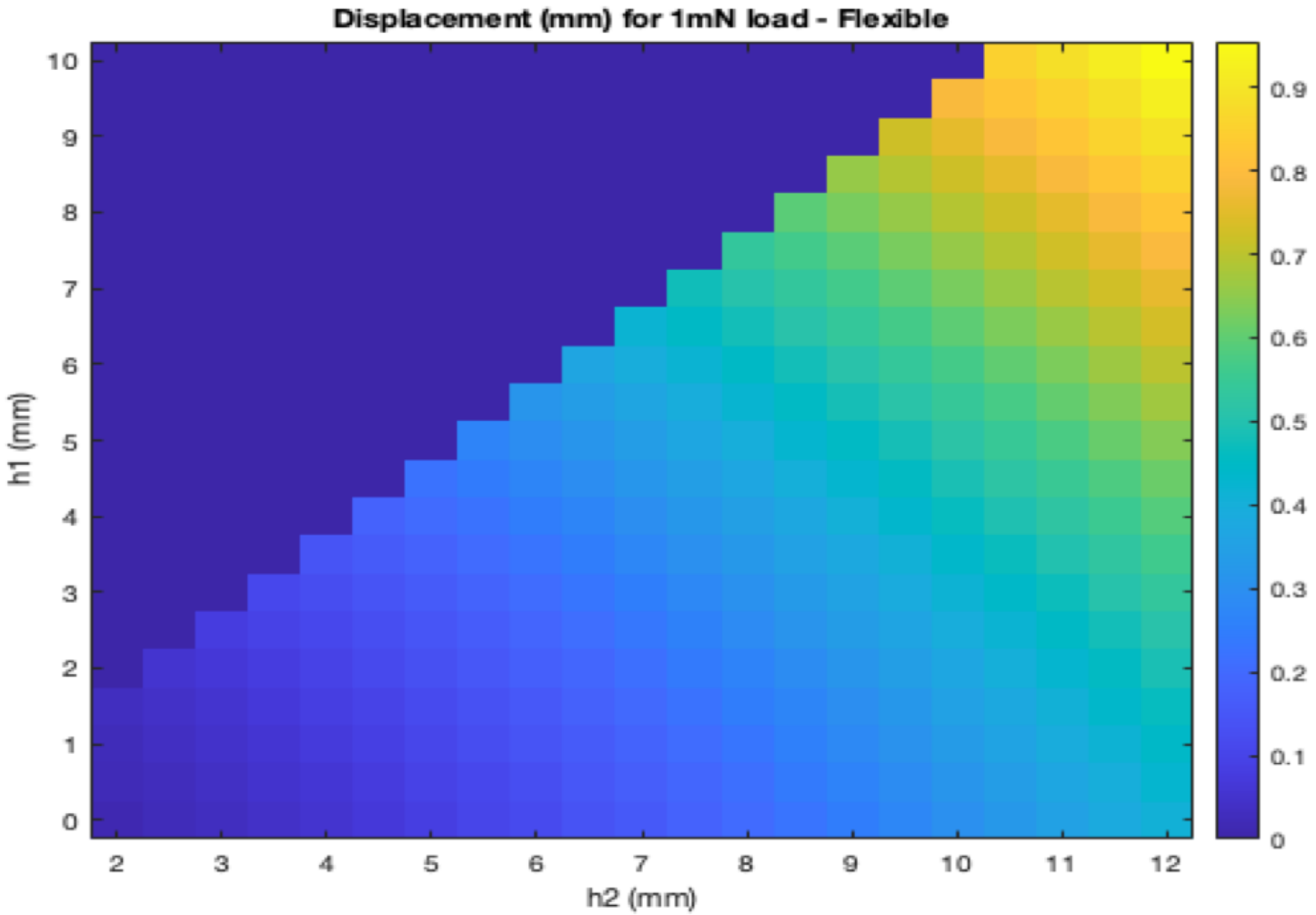

Figure 4.10 –An analytic model was used to estimate the deflection of a partially distributed load of various dimensions along a cantilever beam fixed at one end. h1 and h2 refer to the upper and lower heights/attachments of the hydrogel on the post which is a cantilever beam fixed at the base. The colour gram assigns lighter colours to increasing deflection distances generated by larger hydrogel distances acting on the beam.

4.3.3 Analysis Of Skeletal Muscle Differentiation in 3D cultures

Figure 4.11 shows a heatmap of skeletal muscle differentiation markers that reached statistical significance from bulk RNA sequence analysis. Heatmap of counts, Heatmap of sample to sample distances and principal component analysis for 4 hours day 7 data can be found in Chapter 4 appendices. Constructs were stored for gene expression analysis at day 2, day 7 and day 13 after production and their gene transcription compared to hydrogels that were cultured in growth media alone. The heatmap shows the upregulation in transcription of Myogenin (*Myog*), Myosin Heavy Chain isoforms (*Myh*), Myoblasts protein 1(*Myod*) and the paired box genes (*Pax)*. This can be visually compared to the expression of the endogenous control *Pum*. Pum1 was selected as the endogenous control sequencing data across timepoints (outlined in methods). The full lists of endogenous controls and their expression is found within the chapter 4 appendices. This data correlates with published literature on C2C12 gene expression in differentiation (157). In particular, *Myf5* expression decreases from day 2 to day 13, whilst myosin heavy chain (actin based motor proteins such as *Myh1, Myh3 & Myh2*) expression strengthens. *MyoD* (myoblast determination protein 1) expression, that regulates myogenesis, is notably downregulated at day 2 (during culture in growth media), then increases at Day 7 and 13. A stronger *MyoD* expression was expected. The paired box gene *Pax 7*, a transcription factor in myogenesis, shows upregulation between day 2 and day 13. This data confirms the microscopy observations in figure 4.9(D) and demonstrates the cells were expressing genes consistent with myotube differentiation.

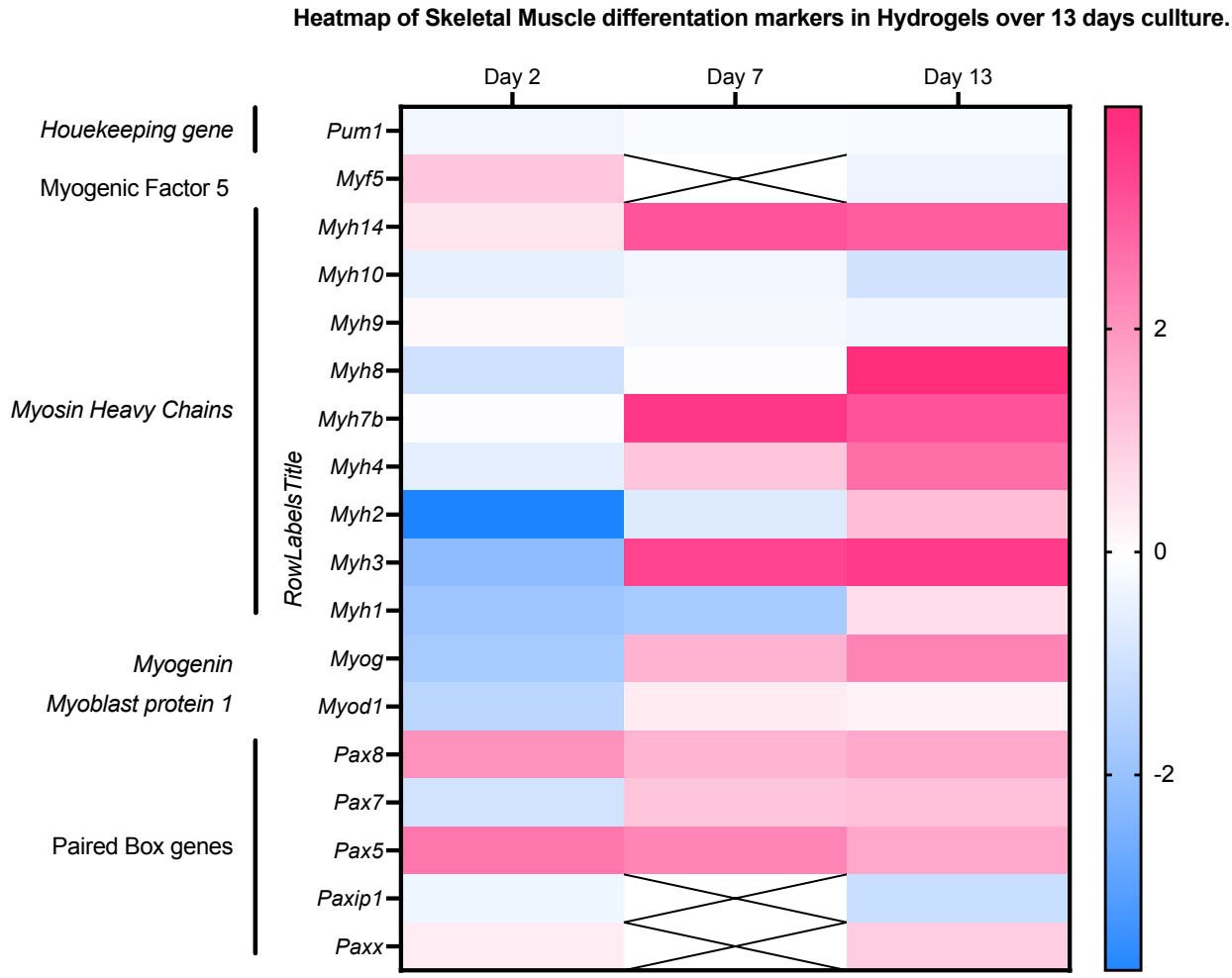

Figure 4.11: Heatmap of log2fold change of genes associated with skeletal muscle differentiation expressed in 3D hydrogels over 13 days of culture. Log2Fold expression is comparing gene expression in differentiated hydrogels to undifferentiated hydrogels. The endogenous control *Pum1* is presented for comparison. The colour bar shows Red infers increased Log2Fold expression, and blue infers decreased log2fold expression. A X or cross in a box means that counts/expression data for this gene was not found at that particular timepoint.

4.3.4 Development of an injury protocol for 3D muscle constructs

4.3.4.1 Analysis of injury after H_2O_2 treatment in monolayers

Figure 4.12 shows a bar graph of cell metabolism after hydrogen peroxide incubation. It presents the percentage change (compared to pre injury) of cell metabolism from monolayer samples at 30 minute intervals after injury. It shows that only 5mM of Hydrogen Peroxide results in a consistent reduction in cell metabolism over 90 minutes.

Figure 4.13 presents representative images taken of C2C12 monolayers after injury with hydrogen peroxide. The image shows that the hydrogen peroxide treatment results in cell death in 2D monolayers. The cells were stained using an apoptosis (green)/necrosis(red) kit to determine which cell death mechanism predominated using the concentration of H_2O_2 adopted. The images were unable to determine which cell death mechanism predominated in the monolayer cultures. To evaluate this further, bulk sequencing of RNA transcription was undertaken on these monolayer cultures.

Figure 4.14 shows genes associated with apoptosis or necrosis that reached statistical significance in the samples. Notably, early growth response 3 *(Egr3)*, a gene that regulates genes involved in biological rhythm, achieved the greatest log fold change within the apoptosis geneset. *Timp3* had the next highest upregulation. *Timp3* is a tissue inhibitor of metalloproteinases whose epigenetic control is critical for manipulation of cell death, growth or angioinvasion. *Gadd45b*, which is downregulated in 2D samples, is a known positive inducer of apoptosis by increasing interaction between *p38* and *Rb* in FAS- induced apoptosis. The downregulation in the 2D samples perhaps indicates that apoptosis was not the mechanism responsible for cell death in H_2O_2 injury. Interestingly, *Nupr1* is downregulated in 2D samples. *Nupr1* downregulation has been implicated in inducing cell death through endoplasmic reticulum stress (158).

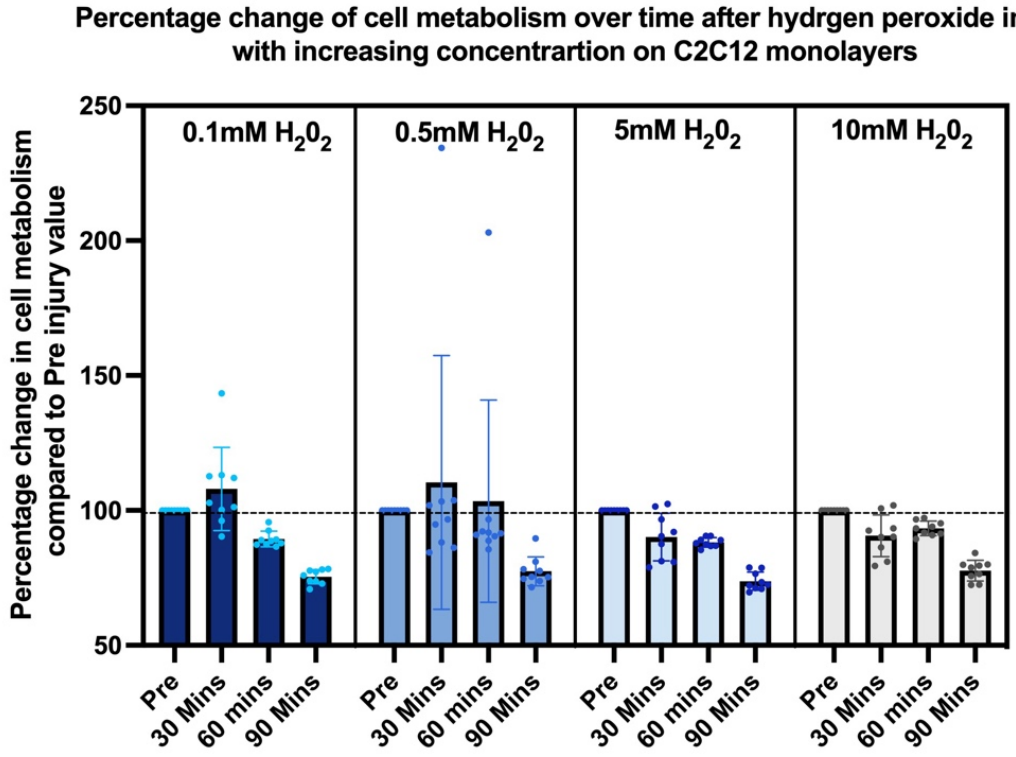

Figure 4.12: Percentage in C2C12 monolayer metabolism after hydrogen peroxide injury for a range of concentrations. A positive control was freezing at -20ºC. Fig 4.13 graph shows changes due to time at 30, 60 and 90 minutes.

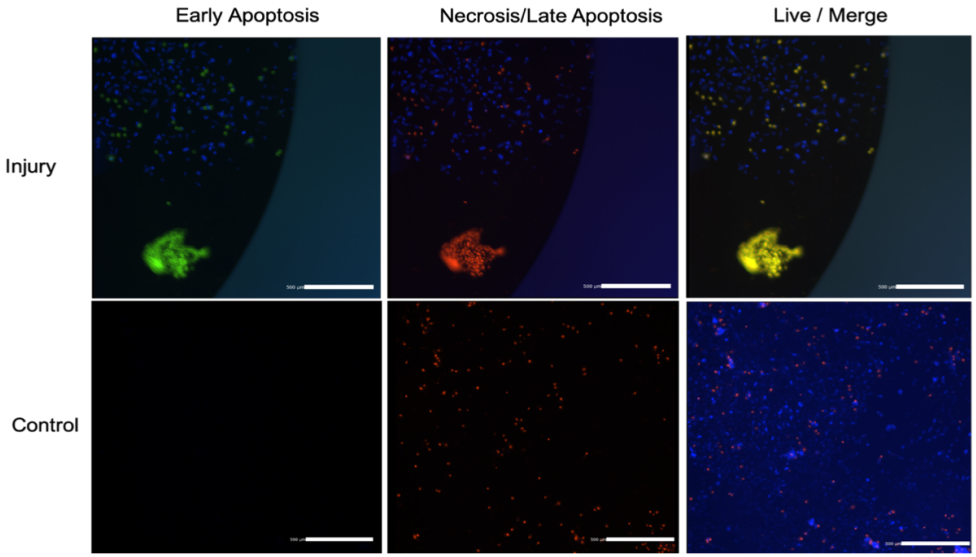

Figure 4.13: Representative images of Apoptosis/Necrosis stain in monolayer cultures after exposure to Hydrogen Peroxide. Culture exposed to 5mM of Hydrogen Peroxide. Scale bar is 500μm.
Blue indicates live cells, Green indicates phosphatidylserine (PS) labelled apoptotic cells. Red indicates cytocalcein labelled necrotic cells.

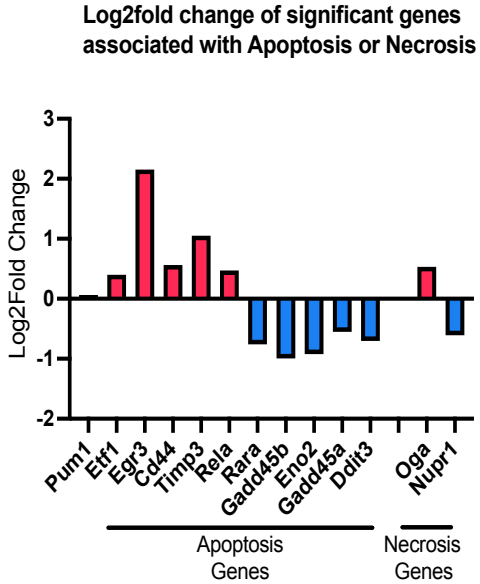

Figure 4.14: Bar chart of genes with significant changes in log 2 fold expression associated with gene sets for apoptosis, necroptosis and necrosis. Monolayer exposed to 5mM of Hydrogen Peroxide, samples stored immediately for RNA extraction.

4.3.4.2 Analysis of H_2O_2 injury in 3D constructs

Based on the findings from the 2D monolayers, H_20_2 injury was likely to provide an injury mechanism in 3D hydrogels. To confirm that the H_20_2 was able to induce an injury in the hydrogels, cell metabolism was assessed after 5mM injury. Figure 4.15 shows the change in cell metabolism over time in 3D constructs using Presto Blue.

To quantify the functional changes after injury, the degree of post deflection was evaluated before and after injury (Figure 4.16). The figure shows that there was no difference compared to the control in the distance between posts as a result of injury. In particular the distance between the posts did not change as a result of the loss of function due to injury. This suggests either the apparatus was not sensitive enough to detect changes or that there were no changes.

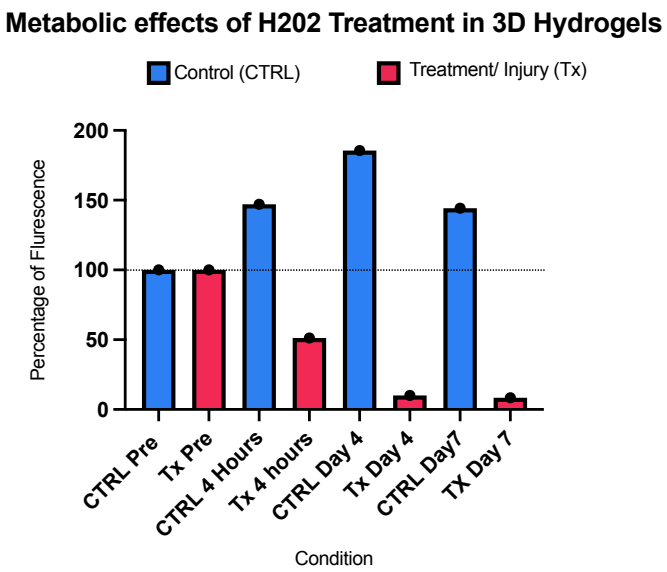

Figure 4.15: Metabolic effects of H_2O_2 treatment in 3D hydrogels. Control hydrogels showed increases in cell metabolism above baseline over time. Treatment (injury) hydrogels showed continued reduction in cell metabolism over time compared.

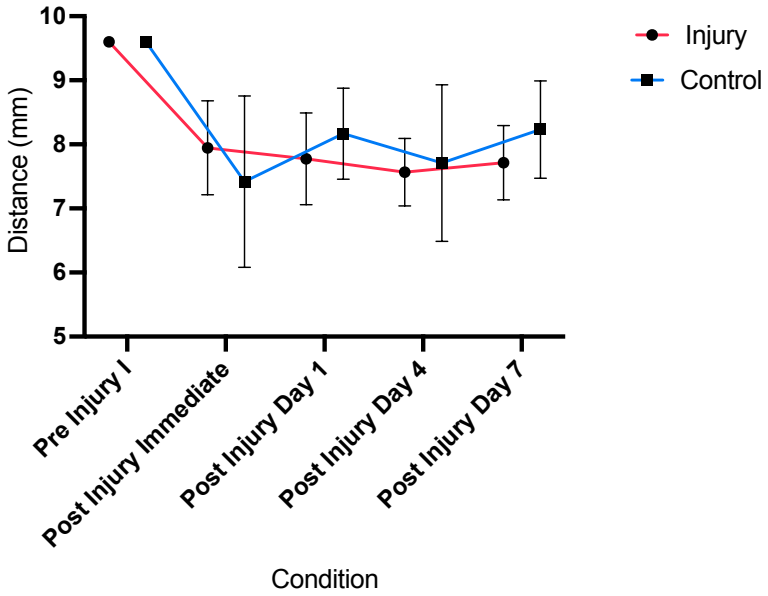

Figure 4.16: Line graph of changes to hydrogel length after exposure of hydrogel to hydrogen peroxide.

4.3.5 Gene Transcription After Hydrogen Peroxide Injury

Gene transcription was evaluated up to seven days after 5mM hydrogen peroxide injury. To evaluate gene expression at each time point, samples were compared to matched controls using the Wald pairwise comparison. Figure 4.17 shows volcano plots of gene expression at 4 hours and day 7. At 4 hours, the majority of genes transcribed that reached statistical significance were upregulated. *Fos*, which regulates cell proliferation and differentiation, was the gene that reached the greatest log fold change and significance. Comparatively, at day 7 the volcano plot shows that gene downregulation predominates. These genes include Ttekt5, involved in cell motility, *Rgcc*, a regulator of cell cycle, *Actc 1*, actin alpha cardiac muscle and *Pde1B*, an enzyme involved second messenger regulation. Those genes that were upregulated were involved in microtubule dynamics, *Mark4,* or chromatin modelling, *Ccnd1* and *Tpsab1* (a beta tryptases released from mast cells).

A gene set enrichment analysis (GSEA) was then applied to the results to evaluate the Molecular Functions (MF), Biological Processes (BP) and Cellular Components (CC) of the genes transcribed. Figure 4.18 present dot plots for the biological processes at two time points (See Appendix for Molecular Function and Cellular component dot plot). The plots show gene ratios for biological pathways with the greatest number of genes found in the datasets. It also shows an adjusted p value calculated for these gene ratios. The plots show that at 4 hours there was activation of immune responses to external stimuli and extracellular matrix organisation. There was also downregulation of RNA modification and processing. Comparatively, at day 7 there was widespread activation of cellular responses to DNA damage, cell division, RNA processing and suppression of skeletal muscle contraction and muscle development.

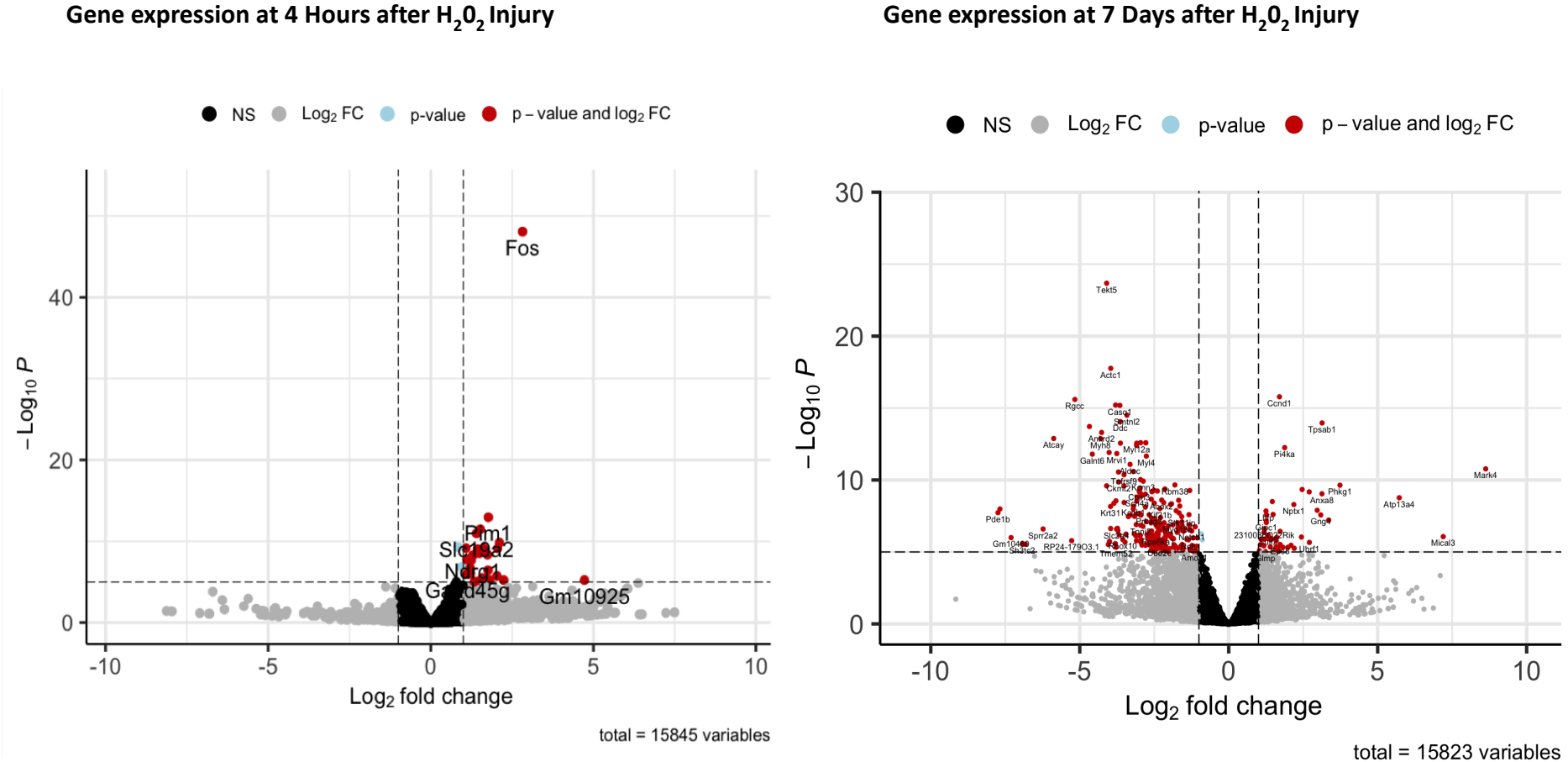

Figure 4.17: Volcano plot of gene expression at timepoints after injury with Hydrogen Peroxide. (a) – Gene expression at 4 hours after injury. The majority of significant genes are upregulated (b) – Gene expression at 7 days after injury. The majority of genes are downregulated. Gene expression significance threshold was set at p<0.05 (dotted vertical lines). Log2Fold expression threshold was set at ±2 (dotted horizontal lines).

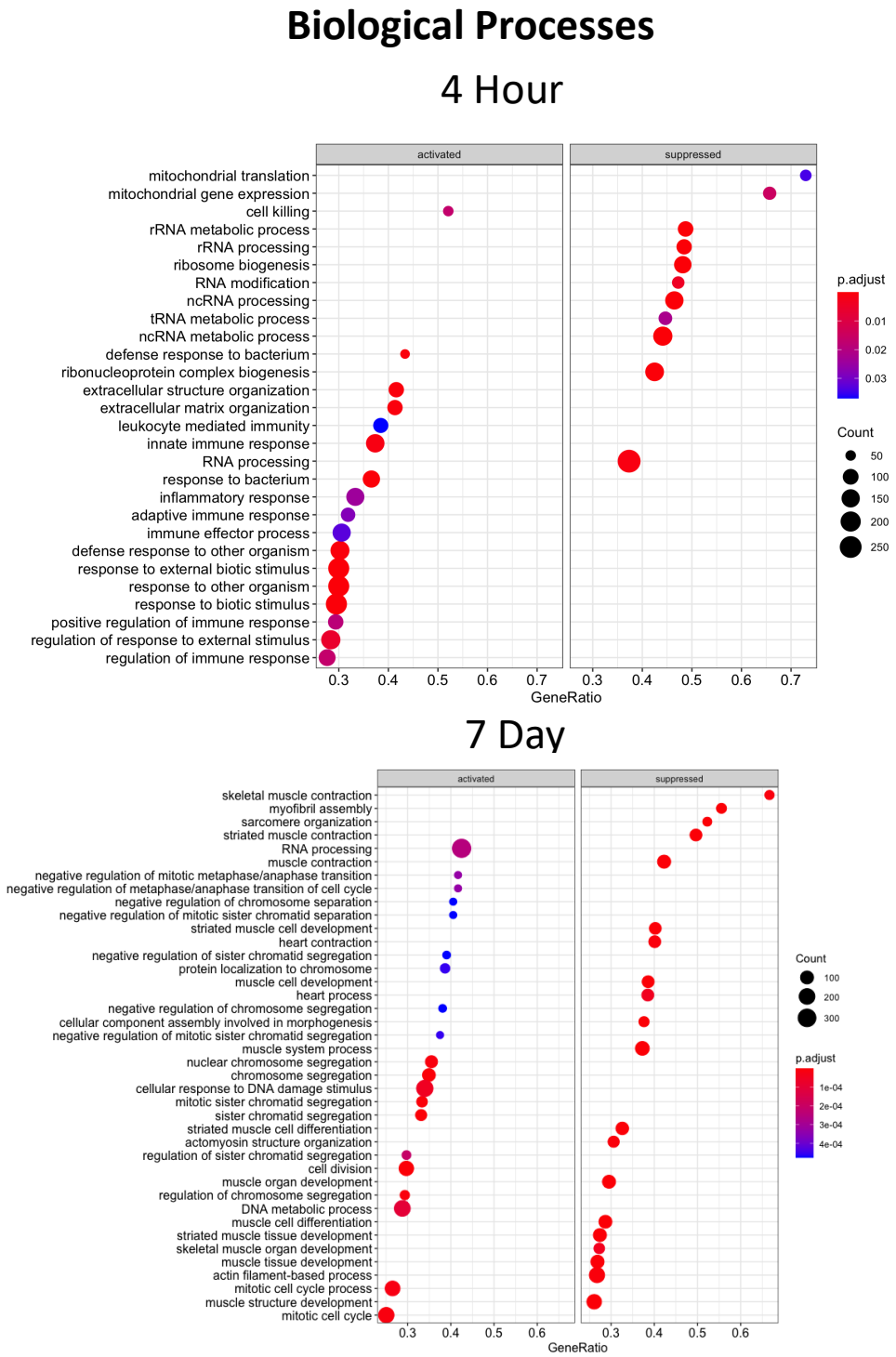

Figure 4.18: Dot plots of activated and suppressed genes associated with biological processes at 4 hours and 7 days after hydrogen peroxide injury. Gene Ratio is the number of genes found in a sample out of the total number of genes in the gene set. The colour bar refers to the adjusted p value which is calculated for each pathway across all samples.

4.3.5.1 Expression Of Genes Associated With Apoptosis, Necroptosis And Necrosis.

Figure 4.19 shows heatmaps of genes involved in a GSEA for necroptosis (4.19A), necrosis (4.19B) and apoptosis (4.19C) that reached significance in the data. It also shows the gene overlap between necroptosis and necrosis gene sets. In particular the data shows an upregulation of *Ripk1,* a potent initiator of necroptosis, alongside *Casp 8* which is believed to be the molecular switch between apoptosis, necroptosis and pyropotosis (159). Of the apoptotic gene set only *F2*, prothrombin, was found to be significantly regulated.

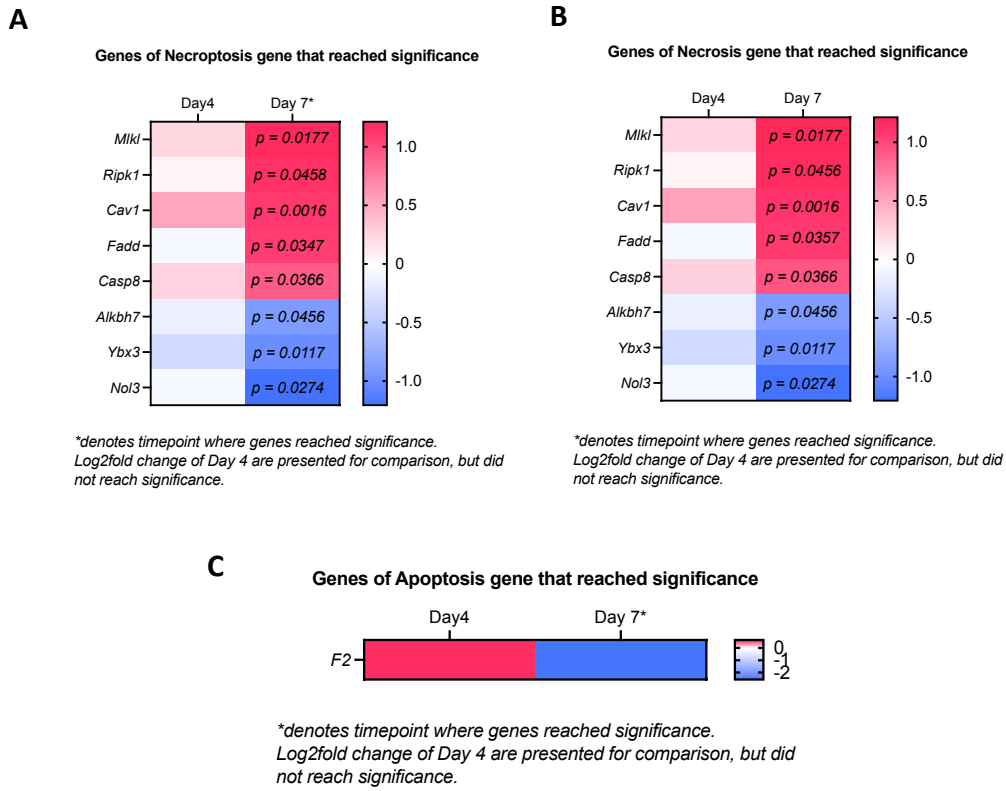

Figure 4.19: Heatmaps of significant changes in log2fold in genes found in cell death. (A) shows genes found in Necroptosis. (B) shows genes found in Necrosis. C) shows the single gene, F2, found in Apoptosis. The Heatmaps show lo2fold change, the p value at Day 7 is presented over the heatmap colour value for log2fold change.

4.3.6 Evaluating Gene Expression Over Time

To appreciate the evolution of gene changes over time, the top 25 significantly expressed genes were reviewed. Table 4.1 and 4.2 show these genes at 4 hours and 7 days. Table 4.1 shows *Nd5*, *Nd6* and *Nd4l* showed a large differential expression. These genes are involved in the respiratory chain and electron transfer. At day 7, the most significant gene was *Tekt5*,log fold change -4.097, that is involved in flagella formation during spermatogensis, Actc1, involved in cardiac muscle contraction, and *Ccnd1* which inactives the *Rb* protein and promotes progression of the cell cycle through the G1-S phase.

To explore these gene changes over time, the list of top 10 significant genes at 4 hours was searched through the 7 day gene list. The change in log2fold expression was then plotted in Figure 4.20 to give an appreciation of gene changes over time.

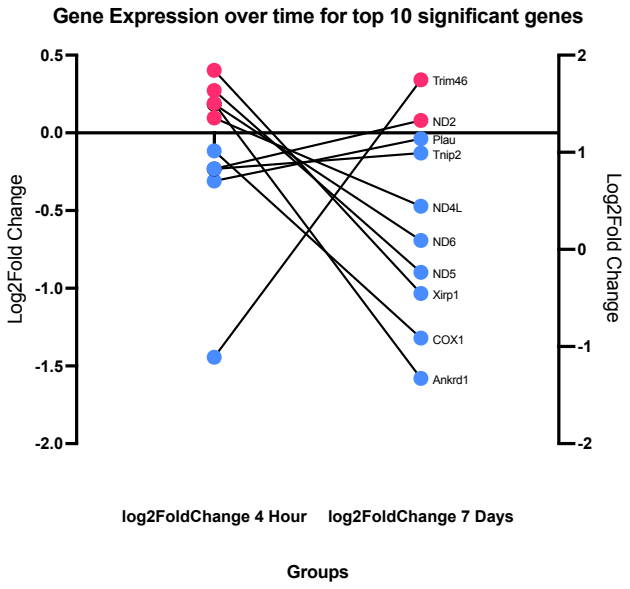

Figure 4.20: Line graph of gene expression for the top 10 significantly expressed genes. The top 10 significant genes at 4 hours and their subsequent expression at 7 hours.

Table 4.1 : Top 10 Significant Genes at 4 hours

SYMBOL	Log2FoldChange	padj	Gene Name
Nd5	1.634	1.77E-21	NADH dehydrogenase subunit 5
Nd6	1.496	1.45E-13	NADH dehydrogenase subunit 6
Nd4l	1.354	7.23E-11	NADH ubiquinone oxidoreductase chain 4L
Trim46	-1.110	5.64E-09	Tripartite motif containing 46
Xirp1	1.844	5.64E-09	Xin Actin binding repeat containing 1
Cox1	1.015	6.01E-08	Cytochrome C oxidase subunit I
Ankrd1	1.502	2.70E-07	Ankyrin Repeat Domain 1
Rbm12	1.546	5.91E-07	RNA Binding motif protein 12
Zfp219	-1.474	1.27E-06	Zinc Finger protein 219
H1f2	1.183	1.27E-06	H1.2 linker histone

Table 4.2 : Top 10 Significant Genes at Day 7

SYMBOL	Log2FoldChange	padj	Gene Name
Tekt5	-4.097	2.94E-20	Tektin 5
Actc1	-3.960	1.22E-14	Actin alpha cardiac muscle 1
Ccnd1	1.702	7.68E-13	Cyclin D1
Rgcc	-5.164	8.79E-13	Regulator of Cell Cycle
Casq1	-3.653	1.52E-12	Calsequestrin 1
Ankrd23	-3.798	1.52E-12	Ankrin Repeat Domain 23
Smtnl2	-3.417	6.20E-12	Smoothelin Like 2
Ddc	-3.640	1.52E-11	Dopa Decarboxylase
Tpsab1	3.134	1.68E-11	Tryptase Alpha/Beta1
Myh7	-4.676	2.67E-11	Myosin Heavy Chain 7

4.3.6.1 Likelihood Ratio Test

To evaluate the effects of time on gene expression, the log2fold expression of the top 10 significant genes was plotted from both timepoints (Figure 4.20). However, this snapshot does not give a broader insight of these genes in relation to cell function. To gain a greater insight on the effect of time on gene expression, a likelihood ratio can be applied to the data and the cluster profiler package applied. Figure 4.21 shows the gene groups identified in the treatment and control groups after use of the LRT test. A p value threshold of 0.01 was applied to the

data. Figure 4.21 shows the data for the control hydrogels. The LRT and cluster profiler revealed that the largest cluster of genes was associated with gene upregulation (group 1 – 235 genes) and downregulation (Group p2 – 217 genes). Figure 4.21 shows these groups in detail and the variation in the groups at each timepoint. In particular, this identifies that the largest gene change takes place between day 4 and 7 in the control group. Figure 4.21 shows the largest group of genes in the treatment group was associated with downregulation (Group 1- 1369), and upregulation (Group 2 – 1281) and up and down regulation over time (Group 3-57). Figure 4.21 shows the largest groups in detail. Compared to the control data, small changes can be observed between the zero and four hour timepoints with larger changes at the four hour to seven day timepoint.

To examine what genes are involved in each of these groups, the gene lists were extracted and plotted as cluster dot plots. The top 50 most significant genes are shown in each cluster. These are presented in the chapter 4 appendices.

The plots show the log10 normalised counts of genes over day 1, day 7 and day 7 and two experimental conditions for the top 50 genes. The top four upregulated genes in the treatment group over time(Figure 4.18) are epoxide hydrolase(*Ephx1)*, Ferritin light chain(*Ftll1)*, adipose differentiation related protein(*Plin2)* and P62(*Sqsttrm1).* The top 4 downregulated genes in the treatment group over time are Aldolase *(Aldoc*), Basigin (*Bsg),* Glyceraldehyde-3-phosphate dehydrogenase *(Gm13394)* and Myosin heavy chain 3 (*Myh3).* GSEA analysis of the LRT treatment results show that these genes affect pathways associated with the suppression of skeletal muscle contraction, structure or sarcomere organisation (chapter 4 appendices). They are also associated with upregulation of nuclear DNA replication or DNA conformational changes. This data potentially suggests that this injury mechanism inflicts more long term damage to the cell population, rather than transient injury which was initially expected.

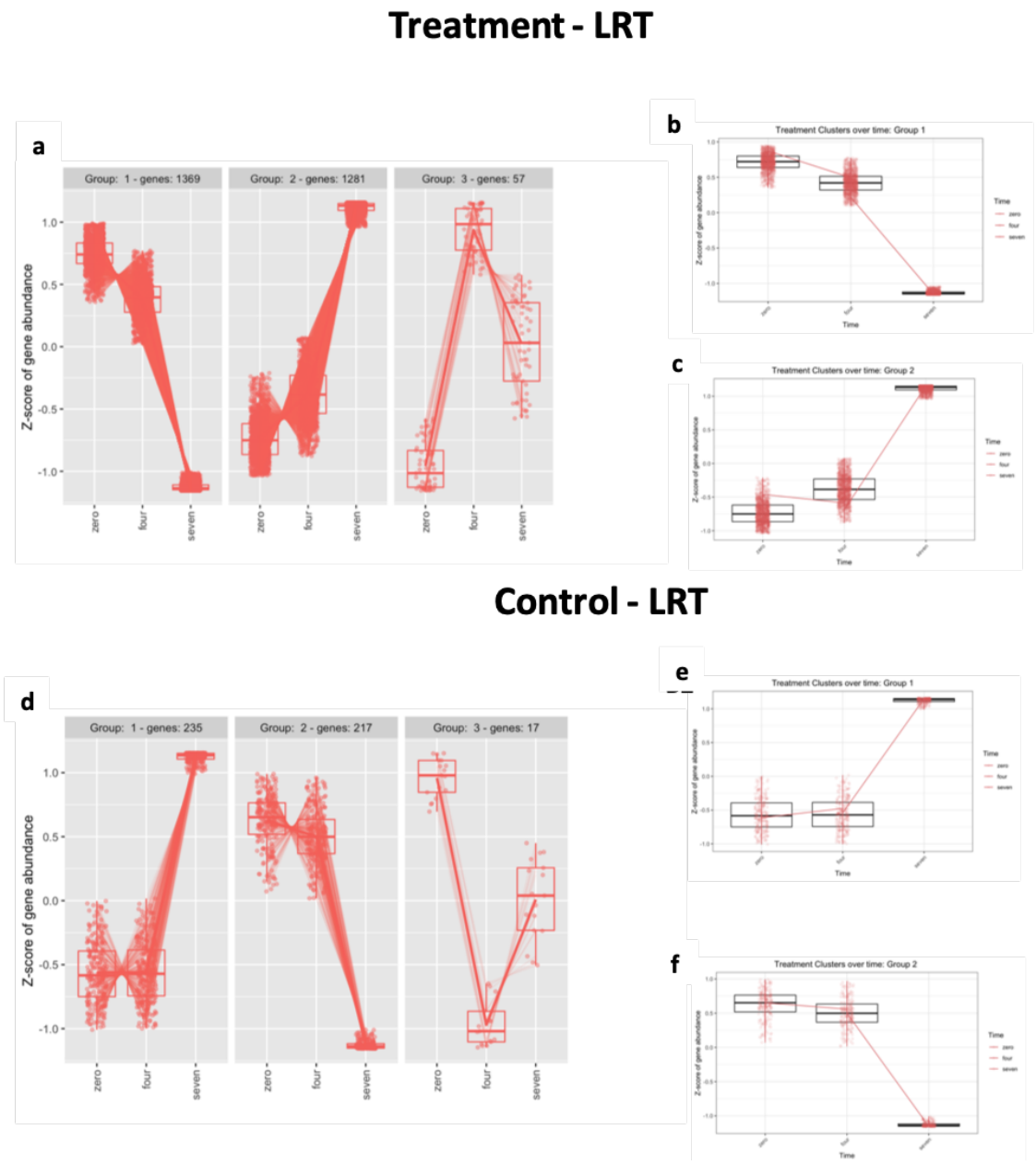

Figure 4.21: Cluster diagrams from liklihood ratio test analysis of injury experimental data.
a. The graph shows the three clusters of genes identified from the LRT data. These clusters show trends of gene changes over time. The clusters are listed frrom the cluster with the largest number of genes to the smaller (Group 1- 1369 – Group 3 – 57).
b & c. The box and whisker plots to the left show the top 2 cluster groups in detail. They identify the width and overlap of the boxes, as well as the spread of the data.
d. Shows LRT cluster data from the control group. The genes in each group are lower than the treatment groups (235 vs 1369).
e & f. presents box and whisker plots of the largest clusters, Group 1 & 2.

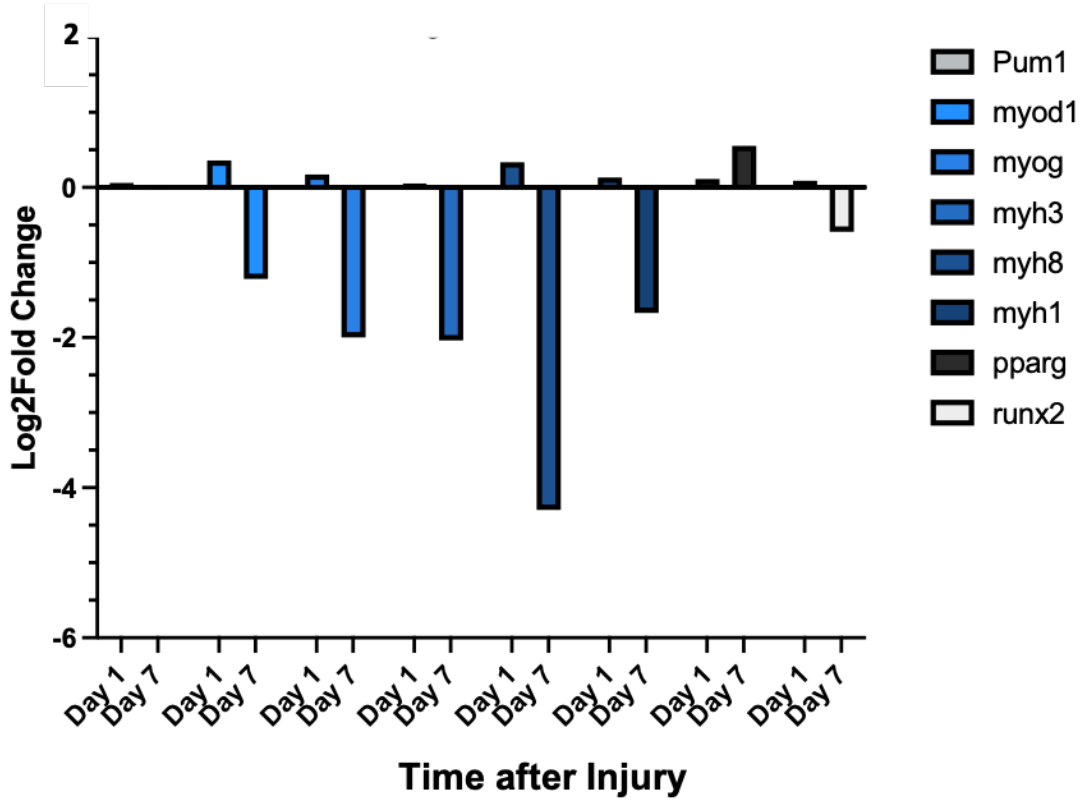

Figure 4.22: Gene changes associated with skeletal muscle regeneration

4.3.7 Regenerative Capacity

Although immortalised cells lack a stem cell niche, the committed myogenic compartment of regeneration can be assessed. Expression of *Myod1* and *Myog* can be evaluated as to whether cells are committed to myogenesis. Figure 4.22 shows the expression of genes associated with myogenesis at day 1 and day 7. The log2fold change of the genes was not significant at either timepoint. The graph shows that all but *pparg* were downregulated 7 days after injury. *Pparg* is associated with adipocyte phenotype commitment. This was corroborated by downregulation of myosin heavy chain.

4.4 Discussion

To study the effects of blast shock wave on skeletal muscle, an *in vitro* three dimensional model was developed to enable utilisation across a range of shock wave modalities. This model was then characterised to demonstrate functional and transcriptional characteristics of native skeletal muscle. Finally, a model of chemical injury was developed as a potential positive control to compare against other mechanisms of injury.

4.4.1 Model Optimisation

The model presented was designed to be utilised across multiple experimental platforms for generating loading conditions similar to explosive scenarios. As outlined in chapter 3, one of the major limitations in current published models of skeletal muscle was their construction and adherence to cell culture plates. This prohibited, or complicated, their use in apparatus that requires sample confinement or a limited sample number. The 3D model was also tested on a Hopkinson bar (data not shown) and it was found to work for that geometry.

Previously models have used manufactured or cast posts made from PDMS (as outlined in Chapter 3). Recent work has generated 3D printed structures for culturing skeletal muscle hydrogels. These approaches have used Fused Deposition Modelling (FDM) techniques for printing. FDM printers do not have the same printing definition when compared to stereolithographic systems. Furthermore, although open source, the designs used were unsuitable for adoption on the scales required for shock wave apparatus. The dimensions were too large for shock wave apparatus, or not for individual handling. Hence a new approach was required. To ensure biocompatibility, ductile resins required coating in PDMS for cell culture use. As an alternative material, the Formlabs Dental SG resin could be used as this resin is biocompatible, but it is also rigid and brittle which made it unsuitable for observing passive tension and deflection.

The 3D skeletal model system described here was use to cast over 700 hydrogels for blast trials.

4.4.2 Model Characterisation

The model presented in this work uses the C2C12 mouse muscle line. As outlined in Chapter 3, models using induced pluripotent stem cells (iPSCs), primary animal or human muscle have already been demonstrated (138, 160, 161). Three dimensional models have also been co-cultured with macrophages and neural cell populations (142, 162). However the majority of published studies have adopted the C2C12 cell line due to its capacity for straightforward large scale culture. The C2C12 line is modified to enable long term survival; however, it lacks some of the advantages of primary cells. These include the genetic variability of cell lines from multiple donors, the breadth of cell populations from differentiation and the capacity for regeneration. Nevertheless, in this application the immortalised cell line is preferable for its capacity for proliferation that is crucial in such a large volume application, which is not achievable with primary or stem cell lines.

Previous models of skeletal muscle have used quantitative polymerase chain reaction (PCR) to evaluate gene expression during myogenic commitment. In this model bulk RNA sequencing was utilised. As bulk sequencing evaluates gene transcripts directly, rather than through an optimised primer, sequencing is believed to be more accurate. Furthermore, it gives a picture of the entire transcriptome, not only a select few genes. The sequencing data enabled the optimum housekeeping gene to be evaluated (see Chapter 4 Appendix), and then the genes associated with skeletal muscle differentiation.

The data presented in Figure 4.11 shows significant log 2 fold change data for genes associated with skeletal muscle differentiation. The heatmap shows that the model achieved a degree of late differentiation. Myosin Heavy chains 8 & 1 have been shown to be associated with a mature cell phenotype. In this 3D model, *Myh 8* had a large log2fold change of 3.98 at

day 13, whilst Myh1 had a smaller log2fold change of 0.66. *Myh 6* (also known as *Mrf 4*) is required to induce skeletal muscle differentiation, and its expression peaked at day 4 (log2fold change 1.5). *Myh6* expression is associated with the transition from early to later differentiation but was not found to be significant in this data.

4.4.3 Functional Characterisation

The functional capacity of *in vitro* models can be assessed by the force the cell construct can generate to deflect the 3D printed posts. Published models have utilised several methods to estimate the force generated by skeletal muscle *in vitro* (163). These techniques include measuring passive contraction by estimating the deflection of a beam (112, 118) or testing active contraction with electrical stimulation(164). In this circumstance, passive contraction refers to the remodelling action of the cells and hydrogels acting together in alignment such as found in wound healing contraction(163). In order to relate beam deflection to the passive force generated by hydrogel and cell contraction it is necessary to accurately define the loading parameters on the beam. One approach adopted has been to define a point load on the beam by calculating a mean distance between heights of the hydrogels attachments on the beam. However, the drawback of this approach is that it may overestimate the force generated. Conversely, another approach has modelled the load uniformly across the beam. This approach underestimates the force created by the hydrogel.

In this model the force generated was estimated by modelling a partially distributed load across the beam. An analytical model was compared to an FE model and shown to be in good agreement. The analytical model was used to generate a calibration map from which measurements of muscle attachment on post deflection could be used to estimate loading by the muscle hydrogel.

However, when post deflection was evaluated after injury with hydrogen peroxide, it was not sensitive enough to observe changes in force. One explanation could be the sensitivity of the experimental set up to evaluate changes in post position. Alternatively, although the chemical

induces cell injury it may not induce structural changes to the myotube that result in changes in force. Finally, the contraction and crosslinking of the remodelled fibrin matrix could prohibit myotube relaxation being measured. Such considerations could not be validated in this experimental work.

4.4.4 Development Of Injury Model

In order to provide contextual data to future blast experimental work, a positive control data set was necessary. Invoking an injury phenotype in skeletal muscle models has been achieved previously using toxins such as animal venom or through chemical injury. The restrictions on importing snake venom to the United Kingdom precluded the use of cardiotoxin as an injury mechanism in this experimental work. This approach is commonly in models published from the United States. Examination of data from chemical injury using Barium Chloride identified it to cause a predominately morphological injury (disruption of myofiber structure) rather than widespread cell death (138). Instead an oxidative injury was felt the most appropriate, utilising hydrogen peroxide. Hydrogen peroxide is known to initiate different cell death mechanism depending on the dose used(165). Previous experimental work at Dstl had demonstrated that at low doses, hydrogen peroxide induced apoptosis, whilst at high doses, hydrogen peroxide induced necrosis. In order to calibrate this for the hydrogel model, the dose and duration of hydrogen peroxide was evaluated in C2C12 monolayers. Then, an identified dose and duration was used to injure the 3D model. To evaluate whether hydrogen peroxide induced an injury, cell metabolism was measured. Figure 4.15 outlined the metabolic changes over time in the 3D model after injury. The data confirms that the hydrogen peroxide induced a significant metabolic injury up to 7 days after injury. This metabolic injury progressed over time and did not recover to baseline.

Compared to published models of cell injury, the approach in this chapter quantifies the model through gene transcription and cell metabolism, rather than through cell morphology or

staining. Furthermore work to quantify any morphological, functional or protein expression changes would give further characterisation of this injury technique.

4.4.5 Bulk Sequencing Shows Changes In Gene Expression At Different Timepoints After Injury

The aim of applying bulk sequencing techniques was to appraise broadly both the individual genes transcribed and the potential pathways enriched after injury. At four hours (Fig 4.17) there are few genes that show significant gene changes. Most notably the *Fos* gene achieves the most significant log fold change. Comparatively at 7 days, a large proportion of significant gene changes are negative log fold changes. These downregulated genes include *actin alpha cardiac muscle* (*ACTC*), the *regulator of cell cycle* (*RGCC*), *Casequestrin* (Casq1) and *dopa decarboxylase* (*Ddc*). These changes in global expression are only at two timepoints, but are consistent with evolution of cellular injury over time. The GSEA of these gene at 4 hours, showed that pathways involved in innate immune response, inflammatory response and cell killing had the greatest gene ratio and adjusted p value. Mitochondrial gene expression, rRNA metabolic processes, rRNA processing and RNA modification were downregulated at four hours. This finding supports what was expected, which would be a cellular responses affiliated with immune responses.

At 7 days, the largest pathway activation was associated with RNA processing, cellular response to DNA damage, cell division and DNA metabolic processes. Pathways involved in skeletal muscle contraction, sarcomere organization and myofibril assembly were strongly downregulated. These findings support expectation of a cell in repair and regeneration. The upregulation of 'response to DNA damage' is particularly interesting, as it implies that the H_20_2 injury has induced long term DNA changes. DNA damage can influence the rates of apoptosis through activation of P53. P53 binds MDM2 to induce cell arrest and apoptosis. In this dataset, genes such as *Bax, Bak* and *Bcl* (which are associated with cytoplasmic induced apoptosis) were not significantly altered. However, *GADD45* a growth and DNA damage inducible gene

that is regulated in response to stressful stimuli, was significantly altered. Whether *Gadd45* has a role in inducing apoptosis is unclear. This will require more detailed characterisation.

The Wald test analysis only evaluates gene changes at single timepoints. The LRT test can estimate the likely effect time, as a condition, has on gene transcription. The cluster profiler library utilised with the LRT data, to demonstrated (Fig 4.21) that the largest clusters (1369) were associated with downregulation and upregulation (1281). There is a large difference in the gene numbers between the treatment and control clusters, perhaps reflecting the effect of the injury on gene transcription. Interestingly, in both groups, the largest changes in gene regulation occurred between 4 hours and 7 days as opposed to immediately after injury.

4.4.6 Programmed Cell Death

To further probe the mechanisms of cell death, monolayers were stained to differentiate between apoptosis and necrosis microscopically. This stain had previously been used in monolayer experimental work on hydrogen peroxide injury at Dstl. However this staining technique was unable to determine which mechanism was induced with the concentrations used. Monolayer sequencing data, Figure 4.14, showed that Nupr1 was downregulated, which could imply that hydrogen peroxide was invoking necrotic cell death. However this data was only captured at an immediate timepoint after injury, and too few of the genes involved in each gene set were significantly altered to make definitive deductions.

The sequencing data in the 3D model gives more clarity. It shows that five genes were significantly upregulated at day 7 (Figure 4.19): *Ripk1*, *Mlkl*, *Fadd* and *Casp 8*. These genes are all implicated in cell death, but through different mechanisms. *Ripk1* can induce necroptosis through necrosome formation and *Mlkl* membrane translocation and disruption. However, *Ripk1* interaction with *caspase 8* initiated an inhibitory process through formation of the *caspase 8* homodimer. This cascade inhibits necroptosis but induces apoptosis. Therefore this gene data could suggest that necroptosis is inhibited for apoptosis. However, the

transcription data alone is not sufficient to discern the predominate mechanism in this experiment (166).

Published models invoking ROS in C2C12 skeletal muscle quantified the damage through intracellular reactive oxygen species intensity, myotube diameter, myosin heavy chain intensity and oxidized DNA damage intensity. Prochniewicz used 1mM of hydrogen peroxide to induce apoptosis(167), which is much less than the 5mM that was needed in this chapter to produce injury at 30 minutes. The authors did not confirm apoptosis through staining, protein or gene evaluation, unlike in this chapter where a geneset enrichment approach was adopted. Nevertheless they did demonstrate significant increase in ROS intensity, oxidised DNA damage and a reduction in myotube diameter. Such characterisation would have been helpful corroboration to the metabolic data presented in this model.

However, the data in this chapter demonstrates the challenges of inducing a defined cell death in skeletal muscle populations. Furthermore, it confirms the overlap between necroptosis and apoptosis as cell death mechanisms and therefore the challenges in isolating either one as a causative factor in tissue loss. Finally, the application of sequencing gives a novel picture of the effects of this injury on skeletal muscle over time.

4.4.7 Skeletal Muscle Regeneration

Published data has evaluated skeletal muscle regeneration by observing specific gene changes. Figure 4.22 shows specific genes as markers of regeneration. C2C12 cells are immortalised cell populations, so only commitment to myogenesis can be evaluated as a marker of regeneration. The data show that predominately genes were downregulated, in particular *Myod1* and *Myog*, gatekeepers for myogenesis, were downregulated at day 7. *Myh 3, Myh 8, Myh 1* were also strongly downregulated. The only unregulated gene at day 7 was *Pparg*, which controls adipocyte phenotypic differentiation amongst skeletal muscle cells. This data indicates that the hypoxic injury from hydrogen peroxide could inhibit skeletal muscle myogenesis as a regenerative mechanism.

4.4.8 Limitations

The aim of this chapter was to design and develop a three dimensional model of skeletal muscle that could be used by multiple platforms to investigate the effects of explosive shock waves on cell signalling and function. The secondary aim was to develop a repeatable method of inflicted damage on the model. The final aim was to attempt to characterise the type of cell death inflicted upon the model during injury as a potential positive control for other experimental work.

There are some experimental limitations to the model proposed. Firstly, the model used sizeable quantities of both the fibrinogen and thrombin/cell mixture, therefore generating relatively large sized hydrogel. Models discussed in chapter 3 use smaller volumes to yield skeletal muscle hydrogels, which facilitates imaging techniques for quantification. The hydrogels outlined in this chapter were larger by comparison and challenging to image. This precluded validation of RNA data with immunofluorescence, to show protein synthesis.

Further to this, the cell death staining may not have been adequately optimised for use in this experiment. The results of this work could not corroborate previous attempts to use this staining kit, perhaps demonstrating that further work would need to be done to optimise this staining technique. This may undermine the sensitivity of the data presented to characterise what cell death mechanism was resulting after hydrogen peroxide injury.

The large cell numbers required for this model resulted in high passage numbers (passage number greater than 16) during culture. Repeated passage of cell populations preferences cells that strongly replicate over those with a preference for myogenic differentiation. This could explain some of the findings with regards to myogenic differentiation markers and their non-significant log fold change.

In this work the functional capacity of the hydrogel was quantified using image analysis of post deflection. Whilst this analysis accurately adopted Euler Bernoulli theory to estimate beam deflection, It was not sensitive enough to evaluate changes in force generation after injury.

Previously published models have employed electrical stimulation to evaluate tetanus, twitch and peak force in equivalent models. The adoption of this technique could have provided valuable validation data for the Euler Bernoulli data. However the development of this protocol was not feasible in the timeframe available.

4.5 Conclusions

This chapter has proposed a novel model of skeletal muscle for probing the cellular effects after blast shock wave exposure. Adopting findings from Chapter 3, the data attempted to quantify both passive hydrogel contraction and gene level properties. Functional assessment data shows that the model demonstrates passive tension over the culture period, whilst imaging confirms signs of myofiber fusion with multiple nucleus. The bulk sequence data showed that after 13 days of culture the model achieved mature differentiation.

In order to characterise the model further, an injury mechanism was selected in order to generate a picture of gene transcription and functional capacity. Metabolic assessment showed that the model failed to recover back to baseline after injury. Whilst no predominate cell death mechanism could be observed, gene changes indicated that cell death could be activated through the RIPK1 mechanism. Finally, bulk sequencing data characterised the pathway enrichment both immediately and 7 days after injury.

This characterisation work should provide a useful positive control dataset to compare with future blast data. Future work should employ this model in an environment capable of generating an appropriate shock wave.

5

Development Of A Frustum Pyramidal Shock Tube For Cell Culture.

5.1 Introduction

The best means of testing cells for primary blast injury is to use live explosives of an appropriate size and repeatability. This is the most mechanobiologically relevant stimulus. However, utilising such live explosive firing to load cell culture comes with significant costs and practical difficulties to ensure experimental precision. Furthermore, the influence of cell culture conditions on *in vitro* systems may play a major role in obfuscating the interpretation of results taken from such explosive experiments. As described in Chapter 1, alternative means such as cylindrical gas driven shock tubes have prevailed. Conical shaped tubes are an alternative approach to employing explosive conditions that are well established in nuclear testing. Conical tubes have the advantage of allowing smaller quantities of explosive to be utilised to recreate larger scale explosive events. This platform is based on the premise that the cone shape, with its apex at the origin of the blast source encapsulates a sample volume of the full blast environment of interest. Although applied to replicate nuclear sized explosions, such a system has not been applied to load cell culture or *in vivo* samples, with combat relevant explosive charges.

This chapter outlines the design and development of a frustum shock tube (the rectangular cross sectional equivalent of a cone). It also describes the design and development of a tissue culture apparatus for use in this tube. This chapter outlines the limitations of a prototype tube and describes the repeatability of the measured output.

The shock tube presented in this chapter was designed by Dr Andy Sedman, Injury Modeller at Dstl, and built by the engineering team at Dstl. The work described herein summarises work undertaken with Dr Sedman, Dr Spear and wider team at Dstl to characterise the tube for use with the subsequent *in vitro* model.

5.1.1 Review Of Blast Parameters And Other Shock Tubes

This work seeks to examine the cellular signalling within skeletal muscle (such as in the lower extremity) exposed to relevant airborne shock wave. As discussed in Chapter 1, this work considers shock waves that may be experienced by a soldier outside the fireball (the mid field), or immediate detonation, of the type of buried improvised explosive device (IED) encountered by infantry patrols on Operation Herrick (the name for UK military operations in Afghanistan 2004-2016). Through discussion with injury modellers at Dstl, a suitable blast source was considered to be a hemispherical surface burst of 4 kg TNT at 2 metres.

5.1.2 Improvised Explosive Device

An improvised explosive device (IED) is a homemade or makeshift explosive device that generally contains four main components; a power supply, a switch or trigger, an initiator, and an explosive. The term IED covers a range of device sizes from small packages to vehicle borne devices (VBIED). Table 5.1 outlines the estimated explosive weight of different IED devices. The explosive equivalent to our blast source is a FedEx package.

Device Description	Explosive Capacity (kg)
Letter	0.5 kg (1lb)
Pipe bomb	2 kg (5lb)
FedEx package	5 kg (10lb)
Vest/container bomb	9 kg (20llb)
Parcel package	22 kg (50lb)
Compact car	226 kg (500lb)

Table 5.1 (Adapted from US homeland security document (168, 169)). The explosive capacity is expressed at TNT equivalence. TNT equivalence is a method of expressive energy released in an explosion. A ton of TNT is the unit of energy defined as 4.184 gigajoules, the energy released in the detonation of a metric ton (1000 kg) of TNT. Therefore each gram of TNT detonated, 5.184 kilojoules of energy are released.

5.1.3 Existing Shock Tubes

A variety of gas and explosive driven shock tubes have been detailed in the literature. A selection of these are outlined in Table 5.2. Figure 5.1 shows the peak overpressure and duration data from these publications plotted on representative Bowen lethality curves for a 70 kg human (170, 171). The table also provides the equivalent explosive charge stand-off distances. The expression of blast equivalence between each published tube differs making biological comparisons difficult. Designing a custom explosive system for cell culture will allow comparison of cellular data between different *in vitro* systems.

Table 5.2: Literature shock tube data

Author	Stated IED/Blast Equivalence	Stand off	Peak Overpressure	Duration	Ref
Panzer	*105/155mm Artillery Round*	1-5m	*50-1000kPa*	2-6ms	(44)
Wood	*7.5kg*	Not stated	*Not stated*	Not stated	(172)
Shridharani	*50g TNT equivalent*	7-10m	*11-760kPa*	1.3-6.9ms	(36)
Varas	*Shock tube*	Not stated	*10-200kPa*	4-10ms, 6ms	(173)
Nyein	*Simulation of 3.16g TNT*	0.12m	*1013kPa*	Not stated	(174)
Moss	*2.2kg TNT*	Not stated	*212kPa*	2.3ms	(175)
Sundaramurthy	*C4 1-100kg – 2.56kg, 7.68kg, 1408kg & 96kg TNT*	5.18m 5m 5.7m 8.5m	*60-450kPa*	2-8ms	(176)
Goldstein	*5.8kg TNT*	5.5m	*77kPa*	4.8±0.1ms	(40)

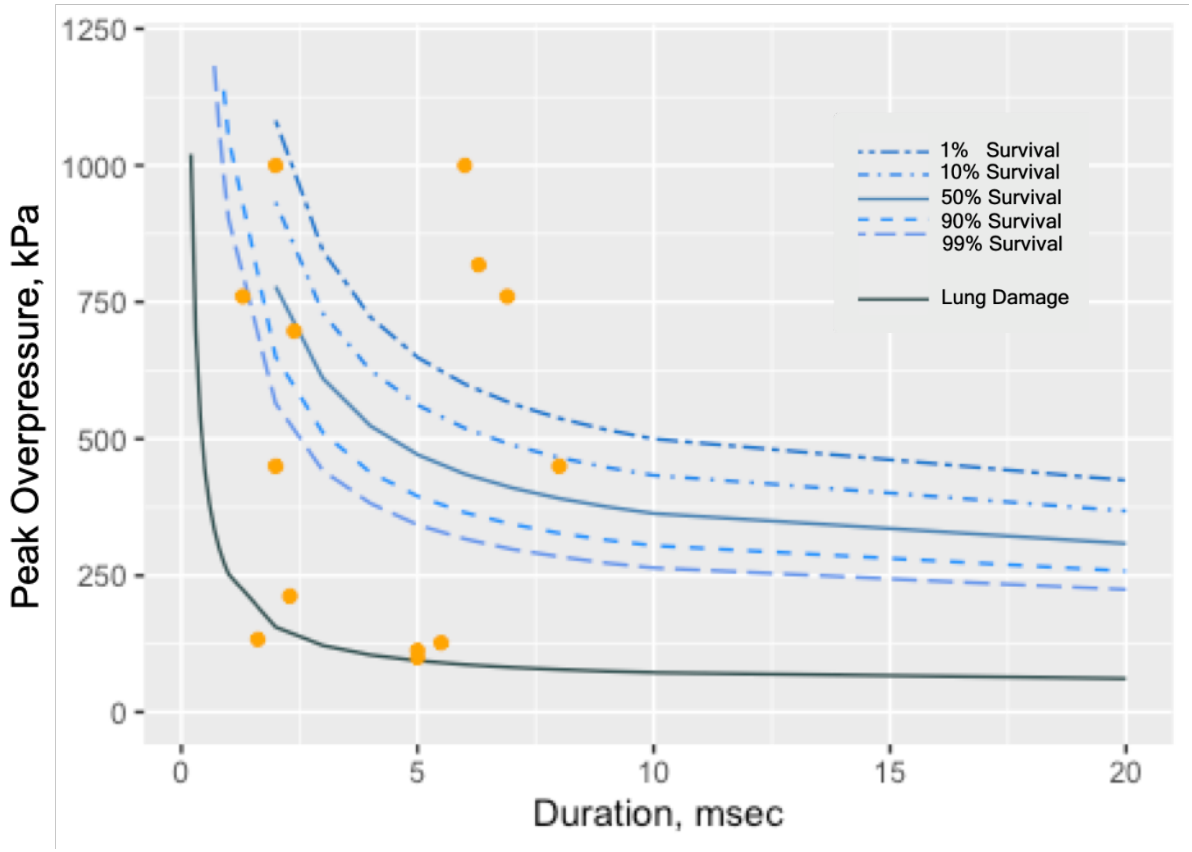

Figure 5.1: Literature shock tube data (duration and peak overpressure) overlaid on Bowen Curves of lethality. The Bowen lethality curves are plotted for a 70kg human. The curves shows the survival and lung damage thresholds. The peak overpressure and duration of literature data presented in Table 5.2 are then plotted on the Bowen curves (yellow dots). Each overpressure is plotted with a minimum and maximum duration. The data demonstrates the variability in published literature values of explosive conditions. It also highlights the breadth of injury resulting from these conditions (lung damage through to 1% survival).

5.2 Considerations For Design Of A Conical Shock Tube

5.2.1 Target Size

When conducting trials using whole animals to represent people the difference in target size in relation to the blast wave needs to be considered (Bowen et al (170, 171) do this via mass scaling). Through mass scaling the blast wave for a smaller animal has a shorter duration. This issue was considered within the current study, as it effectively transforms the real-world blast loading into the equivalent that should be used in the experimental platform. However, as the target used in the current study is unscaled (at the cellular level) such scaling was

considered less important, as long as the overall target (that containing the cells) was also of a representative size (or aspect ratio) to the tissue or body part that contains such cells. For this, and practical reasons, the target was based on a standard 24 well cell culture plate containing 3D models. Defining this target size informed the design of the shock tube, as via the desired blockage ratio, it determines the cross sectional area at the target location.

5.2.2 Frustum Geometry

In this case the conceptual conical shock tube encapsulates a sample of a hemispherical surface (HSB). The theoretical charge ratio expresses the quantity of explosive in the HSB, 4 kg in this case, compared to that contained in the cone. The quantity of explosive within the cone is determined by the cone angle, the wider the cone the more explosive it will contain. In the extreme, a cone angle of 180° would represent a flat surface and contain all 4 kg. An alternative way to consider the theoretical charge ratio, is to consider the ratio of the areas of the shock front for the full and in-cone blasts (177). This is expressed in terms of the charge ratio, CR:

$$CR = \frac{\mathrm{A}}{A_s} = \frac{2\pi r^2}{A_s} \qquad (5.2)$$

Where,

A is the area for a hemisphere at a distance *r* from the centre of the charge and

A_s is the area of the conical shock tube at the same distance *r* from the apex of the cone.

In order to use the smallest mass of explosive, it is preferable to have as small an area as possible.

5.2.3 Calculation of Blockage Ratio (BR):

The Blockage ratio refers to the proportion of the cross sectional area of the tube that is taken up by the target.

$$BR = \frac{A_S}{A_T} \quad (5.1)$$

$A_s - refers\ to\ the\ cross\ sectional\ area\ of\ the\ tube\ at\ distance\ r\ from\ the\ source.$

$A_T - refers\ to\ the\ cross\ secional\ area\ of\ the\ target$

To reduce secondary wave effects on the incident wave and subsequent extra loading on the target (including that due to flow), an optimal blockage ratio of less than 10% has been suggested(178). This value, combined with the 2 m distance from the suitable blast source defines the change in cone area along its length and the cone angle. Table 5.4 shows the parameters of the tube.

Table 5.4: Parameters Of Tube.

Cone Angle	Blockage Ratio	Charge ratio	Output aperture dimension
11.41°	10%	1:201	1020 x 1020 mm

5.2.4 Cross Sectional Shape

Although the term cone has been used thus far to describe the conceptual design of the shock tube, theoretically the cross section is not limited to a circle. For ease and cost of manufacture and the ability to include viewing windows for high speed filming, a square cross section was selected, as shown schematically in Figure 5.2 and Table 5.3, which makes the tube a frustum.

Table 5.3: Design considerations of shock tube

Key design decisions	Main influence(s) on decision	Decision
Blast characteristics Upper bound blast characteristics, expressed in terms of charge size and distance	Representable loading to Herrick scenario (2 metre, outside fireball). Full body exposure lethality taken as upper limit	Hemispherical burst – 4kg TNT at 2 metres
Target size	Desire to use standard cell culture plate. Some allowance for mounting Will limit cross sectional area of tube and therefore target size based on blockage ratio. So only for cell culture facilities	Standard culture plate – 127mm x 84mm
Blockage ratio (percentage of cross-section taken by target)	Set at 10% to reduce distortion of shock wave	10% of total output cross sectional area
Cross sectional shape	Capability for shadowgraph thus desire for windows to enable filming of target under load. Material costs and ease of manufacture	Square/Rectangle shape
Post target length	Desire to delay arrival of end wave effects at target until after positive phase completed.	Determined by spreadsheet
Tube Material	Cost – Materials and construction of prototype model	Wood

5.2.5 Tube Design Downstream Of The Target

The shock tube is considered to encapsulate a sample of the full blast environment which is only valid until the shock reaches the end of the tube. At that point the lack of restraining walls alters shock wave behaviour, and an “end wave” or “rarefaction wave” reflects from the opening and travels back towards the apex of the cone as an under pressure. To mitigate the interference of this wave with the desired pressure loading the shock tube was extended downstream of the target. The length of that extension was determined from estimates of the travel time of the initial shock to the output aperture and for the (acoustic) end wave to travel to the target. The length was selected such that the end wave arrives after the positive loading has ended. The theoretical length was moderated by practical and financial constraints. While there was an intent to develop an end wave eliminator that was not practical within he scope of this research activity.

5.2.6 Truncation Of The Tube

While the theoretical conical shock tube has the charge at the apex, for practical reasons the cone was truncated. The explosive was contained in a frangible breech block, which was renewed for each firing, so avoiding the issues of deformation even within massive breech blocks. The division between this disposable breech and the reusable sections of the tube was provided by a 25 mm steel plate at the point where the walls of the tube were 100 mm high; the plate hole of 100 mm diameter (coaxial with the shock tube) was able to accept the locating collar of the breech blocks.

5.3 Shock Tube Construction

Figures 5.3 & 5.4 show images of the frustum shaped shock tube constructed at Dstl. The steel plate, visible on the left of figure 5.3, where the breech would be attached, projects beyond the edges of the tube and forms the initial section of the tube. It also offers some additional protection to it and the instrumentation used. The main body of the tube was constructed from plywood. A plate that helps to clamp these materials together is also visible between the breech end and the viewing window.

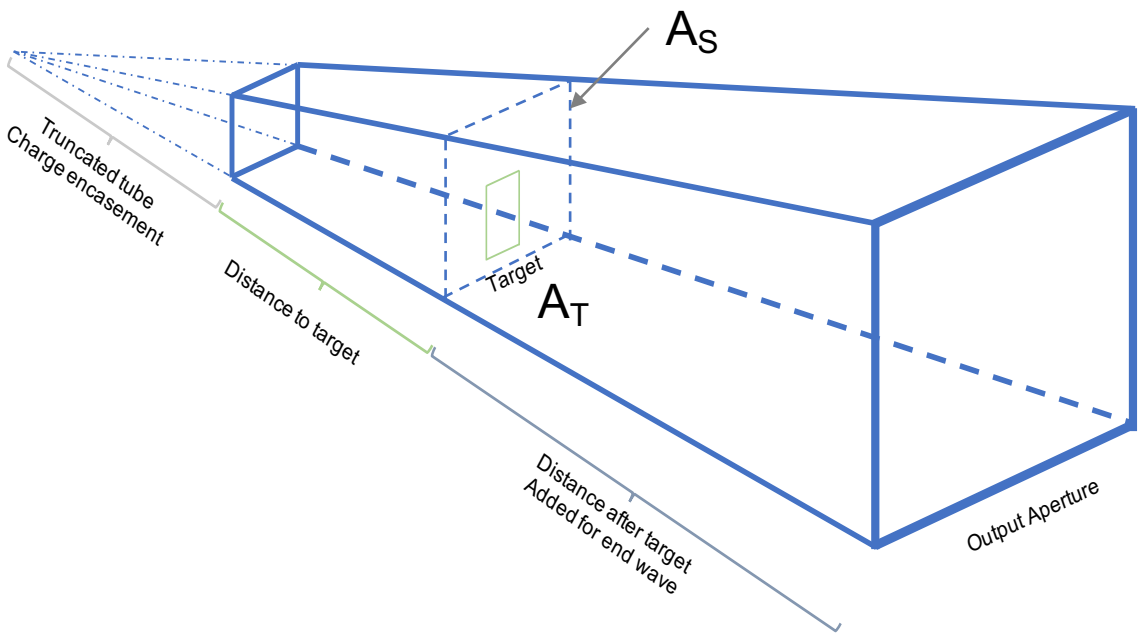

Figure 5.2 Schematic of the shock tube. The shock tube encapsulates a portion of a hemispherical surface burst (HSB). The designated HSB charge size and stand-off distance inform the tube design including the position of the target within the tube ('distance to target'). Along with the target distance, the target dimensions and the blockage ratio govern the cross sectional area of the tube along its length. A_T refers to the area of the target. A_S is the area of the conical shock tube at the same distance from the apex of the cone as the target. The change in surface area along the length of tube to the apex is referred to as the cone angle.



Figure 5.3: Representative image of shock tube with sample arm inserted. The steel plate can be seen on the left of the image at **A**. The plate that clamps the tube components together can be seen at **B**. The side window is shown at **C**. **D** (left of image) labels the sample arm.



Figure 5.4 Pictures of Shock tube during Trials. A labels the target arm. **B** shows the pencil gauges mounted on the end of the target arm. The target arm is taken out of the tube to change mountings on its end. The arm is pushed into the tube so that the target is appropriately distanced from the blast apex.

5.3.1 Gauges

5.3.1.1 Shock Tube Mounted Gauges

The shock tube had five PCB gauges (Model 102B06), flush mounted in its roof. These gauges have a range of up to 3.45MPa (500psi) and a resonant frequency of >500kHz. The key gauges were a pair of gauges mounted above the front of the cell plate (or other target), 2.00 m from the theoretical apex of the shock tube and 45 mm either side of the roof centre line (gauge 2 & 3). Additional gauges were located on the roof centreline 0.5m up and down stream of this pair (gauge 1 & 4) and one near the mouth of the tube (gauge 5). Figure 5.5 shows the positions of gauges mounted within the tube. Gauge 6 & 7 refer to the pencil gauges above and below the target mounted as demonstrated in Figure 5.5.

a.

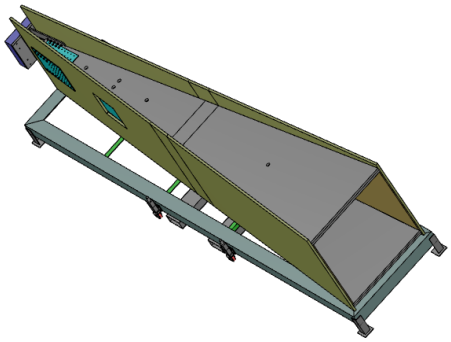

b.

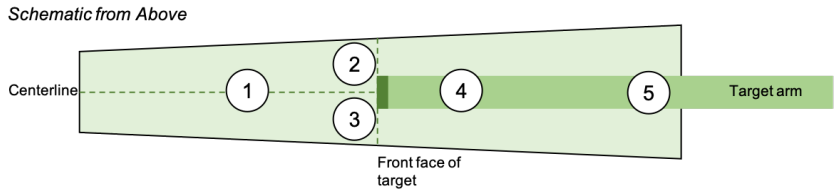

c.

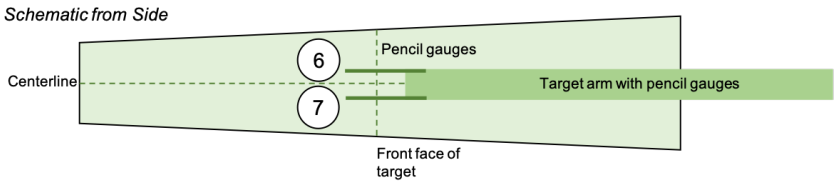

Figure 5.5: Location of mounted gauges within shock tube.
a. Top image show an oblique 3D schematic of the tube with the holes for the gauges in the roof. Image produced by Dstl.
b. Schematic from above, of the position of the gauges on the roof of the tube.
c. The image shows the position of the pencil gauges on the target arm within the tube (the sensors were positioned to be 2.00 m from the apex. Gauges 2 & 3, in the roof, were aligned with the target face within the tube. Pencil gauge sensors (Gauge 6 & 7) were placed under and over the target. The pencil gauge sensors are part way down the pencil gauge length. Schematics reproduced from Dstl.

5.3.1.2 Target Arm Mounted Gauges

Target mounted gauge measurements could not be conducted during firings in which a cell culture plate was loaded within the tube. The target mounted gauge was installed instead of a tissue culture plate within the tube. Figure 5.6 details the position of gauges on the target mounted pressure plate.

The incident pressure within the test volume was monitored using two pencil gauges (PCB type 137A22) attached to the target arm in place of the cell plate. The sensors on these gauges are on one side of the probe and were positioned so that they were 2.00m from the theoretical apex of the shock tube, with the gauges being one above the other.

In separate firings, pressures at the face of the target were measured with four pressure gauges mounted in a model of the cell plate. These gauges recorded the pressure loading on the front exposed face of the model plate (PCB type 102B06 or type 102B, the latter having a range up to 34.5MPa). The gauge adapted model plate was the same size as the cell plate, and the gauges were flush mounted at well locations. Two gauges were at peripheral well locations (14 mm from the closest edge) and two at more central locations (33 mm from the closest edge).

All gauges were used with signal conditioners (PCB type 482A22), the output of which was recorded at a rate of 3 MHz for 0.5 s; this included 25 ms before the trigger signal (from a fibre optic positioned within the breech to detect the flash from the detonation)

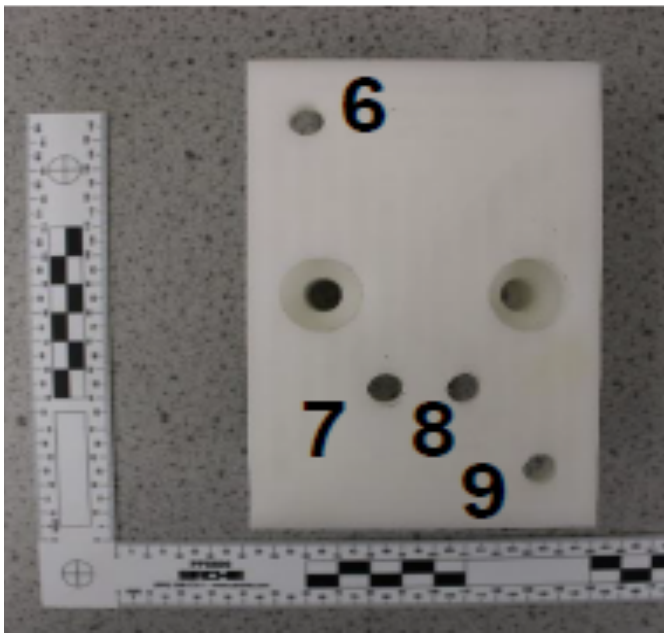

Figure 5.6: Pictures of target mounted pressure plate with gauges 6,7,8,9**.** Plate with gauge positions labelled 6-9. Note gauges 6 & 9 at the peripheral opposite corners of the plate, and 7&8 located centrally. Note the two holes for attachment to the target arm.

5.4: Development Of Flexible Tissue Culture Plate

The materials and design of a standard tissue culture plate does not mirror adequately the material properties of tissue such as muscle that may have a more dynamic response to blast loading. In addition, the plastic of a TCP is brittle and likely to fracture in response to a blast, resulting in spillage into the tube and loss of sample. Therefore a custom tissue culture plate was designed. The design requirements for the custom plate were as follows; It must be flexible, fracture resistant when exposed to high strain rate loads and sealable to prevent loss of contents. The plate must also be the same dimensions as a TCP that was used as the dimensions of the shock tube. Finally, the container must be manufactured from a cytocompatible material that can be sterilisation for use with cell culture. A silicone plate was developed and Table 5.5 gives the key design considerations.

Table 5.5: Design considerations of culture plate.

Version of Cell Plate	Aim	Design	Design Concept	Drawbacks of Design	Outcome	Image
Version 1	Design for use in Trial 1 Validation	3D printed 24 well plate with silicone coating.	Elastic resin has similar mechanical properties to Sylgaard 184 (Sigma Aldrich Ltd). Printed mould is then coated in biocompatible Sylgaard 184.	Extensive printing time and post processing precludes mass manufacture of cell plates for large trial. Elastic resin is cytotoxic. Coating with Sylgaard 184 is time consuming but overcomes biological issues.	Discontinue. Although plate is ductile, its manufacture is too time consuming for large scale adoption.	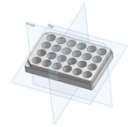
Version 2	Design for use in Trial 1 validation	Sylgaard 184 (PDMS) cast 24 well plates	Negative models of 24 well cell culture plates made using 3D printed tough resin jigs. Sylgaard 184 silicone is then poured into the mould and cured in a layer by layer approach	Variability between plates. High rate of plate failure. Large volume of silicone required to produce one plate. Fragile once produced. No lid to ensure sealing or contamination of cell culture.	Continue. Plate used in commissioning trial. Plate did not fracture. Did not have sealable lid.	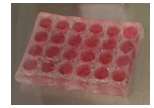
Version 3	Design for Trial 2	24 well plate with rectangular wells. Manufactured from Sylgaard 184	Adoption of rectangular wells instead of cylinders. Wells centrally located on plate to reduce loading changes found at the edge of the plate	Tough resin moulds prone to warping at high temperature curing. Sylgaard 184 plates prone to fracture when removed from mould. Similar drawbacks to Version 2	Discontinue using Sylgaard 184 silicone to produce plate. Design of plate appears valid. Explore other silicone sources.	 
Version 4	Design for Trial 2	2 part metal moulds to manufacture wells, base and lid for plate. Food grade silicone used for mould	Food grade silicone (Platsil) use for other experimental work can be synthesised with similar mechanical properties as Sylgaard 184. Metal moulds facilitate easier removal of cured silicone.	High cost of metal mould production to enable manufacture.	Continue/adopted. Plate used in shock tube trials 2 & 3. Plastil tested for cytocompatibility and found to make no difference.	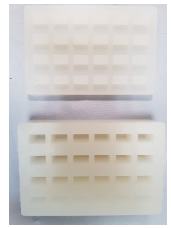

5.5 Validation Of Frustum Shock Tube

5.5.1 Commissioning Trial

As part of the commissioning of the shock tube, experimental trials measuring the pressure in the tube and at the target were undertaken.

5.5.2 Peak Pressure And Driver Charge Mass

In this trial a stepwise increment of charge size was employed and the pressure wave-forms measured. This experiment had a number of aims. First, to evaluate the quality of the waveforms generated and general function of the tube. Second, to assess the maximum quantity of charge the tube was capable of using without damaging the structural integrity of the tube. Third, to identify a driver charge mass that delivered an equivalent pressure to a 4 kg HSB into the test volume, as assessed from the peak incident pressure recorded by the pencil gauges. Fourth, to highlight any modifications required to support the experimental campaign. This validation exercise determined the charge masses for the subsequent cell culture experiments. Figure 5.7 and Table 5.6 outlines the charge mass and peak overpressures obtained from the commissioning experiment.

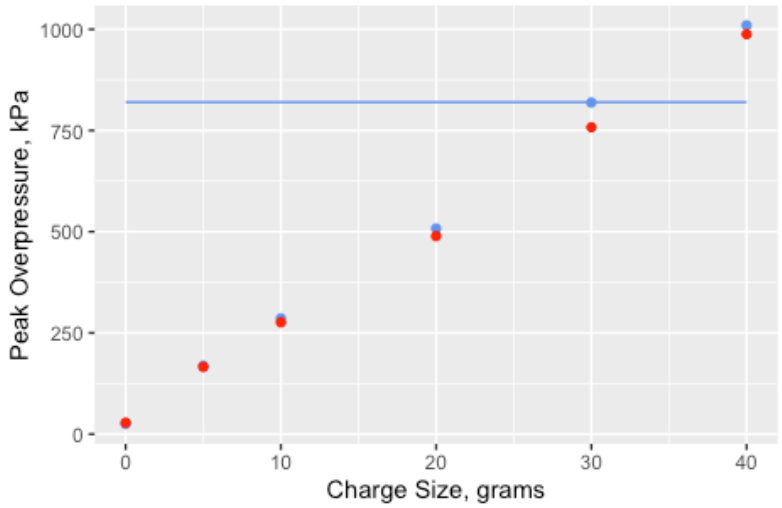

Figure 5.7: Trial 1: Peak incident pressure and driver charge mass (in addition to the detonator): Plot of increasing charge mass against measured peak overpressure in shock tube. The blue line indicated the target peak overpressure.

Charge mass* (g)	**Pressure** (kPa)	**Pressure** (kPa)
0	25	28.2
5	169	166
10	286	176
20	508	489
30	819	758
40	1010	988
* Mass of PE7 only, excludes detonator		

Table 5.6: Table of charge mass and peak incident overpressure (in kPa) measured by two pencil gauges on the target arm in the tube.

Figure 5.8 plots the peak incident overpressure and charge mass in firings from Trial 1.The target incident overpressure for a 4 kg charge at 2 m was 820 kPa which is indicated by the blue line. The estimated target overpressure was calculated using ConWep (US Army Engineer Research and Development Centre Computer Code ConWep 2.2.3.0, Vicksburg, Miss, USA). The graph shows pressure readings from both pencil gauges. The data

demonstrates that the target pressure was reached at 30 g of PE7 charge. Gauge readings from these firings are presented in Table 5.6. To provide some context for these pressure values, they and their associated positive phase durations were plotted on Bowen curves for a 70 kg human as was done with data from the literature in Figure 5.1. This is displayed in Figure 5.8 and illustrates how the lethality of the overpressures increases as the charge increases.

Observational data from camera recordings during calibration work showed that that 40 g explosive resulted in significant tube damage. This included wall panel loosening and cracked glass that required repair. Therefore, 30 g of explosive was considered the upper limit to be used in the tube. That damage was repaired, and other modifications to the tube such as an access door to ease sample placement and a breech block were made. The alteration to the breech block is considered the most likely reason for a reduction in pressure, for the same charge masses, in subsequent trials.

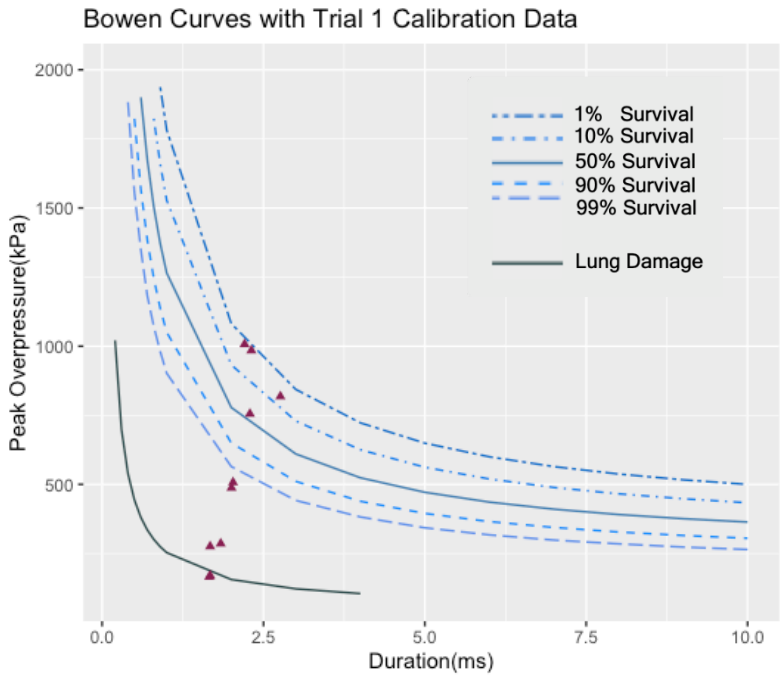

Figure 5.8: Bowen Curves With Calibration data. Data represents measured data from the shock tube. A charge of 30 grams sits just about the 50% Bowen curve lethality.

Utilising the data on driver charge mass and incident peak pressure, two charge masses (5g and 30g) were selected for use in subsequent mechanobiological tests. The two charge masses selected were 5 g and 30 g PE7. PE7 is a form of plastic explosive consisting of 88.0% RDX (Research Department eXplosive or Hexogen, $(O_2N_2CH_2)_3$), 1.0% DMDNB (2,3-dimethyl-2,3-dinitrobutane) and 11.0% binder of low molecular hydroxyl-terminated polybutadiene and an antioxidant.

These two charge sizes, and a control, enabled a three-armed trial design, in which *in vitro* samples would be exposed to two levels of shock waves, “low” and “high”, along with a control which would have no shock wave exposure. Charge masses were selected on two criteria. First, the charges must be sufficiently different in their blast output to in order to generate different cellular effects. Evidence from Figure 5.8 was used in this regard. Second, the upper limit of charge size must not damage the tube so far as to discontinue the trial before it had recruited enough samples taken from multiple firings (greater than 6).

5.5.3 Characterisation Tests

Tests were conducted to characterise the pressure in the section of the tube where the cell plate is located. This included measurements of both the incident pressure (via pencil gauges) and the pressure on the surface of the model plate (from the target pressure plate). After adaptions to the breach, the mean peak incident pressure and positive phase duration for the high charge (30 g) was 697 kPa and 2.39 ms and for the low charge (5 g) was 113 kPa and 1.62 ms. These values differ from those presented in Table 5.6, which were recorded using a different breach design that had to be modified due to the risk of fire. The equivalent hemispherical burst charge masses for these overpressures were 3.23 kg and 0.36 kg respectively. The overpressure produced from the high charge is therefore slightly less than the desired 4 kg device.

Figure 5.9 presents unfiltered pressure waveforms of the incident pressure data with six records for both charge sizes. The plots outline the distinct Friedlander waveform, followed by the reflected end wave at 20-30 ms. Figure 5.10 presents this data within a shorter time duration.

Figure 5.11 plots the overpressure values from these firings on Bowen curves for a 70 kg human. The plot shows that the high charge produces an overpressure related to 50% lethality, and the low charge is below the lung injury threshold.

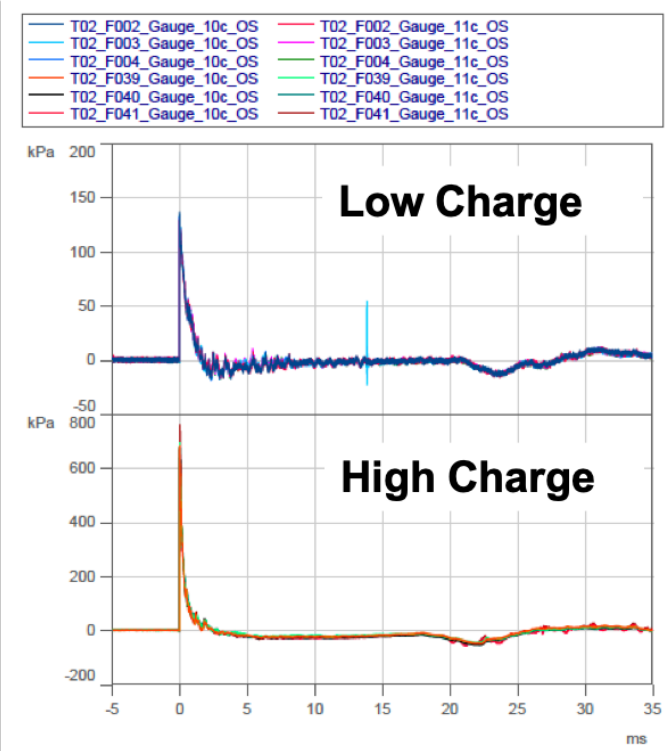

Figure 5.9: Section of (unfiltered) pressure records for incident pressure gauges mounted at target location (target removed).

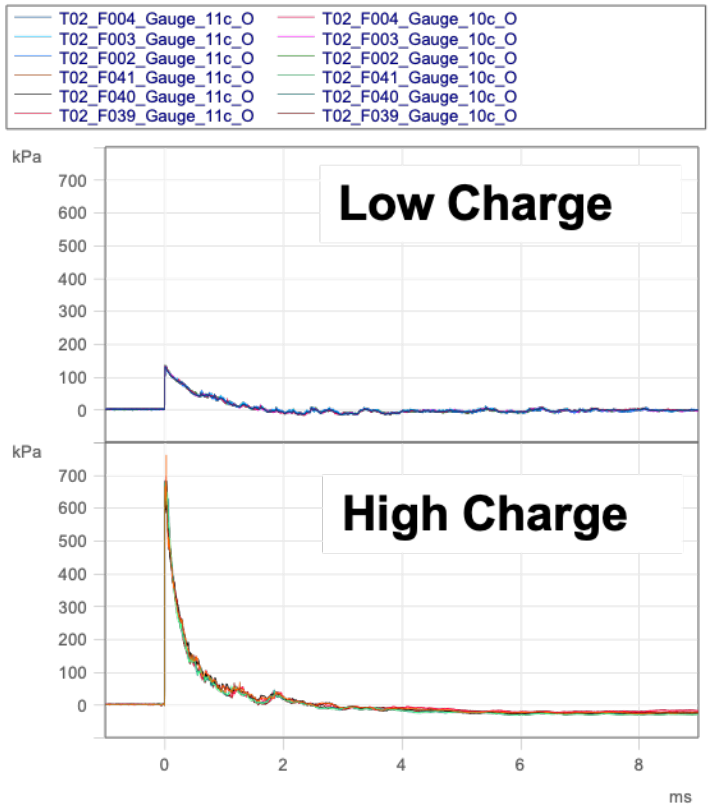

Figure 5.10: Section of (unfiltered) pressure records for incident pressure gauges mounted at target location (target removed).

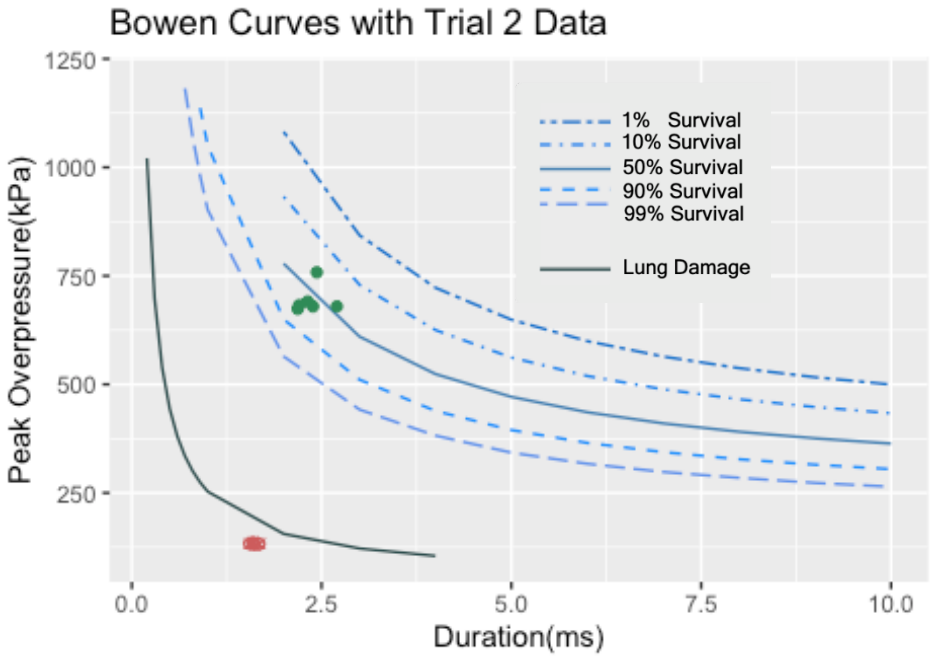

Figure 5.11: Bowen curves with peak overpressure & duration data from high (green dots) and low (red cross) blast exposure groups.

5.5.4 Tube Characterisation

To understand the waveform produced in the tube, the gauge data from the incident gauges and roof data were compared. The reflection coefficient (R) is calculated as per the relationship in Equation 5.3.

The reflection coefficient for a shock wave in air is given by:

$$\textbf{R Coefficient} = \frac{2(7Po+4Pinc)}{7Po+Pinc} \quad (5.3)$$

Where P_O is the Ambient pressure and P_{inc} is the Incident pressure. The total pressure at a reflection interface is the sum of the incident and reflected pressure.

$$\textbf{P}\textit{predicted} = Pinc + R*Pinc \quad (5.4)$$

The predicted target pressure is estimated from the relationship in Equation 5.4. Figure 5.12 plots the incident pressure data against roof mounted data. Figure 5.13 plots the measured roof pressure gauge overpressure, the measured pressure at the target face and the predicted pressure at the target. The predicted target pressure is calculated from the estimated reflection coefficient (outlined in equation 2). This figure demonstrates that the measured target pressure (which includes the incident overpressure and reflected pressure) is ~69% of the predicted target pressure.

Figure 5.6 shows the target pressure gauges and their location of the gauges on the target. The pressure time histories recorded from these gauges are then displayed in figures 5.14 & 5.15 for the low and high charges respectively. These two figures show small detectable differences in the positive phase duration recorded at gauges located at the periphery compared to the central location on the plate. These differences suggest subtle differences in the loading conditions experienced by 3D constructs at these positions in the plate.

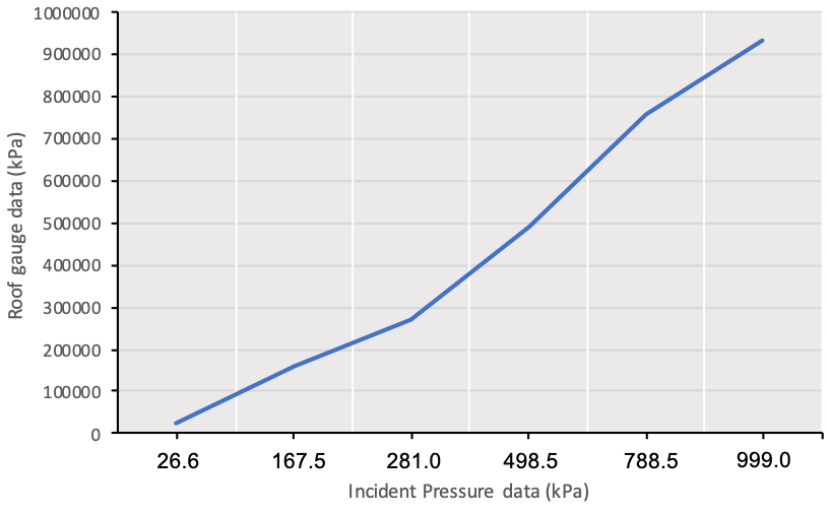

Figure 5.12: Roof gauge pressure plotted against measured incident pressure

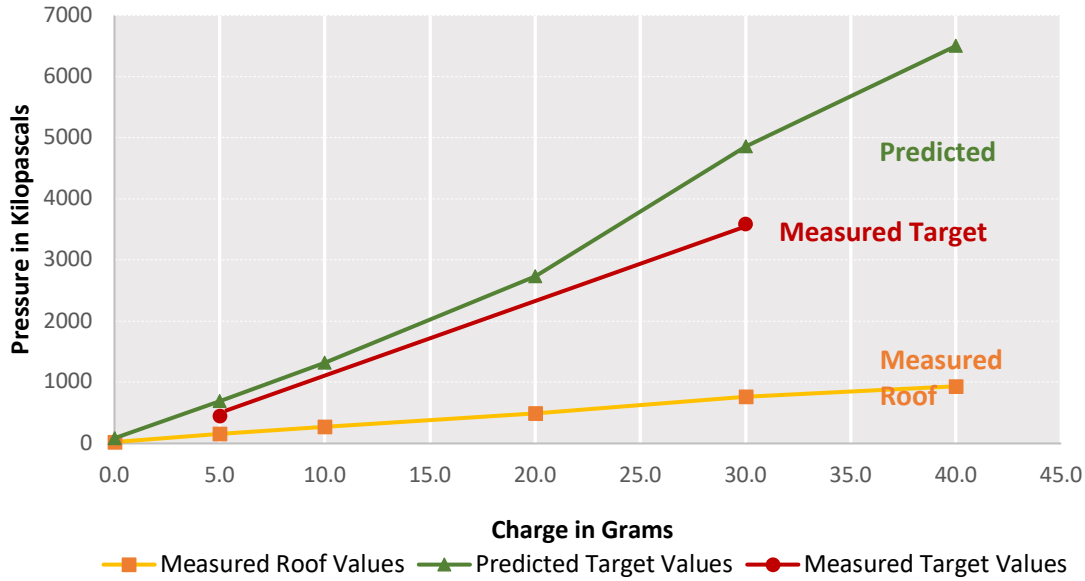

Figure 5.13: Reflection coefficient of Measured Incident Pressures. **Measured Roof:** Pressure measured at roof mounted gauges over increasing charge size. **Measured Target:** Pressure measured at target mounted gauges at two charges. **Predicted target pressure:** Calculated with data from incident pressure and reflection coefficient. *Zero grams of explosive charge still has a detonator, and therefore still results in an R Coefficient value.*

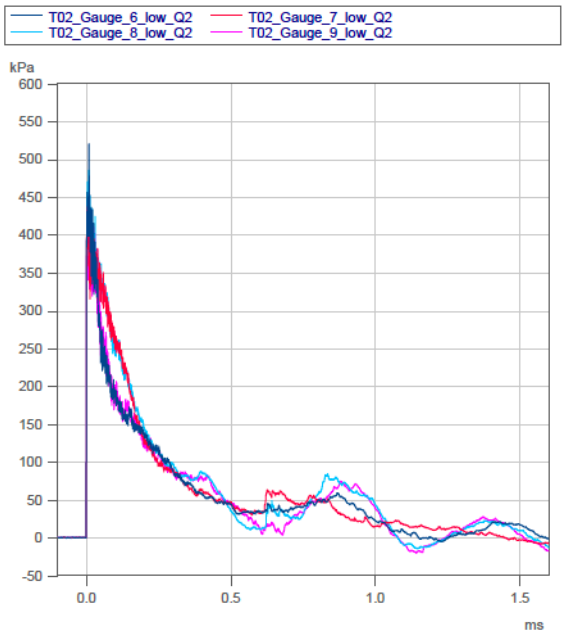

Figure 5.14 : Pressure waveforms recorded from 4 gauges on target plate for the low charge.

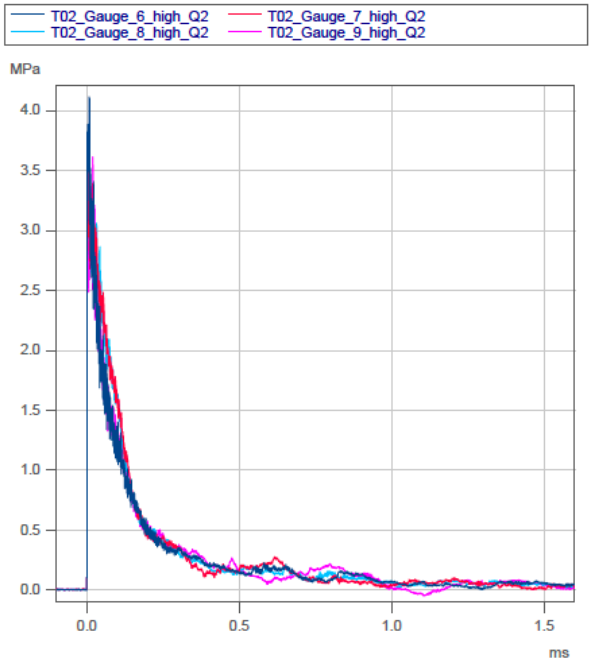

Figure 5.15: Pressure waveforms recorded from 4 gauges on target plate for the high charge.

5.6 Design Considerations Of Culture Plate

Table 5.5 outlines the design considerations for the biocompatible flexible cell culture plate. After exploration of a range of materials and production methods the final approach adopted was to use a metal mould and a food grade silicone as a material for casting the plate. This method is outlined in Figure 5.16 & 5.17. The metal moulds were manufactured from Aluminium by Dstl engineering workshop. Metal moulds accelerated the silicone curing process due to heat transfer through the metal. Metal also had lower adhesion to the silicone, which made it easier to remove the casted silicone after curing. The manufacture of numerous moulds also allowed several plates to be manufactured simultaneously, with no loss of quality. The food grade silicone (Platsil Gel 25) was significantly cheaper to use at the scale required than Sylgaard 184.

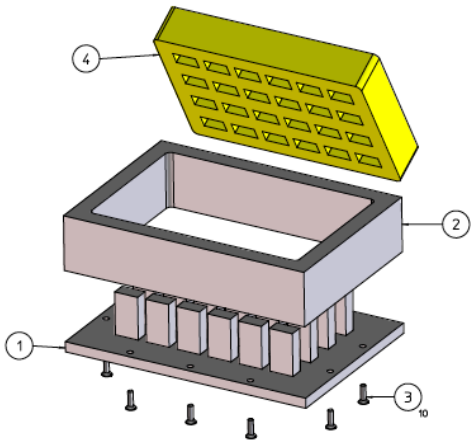

Figure 5.16: Schematic of the components of the mould for cell culture plate. (1.) Baseplate with well positive mould and screws (3). (2.) Wall of mould that attaches to (1) through screws (3). (4) The resultant silicone mould. A base for the mould was manufactured separately from platsil silicone, then the base and (4) were secured together by platsil silicone. A reverse mould of this was used to manufacture the lid of the plate.

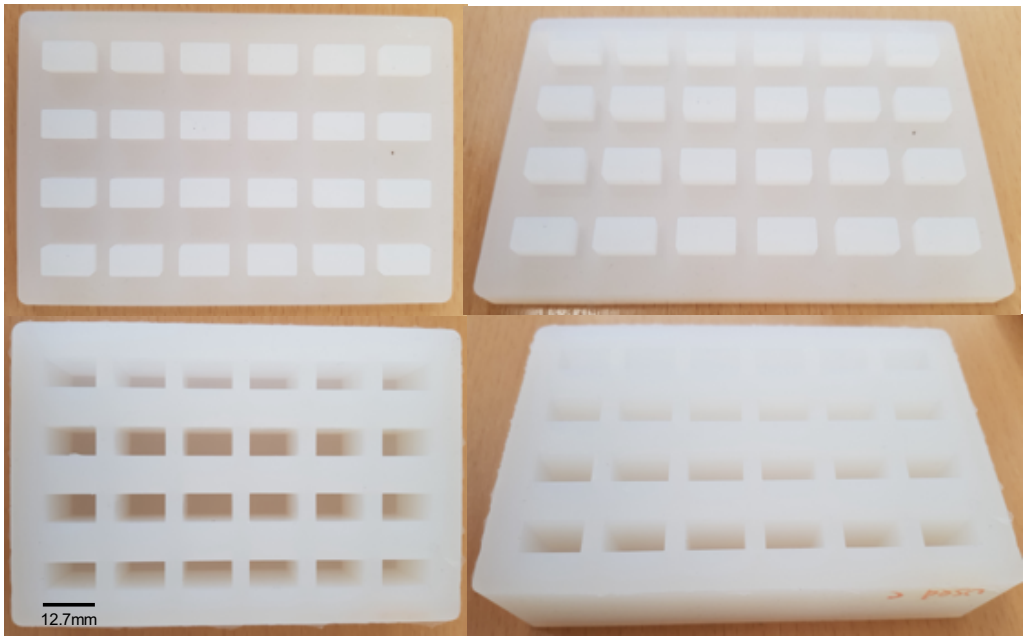

Figure 5.17: Picture of Silicone plate. Oblique and transverse views of the manufactured silicone plate cast from platsil silicone. The top images show the lid, which had outdents to seal the individual wells, and therefore reduce leakage from the wells (and plate).

5.7 Discussion

The aim of this chapter was to describe the design and develop an explosive driven shock tube for loading *in vitro* cell culture. A method of encapsulating *in vitro* samples was developed. The results in this chapter demonstrate that a reproducible blast waveform could be generated within an explosively driven frustum shaped shock tube.

The use of cylindrical shock tubes is widespread in blast literature (Chapter 1, table 1.1)(26, 28, 29, 31, 35-37, 179-181). However, as alluded to in chapter 1, these tubes do not always accurately represent real explosive environments often experienced by casualties of blast. Shock wave propagation in a cone shape more closely represents a hemispherical detonation. Furthermore, the length of the shock tube can be adapted to prolong the duration between the incident wave and end waves hitting the target. This is particularly useful for gathering incident gauge data within the tube. These advantages make the shock tube design useful, as secondary loading on the target has been reduced, which allows an appreciation of the effects of primary explosive shock waves on tissue.

This system characterised a shock tube designed to mimic a 4kg hemispherical burst at 2 metre stand-off from the epicentre. This was perceived to be equivalent to size of device used against dismounted troops such as those on foot in Afghanistan. Data also shows this to be equivalent in size to a civilian sized FedEx package (table 5.1). In the first trial, the tube was able to generate a peak pressure larger than the desired conditions using a higher quantity of explosive. This suggests that had the tube been constructed from a more robust material than wood, such as metal, the tube could have been used to mimic larger devices (such as a protective vest – 9.5kg).

The waveform produced from explosive detonation was consistent across firings. The mean durations of the positive phase was 2.39ms for high charge and 1.62ms for low charge. This

characterisation data is reassuring when adopting these facilities for biological experimentation. The waveforms are measured before any reflected waves return up the tube towards the target. Figure 5.9 shows the reflected waveform within the tube occurring between 20 - 30ms. It is distinct from the initial peak overpressure and decay. To allow the incident waveform to be captured prior to interference from end waves in the tube, the tube was lengthened after the target segment. This prolonged the time interval before any reflected waveform would return and be picked up by gauges at the target site, thus enabling analysis of the incident waveform specifically. The reproducibility of this waveform, in particular the consistency between charge sizes, is a key strength in the adoption of the shock tube apparatus for experimental work.

One object of this work was potentially to enable indoor explosive trials which would reduce the significant cost of experimental work involving explosives outdoors. This influences the constraints on the tubes size and adoption of smaller explosive quantities. The data in Table 7 shows that the high charge overpressure produced a TNT equivalence of 3.23kg, and the low charge overpressure an equivalence of 0.36kg, around a 10X difference. The tube was truncated to enable a custom breech for loading the explosives. It is believed that the combination of tube truncation and custom breech resulted in the lower peak pressure achieved by 30 grams of PE7 in the tube. Therefore the 30g PE7 waveform produced in the tube mimics a slightly smaller device than what was conceptualised on paper and predicted on conwep.

Health and safety regulations, as well as licensing, have precluded the testing of the shock tube in an indoor environment. However, during trials 2 and 3 the tube was fitted within a shipping container to facilitate storage of the device. This enabled the tube's usage in more confined spaces somewhat to be observed. The cost of explosive trials has always been one of the major shortcomings of their widespread use. Should regulations allow such a device to be deployed in confined or indoor settings, it would enhance the usage of this platform for regular experimental investigation.

Previously published shock tubes studies achieved a range of overpressures and durations (figure 5.1, table 5.2). When overlaid on Bowen curves, the published data spans the full breadth of lethality (lung threshold to 1% survivability). There is little consistency on the desired lethality's amongst other published shock tubes. By comparison, the calibration data from this tube was able to precisely map different lethality's given different explosive quantities. Although the shock tube design had considerable planning and modelling prior to construction, the accuracy and repeatability of the data recorded is a considerable achievement (figure 5.11). This reflects the quality of the tube constructed by Dstl.

The benefit of investigating the effect of 99% lethality (1% survivability) on tissue/ animal physiology for characterising potential regeneration is debatable. A lethality of greater than 90% was initially set as the upper target for experimentation and a design requirement for the proposed tube. The 'High' overpressure achieved in this work was just over 50% lethality in this shock tube model. Post hoc reflections on the design requirement identified that a 50% lethality is perhaps more useful for making biological deductions due to a larger remaining viable cell population. These lethality's refer to whole organism mortality, not *in vitro* cell populations. However, it would be little benefit to assessing the mechanobiology of extremity soft tissue with the view of finding targets for progressive tissue loss if whole organism hasn't survived the insult. In tissues that have been exposed, any remaining viable cell population could be in a pendulum between survival and programmed cell death. Transcriptomics analysis can be used to determine whether this is true. The 'Low' overpressure was below the threshold for inducing lung injury on the overlaid Bowen curves. As Figure 5.11 demonstrates, the firings in each group were consistent and produced two distinct groups. This consistency is further corroborated in the pressure/ time history plots of firings for each loading condition (Figure 5.9 & 5.10). It is expected that that these two distinct overpressures would yield significant differences at the cellular transcription level.

To verify the loading conditions on the face of the silicone cell culture plate, measured target incident pressure was plotted against predicted target values. Figure 5.13 shows this data, where the measured target incident pressure is ~69% of the predicted value, suggesting the data collected in the tube is close to that modelled. To characterise whether the loading on the surface of the target plate was uniform, the corresponding target plate had pressure gauges at two different locations (peripheral and central). Figure 5.14 and 5.15 illustrate the pressure/time histories recorded at these gauges during high and low charges. The figures show some slight change in the shoulder at around 0.15ms, but otherwise the waveforms are similar. This small difference, and its effect on the area under the curve, has not been investigated. It is unclear whether this change could represent altered loading between the central and peripheral regions of the silicone plate. Such loading differences could be explained by wrap around effects at the edge of the silicone plate. Attempts were made to mitigate this by thickening the outer walls of the silicone plate. These edge effects would have some effects on the type of loading (compression or tensile loading) seen on the hydrogel sample.

There are some limitations to this shock tube. Firstly, the characterisation data of the incident and reflected waveforms is limited and requires more data collection to characterise fully the tube. Further analysis of shadowgraph data captured during the firings would perhaps validate some of the gauge data. Quantification of the gauge data would allow a deeper understanding of the loading at the target face. In particular this could aid computational modelling of the target plate to increase the understanding of the loading on the individual constructs. Finally there is a lack of statistical analysis on the gauge data collected from the tube, in particular the differences in peak overpressure, duration and the variation in data between firings.

The tube was built as a feasibility prototype exercise on a limited budget. As such it was built of low cost materials. Although the wood design lasted longer than expected, there were some structural issues (loosening of screws/bolts/panels) that may have influenced the gauge data. However, it is difficult to quantify what effect, if any, this would have had.

5.8 Conclusions

In conclusion, this chapter outlines the design considerations, validation and quantification of an explosively driven frustum shock tube for cell culture. The data demonstrates that reproducible waveforms of two different explosive quantities can be characterised within the tube. These waveforms measured at the target are close to those predicted, and these represent a 50% and below threshold lung injury when plotted on corresponding Bowen curves. Finally, a silicone cell culture plate was developed for use within the tube.

6

The effect Of Primary Shock Wave On Skeletal Muscle *in vitro*.

6.1 Introduction

To improve the understanding of the effects of primary blast on soft tissues, such as skeletal muscle, a new approach is required. This requires a model that can probe the cellular and molecular mechanisms in depth.

Chapter 1 reviewed the considerations for developing experimental apparatus to explore the cellular response to primary blast shock wave. Ouellet also discusses the challenges of this multidisciplinary field(178). Ouellet identifies two main problems; the first is the lack of blast facilities capable of integrating with biological models (in vivo or in vitro). The second problem is a lack of understanding of the biophysical interactions from blast with biological systems. A limitation that Ouellet does not discuss is the disconnect between military and civilian research teams. As public information about military munitions and operational experience is limited for security reasons, civilian researchers are often limited to building experiments based on publicly sanitised information regarding explosive events and munitions. As such, educated assumptions are made on munition sizes, environmental conditions and operational relevance in order to frame the research project, rather than using more accurate operational data that is too sensitive for public release. This limitation can reduce the relevance or applicability of data garnered from these experiments.

In this chapter, a model of explosive loading on *in vitro* culture is developed and validated. To enable the development of this model, due consideration is given to the logistical bottlenecks that could need optimisation. The primary aim of this work was to demonstrate proof-of-concept for the exposure of skeletal muscle cells in 3D *in vitro* culture to a shock wave from live explosive in a prototype shock tube. The secondary aim was to make some preliminary analyses of the molecular and cellular responses to the blast shock wave in this *in vitro* model.

6.2 Methods

To examine cellular signalling after blast injury, the *in vitro* model proposed in chapter 4 was tested within the shock tube presented in Chapter 5, in a set of experimental explosive field trials conducted on the test range at Dstl.

6.2.1 Explosive Trial Logistics

6.2.1.1 *Trial Methodology*

The shock tube was sited in a double ISO shipping container outdoors on the range at the Defence Science and Technology Laboratory (Dstl), Porton Down. In this chapter the term 'trial' is employed to refer to experiments conducted using the shock tube facilities on the outdoor range. Experiments were run in week-long blocks. Two separate weeks of testing were required to collect the data presented in this chapter. Chapter 5 referred to a commissioning trial which was also termed Trial 1. Trial 2 refers to a week of experiments conducted in December 2020. Trial 3 refers to a week of experiments conducted in July 2021.

6.2.1.2 Target

Hydrogels were constructed as described in chapter 4. Hydrogels were first cultured in growth then differentiation media for 13 days prior to being exposed to explosive shock waves on day 14. All cell handling was undertaken in Class II tissue culture hoods.

6.2.1.3 Silicone Culture Mould

Silicone cell culture plates were cast from food grade silicone in custom made metal jigs as described in Chapter 5. Cell culture plates were sterilised in a tissue culture hood by immersing in 70% ethanol then washing by submerging in sterile PBS. Sterilised culture plates were left to dry in the tissue culture hood prior to use.

6.2.1.4 Cell Culture Logistics

Cells were plated in a main laboratory facility at Dstl. They were then placed in a portable incubator (Cell Box Ground, Cell Box solutions ltd) for transport to the blast trial site (~20 minutes by vehicle). Plates were removed from the incubator 5 minutes before blast loading, in order for the hydrogels to be transferred to a silicone cell pate. Silicone cell plates were sealed with parafilm (www.parafilm.com) , fastened to a wood sample holder, placed within the blast tube then subjected to a blast wave. After firing, plates were removed from the tube and hydrogels were divided for analysis. Hydrogel samples required for analysis (presto blue, fixation, storage in RNA preservation solution) were placed in relevant storage or solutions. Remaining hydrogels were transferred back to a standard tissue culture plate (TCP) containing warm differentiation media.

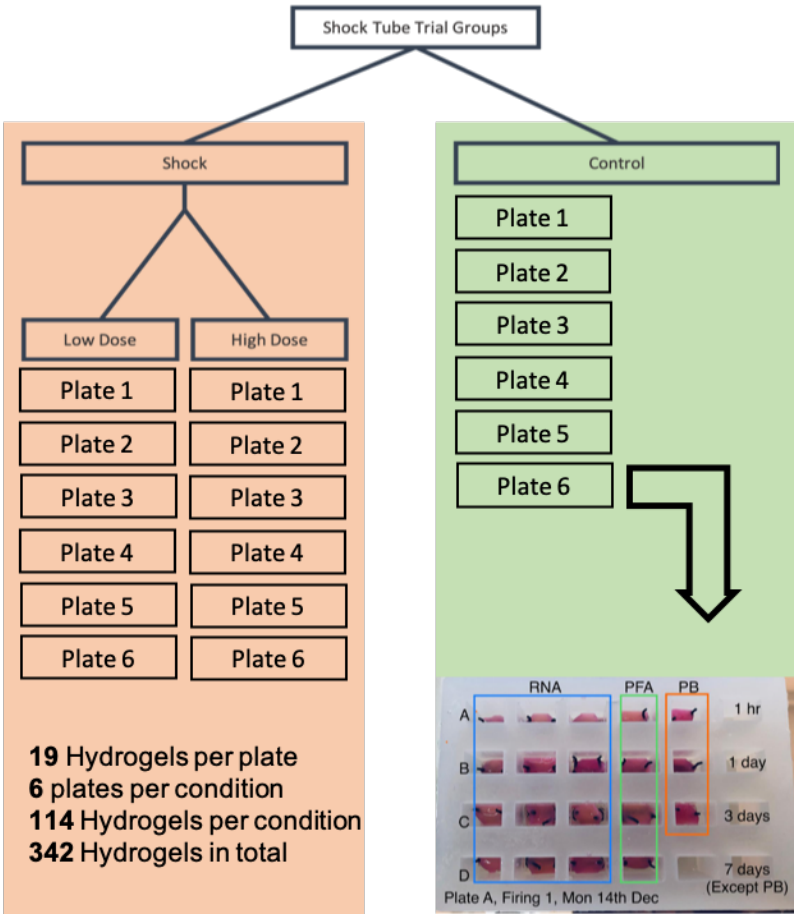

Figure 6.1 Layout of samples in cell culture plate for trial. The flow diagram outlines the different conditions in the experimental work, the number of cell plates within each arm/condition and the number of samples in each plate. Finally, the diagram presents the total hydrogels in each condition and for the whole trial.

6.2.1.5 Experimental Power

To ensure adequate experimental power and plan the number of samples required for each group power calculations were undertaken on skeletal muscle hydrogels. To determine potential sample size for statistical deductions of RNA sequence as a primary outcome, a power calculation was undertaken on pilot data obtained from the first shock wave test trial. Normalisation counts from bulk RNA sequence data from 6 hydrogels exposed to blast waves (3 controls and 3 treatment hydrogels) were extracted and analysed using the *'RNASeqSampleSize'* library package in R. Count data from sequencing was used to estimate sample size for increase experimental power. The estimated sample size was then plotted against experimental power. To confirm these pilot findings, power calculations were

subsequently repeated on hydrogel samples exposed to hydrogen peroxide injury (total n = 8, control = 4, treatment = 4). Counts data was then used too estimate sample size, and experimental power was then plotted against sample size.

Following on from power calculations conducted for RNA sequence data, post hoc power calculations were undertaken based on mean Presto Blue data obtained from Trials 1 & 2. The Pre Blast & 2 Hour High data was used to estimate post hoc power.

The number of firings that could be achieved in a single day on the range at Dstl was limited by working daylight hours, which was one of the reasons that only two charge quantities could be tested – high (30grams PE7) and low (5g PE7), along with a control condition that had no firing of the shock tube. Each trial conducted six exposures, six plates of *in vitro* samples, for each condition (control, low and high). Each cell culture plate contained nineteen 3D *in vitro* models (as described in Chapter 4 and Figure 6.1).

6.2.2 Trial Methodology

6.2.2.1 Loading Silicone Moulds

Hydrogels were loaded into sterile silicone cell culture plates (described in Chapter 4). After the hydrogel was loaded the wells were filled with warmed differentiation media (DM). To reduce air bubbles, DM was filled into the silicone well until it formed a positive liquid meniscus. It was hoped this would reduce bubble capture within the well when it was sealed. The wells were covered with the silicone lid and then sealed with parafilm to prevent fluid leakage. None of the media was degassed during preparation. Silicone cell culture plates were filled immediately prior to being installed into the shock tube. Sealed plates were returned to the portable incubator for storage until they were due to be installed within the tube.

6.2.2.2 Treatment Plates

Hydrogel plates (12 well plates) were not randomised but alternatively assigned to either treatment, high or low blast, or control groups. Treatment plates were assigned sequentially to receive either a low quantity of explosive (5 g) or a high quantity of explosive (30 g). To reduce the risk of damage to the tube, the low firings were conducted first (n= 6), followed by the High firings (n = 6).

To install cell culture plates assigned to the treatment arm within the shock tube, the silicone plates were secured to a custom holding device using strong adhesive tape. This system was then fixed onto the holder arm in the central portion of the tube through a sealable window. Images of this apparatus can be found in chapter 6 appendix.

6.2.2.3 *Control Plates*

Control plates were loaded and wrapped as per treatment plates They were placed inside the ISO container, but away from the shock and blast waves. They were left in this position for the same amount of time that plates for exposure spent in the ISO container once loading into the tube, shock wave exposure, 'make safe' time and unloading the plate, took for experimental samples (c. 30 min). Control plates were conducted intermittently between live explosive firings throughout the experimental week. This was done in order to account for differences in ambient conditions over the week.

6.2.2 Post blast exposure analysis

6.2.3.1 Timepoints

Hydrogels were analysed at four timepoints after exposure (or control): 1hour, 1 day, 3 day, 7 day.

6.2.3.2 Metabolic Assessment

To quantify the effects of blast shock wave on cell metabolism, as an indirect marker of cell injury, Presto blue™ viability reagent was used. Presto blue reagent was used as described in Chapter 4. Three wells of presto blue only (no cells) were measured for each plate to control for background fluorescence.

6.2.3.3 Cell Culture Media

Cell culture media that had been placed around the hydrogels in the silicone plates was transferred to the standard tissue culture plates when the constructs were removed after exposure, and aspirated at the 2 hr timepoint and stored for subsequent analysis. This was also conducted at the 1 day, 3 day and 7 day timepoints. It is worth noting, however, that fresh media had been put onto the constructs every 48 hr For the 2 hr timepoint media was temporarily stored at 4°C on the range, then transferred for long term storage to -20°C. For the other timepoints media was stored immediately at -20*C.

The trial sequence was as follows:

1. Cells transferred from incubator to portable incubator.
2. Cells driven to field site in portable incubator. (Drive time 20 minutes).
3. Cell plates removed from portable incubator, moved too tissue culture hood and hydrogels loaded into sterile silicone plates.
4. Silicone plate filled with warmed differentiation media and sealed with paraffin tape.
5. **Treatment:** Silicone plate attached to holder arm, then carried outside to shock tube and installed within tube.
6. Shock tube lacked down to initiate firing sequence.
7. After safety period, silicone plate removed from shock tube and returned to tissue culture hood.
8. **Control**: Silicone plate carried outside, not on holder arm, and placed at the mouth of the ISO container next to shock tube to expose hydrogels to ambient outdoor conditions.
9. **Post Exposure: Immediate Timepoints:** Individual hydrogels placed in Presto Blue solution, RNA Preservation solution, media aspiration and 4% Paraformaldehyde).
10. **Post Exposure: Late Timepoints:** Individual hydrogels returned to tissue culture plastic containing differentiation media and placed back in portable incubator.

TIMEPOINT ⇒ *ANALYSIS:*	PRE	2 HOUR	DAY 3	DAY 7
RNA	n = 3	n = 3	n = 3	n = 3
PRESTO BLUE	n = 3	n = 3	n = 3	n = 3
DMEM	n = 3	n = 3	n = 3	n = 3
IMAGING	n = 1	n = 1	n = 1	n = 1

Table 6.1: Sample requirements for analysis. The number of replicates required for each timepoint and analysis. His corresponded to 19 hydrogels in each plate/firing of the trial, and 6 plates in each trial (12 plates over 2 trials). The table also shows which timepoints were not measured for image analysis.

6.2.3.4 RNA Preservation

Hydrogels were stored in RNA stabilisation solution (4 degrees 24 hours, then -20 degrees, RNA Stabilisation solution, Merck Ltd).

6.2.3.5 RNA Extraction

To extract RNA, samples were thawed and then homogenized using a Qiagen tissueruptor 2 device as described in Chapter 4. RNA was then extracted using a Qiagen Qiacube extraction robot with a customised RNeasy Fibrous tissue kit protocol (Chapter 6 appendix)(Qiagen Ltd).

6.2.3.6 Library Preparation and Sequencing

RNA extracted from the trial samples was sent to Source biosciences Ltd (www.sourcebiosciences.com) for library preparation and sequencing. A total of 184 samples were sent for library preparation and sequenced across the two trials. Samples were sequenced twice in order to increase the depth of reads for each sample.

6.2.3.7 Storage for Imaging

One hydrogel from each plate was fixed in 4% paraformaldehyde (Merck Ltd) for 15 minutes followed by storage in phosphate buffered saline solution (Thermofisher Ltd) at 4°C for imaging at all timepoints.

6.2.3.8 Creatinine Kinase

Creatinine kinase was assessed with the mouse CKM ELISA kit (2B Scientific Ltd, EKE61593) as per manufacturer's instructions. Media from plates was stored at -20°C prior to analysis.

6.3. Results

6.3.1 Experimental Power

Figure 6.2 presents two power curves plotted from normalization counts of bulk RNA sequence data. Figure 6.3A shows the power and sample size estimated from four hydrogels manufactured using an early methodology. This method adapted tissue culture plastic 48 well plates to cast hydrogels between posts. Figure 6.2B presents the power and sample size calculated from four hydrogel samples manufactured using the methodology presented in chapter 4.

The graphs show that to achieve a power of 0.8, with a false discovery ratio of 0.05, the sample size increases from 15 to 25 for the later manufactured hydrogels. In total, 12 plates were exposed to each set of conditions over two trials periods. Based on the figures presented this would give the experimental power between 0.6 and 0.8.

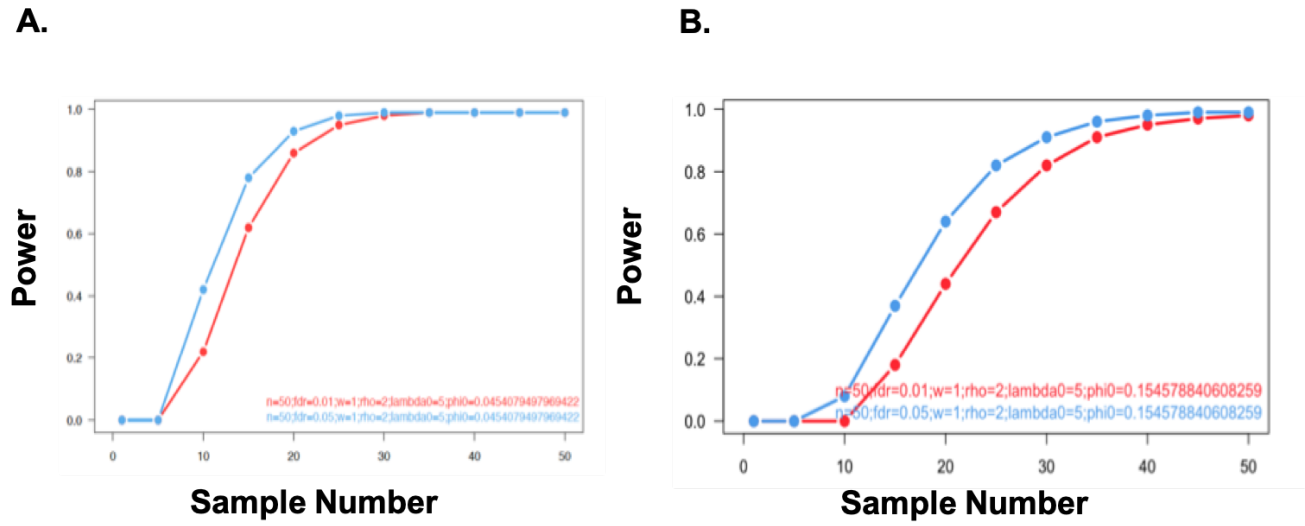

Figure 6.2: Power curve of hydrogels. A: Power curve based on normalisation counts from RNA extracted from early *in vitro* samples. **B**: Power curve based on normalisation counts from RNA extracted from later iterations of the *in vitro* model. The red line corresponds to a significance of 0.01, the blue line corresponds to a significance of 0.05.

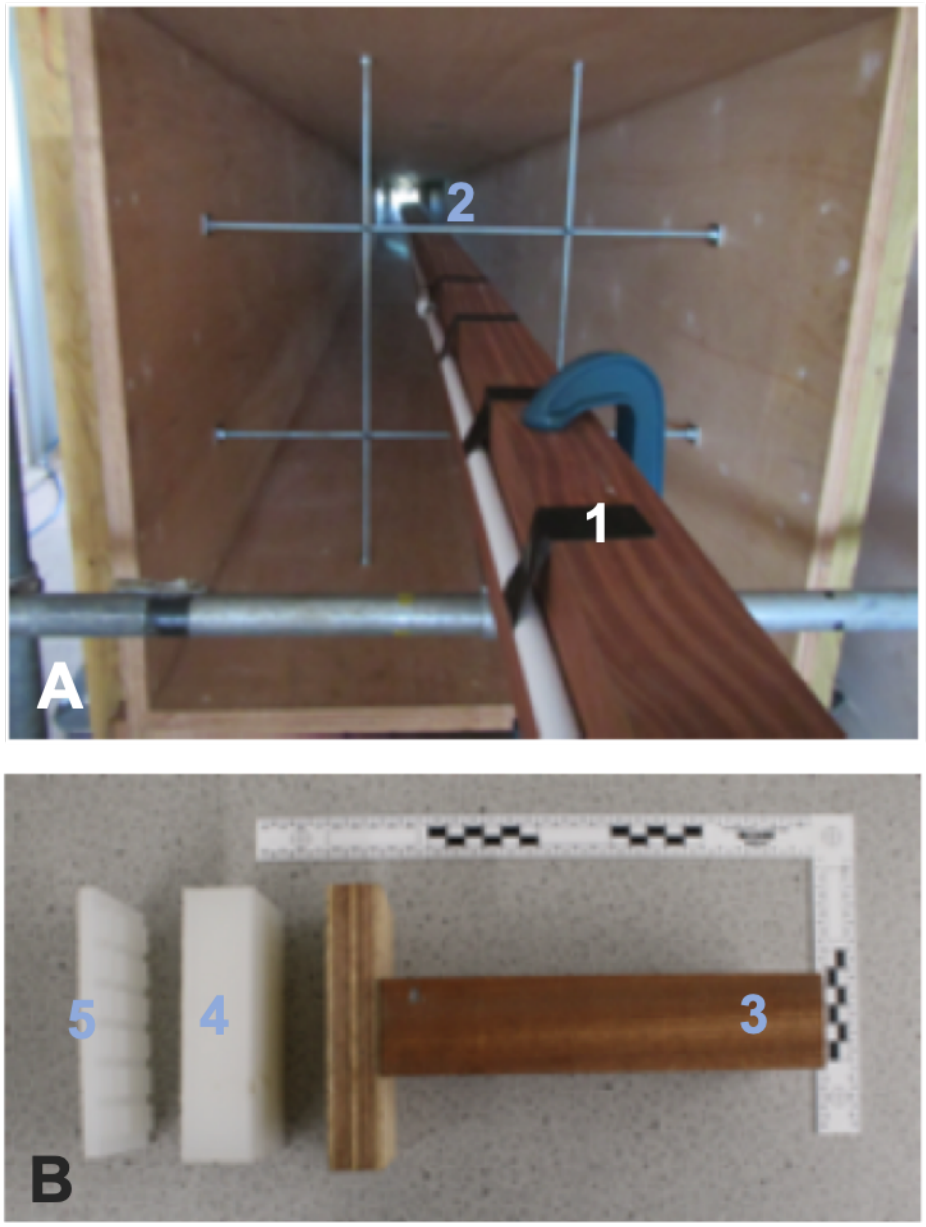

Figure 6.3: Shock tube set up. 6.4(A) shows the end of the tube with the specimen holder (1) inside the tube. The end of the arm (2) is placed 2 metres source of the explosion. **6.4 (B)**: shows the cell culture mounting apparatus. The plate holder (3) is made of wood. The cell culture plate (4) and lid (5) is attached to the plate holder (3) using duct tape. The lid design (3) includes individual plugs for each well to prevent fluid leakage.

6.3.2 Cell Metabolism

Figure 6.4 presents the fluorescent readings from control and treatment samples over time. The graph shows fold change over pre blast readings, with error bars showing the standard deviation. The data presented is from two explosive trials and a total of 12 plates per condition (total n = 36 across all conditions). Separate metabolic data for each trial is found in the appendices. A two way analysis of variance (ANOVA) was applied to the data means between groups. The accompanying table shows the ANOVA data for each condition compared to control. There was a significant change seen in control sample metabolism at 2 hours, and also at 7 days. There is no significant difference between pre blasts samples and day 1 or day 3 data. The significant reduction in cell metabolism within the constructs at 2 hr is likely to be attributed to their handling on the day of the trial. For example, although they were transported in a portable cell incubator which kept the cells at 37°C, 5% CO_2 due to the size of the incubator the temperature and CO_2 conc. changed more significantly than a large incubator after every opening. The cells were transported from the lab in a vehicle to the range, this may have had confounding, and unquantified, effects on results. The standard deviation shows a relatively high variability within all groups, although not unexpected for this type of 3D model and very complex experiment. Power calculation based on the Presto blue data alone suggested a post hoc power of 100% based on a sample size of 12 and an alpha of 0.01. Therefore the number of plates recruited to this work suggests statistical analysis should be able to accurately reflect the probability of the observed events.

In the low treatment group there is statistically significant increase in cell metabolism between pre blast and 2 hours, 3 day and 7 day samples.

Within the high treatment group, there is a significant reduction in cell metabolism by 2 hours after exposure, compared to pre blast levels. This significant reduction is also present at day 3 but not at day 7. When the trial 2 data is analysed alone (see Chapter 6 appendix) the cell metabolism fails to return to baseline by day 7.

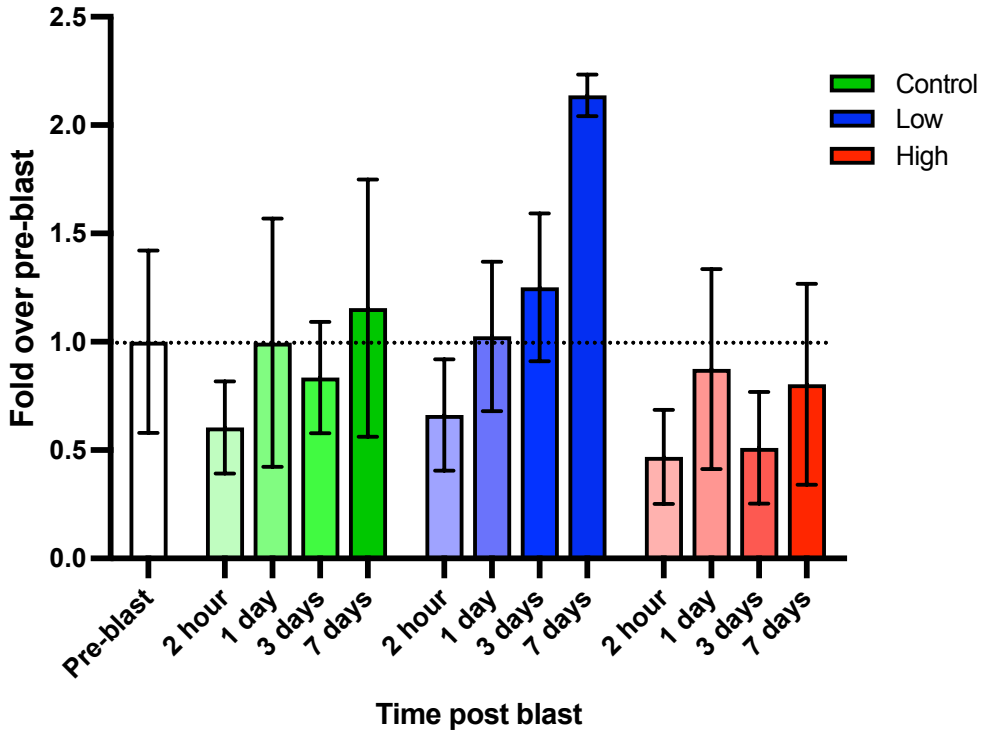

	2 HOUR	1 DAY	3 DAY	7 DAY
PRE BLAST	***	ns	ns	*
LOW	*	ns	**	****
HIGH	****	ns	**	ns

Figure 6.4: Cell Metabolism of treated and control samples. The graph plots fold over pre-blast for control, high and low conditions. The graph shows error bars of standard deviation. Fold change is computed as a ratio of the change between final value and the original value over the original value.
Table shows the pairwise comparisons between Pre-blast and subsequent timepoints (2 hours, 1 day, 3 day & 7 day) in treatment and control samples. */**/***/**** - denote level of significance from ANOVA. ns – not significant.

6.3.3 Creatinine Kinase

Figure 6.5 presents the creatine kinase concentration in media after injury in treatment and control groups. Error bars are of standard deviation. A two way analysis of variance was applied to the data. The figure shows that there was a significant release of creatinine kinase immediately after injury, when compared to control. This release was significantly greater than the release in the high treatment group. This creatinine kinase release peaked on day 1 in both groups. However, this concentration was highest in the low treatment samples than in high treatment group. The concentration of creatinine kinase returns to below baseline by day 7. Unlike the low treatment group, the high treatment group creatinine kinase concentration does not differ from controls across all timepoints. The high samples have a narrower standard deviation compared to the low treatment groups. In particular the variation in the day 1 and 3 is notably wide.

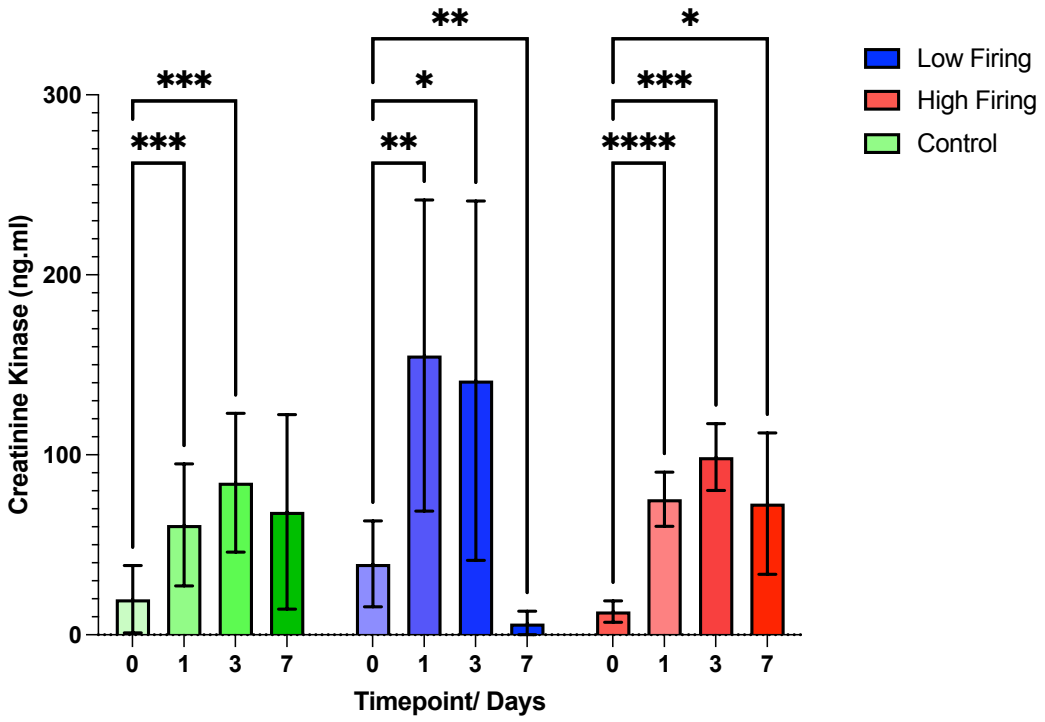

Figure 6.5: Creatinine Kinase on treatment and control samples. Error bars show standard deviation standard deviation. Pairwise comparison from ANOVA are shown (* denotes significance, ns denotes non significance). The data shows a significant increase in CK concentration in Low firings compared to controls. The data also shows no difference in CK concentration between high firings and control.

6.4 Discussion

The main objective of this thesis is to understand the role primary blast shock wave may have in propagating progressive tissue necrosis. The primary aim of this chapter was to develop a field shock tube trial on skeletal muscle hydrogels. The secondary aim was to understand what effect, if any, primary blast had on skeletal muscle hydrogels. To address these aims and objectives, this chapter demonstrates new experimental methodology for investigating the effects of primary blast shock waves on skeletal muscle. Several quantitative techniques namely assays for cell metabolism and gene transcription looked at cellular function for up to 7 days after injury. This work demonstrates the substantial logistical requirements needed in order to adopt *in vitro* models appropriately within an explosive shock tube. The trial design reflects the balance struck between experimental power and constraints. The results highlight that the quantity of explosive loading has diverse effects on cell metabolism and creatinine kinase release.

Chapter 1 suggests limitations in published literature on the cellular effects of blast. Firstly, experimental modalities for blast contained inconsistencies that precluded direct comparison. Secondly, the models used did not represent normal tissue. Thirdly, only a narrow set of markers were available. Lastly, most of the literature has focused on brain or bone, with little focus on skeletal muscle tissue. This work utilised a 3D model of skeletal muscle exposed to live explosive using a frustum shock tube. The results show that although it is technically challenging, it is achievable to apply broader cellular analysis in this context. Nevertheless it must be noted that the installation of cell culture facilities adjacent to the shock tube enabled the adoption of more advanced downstream cellular analysis, as it ensured samples could be cultured or store under sterile conditions.

The methodology developed in this chapter was dependent on several items of infrastructure that broadened the available capability for experimental design. Although the cost of a shock

tube may be a significant prohibitive hurdle for the vast majority of research groups, it is not the most rate limiting step. The limited facilities with licences to handle and use explosives is prohibitive to many research groups adopting such apparatus in the laboratory. This is therefore an important technical capability that when used may allow a series of experiments to understand better cellular blast injury.

To reduce the confounding factors, such as time outside of incubators or handling outside of tissue culture facilities on *in vitro* cultures, there were two logistical shortcomings that needed to be overcome. First, tissue culture facilities had to be deployed adjacent to the shock tube on the Dstl range, to allow the aseptic handling of *in vitro* samples close to the tube. Second, the adoption of a portable incubator ensured that hydrogel samples remained at appropriate conditions during transport to and from the range. These approaches reduced the influence of any potential confounding environmental variables, which is often one criticism levelled at *in vitro* work. This kit also extended the potential length of post-hoc analysis of shocked samples. Few *in vitro* studies have conducted analysis of shock samples beyond 24 hours. Almeida analysed hippocampal slice cultures for up to 48 hour after exposure to RDX air blast(182). In Almeida's experimental set up, the cultures were sealed in air tight containers and then fixed into a temperature controlled water bath for shock wave exposure. This ensured that the cell culture was maintained at 37°C. However, approach is unable to replicate incubator culture conditions. Hence the movement between these facilities, and this issue, would have some influence on the hippocampal slices. The method put forward in this chapter advances the literature by providing key details on how to minimise environmental influences on cell culture for such logistically complex experiments. This shock tube development represents 'sovereign capability' for the United Kingdom amongst its allies in their capacity to undertake such experimental work.

The findings from this chapter contribute to the field by adopting a variety of analytical techniques to look at the effects of blast on cells over time. To quantify the injury, the cells metabolic capacity was evaluated over 7 days. The power calculations done on the Presto

Blue data suggest that enough samples were tested in order to achieve a power of 0.9. Recent work by Stewart also adopted metabolic analysis for 2D cell culture but only for a single timepoint(183). Hence this work has not only extended the time period of analysis, but applied it to a new 3D model. The experiments collected culture media from the control and treatment samples for later analysis. In this chapter the data presented was from media analysed for creatinine kinase release; however, a variety of other assays could be applied to this stored material.

Finally, although not presented here, the experiment also stored samples for imaging and bulk RNA sequencing. Sequencing data should be able to assess gene expression changes over time and may give a better understanding of cell transcription that has not been published in this cell and tissue type to date.

The available trial data shows interesting findings for discussion. The metabolic data (figure 6.4), suggests there are marked differences in the responses of cells exposed to low or high quantities of explosive. It was hypothesised that primary blast shock waves would induce a progressive cell death, which would manifest itself as a gradual reduction in metabolic activity over time since exposure.

The Presto Blue assay measures cellular metabolism and a reduction may indicate either the death of a portion of the cell population, or stress on the cells that reduces their metabolic output. The analyses conducted to date do not delineate between these possible outcomes. Conversely, the low samples recover to baseline by day 3. Furthermore, their recorded metabolic activity exceeds baseline considerably by day 7. The statistical significance of this change over pre blast samples increases from day 2, to day 3 and day 7.

The low exposure data is interesting, as it shows that despite an early reduction in cell metabolism, there is a large reciprocal increase at day 7. The low exposure in this trial (~130kPa) was below the threshold capable of inducing primary blast injury on Bowen's curves (Figure 5.11)(184). Data in the wider shock wave literature shows that low intensity shock waves have been implicated in driving cell metabolism(185, 186). For example, Weihs's and

colleagues exposed murine mesenchymal progenitor cells to multiple shock waves from electrohydraulic lithotripters(187). Their data demonstrated shock waves increased metabolic activity 15 hours after treatment but at no later timepoints. Their data also demonstrated a rise in ATP production, which was not measured in the trials conducted in this chapter. A major limitation of comparing to other published shock wave data is the differences in the application on the cell culture. In Weihs's work, 10-300 pulses of shock waves were applied to cell culture, whereas in this data the cells were exposed to a single blast wave. The overpressures and durations of the waveforms in these two experiments also differed. Nevertheless, the findings in this work concur with similar conclusions made using other modalities and with different cell types.

Creatine kinase is an enzyme found in skeletal tissue and brain amongst other tissues. It catalyses the conversion of creatine using adenosine triphosphate to build phosphocreatine (PCr) and adenosine diphosphate (ADP). Unexpectedly the data from the shock trial revealed no difference between the high treatment group and control at any timepoint. However there were significant differences between the low group and control at timepoint 0 (immediate), day 1 and at day 7. Interestingly the trend for this group was a large rise at timepoint 1 and day 3, followed by a decrease to below baseline (control) at day 7. It was hypothesised that creatinine kinase release would be proportional to the size of the explosive stimulus. The data presented here does not support this theory. The results are likely influenced by storage conditions, however. The media samples were stored at -20*C for several months before analysis but, more detrimentally, they were not centrifuged at high speed prior to storage, as recommended in the CK ELISA kit, but only realised after collection and storage. This requirement for centrifugation for CK analysis is to remove cellular debris which may contain CK which would then be released on thawing of the samples. This likely accounts for the variability and inconclusive nature of our results and is a point of learning that will be taken through to future trials.

There are several limitations to the work presented in this chapter. The lack of sequencing data at the time of writing prevents a deeper discussion on transcriptional changes after primary blast injury.

In contrast to the power calculations undertaken on normalisation counts from sequencing data (likely power of 0.6 instead of > 0.8), the post hoc power calculations on presto blue data suggest that the work was adequately power (power of 1.0/ 100%, alpha 0.01). The power means that there is a greater 90% chance of finding a statistically significant difference, if the difference is as big as hypothesised. Separate power calculations on different sequencing data from the model shows that this variation and sample size was inconsistent between hydrogel batches. This could be explained by the different injury methodologies utilised for each data set (blast and hydrogen peroxide injury). This limits the deductions on variability that can be made between the two power calculations. Further power calculations on counts data will be undertaken when the blast sequencing data is received from the trials. Conversely a smaller sample size and greater power was estimated when using the presto blue data. This perhaps suggests that different sample sizes are required to make statistical inferences from different analytical techniques. The experiments were conducted during the COVID-19 pandemic and this somewhat limited both characterisation of the models and data acquisition. Finally, although the trial was powered, the samples were non randomised. It was felt that adopting an alternating methodology of assigning cell culture plates to groups would reduce inherent bias. Furthermore the adoption of a randomisation protocol would complicate an already challenging experimental process without a significant gain in experimental validity.

6.5 Conclusions

In conclusion this chapter presents a robust model for exploring the cellular and molecular effects of blast shock wave on cells. The work illustrates the challenges in balancing experimental biological considerations against physical constraints to achieve optimal

methodology. In conclusion, data from the trials reveals differences in cell metabolism and creatinine kinase release when exposed to different degrees of primary blast shock wave.

7

Conclusions & Future Work

7.1 An Overview Of Blast

The field of mechanobiology aims to understand how cellular process are controlled by mechanical forces acting on the cell or tissue. The focus of this thesis has been to evaluate the impact of primary blast on skeletal muscle tissue and in particular to get insight into the cellular insights.

In chapter 1 this thesis appraised the concepts of blast loading. In particular it reviewed what factors influence explosive events and the types of experimental work that had been conducted in the field to date. It then outlined the important considerations for designing more mechanically appropriate experimental models within this area of research. As blast injury research has evolved from the study of the whole body, to whole organ and now to the whole cell response, so too should the fidelity of the experimental models employed. Chapter 1 shows that many of the models of tissue employed to study blast (particularly of the extremities) lack parity to the *in situ* environment. Furthermore, the analytical techniques adopted are narrow and limited in capturing temporal changes to the cell.

Finally this chapter outlined the aim of this thesis, namely the development of a mechanically relevant model of primary blast shock wave exposure in order to evaluate the molecular and cellular response to this injury.

7.2 Association Of Bulk RNA Sequencing To Blast Exposed Skeletal Muscle From Two Different In Vivo Models.

Chapter 2 outlines a major clinical problem facing combat casualties injured from improvised explosive devices on operations in Afghanistan. The chapter reviews the clinical phenomenon of progressive tissue necrosis, and the potential pathophysiological mechanisms that could cause this disease state. One plausible theory put forward in this chapter is that controlled cell death could be responsible for this progressive loss of muscle tissue. To evaluate this theory, Chapter 2 applies transcriptomics to animal skeletal muscle samples taken from two separate models of blast injury. The aim of this chapter was to build analysis pipelines for probing RNAseq data downstream of these type of injury experiments and also to make an initial assessment of changes at the transcription level in pathways involved in cell death using relevant archived material. tissue may be too damaged to allow RNA extraction for sequencing.

In one model, live explosive was used to expose terminally anaesthetised pigs to blast as part of a broader study examining resuscitation after blast injury. In a second model, an air pressure gun was used to expose the gastrocnemius muscle of the rabbit hindlimb to shock waves similar to explosive detonation.

As expected the models produced markedly different transcriptional profiles. Although both sample types were skeletal muscle exposed to a blast-relevant shock wave, the muscle samples were from different species, taken at different timepoints, with different levels of blast exposure. However when a gene set enrichment was applied to both datasets, remarkably, several common cellular pathways were commonly regulated. This included TNFα signalling via NF$\kappa\beta$, Oxidative phosphorylation, Myc targets V1, inflammatory response and IL6 Jak stat3 signalling.

To investigate the effects of blast on cell death mechanisms, gene sets for apoptosis, necrosis and necroptosis were applied to the gene data. This demonstrated markedly similar

distributions of gene expression associated with each cell death mechanism with none predominating. Whilst some of the mediators of cell death are shared between different pathways it suggests that cell death does occur after exposure of skeletal muscle to a primary blast shock wave, but with no one mechanism or pathway predominating

Chapter 2 therefore demonstrated the feasibility of applying a broad analytical technique such as bulk RNA sequencing to blast exposed muscle biopsies. These data provide an invaluable insight of soft tissue injury from blast and what may cause progressive tissue necrosis. It gave novel insights in the similarities of RNA expression between two different models of blast injury.

7.3 A Systematic Review Of Three Dimensional Models Of Skeletal Muscle Under Tension And Methods To Induce Traumatic Injury.

In order to build a more useful model of skeletal muscle, a systematic review of current 3D models of skeletal muscle, as well as approaches to damage these models was undertaken. The review employed systematic review methodology as outlined by the Cochrane handbook of systematic reviews.

The data from these articles showed that 3D models of skeletal muscle predominately used immortalised cell lines (C2C12) in fibrin or collagen matrices. Models utilised a combination of PCR, microscopy or force quantification as a means of characterisation. The data demonstrated there was no consistency across publications in what differentiation markers or functional methods were employed.

Amongst models that test an injury technique, there was a predominance for primary cell types. Toxin injury using snake venom (Cardiotoxin) was the most often used in the literature. Again there was no consistency amongst the literature on methods used to characterise these techniques.

The review highlighted several research gaps for adopting 3D models for blast injury research. Firstly, the review identified no model previously used in blast injury research that was not

tethered to the tissue culture plastic they were cultured in. This would preclude current available models for direct adoption in blast injury research. It also demonstrated the need for a new approach. Secondly, the review found no model that had employed broad unbiased techniques as part of characterisation. It also demonstrated the need for a set of core outcome for reporting 3D models in the literature. Lastly it showed that whilst damage could be inflicted on models, how this affected downstream cell processes was poorly defined.

These findings gave some framework for the development of a new model of skeletal muscle for use in exploring the effects of primary blast shock waves.

7.4 Development And Validation Of A Three Dimensional *In Vitro* Model Of Skeletal Muscle For Blast Loading.

Chapter 4 outlined the design and characterisation of a new 3D model of skeletal muscle. This work takes into account the research gaps outlined in the systematic review in Chapter 3. The model uses 3D printed anchors to culture fibrin hydrogels and C2C12 cells in order to induce myotube alignment and contraction. Unlike previous models, this set up allows the hydrogel constructs to be individually handled. Such a feature is important for models to be used in a variety of loading apparatus such as a Hopkinson bar, lithotripter or shock tube.

To characterise the model, functional and transcriptomic techniques were used. First, passive tension generated by hydrogels was evaluated by measuring post deflection. An analytical model of the predicted post deflection from a partially distributed load with Euler Bernoulli theory was then used to estimate the passive tension from the hydrogels. This showed that hydrogels had a marked increase in deflection on day 4, compared to baseline, and the passive tension was estimated as 0.5mN. This is a key functional characteristic as it shows that cell were orientating along the axis of strain.

To show that the hydrogels were differentiating into aligned myotubes, constructs were stained with phalloidin. Concurrently, RNA was extracted from differentiated constructs and sequenced. Analysis showed widespread upregulation of key markers of muscle

differentiation over 13 days of culture. These included myosin heavy chain isoforms, Paired box protein (PAX) and Myoblast determination protein 1.

Sequencing data form blast injury on its own would be difficult to contextualise. To fully appreciate the magnitude and breadth of observed changes, data from other mechanisms of cell damage would be useful contextual information. To address this, a method of cell injury was developed as on the proposed 3D model and characterised with RNA sequencing (amongst other techniques).

The results showed that using the method employed in this thesis to evaluate changes in passive tension was not sensitive enough to pick up small changes in tension after injury. Gene transcription was most notably altered by day 7, and significantly altered genes were potentially involved in DNA damage. This is a particularly interesting finding as it suggests this injury did not produce transient effects on cell behaviour, but long term alterations to cellular processes. DNA damage can be associated with therapeutic resistance or altered rates of apoptosis amongst many other processes.

A likelihood ratio test was applied to the data to evaluate the effects of time on gene regulation. It showed that that in the treatment group, three gene clusters trends were found. The largest cluster concerned gene downregulation over time. These genes were involved in muscle system process, muscle structure and contraction. Compared to control, the processes did not differ but were more strongly downregulated.

Chapter 4 developed and characterised a new model of skeletal muscle. It also demonstrated a method for induced repeatable damage and quantified this over time. This fulfilled research gaps identified in chapters 1 & 3, using techniques validated in Chapter 2.

7.5 Development Of A Frustum Pyramidal Shock Tube For Cell Culture.

To gain a detailed picture of a cell's response to primary blast loading a blast tube employing live explosives was developed and built. It used a frustum design which allowed for small quantities of explosive to be detonated to generate larger representative peak overpressures. Through a commissioning field trial, the tube was characterised across a range of increasing charge quantities of PE7 explosive. This work shows that the actual peak overpressures generated by the tube correlate closely with the modelled overpressures for the tube. Conwep software was used to estimate the peak overpressure at 2 metres of a 4kg HSB and the tube produced that overpressure with 30 g of PE7. Two charges were used in experiments, 5g and 30g, and pressure waveforms measured in the tube were consistent over multiple firings.

7.6 A Model To Assess Effects Of Primary Shock Wave On *In Vitro* Skeletal Muscle.

Utilising the models and platform validated in Chapter 4 & 5, a set of experiments were conducted to load *in vitro* models with primary blast shock wave. A three arm trial where hydrogel samples were assigned to one of high blast (30 grams PE7 charger), low blast (5g PE7 charge) and control (no charge, ambient conditions of shock tube). Hydrogels were tested for changes in cell metabolism and transcriptional effects for up to 7 days. Sample media was stored and then analysed for creatinine kinase release.

The metabolic data showed that hydrogel samples exposed to low blast recovered their metabolic function to baseline by day 3. This was then followed by a significant increase over baseline at day 7. This suggests that low dose shock waves increase cellular metabolism. In contrast, hydrogels exposed to high blast (30g) failed to recover their metabolism to baseline by day 7.

Creatinine kinase data also showed similar findings. Media from low samples showed large CK concentrations at early timepoints that decreased by Day 7. Media from high samples

showed no change in SK concentration compared to control. Due to the time constrains of this doctoral work, sequencing data was not ready for analysis at the time of submission. This will form part of post-doctoral work.

7.7 Future Directions

The work in this thesis has sought to be build a novel model for assessing the effect of a blast shock wave on skeletal muscle in way that permits detailed molecular and cellular analysis to understand the contribution of primary blast to progressive tissue death. To do this an *in vitro* model was developed, in order to allow a higher throughput of exposures and timepoints for analysis but with particular attention given to the fidelity and relevance of the shock wave input, and the tissue mimetic nature of the model itself. One oft-touted aspiration for the field of trauma is the unearthing of potential targets or drugs that could be used to treat these devastating injuries. However the process of target and drug discovery requires step wise experimentation and data validation in increasingly complex models. Furthermore it requires clear strategic direction in order to achieve this.

There are several future directions this work in this thesis could take to progress towards the aspiration of target discovery. One avenue would be to undertake further experimental work using *in vitro* models, particularly those that adopt primary cell lines. Preliminary work in this area is being pursued under the National Centre for the Replacement, Refinement and Reduction programme NC3Rs CRACK-IT challenge project STRATIS. Project STRATIS is designed to develop more complex *in vitro* models of human skeletal muscle which include innervation and vascularisation that could then be deployed in the sort of blast injury experiments detailed here. This will move the work forward to more human-relevance (in using primary human cells) thus providing another significant advantage over animal models, and will also allow the contribution from the mechanobiological effects of shock wave exposure on the neuromuscular junction and vascular structures to be investigated.

The use of multi cellular models in the tube would open up other avenues for analysis. In particular the use of single cell sequencing techniques. Single cell analysis would allow an appreciation of the contribution of different cell types, within multicellular tissues, to the diseased state and their gene transcription. In essence this work would allow a cellular atlas of blast injury to be constructed. The human cell atlas is an important current area of research in non-diseased tissue and would provide an interesting comparison to injured data. Single cell sequencing could also be applied to biopsy tissue from ongoing animal models of blast injury. Therefore it could provide primary cell *in vitro* data validation. The advantage of these two approaches is that it doesn't require any new models, but instead applies established capability to existing work.

Additional work could also focus on changing and isolating parameters of the shock wave itself to more fully understand the mechanical mechanisms causing particular biological responses. The identification and validation of targets for the amelioration of progressive tissue loss after blast injury requires the comparison, integration and validation of data from a variety of different models. This will include *in vivo* models but new *ex vivo* models also present a huge opportunity here. To achieve this, ex vivo perfusion models hold the most promise. Existing work on composite tissue allotransplantation has already developed perused models of whole limb tissue. Surgeons also already harvest islands of tissue on known blood vessels containing muscle, nerves, skin and bone for surgical reconstruction (termed free tissue transfer or free flaps). Such islands can be sized to fit wound defects. These islands could therefore be potentially perfused and loaded within the shock tube. This may generate human or animal tissue data for gene and protein analysis. It would also facilitate true direct comparison between ex vivo and *in vitro* models injured from primary shock waves from exactly the same source, where the ex vivo tissue is likely a much better surrogate for in vivo conditions.

Lastly, clinical level data is invaluable for moving a field towards its goal. The use of sequencing to map tissue and disease signalling is becoming normal practice. A concerted effort should be made to recruit, biopsy and sequence soft tissue from patients that have been

exposed to blast. Ideally this would be in the acute phase. However, a coordinated effort in this area remains to happen, but it would be invaluable progress in this field.

7.8 Conclusion

In conclusion this thesis has carried out a detailed appraisal of the field of blast wave injury on musculoskeletal tissue. A new model of skeletal muscle specifically for use in experimental work to understand the effects of blast loading on muscle function was developed.

The model employed 3D culture techniques to produce functional muscle tissue. The exposure of this model to primary blast with a frustum shock tube gave novel insights into the cellular behaviours of skeletal muscle cells.

References

1. US Department of Defence Blast Injury Research Coordinating office 2021 [Available from: https://blastinjuryresearch.health.mil/index.cfm/blast_injury_101/what_is_blast_injury.
2. Lord JM, Midwinter MJ, Chen YF, Belli A, Brohi K, Kovacs EJ, et al. The systemic immune response to trauma: an overview of pathophysiology and treatment. Lancet (London, England). 2014;384(9952):1455-65.
3. Xiao W, Mindrinos MN, Seok J, Cuschieri J, Cuenca AG, Gao H, et al. A genomic storm in critically injured humans. The Journal of experimental medicine. 2011;208(13):2581-90.
4. Gordon W, Talbot M, Fleming M, Shero J, Potter B, Stockinger ZT. High Bilateral Amputations and Dismounted Complex Blast Injury (DCBI). Military medicine. 2018;183(suppl_2):118-22.
5. Sory DRR. Dynamic Loading of Periosteum-derived mesenchymal stromal cells: Imperial College London; 2018.
6. Ngo T, Mendis P, Gupta A, Ramsay J. Blast loading and blast effects on structures–an overview. Electronic Journal of Structural Engineering. 2007;7(S1):76-91.
7. Sylven ET, Agarwal S, Briant CL, Cleveland RO. High strain rate testing of kidney stones. J Mater Sci Mater Med. 2004;15(5):613-7.
8. Evriviades D, Jeffery S, Cubison T, Lawton G, Gill M, Mortiboy D. Shaping the military wound: issues surrounding the reconstruction of injured servicemen at the Royal Centre for Defence Medicine. Philosophical transactions of the Royal Society of London Series B, Biological sciences. 2011;366(1562):219-30.
9. Staruch RMT, Jackson PC, Hodson J, Yim G, Foster MA, Cubison T, et al. Comparing the surgical timelines of military and civilians traumatic lower limb amputations. Ann Med Surg (Lond). 2016;6:81-6.
10. Maryland Uo. National Consortium for the Study of Terrorism and Responses to Terrorism (START) - The Global Terrorism Database (GTD). 2019.
11. Edwards DS, Phillip RD, Bosanquet N, Bull AM, Clasper JC. What Is the Magnitude and Long-term Economic Cost of Care of the British Military Afghanistan Amputee Cohort? Clin Orthop Relat Res. 2015;473(9):2848-55.
12. Blough DK, Hubbard S, McFarland LV, Smith DG, Gambel JM, Reiber GE. Prosthetic cost projections for servicemembers with major limb loss from Vietnam and OIF/OEF. J Rehabil Res Dev. 2010;47(4):387-402.
13. Wild H SB, Leboa C, Stave CD, Wren SM. Epidemiology of Injuries Sustained by Civilians and Local Combatants in Contemporary Armed Conflict: An Appeal for a Shared Trauma Registry Among Humanitarian Actors. World journal of surgery. 2020.
14. National Centre for the Replacement RRoAiRNR. Soft Tissue Regeneration after Traumatic Injury (STRATIS) 2022 [Available from: https://nc3rs.org.uk/crackit/sites/innovation/files/2021-06/Challenge%2037_STRATIS_Final.pdf.
15. Zuckerman S. The Problem of Blast Injuries: (Sections of Surgery and Pathology). Proc R Soc Med. 1941;34(3):171-92.
16. Defence USDo. Medical Research for Prevention, Mitigation, and Treatment of Blast Injuries. In: Defense, editor. 2006.

17. Leggieri Jr MJ, Bieler D, Bjarnason S, Cernak I, Franke A, Kirkman E, et al. Environmental toxicology of blast exposures: injury metrics, modelling, methods and standards. Journal of the Royal Army Medical Corps. 2019;165(1):7-9.
18. Baker WE. Explosions in air1973.
19. Friedlander FG. The diffraction of sound pulses. I. Diffraction by a semi-infinite plate. . Proceedings of the Royal Society of LondonA. 1946;186:322-44.
20. Dewey JM. The Friedlander Equations. In: Sochet I, editor. Blast Effects: Physical Properties of Shock Waves. Cham: Springer International Publishing; 2018. p. 37-55.
21. Hopkinson B. British ordnance board minutes 13565. The National Archives, Kew, UK. 1915;11.
22. C C. Lehrbuch der Balistic. Berlin1926.
23. Rigby SE, Tyas A, Clarke SD, Fay SD, Reay JJ, Warren JA, et al. Observations from Preliminary Experiments on Spatial and Temporal Pressure Measurements from Near-Field Free Air Explosions. International Journal of Protective Structures. 2015;6(2):175-90.
24. Mitra G. High-intensity air explosion induced shock laoding of structurs: consideration of a real gas in modelling a nonlinear compressible medium. . Proc of the Royal Society A: Mathematical, Physical and Engineering Sciences 2015;8(471).
25. Li D. Shock reflection and oblique shock waves. Journal of Mathematical Physics. 2007;48(12):123102.
26. Sonden A, Svensson B, Roman N, Brismar B, Palmblad J, Kjellstrom BT. Mechanisms of shock wave induced endothelial cell injury. Lasers in surgery and medicine. 2002;31(4):233-41.
27. Ning YL, Zhou YG. Shock tubes and blast injury modeling. Chinese journal of traumatology = Zhonghua chuang shang za zhi. 2015;18(4):187-93.
28. Tasissa AF, Hautefeuille M, Fitek JH, Radovitzky RA. On the formation of Friedlander waves in a compressed-gas-driven shock tube. Proceedings Mathematical, physical, and engineering sciences. 2016;472(2186):20150611.
29. Krassioukov AV, Ackery A, Schwartz G, Adamchik Y, Liu Y, Fehlings MG. An in vitro model of neurotrauma in organotypic spinal cord cultures from adult mice. Brain research Brain research protocols. 2002;10(2):60-8.
30. Faragher SR, Cleveland RO, Kumar S, Wiseman OJ, Turney BW. In Vitro Assessment of Three Clinical Lithotripters Employing Different Shock Wave Generators. Journal of endourology. 2016;30(5):560-5.
31. Nguyen TT, Pearce AP, Carpanen D, Sory D, Grigoriadis G, Newell N, et al. Experimental platforms to study blast injury. J R Army Med Corps. 2019;165(1):33-7.
32. Chen WW, Hudspeth MC, Claus B, Parab ND, Black JT, Fezzaa K, et al. In situ damage assessment using synchrotron X-rays in materials loaded by a Hopkinson bar. Philosophical transactions Series A, Mathematical, physical, and engineering sciences. 2014;372(2015):20130191.
33. Sarntinoranont M, Lee SJ, Hong Y, King MA, Subhash G, Kwon J, et al. High-strain-rate brain injury model using submerged acute rat brain tissue slices. Journal of neurotrauma. 2012;29(2):418-29.
34. Rotbaum Y, Puiu C, Rittel D, Domingos M. Quasi-static and dynamic in vitro mechanical response of 3D printed scaffolds with tailored pore size and architectures. Materials science & engineering C, Materials for biological applications. 2019;96:176-82.

35. Skotak M, Wang F, Alai A, Holmberg A, Harris S, Switzer RC, et al. Rat injury model under controlled field-relevant primary blast conditions: acute response to a wide range of peak overpressures. Journal of neurotrauma. 2013;30(13):1147-60.
36. Shridharani JK, Wood GW, Panzer MB, Capehart BP, Nyein MK, Radovitzky RA, et al. Porcine head response to blast. Frontiers in neurology. 2012;3:70.
37. Sawyer TW, Wang Y, Ritzel DV, Josey T, Villanueva M, Shei Y, et al. High-Fidelity Simulation of Primary Blast: Direct Effects on the Head. Journal of neurotrauma. 2016;33(13):1181-93.
38. Panzer MB, Matthews KA, Yu AW, Morrison B, 3rd, Meaney DF, Bass CR. A Multiscale Approach to Blast Neurotrauma Modeling: Part I - Development of Novel Test Devices for in vivo and in vitro Blast Injury Models. Frontiers in neurology. 2012;3:46.
39. Needham CE, Ritzel D, Rule GT, Wiri S, Young L. Blast Testing Issues and TBI: Experimental Models That Lead to Wrong Conclusions. Frontiers in neurology. 2015;6:72.
40. Goldstein LE, Fisher AM, Tagge CA, Zhang XL, Velisek L, Sullivan JA, et al. Chronic traumatic encephalopathy in blast-exposed military veterans and a blast neurotrauma mouse model. Sci Transl Med. 2012;4(134):134ra60.
41. Effgen GB, Vogel EW, 3rd, Lynch KA, Lobel A, Hue CD, Meaney DF, et al. Isolated primary blast alters neuronal function with minimal cell death in organotypic hippocampal slice cultures. Journal of neurotrauma. 2014;31(13):1202-10.
42. Effgen GB, Ong T, Nammalwar S, Ortuno AI, Meaney DF, Dale' Bass CR, et al. Primary Blast Exposure Increases Hippocampal Vulnerability to Subsequent Exposure: Reducing Long-Term Potentiation. Journal of neurotrauma. 2016;33(20):1901-12.
43. Effgen GB, Hue CD, Vogel E, 3rd, Panzer MB, Meaney DF, Bass CR, et al. A Multiscale Approach to Blast Neurotrauma Modeling: Part II: Methodology for Inducing Blast Injury to in vitro Models. Frontiers in neurology. 2012;3:23.
44. Panzer MB, Wood GW, Bass CR. Scaling in neurotrauma: how do we apply animal experiments to people? Experimental neurology. 2014;261:120-6.
45. Josey T, Ouellet S, Bieler D, Cernak I, Franke A, Gupta R, et al. Guidelines for reproducing blast exposures in the laboratory. Journal of the Royal Army Medical Corps. 2019;165(1):10.
46. NATO. Assessment and management of health risks among military personnel, Blast injury - NATO-Research Task Group. NATO - Research Task Group; 2021.
47. Bo C, Proud, William. Investigation of the Effects of High Pressure Pulses on Biological Samples [Phd Thesis]: Imperial College London; 2014.
48. Wang B, Zhou J, Banie L, Reed-Maldonado AB, Ning H, Lu Z, et al. Low-intensity extracorporeal shock wave therapy promotes myogenesis through PERK/ATF4 pathway. Neurourology and urodynamics. 2018;37(2):699-707.
49. Jeffery SLA. The Management of Combat Wounds: The British Military Experience. Advances in Wound Care. 2015;5(10):464-73.
50. Kirkman E, Watts S, Cooper G. Blast injury research models. Philosophical transactions of the Royal Society of London Series B, Biological sciences. 2011;366(1562):144-59.
51. Watts S, Nordmann G, Brohi K, Midwinter M, Woolley T, Gwyther R, et al. Evaluation of Prehospital Blood Products to Attenuate Acute Coagulopathy of Trauma in a Model of Severe Injury and Shock in Anesthetized Pigs. Shock (Augusta, Ga). 2015;44 Suppl 1(Suppl 1):138-48.

52. Lord JM, Midwinter MJ, Chen Y-F, Belli A, Brohi K, Kovacs EJ, et al. The systemic immune response to trauma: an overview of pathophysiology and treatment. The Lancet. 2014;384(9952):1455-65.
53. Johansson PI, Henriksen HH, Stensballe J, Gybel-Brask M, Cardenas JC, Baer LA, et al. Traumatic Endotheliopathy: A Prospective Observational Study of 424 Severely Injured Patients. Annals of surgery. 2017;265(3):597-603.
54. Naumann DN, Hazeldine J, Midwinter MJ, Hutchings SD, Harrison P. Poor microcirculatory flow dynamics are associated with endothelial cell damage and glycocalyx shedding after traumatic hemorrhagic shock. The journal of trauma and acute care surgery. 2018;84(1):81-8.
55. Rodriguez CJ, Tribble DR, Malone DL, Murray CK, Jessie EM, Khan M, et al. Treatment of Suspected Invasive Fungal Infection in War Wounds. Military medicine. 2018;183(suppl_2):142-6.
56. Rodriguez CJ, Weintrob AC, Shah J, Malone D, Dunne JR, Weisbrod AB, et al. Risk factors associated with invasive fungal infections in combat trauma. Surg Infect (Larchmt). 2014;15(5):521-6.
57. Tribble DR, Rodriguez CJ. Combat-Related Invasive Fungal Wound Infections. Curr Fungal Infect Rep. 2014;8(4):277-86.
58. Weintrob AC, Weisbrod AB, Dunne JR, Rodriguez CJ, Malone D, Lloyd BA, et al. Combat trauma-associated invasive fungal wound infections: epidemiology and clinical classification. Epidemiol Infect. 2015;143(1):214-24.
59. Mende K, Stewart L, Shaikh F, Bradley W, Lu D, Krauss MR, et al. Microbiology of combat-related extremity wounds: Trauma Infectious Disease Outcomes Study. Diagn Microbiol Infect Dis. 2019;94(2):173-9.
60. Spear AM, Lawton G, Staruch RMT, Rickard RF. Regenerative medicine and war: a front-line focus for UK defence. NPJ Regenerative medicine. 2018;3:13.
61. Slomka N, Gefen A. Relationship Between Strain Levels and Permeability of the Plasma Membrane in Statically Stretched Myoblasts. Annals of Biomedical Engineering. 2012;40(3):606-18.
62. Sinha B, Köster D, Ruez R, Gonnord P, Bastiani M, Abankwa D, et al. Cells respond to mechanical stress by rapid disassembly of caveolae. Cell. 2011;144(3):402-13.
63. Girton TS, Barocas VH, Tranquillo RT. Confined compression of a tissue-equivalent: collagen fibril and cell alignment in response to anisotropic strain. Journal of biomechanical engineering. 2002;124(5):568-75.
64. Ravin R, Blank PS, Steinkamp A, Rappaport SM, Ravin N, Bezrukov L, et al. Shear forces during blast, not abrupt changes in pressure alone, generate calcium activity in human brain cells. PloS one. 2012;7(6):e39421.
65. Takahashi T, Nakagawa K, Tada S, Tsukamoto A. Low-energy shock waves evoke intracellular Ca2+ increases independently of sonoporation. Scientific Reports. 2019;9(1):3218.
66. Suhr D, Brummer F, Hulser DF. Cavitation-generated free radicals during shock wave exposure: investigations with cell-free solutions and suspended cells. Ultrasound in medicine & biology. 1991;17(8):761-8.
67. Zander NE, Piehler T, Banton R, Benjamin R. Effects of repetitive low-pressure explosive blast on primary neurons and mixed cultures. Journal of neuroscience research. 2016;94(9):827-36.

68. Chavko M, Prusaczyk WK, McCarron RM. Lung injury and recovery after exposure to blast overpressure. The Journal of trauma. 2006;61(4):933-42.
69. Arun P, Spadaro J, John J, Gharavi RB, Bentley TB, Nambiar MP. Studies on blast traumatic brain injury using in-vitro model with shock tube. Neuroreport. 2011;22(8):379-84.
70. Latorre E, Kale S, Casares L, Gómez-González M, Uroz M, Valon L, et al. Active superelasticity in three-dimensional epithelia of controlled shape. Nature. 2018;563(7730):203-8.
71. Zhang J, Shrivastava S, Cleveland RO, Rabbitts TH. Lipid-mRNA Nanoparticle Designed to Enhance Intracellular Delivery Mediated by Shock Waves. ACS Applied Materials & Interfaces. 2019;11(11):10481-91.
72. Barry-Hamilton V, Spangler R, Marshall D, McCauley S, Rodriguez HM, Oyasu M, et al. Allosteric inhibition of lysyl oxidase-like-2 impedes the development of a pathologic microenvironment. Nat Med. 2010;16(9):1009-17.
73. Leeper NJ. The Role of Necroptosis in Atherosclerotic Disease. JACC: Basic to Translational Science. 2016;1(6):548-50.
74. Zhou X, Xie L, Xia L, Bergmann F, Büchler MW, Kroemer G, et al. RIP3 attenuates the pancreatic damage induced by deletion of ATG7. Cell Death & Disease. 2017;8(7):e2918-e.
75. Wang G, Qu FZ, Li L, Lv JC, Sun B. Necroptosis: a potential, promising target and switch in acute pancreatitis. Apoptosis : an international journal on programmed cell death. 2016;21(2):121-9.
76. Zhou M, He J, Shi Y, Liu X, Luo S, Cheng C, et al. ABIN3 Negatively Regulates Necroptosis-induced Intestinal Inflammation Through Recruiting A20 and Restricting the Ubiquitination of RIPK3 in Inflammatory Bowel Disease. Journal of Crohn's and Colitis. 2020;15(1):99-114.
77. Wang R, Li H, Wu J, Cai Z-Y, Li B, Ni H, et al. Gut stem cell necroptosis by genome instability triggers bowel inflammation. Nature. 2020;580(7803):386-90.
78. Gong Y, Fan Z, Luo G, Yang C, Huang Q, Fan K, et al. The role of necroptosis in cancer biology and therapy. Molecular Cancer. 2019;18(1):100.
79. Ito Y, Ofengeim D, Najafov A, Das S, Saberi S, Li Y, et al. RIPK1 mediates axonal degeneration by promoting inflammation and necroptosis in ALS. Science (New York, NY). 2016;353(6299):603-8.
80. Chevin M, Sébire G, Deltenre P, Kadhim H. Necroptotic neuronal cell death in amyotrophic lateral sclerosis: A relevant hypothesis with potential therapeutic implication? Med Hypotheses. 2020;144:110295.
81. Caccamo A, Branca C, Piras IS, Ferreira E, Huentelman MJ, Liang WS, et al. Necroptosis activation in Alzheimer's disease. Nature Neuroscience. 2017;20(9):1236-46.
82. Spear AM, Davies EM, Taylor C, Whiting R, Macildowie S, Kirkman E, et al. Blast Wave Exposure to the Extremities Causes Endothelial Activation and Damage. Shock (Augusta, Ga). 2015;44(5):470-8.
83. Wang H, Zhang W-J, Gao J-H, Liu J-R, Liu Z-Y, Xia B-Q, et al. Global gene expression profiling of blast lung injury of goats exposed to shock wave. Chinese journal of traumatology = Zhonghua chuang shang za zhi. 2020;23(5):249-57.
84. Warren HS, Elson CM, Hayden DL, Schoenfeld DA, Cobb JP, Maier RV, et al. A genomic score prognostic of outcome in trauma patients. Mol Med. 2009;15(7-8):220-7.
85. Xu HT, Guo JC, Liu HZ, Jin WW. A Time-Series Analysis of Severe Burned Injury of Skin Gene Expression Profiles. Cellular Physiology and Biochemistry. 2018;49(4):1492-8.

86. Meng Q, Zhuang Y, Ying Z, Agrawal R, Yang X, Gomez-Pinilla F. Traumatic Brain Injury Induces Genome-Wide Transcriptomic, Methylomic, and Network Perturbations in Brain and Blood Predicting Neurological Disorders. EBioMedicine. 2017;16:184-94.
87. Gallego Romero I, Pai AA, Tung J, Gilad Y. RNA-seq: impact of RNA degradation on transcript quantification. BMC Biology. 2014;12(1):42.
88. Langhans SA. Three-Dimensional in Vitro Cell Culture Models in Drug Discovery and Drug Repositioning. Frontiers in Pharmacology. 2018;9.
89. Khodabukus A, Kaza A, Wang J, Prabhu N, Goldstein R, Vaidya VS, et al. Tissue-Engineered Human Myobundle System as a Platform for Evaluation of Skeletal Muscle Injury Biomarkers. Toxicological sciences : an official journal of the Society of Toxicology. 2020;176(1):124-36.
90. Higgins JP, Thomas J, Chandler J, Cumpston M, Li T, Page MJ, et al. Cochrane handbook for systematic reviews of interventions: John Wiley & Sons; 2019.
91. Page MJ, McKenzie JE, Bossuyt PM, Boutron I, Hoffmann TC, Mulrow CD, et al. The PRISMA 2020 statement: an updated guideline for reporting systematic reviews. Systematic reviews. 2021;10(1):1-11.
92. Ouzzani M, Hammady H, Fedorowicz Z, Elmagarmid A. Rayyan—a web and mobile app for systematic reviews. Systematic reviews. 2016;5(1):1-10.
93. Program NT. Office of Health Assessment and Translation. OHAT Risk of Bias Rating Tool for Human and Animal Studies. 2014.
94. Heher P, Maleiner B, Prüller J, Teuschl AH, Kollmitzer J, Monforte X, et al. A novel bioreactor for the generation of highly aligned 3D skeletal muscle-like constructs through orientation of fibrin via application of static strain. Acta biomaterialia. 2015;24:251-65.
95. Cheema U, Yang SY, Mudera V, Goldspink GG, Brown RA. 3-D in vitro model of early skeletal muscle development. Cell motility and the cytoskeleton. 2003;54(3):226-36.
96. Kim JH, Seol Y-J, Ko IK, Kang H-W, Lee YK, Yoo JJ, et al. 3D Bioprinted Human Skeletal Muscle Constructs for Muscle Function Restoration. Scientific reports. 2018;8(1):12307.
97. Vandenburgh HH, Karlisch P, Farr L. Maintenance of highly contractile tissue-cultured avian skeletal myotubes in collagen gel. In vitro cellular & developmental biology : journal of the Tissue Culture Association. 1988;24(3):166-74.
98. Afshar Bakooshli M, Lippmann ES, Mulcahy B, Iyer N, Nguyen CT, Tung K, et al. A 3D culture model of innervated human skeletal muscle enables studies of the adult neuromuscular junction. eLife. 2019;8.
99. Afshar ME, Abraha HY, Bakooshli MA, Davoudi S, Thavandiran N, Tung K, et al. A 96-well culture platform enables longitudinal analyses of engineered human skeletal muscle microtissue strength. Scientific reports. 2020;10(1):6918.
100. Donnelly K, Khodabukus A, Philp A, Deldicque L, Dennis RG, Baar K. A novel bioreactor for stimulating skeletal muscle in vitro. Tissue engineering Part C, Methods. 2010;16(4):711-8.
101. Acosta FM, Jia UTA, Stojkova K, Howland KK, Guda T, Pacelli S, et al. Diabetic Conditions Confer Metabolic and Structural Modifications to Tissue-Engineered Skeletal Muscle. Tissue engineering Part A. 2020.
102. Ramade A, Legant WR, Picart C, Chen CS, Boudou T. Microfabrication of a platform to measure and manipulate the mechanics of engineered microtissues. Methods Cell Biol. 2014;121:191-211.

103. Powell C, Shansky J, Del Tatto M, Forman DE, Hennessey J, Sullivan K, et al. Tissue-engineered human bioartificial muscles expressing a foreign recombinant protein for gene therapy. Human gene therapy. 1999;10(4):565-77.
104. Player DJ, Martin NR, Passey SL, Sharples AP, Mudera V, Lewis MP. Acute mechanical overload increases IGF-I and MMP-9 mRNA in 3D tissue-engineered skeletal muscle. Biotechnology letters. 2014;36(5):1113-24.
105. Kalson NS, Holmes DF, Kapacee Z, Otermin I, Lu Y, Ennos RA, et al. An experimental model for studying the biomechanics of embryonic tendon: Evidence that the development of mechanical properties depends on the actinomyosin machinery. Matrix Biol. 2010;29(8):678-89.
106. Madden L, Juhas M, Kraus WE, Truskey GA, Bursac N. Bioengineered human myobundles mimic clinical responses of skeletal muscle to drugs. eLife. 2015;4:e04885.
107. Smith AS, Passey S, Greensmith L, Mudera V, Lewis MP. Characterization and optimization of a simple, repeatable system for the long term in vitro culture of aligned myotubes in 3D. Journal of cellular biochemistry. 2012;113(3):1044-53.
108. Fan T, Wang S, Jiang Z, Ji S, Cao W, Liu W, et al. Controllable assembly of skeletal muscle-like bundles through 3D bioprinting. Biofabrication. 2021;14(1).
109. Shah R, Knowles JC, Hunt NP, Lewis MP. Development of a novel smart scaffold for human skeletal muscle regeneration. Journal of tissue engineering and regenerative medicine. 2016;10(2):162-71.
110. Khodabukus A, Baar K. Defined electrical stimulation emphasizing excitability for the development and testing of engineered skeletal muscle. Tissue Eng Part C Methods. 2012;18(5):349-57.
111. Hansen A, Eder A, Bonstrup M, Flato M, Mewe M, Schaaf S, et al. Development of a drug screening platform based on engineered heart tissue. Circulation research. 2010;107(1):35-44.
112. Vandenburgh H, Shansky J, Benesch-Lee F, Barbata V, Reid J, Thorrez L, et al. Drug-screening platform based on the contractility of tissue-engineered muscle. Muscle & Nerve. 2008;37(4):438-47.
113. Rao L, Qian Y, Khodabukus A, Ribar T, Bursac N. Engineering human pluripotent stem cells into a functional skeletal muscle tissue. Nature communications. 2018;9(1):126.
114. Bian W, Bursac N. Tissue engineering of functional skeletal muscle: challenges and recent advances. IEEE engineering in medicine and biology magazine : the quarterly magazine of the Engineering in Medicine & Biology Society. 2008;27(5):109-13.
115. Sato M, Ito A, Kawabe Y, Nagamori E, Kamihira M. Enhanced contractile force generation by artificial skeletal muscle tissues using IGF-I gene-engineered myoblast cells. Journal of bioscience and bioengineering. 2011;112(3):273-8.
116. Dennis RG, Kosnik PE, 2nd. Excitability and isometric contractile properties of mammalian skeletal muscle constructs engineered in vitro. In vitro cellular & developmental biology Animal. 2000;36(5):327-35.
117. Martin NR, Passey SL, Player DJ, Khodabukus A, Ferguson RA, Sharples AP, et al. Factors affecting the structure and maturation of human tissue engineered skeletal muscle. Biomaterials. 2013;34(23):5759-65.
118. Sakar MS, Neal D, Boudou T, Borochin MA, Li Y, Weiss R, et al. Formation and optogenetic control of engineered 3D skeletal muscle bioactuators. Lab on a chip. 2012;12(23):4976-85.

119. Huang Y-C, Dennis RG, Larkin L, Baar K. Rapid formation of functional muscle in vitro using fibrin gels. Journal of Applied Physiology. 2005;98(2):706-13.
120. Powell CA, Smiley BL, Mills J, Vandenburgh HH. Mechanical stimulation improves tissue-engineered human skeletal muscle. American journal of physiology Cell physiology. 2002;283(5):C1557-65.
121. Bian W, Liau B, Badie N, Bursac N. Mesoscopic hydrogel molding to control the 3D geometry of bioartificial muscle tissues. Nature protocols. 2009;4(10):1522-34.
122. Legant WR, Pathak A, Yang MT, Deshpande VS, McMeeking RM, Chen CS. Microfabricated tissue gauges to measure and manipulate forces from 3D microtissues. Proceedings of the National Academy of Sciences of the United States of America. 2009;106(25):10097-102.
123. Lam MT, Huang Y-C, Birla RK, Takayama S. Microfeature guided skeletal muscle tissue engineering for highly organized 3-dimensional free-standing constructs. Biomaterials. 2009;30(6):1150-5.
124. Rhim C, Lowell DA, Reedy MC, Slentz DH, Zhang SJ, Kraus WE, et al. Morphology and ultrastructure of differentiating three-dimensional mammalian skeletal muscle in a collagen gel. Muscle & nerve. 2007;36(1):71-80.
125. Maffioletti SM, Sarcar S, Henderson ABH, Mannhardt I, Pinton L, Moyle LA, et al. Three-Dimensional Human iPSC-Derived Artificial Skeletal Muscles Model Muscular Dystrophies and Enable Multilineage Tissue Engineering. Cell reports. 2018;23(3):899-908.
126. Khodabukus A, Baar K. Regulating fibrinolysis to engineer skeletal muscle from the C2C12 cell line. Tissue Eng Part C Methods. 2009;15(3):501-11.
127. Akiyama Y, Iwabuchi K, Furukawa Y, Morishima K. Electrical stimulation of cultured lepidopteran dorsal vessel tissue: an experiment for development of bioactuators. In Vitro Cell Dev Biol Anim. 2010;46(5):411-5.
128. Juhas M, Engelmayr GC, Jr., Fontanella AN, Palmer GM, Bursac N. Biomimetic engineered muscle with capacity for vascular integration and functional maturation in vivo. Proceedings of the National Academy of Sciences of the United States of America. 2014;111(15):5508-13.
129. Capel AJ, Rimington RP, Fleming JW, Player DJ, Baker LA, Turner MC, et al. Scalable 3D Printed Molds for Human Tissue Engineered Skeletal Muscle. Frontiers in bioengineering and biotechnology. 2019;7:20.
130. Shansky J, Del Tatto M, Chromiak J, Vandenburgh H. A simplified method for tissue engineering skeletal muscle organoids in vitro. In vitro cellular & developmental biology Animal. 1997;33(9):659-61.
131. Xu B, Zhang M, Perlingeiro RCR, Shen W. Skeletal Muscle Constructs Engineered from Human Embryonic Stem Cell Derived Myogenic Progenitors Exhibit Enhanced Contractile Forces When Differentiated in a Medium Containing EGM-2 Supplements. Advanced biosystems. 2019;3(12):e1900005.
132. Vandenburgh HH, Hatfaludy S, Karlisch P, Shansky J. Skeletal muscle growth is stimulated by intermittent stretch-relaxation in tissue culture. The American journal of physiology. 1989;256(3 Pt 1):C674-82.
133. Brady MA, Lewis MP, Mudera V. Synergy between myogenic and non-myogenic cells in a 3D tissue-engineered craniofacial skeletal muscle construct. Journal of tissue engineering and regenerative medicine. 2008;2(7):408-17.
134. Matsumoto T, Sasaki J-i, Alsberg E, Egusa H, Yatani H, Sohmura T. Three-dimensional cell and tissue patterning in a strained fibrin gel system. PloS one. 2007;2(11):e1211.

135. Morimoto Y, Kato-Negishi M, Onoe H, Takeuchi S. Three-dimensional neuron–muscle constructs with neuromuscular junctions. Biomaterials. 2013;34(37):9413-9.
136. Okano T, Matsuda T. Muscular tissue engineering: capillary-incorporated hybrid muscular tissues in vivo tissue culture. Cell transplantation. 1998;7(5):435-42.
137. Vandenburgh H, Del Tatto M, Shansky J, Lemaire J, Chang A, Payumo F, et al. Tissue-engineered skeletal muscle organoids for reversible gene therapy. Human gene therapy. 1996;7(17):2195-200.
138. Fleming JW, Capel AJ, Rimington RP, Wheeler P, Leonard AN, Bishop NC, et al. Bioengineered human skeletal muscle capable of functional regeneration. BMC Biology. 2020;18(1):145.
139. Rajabian N, Shahini A, Asmani M, Vydiam K, Choudhury D, Nguyen T, et al. Bioengineered Skeletal Muscle as a Model of Muscle Aging and Regeneration. Tissue engineering Part A. 2021;27(1-2):74-86.
140. Davis BNJ, Santoso JW, Walker MJ, Cheng CS, Koves TR, Kraus WE, et al. Human, Tissue-Engineered, Skeletal Muscle Myobundles to Measure Oxygen Uptake and Assess Mitochondrial Toxicity. Tissue engineering Part C, Methods. 2017;23(4):189-99.
141. Martin NRW, Aguilar-Agon K, Robinson GP, Player DJ, Turner MC, Myers SD, et al. Hypoxia Impairs Muscle Function and Reduces Myotube Size in Tissue Engineered Skeletal Muscle. Journal of cellular biochemistry. 2017;118(9):2599-605.
142. Juhas M, Abutaleb N, Wang JT, Ye J, Shaikh Z, Sriworarat C, et al. Incorporation of macrophages into engineered skeletal muscle enables enhanced muscle regeneration. Nat Biomed Eng. 2018;2(12):942-54.
143. Tiburcy M, Markov A, Kraemer LK, Christalla P, Rave-Fraenk M, Fischer HJ, et al. Regeneration competent satellite cell niches in rat engineered skeletal muscle. FASEB bioAdvances. 2019;1(12):731-46.
144. Agrawal G, Aung A, Varghese S. Skeletal muscle-on-a-chip: an in vitro model to evaluate tissue formation and injury. Lab on a chip. 2017;17(20):3447-61.
145. Lee PH, Vandenburgh HH. Skeletal muscle atrophy in bioengineered skeletal muscle: a new model system. Tissue engineering Part A. 2013;19(19-20):2147-55.
146. Shimizu K, Genma R, Gotou Y, Nagasaka S, Honda H. Three-Dimensional Culture Model of Skeletal Muscle Tissue with Atrophy Induced by Dexamethasone. Bioengineering (Basel). 2017;4(2).
147. Carter M, Shieh JC. Chapter 13 - Cell Culture Techniques. In: Carter M, Shieh JC, editors. Guide to Research Techniques in Neuroscience. New York: Academic Press; 2010. p. 281-96.
148. Grabowska I, Szeliga A, Moraczewski J, Czaplicka I, Brzoska E. Comparison of satellite cell-derived myoblasts and C2C12 differentiation in two- and three-dimensional cultures: changes in adhesion protein expression. Cell biology international. 2011;35(2):125-33.
149. Langelaan ML, Boonen KJ, Rosaria-Chak KY, van der Schaft DW, Post MJ, Baaijens FP. Advanced maturation by electrical stimulation: Differences in response between C2C12 and primary muscle progenitor cells. Journal of tissue engineering and regenerative medicine. 2011;5(7):529-39.
150. Maganaris CN, Baltzopoulos V, Ball D, Sargeant AJ. In vivo specific tension of human skeletal muscle. Journal of Applied Physiology. 2001;90(3):865-72.
151. Powell PL, Roy RR, Kanim P, Bello MA, Edgerton VR. Predictability of skeletal muscle tension from architectural determinations in guinea pig hindlimbs. J Appl Physiol Respir Environ Exerc Physiol. 1984;57(6):1715-21.

152. Bahler AS, Fales JT, Zierler KL. The dynamic properties of mammalian skeletal muscle. J Gen Physiol. 1968;51(3):369-84.
153. Weisman A, Chou B, O'Brien J, Shea KJ. Polymer antidotes for toxin sequestration. Advanced drug delivery reviews. 2015;90:81-100.
154. Liang C-C, Park AY, Guan J-L. In vitro scratch assay: a convenient and inexpensive method for analysis of cell migration in vitro. Nature Protocols. 2007;2(2):329-33.
155. Mukund K, Subramaniam S. Skeletal muscle: A review of molecular structure and function, in health and disease. Wiley Interdiscip Rev Syst Biol Med. 2020;12(1):e1462-e.
156. Yablonka-Reuveni Z, Nameroff M. Skeletal muscle cell populations. Separation and partial characterization of fibroblast-like cells from embryonic tissue using density centrifugation. Histochemistry. 1987;87(1):27-38.
157. Brown DM, Parr T, Brameld JM. Myosin heavy chain mRNA isoforms are expressed in two distinct cohorts during C2C12 myogenesis. Journal of Muscle Research and Cell Motility. 2012;32(6):383-90.
158. Santofimia-Castaño P, Lan W, Bintz J, Gayet O, Carrier A, Lomberk G, et al. Inactivation of NUPR1 promotes cell death by coupling ER-stress responses with necrosis. Scientific Reports. 2018;8(1):16999.
159. Fritsch M, Günther SD, Schwarzer R, Albert M-C, Schorn F, Werthenbach JP, et al. Caspase-8 is the molecular switch for apoptosis, necroptosis and pyroptosis. Nature. 2019;575(7784):683-7.
160. Khodabukus A, Kaza A, Wang J, Prabhu N, Goldstein R, Vaidya VS, et al. Tissue-Engineered Human Myobundle System as a Platform for Evaluation of Skeletal Muscle Injury Biomarkers. Toxicological Sciences. 2020;176(1):124-36.
161. Cheema U, Yang SY, Mudera V, Goldspink GG, Brown RA. 3-D in vitro model of early skeletal muscle development. Cell motility and the cytoskeleton. 2003;54(3):226-36.
162. Rowan P. Rimington JWF, Andrew J. Capel, Patrick C. Wheeler, Mark P. Lewis. Bioengineered model of the human motor unit with physiologically functional neuromuscular junctions. biorxiv. 2020.
163. Vesga-Castro C, Aldazabal J, Vallejo-Illarramendi A, Paredes J. Contractile force assessment methods for in vitro skeletal muscle tissues. eLife. 2022;11:e77204.
164. Shimizu K, Ohsumi S, Kishida T, Mazda O, Honda H. Fabrication of contractile skeletal muscle tissues using directly converted myoblasts from human fibroblasts. Journal of bioscience and bioengineering. 2020;129(5):632-7.
165. Xiang J, Wan C, Guo R, Guo D. Is Hydrogen Peroxide a Suitable Apoptosis Inducer for All Cell Types? Biomed Res Int. 2016;2016:7343965.
166. Kim W, Kim J, Park HS, Jeon JS. Development of Microfluidic Stretch System for Studying Recovery of Damaged Skeletal Muscle Cells. Micromachines (Basel). 2018;9(12).
167. Prochniewicz E, Lowe DA, Spakowicz DJ, Higgins L, O'Conor K, Thompson LV, et al. Functional, structural, and chemical changes in myosin associated with hydrogen peroxide treatment of skeletal muscle fibers. American Journal of Physiology-Cell Physiology. 2008;294(2):C613-C26.
168. Security. NAoEaNRCftNAaUSDoH. News & Terrorism Communicating in a Crisis. In: Security H, editor. Homeland Security. Web.
169. National Academy of Engineering and the National Research Council of the Nationa Academies USDoHS. IED attack Improvised Explosive Devices. www.dhs.gov.
170. Bowen IG, Fletcher ER, Richmond DR, Hirsch FG, White CS. Biophysical mechanisms and scaling procedures applicable in assessing responses of the thorax energized by air-blast

overpressures or by nonpenetrating missiles. Annals of the New York Academy of Sciences. 1968;152(1):122-46.
171. Bowen IG, Fletcher ER, Richmond DR. Estimate of man's tolerance to the direct effects of air blast. LOVELACE FOUNDATION FOR MEDICAL EDUCATION AND RESEARCH ALBUQUERQUE NM; 1968.
172. Wood GWP, M.B., Yu, A.W., Rafaels, K.A., Matthews, K.A., Bass, C.R. Scaling in blast neurotrauma. Proceedings of the international research council on biomechanics of injury. 2013:549-58.
173. Mediavilla Varas J, Philippens M, Meijer SR, van den Berg AC, Sibma PC, van Bree JLMJ, et al. Physics of IED Blast Shock Tube Simulations for mTBI Research. Frontiers in neurology. 2011;2.
174. Nyein MK, Jason AM, Yu L, Pita CM, Joannopoulos JD, Moore DF, et al. In silico investigation of intracranial blast mitigation with relevance to military traumatic brain injury. Proceedings of the National Academy of Sciences. 2010;107(48):20703-8.
175. Moss WC, King MJ, Blackman EG. Distinguishing realistic military blasts from firecrackers in mitigation studies of blast-induced traumatic brain injury. Proceedings of the National Academy of Sciences. 2011;108(17):E82-E.
176. Sundaramurthy A, Chandra N. A Parametric Approach to Shape Field-Relevant Blast Wave Profiles in Compressed-Gas-Driven Shock Tube. Frontiers in neurology. 2014;5.
177. Sedman A. Using a small explosive charge to produce the on-target effect of a large explosive charge (including the negative phase). . In: Staruch RMT, editor. 2017.
178. Ouellet S, Petel OE. On the prospective contributions of the shock physics community to outstanding issues concerning blast-induced traumatic brain injury. Shock Waves. 2017;27(6):821-7.
179. Sawyer TW, Ritzel DV, Wang Y, Josey T, Villanueva M, Nelson P, et al. Primary Blast Causes Delayed Effects without Cell Death in Shell-Encased Brain Cell Aggregates. Journal of neurotrauma. 2018;35(1):174-86.
180. Kumar R, Nedungadi A. Using Gas-Driven Shock Tubes to Produce Blast Wave Signatures. Frontiers in neurology. 2020;11:90-.
181. Nguyen T-TN. The Characterisation of a Shock Tube System for Blast Injury Studies: Imperial College London; 2016.
182. Almeida MF, Piehler T, Carstens KE, Zhao M, Samadi M, Dudek SM, et al. Distinct and dementia-related synaptopathy in the hippocampus after military blast exposures. Brain Pathol. 2021;31(3):e12936.
183. Stewart S. Fracture non-union: using the blast wave to our advantage. Imperial College: Imperial College London; 2022.
184. Bowen I.G FER, Richmond D.R. Effect of man’s tolerance to the direct effects of air blast. Defence Atomic Support Agency; 1968.
185. Salcedo-Jiménez R, Koenig JB, Lee OJ, Gibson TWG, Madan P, Koch TG. Extracorporeal Shock Wave Therapy Enhances the In Vitro Metabolic Activity and Differentiation of Equine Umbilical Cord Blood Mesenchymal Stromal Cells. Frontiers in Veterinary Science. 2020;7.
186. Chao Y-H, Tsuang Y-H, Sun J-S, Chen L-T, Chiang Y-F, Wang C-C, et al. Effects of Shock Waves on Tenocyte Proliferation and Extracellular Matrix Metabolism. Ultrasound in medicine & biology. 2008;34(5):841-52.

187. Marom A, Berkovitch Y, Toume S, Alvarez-Elizondo MB, Weihs D. Non-damaging stretching combined with sodium pyruvate supplement accelerate migration of fibroblasts and myoblasts during gap closure. Clinical biomechanics (Bristol, Avon). 2019;62:96-103.